Orai1 as a novel target in hypoxia-induced pulmonary VSMC remodelling

Emily Marie Woodhouse

Submitted in accordance with the requirements for the degree of Doctor of Philosophy

The University of Leeds
Leeds Institute of Cardiovascular and Metabolic Medicine
School of Medicine

October 2019

Intellectual property and publication statements

The candidate confirms that the work submitted is her own and that appropriate credit has been given where reference has been made to the work of others.

Acknowledgements

First and foremost, I would like to thank Professor Chris Peers who is sadly no longer with us. Chris approached me with a project funded by the British Heart Foundation and changed my life. After his passing and despite the struggles that followed, I have kept Chris at the forefront of my mind to ensure his investment in me was worthwhile and to ensure his legacy continues. Thank you for putting your faith in me. These thanks extend to the British Heart Foundation for providing funding for this project.

My utmost thanks goes to Dr Marc Bailey. Although Marc didn’t know me, he picked up the pieces after Chris’ passing and took me under his wing. The support Marc has given me is second to none, and I thank him for sharing his expertise with me, allowing me to grow and far surpass my expectations of myself. I am eternally grateful for your support and for believing in me. These thanks extend equally to Professor David Beech, Dr Jian Shi and the rest of the Bailey group.

I am thankful to the close friends I have made throughout my journey, for the training and support you have provided me with, and most importantly for the time we spent together to stay sane and grounded: Drs Jack Garnham, Faye Garrod, Hannah Kirton, Hayley Duckles, John Boyle and Mr Yuan-Ming.

Forever the Peers group.

Thank you to Dr Sarah Calaghan. You are my role model. You are an example of a strong successful woman in science. I am eternally grateful to you.

Special thanks to David Myers and Simon Futers for all your assistance with my *in-vivo* experiments. When difficulty arose, you were willing to give your time up

to ensure things ran smoothly. You are caring people, and this should never go unnoticed. I will remember you. Alan Burnett, these thanks extend to you. Thank you for believing in me and for your words of encouragement.

Thank you to my family and to my best friend and fiancé, Jamie, for inspiring me to keep going when I almost gave in. You believed in me when I didn’t believe in myself and with each new day, you continue to believe in me. What I have achieved over the last six years wouldn’t have been possible without your love. I am truly blessed.

Abstract

Pulmonary hypertension (PH) presents with excessive vasoconstriction and vascular smooth muscle cell (VSMC) proliferation, which contribute to right ventricular (RV) failure and death. Therapeutic strategies target vasoconstriction but are only effective in a small proportion of patients. Thus, novel anti-proliferative therapeutics may be pivotal in PH management. Orai1-mediated store-operated Ca^{2+} entry (SOCE) and T-type Ca^{2+} channel-mediated voltage-dependent Ca^{2+} entry are associated with proliferation in multiple diseases including PH.

To investigate the potential of these Ca^{2+} channels as anti-proliferative targets, human pulmonary artery smooth muscle cells (HPASMCs) were validated as a suitable *in-vitro* model to study the mechanisms of hypoxia-induced pulmonary VSMC proliferation. Widely used T-type Ca^{2+} channel inhibitors, mibefradil and NNC55-0396, reduced proliferation of HPASMCs ($p<0.05$), but demonstrated poor selectivity due to off-target modulation of Orai1-mediated SOCE with IC_{50} values of 10.38 and 10.21 µM, respectively. This effect was observed in the absence of T-type Ca^{2+} channel expression in wild type HEK293 cells. These data add to the plethora of off-target effects previously demonstrated by these inhibitors. T-type Ca^{2+} channels were not upregulated in hypoxia either *in vitro* or *in vivo*, pivoting the focus to Orai1.

Significant upregulation of Orai1 was observed *in vitro* ($p<0.05$), which was paralleled by marked Orai1 upregulation *in vivo*. The novel, selective Orai1 inhibitor, JPIII, significantly reduced HPASMC proliferation *in vitro* ($p<0.0001$), an effect that was not observed in normoxia. Continuous infusion of JPIII in an *in-vivo* model of CH-induced PH protected from the increase in RV hypertrophy

and distal muscularisation observed in the vehicle-treated CH-induced PH cohort ($p<0.05$).

In conclusion, no hypoxia-induced upregulation in T-type Ca^{2+} channel expression, combined with a limited number of selective inhibitors and complete lack of inhibitors in the clinic limit the potential of T-type Ca^{2+} channels as anti-proliferative targets in CH-induced PH. Hypoxia-induced upregulation of Orai1 both *in vitro* and *in vivo*, the anti-proliferative effects of JPIII *in vitro* and the ability of JPIII to protect from RV hypertrophy and distal muscularisation *in vivo* support Orai1 as a viable anti-proliferative target in CH-induced PH for a translational drug development programme.

Table of contents

List of figures

List of tables

Abbreviations

5-HT	Serotonin
α-SMA	α-smooth muscle actin
A7R5	Rat aortic smooth muscle
ACTB	β-actin
ADP	Adenosine diphosphate
ANS	Autonomic nervous system
ARC	Arachidonic acid-regulated channel
ATP	Adenosine triphosphate
B2M	β-2 microglobulin
BACE-1	β-secretase 1
BMPR2	Bone morphogenetic protein receptor 2
BSA	Bovine serum albumin
Ca^{2+}	Calcium
Cl^{-}	Chloride
$[Ca^{2+}]_{cyt}$	Cytosolic Ca^{2+} concentration
$[Ca^{2+}]_{e}$	Extracellular Ca^{2+} concentration
$[Ca^{2+}]_{i}$	Intracellular Ca^{2+} concentration
Ca_{v}	Voltage-gated Ca^{2+} channel
CaMK	Ca^{2+}/calmodulin-dependent protein kinase
cAMP	Cyclic adenosine monophosphate
CB	Cannabinoid
cDNA	Complementary deoxyribonucleic acid
cGMP	Cyclic guanosine monophosphate
CH	Chronic hypoxia
CMC Na^{+}	Carboxymethylcellulose sodium
CO	Cardiac output
CO_2	Carbon dioxide
COPD	Chronic obstructive pulmonary disease

CRAC	Ca^{2+} release-activated channels
CREB	cAMP response element-binding protein
C_t	Threshold cycle
DAG	Diacylglycerol
DAPI	4',6-diamidino-2-phenylindole
DMEM	Dulbecco’s modified eagle medium
DMSO	Dimethyl sulfoxide
DPBS	Dulbecco’s phosphate-buffered saline
E_a	Arterial elastance
EA	Englerin A
ECACC	European Collection of Authenticated Cell Cultures
EF	Ejection fraction
E_m	Membrane potential
ESP	End systolic pressure
ET	Endothelin
ESV	End systolic volume
FBS	Foetal bovine serum
FS	Fractional shortening
Fura-2-AM	Fura-2-acetoxylmethyl ester
GAPDH	Glyceraldehyde 3-phosphate dehydrogenase
GFP	Green fluorescent protein
GPCR	G protein-coupled receptor
hEGF	Human epidermal growth factor
hFGF-B	Human fibroblast growth factor
HIF1α	Hypoxia-inducible factor 1α
HPASMC	Human pulmonary artery smooth muscle cell
HPRT1	Hypoxanthine phosphoribosyltransferase
HPV	Hypoxic pulmonary vasoconstriction
HR	Heart rate
HUVEC	Human umbilical vein endothelial cell

HVA	High-voltage-activated
IP_3	Inositol 1,4,5-trisphosphate
iPAH	Idiopathic pulmonary arterial hypertension
K^+	Potassium
K_v	Voltage-gated K^+ channel
LSM	Laser scanning microscope
LV	Left ventricle/ventricular
LVA	Low-voltage-activated
MCT(P)	Monocrotaline pyrolle
MEM	Modified eagle medium
MFI	Mean fluorescence intensity
Mg^{2+}	Magnesium
mGFP	Membrane green fluorescent protein
MLCK	Myosin light-chain kinase
MLCP	Myosin light-chain phosphatase
mRNA	Messenger ribonucleic acid
NaOH	Sodium hydroxide
NEAA	Non-essential amino acid
NFAT	Nuclear factor of activated T-cells
N_2	Nitrogen
Ni	Nickel
NO	Nitric oxide
O_2	Oxygen
PA	Pulmonary artery
PAH	Pulmonary arterial hypertension
PAP	Pulmonary arterial pressure
PDE5	Phosphodiesterase type-five
PDGF	Platelet-derived growth factor
PFA	Paraformaldehyde
PH	Pulmonary hypertension

P_i	Free phosphate
PIP_2	Phosphatidylinositol 4,5-bisphosphate
PLC	Phospholipase C
PO_2	Partial pressure of O_2
PV	Pressure volume
PVR	Pulmonary vascular resistance
RNA	Ribonucleic acid
ROC	Receptor operated Ca^{2+} channel
ROCE	Receptor-operated Ca^{2+} entry
qPCR	Quantitative polymerase chain reaction
ROS	Reactive O_2 species
RT	Room temperature
RTK	Receptor tyrosine kinase
RV	Right ventricle/ventricular
SERCA	Sarco/endoplasmic reticulum Ca^{2+}-ATPase
SFM	Serum-free medium
sGC	Soluble guanylate cyclase
siRNA	Small interfering RNA
SMMHC	Smooth muscle-myosin heavy chain
SNP	Single nucleotide polymorphism
SOC(E)	Store-operated Ca^{2+} (entry)
SmBM™	Smooth muscle basal medium
SR	Sarcoplasmic reticulum
STIM	Stromal interaction molecule
SuHx	SU5416 + hypoxia
TG	Thapsigargin
TIMP3	Metalloproteinase inhibitor 3
TRP(C)	Transient receptor potential (canonical)
VDCC	Voltage-dependent Ca^{2+} channel
VEGF	Vascular endothelial growth factor

VSMC	Vascular smooth muscle cell

Chapter 1

Introduction

This thesis is focused on understanding the role of Ca^{2+}-selective ion channels in the VSMC proliferation induced by chronic hypoxia (CH) that is known to play an important role in CH-induced PH. Whilst the initial focus of the research was on T-type Ca^{2+} channels, the discoveries made shifted the focus towards store-operated Ca^{2+} entry (SOCE) and the Orai1 channel. The thesis uses a combination of *in-vitro* and *in-vivo* approaches to determine if selective Orai1 inhibition could be a useful anti-proliferative target in CH-induced PH for a translational drug development programme.

1.1 The pulmonary vascular system

After deoxygenated blood returns to the right side of the heart via the systemic venous system, the entire cardiac output (CO) must pass through the pulmonary arterial system to be reoxygenated, before it is returned to the left side of the heart via the pulmonary venous system. The pulmonary arterial system between the RV and the lung alveoli is comprised of the left main pulmonary artery, which branches into two lobar arteries; and the right main pulmonary artery, which branches into the truncus anterior and two interlobar arteries. These arteries branch into segmental arteries, subsegmental pulmonary arteries, and intralobular arteries at the distal end of the pulmonary arterial tree. The pulmonary arterial tree subdivides into arterioles, pulmonary capillaries, and venules, which densely encompass around 70% of the alveolar wall (Figure 1.1). There are approximately 700 million alveoli in the lungs, which

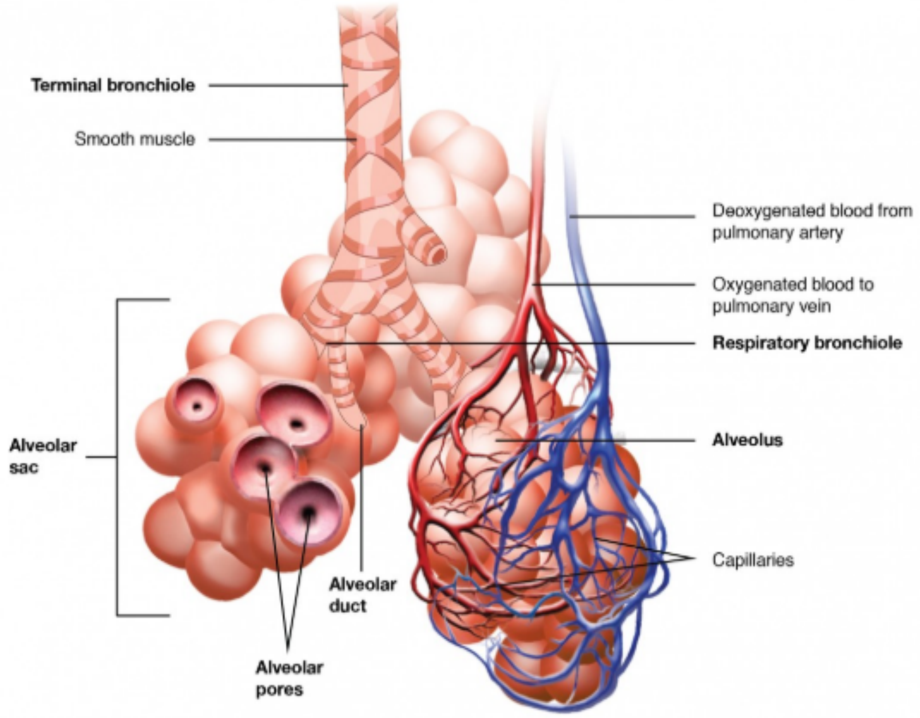

Figure 1.1. Pulmonary arterioles, capillaries and venules densely surround alveoli providing a large surface area for gas exchange.

Respiratory bronchioles divide into alveolar ducts, which in turn supply inhaled air to a group of alveoli. Each alveolus is about 200 μm in diameter and has elasticated walls that allow it to expand during inhalation. The alveoli are densely encompassed by arterioles, capillaries and venules. Gases diffuse between the alveoli and the vessels to allow deoxygenated blood (carried by pulmonary arterioles) to be reoxygenated and carried back through the pulmonary venous system via the venules. Image taken from Betts et al. (2017). Available to download for free at: https://openstax.org/details/books/anatomy-and-physiology.

provide a large surface area of around $70m^2$ for gas exchange (Kandathil and Chamarthy, 2018).

1.2 Blood vessel structure

As illustrated in Figure 1.2, blood vessels (excluding capillaries) are comprised of three layers—the tunica intima, tunica media and tunica adventitia. The innermost layer, the tunica intima, is lined by endothelial cells and permits the smooth passage of blood. The outermost layer, the tunica adventitia (or tunica externa), provides structural support to the vessel. The middle layer, the tunica media, comprises a variable degree of smooth muscle and elastic tissue. The degree of muscularisation within a vessel depends on the size and location of the vessel (Tucker and Mahajan, 2019).

In general, larger arteries such as the pulmonary artery, consist of abundant elastin and less smooth muscle in the medial layer. Elastin helps to minimise pressure fluctuations and ensures large vessels can withstand the impact of substantial volumes of blood over long periods. As the diameter of blood vessels decreases, so does the velocity of blood flow. Thus, small vessels such as the small arterioles that encompass the lung alveoli, do not need to withstand high pressures and they therefore contain much less elastin than large arteries. Instead, small vessels consist of an abundance of smooth muscle. Smooth muscle enables small vessels to adapt their degree of vascular tone. Regulation of vascular tone allows modulation of blood flow, and enables small vessels to respond to changing environmental cues, such as changes in oxygen (O_2) availability or changes in the demand of tissues for O_2 (Tucker and Mahajan, 2019). As depicted in Figure 1.3, as small vessels divide further into pre-capillary arterioles, the degree of muscularisation is variable. Some vessels are partially muscularised while others are non-muscularised (Townsley, 2012).

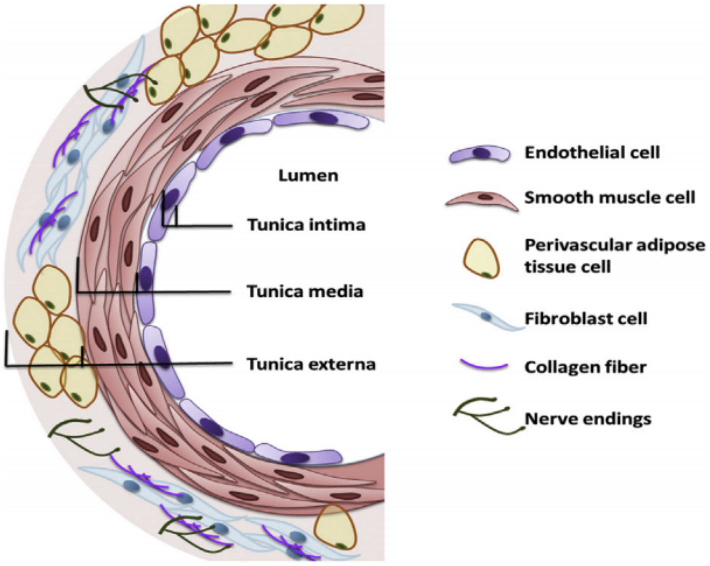

Figure 1.2. Illustration of the three layers of the vessel wall.

Arteries comprise three layers. The tunica intima consists of endothelial cells and the internal elastic membrane. The tunica media comprises VSMCs and the external elastic membrane. The tunica adventitia (also called the tunica externa) comprises perivascular adipose tissue, fibroblasts, nerve endings and connective tissue for structural support. Image taken from Zhao et al. (2015).

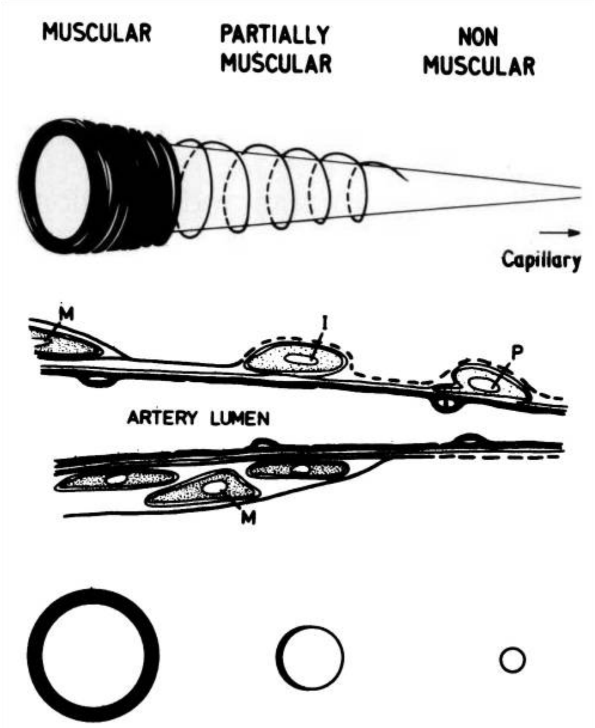

Figure 1.3. The degree of vessel muscularisation depends on the location of the vessel along the pulmonary arterial tree.

Top: Graded muscularisation of small arteries (left) down to arterioles (middle) and pre-capillary arterioles (right). Middle: Illustration of the transition from smooth muscle-lined vessels to intermediate cell- and pericyte cell-lined pre-capillary vessels. Image taken from Townsley (2012).

1.3 Vascular tone and regulation of pulmonary arterial pressure

The degree of vascular tone within a vessel determines the intraluminal radius of that vessel, which in turn influences pulmonary vascular resistance (PVR) according to the following relationship: $PVR \propto 1/r^4$. Importantly, in this equation the intraluminal radius is raised to the fourth power. Therefore, even a small change in the intraluminal radius leads to a large change in PVR. Along with CO, PVR determines pulmonary arterial pressure (PAP) according to the following equation: CO x PVR = PAP.

This relationship between CO and PVR is well illustrated during the transition from gestation to birth. During gestation, gas exchange is governed by the placenta, so the pulmonary vascular system receives only 10%–20% of the total foetal CO. A thick layer of immature smooth muscle and a low intraluminal radius in foetal pulmonary arteries result in a high PVR, according to the above relationship ($PVR \propto 1/r^4$). Consequently, during gestation, the pulmonary vascular system is a high resistance, low flow circuit.

Postnatally, as the role of the placenta in gas exchange subsides, pulmonary blood flow increases to accommodate total CO (Rudolph, 1979; Suresh and Shimoda, 2016), enabling the pulmonary vascular system to take on the role of gas exchange. Accordingly, there is an increase in intraluminal radius and a reduction in PVR. Since CO x PVR = PAP, these adaptations culminate in a physiological PAP of 8–20 mmHg in the mature pulmonary arterial system, much lower than mean systemic arterial pressure, which ranges from 70–105 mmHg (Kuhr et al., 2012). Thus, in a healthy pulmonary vascular system, low vascular tone enables pulmonary arteries and arterioles to accommodate CO while maintaining a low physiological PAP.

Upon exertion, CO is increased but PAP must be maintained within the physiological range. To accommodate an increase in CO, pulmonary arteries distend, and otherwise latent blood vessels are recruited. Distension and recruitment accommodate the increase in CO by increasing the intraluminal radius and the total cross-sectional area, which in turn reduce PVR, maintaining physiological PAP.

The ability of blood vessels to modulate their degree of vascular tone and maintain physiological PAP is governed by VSMCs within the medial layer of the arterial wall.

1.4 VSMC physiology

As a single unit, VSMCs are approximately 200 μm in length and 6 μm in diameter. They comprise a central nucleus that is encompassed by a dense Golgi apparatus and a network of modified endoplasmic reticulum (ER), termed the sarcoplasmic reticulum (SR). The poles of VSMCs are tapered (Figure 1.4) and consist of invaginations that increase the surface area for gap junctions (Wilson, 2011), the function of which is to facilitate synchronous contraction of VSMCs. Since the primary role of differentiated VSMCs in mature blood vessels is regulation of vascular tone, VSMCs are described as having a quiescent and contractile phenotype, which translates to a very low rate of proliferation.

Contraction of VSMCs is involuntary and is regulated by two main mechanisms. First, neuronal axons from the autonomic nervous system (ANS) weave through smooth muscle tissue, forming a series of neurotransmitter-containing varicosities, termed motor units. Upon ANS stimulation, neurotransmitters are released from these varicosities, initiating VSMC depolarisation, voltage-dependent Ca^{2+} entry and contraction.

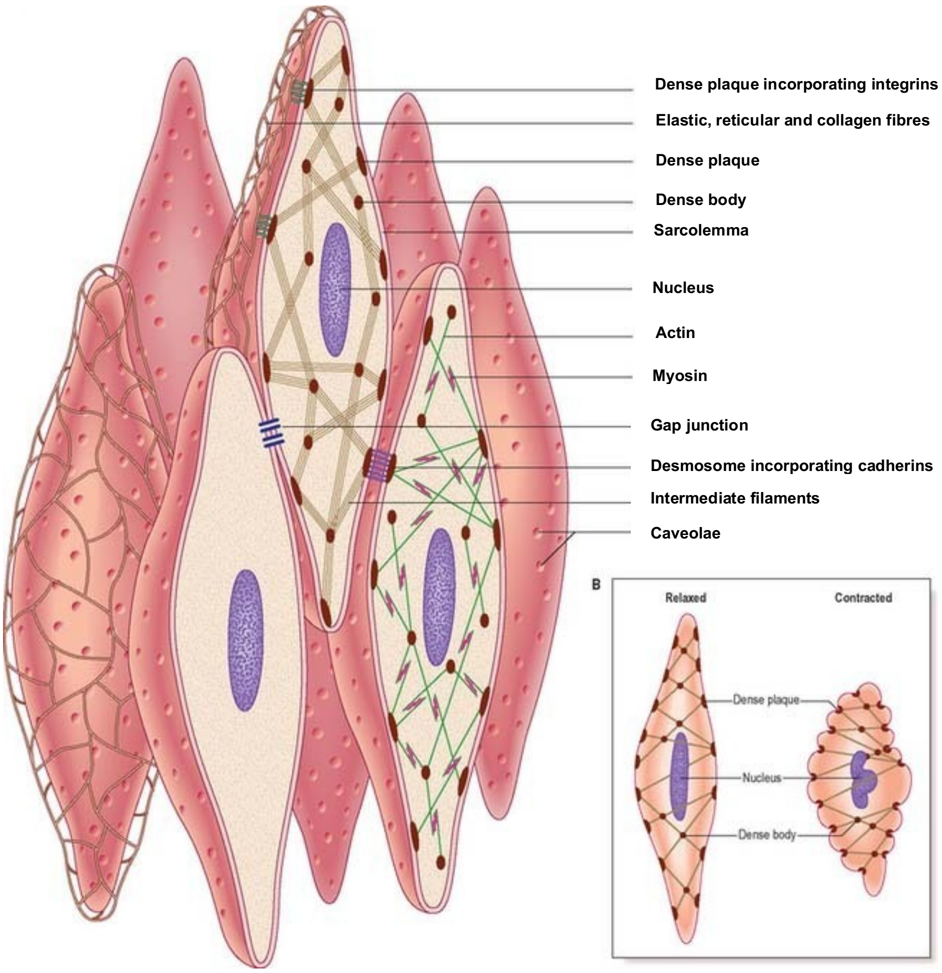

Figure 1.4. Schematic of the VSMC.

VSMCs comprise a central nucleus and are connected to each other via the cell-cell adhesion molecules, integrins and cadherins. The sarcolemma contains caveolae, which are microdomains that contain a multitude of receptors and ion channels. Gap junctions allow synchronous contraction of VSMCs. The contractile proteins, actin and myosin, and the intermediate filaments attach to dense bodies, which are the functional equivalent of the z-discs in cardiac and skeletal muscle. Taken from Aherarrou (2018). VSMC, vascular smooth muscle cell.

Contraction of VSMCs is also controlled by hormonal regulation. Autocrine and paracrine hormones including noradrenaline, adrenaline and angiotensin II function through phospholipase C (PLC)-linked G protein-coupled receptors (GPCRs). Briefly, PLC is an enzyme which, upon activation of a GPCR, hydrolyses the membrane phospholipid, phosphatidylinositol 4,5 bisphosphate (PIP_2) into the second messengers, inositol 1,4,5-trisphosphate (IP_3) and diacylglycerol (DAG). Both IP_3 and DAG mediate Ca^{2+} entry into the cytosol, either from the SR by activation of the IP_3 receptor or from the extracellular milieu by activation of either receptor-operated Ca^{2+} (ROC) channels, store-operated Ca^{2+} (SOC) channels or voltage-dependent Ca^{2+} channels (VDCCs) (Figure 1.5).

1.5 Physiological Ca^{2+} regulation in pulmonary VSMCs

Under physiological conditions, the cytosolic Ca^{2+} concentration ($[Ca^{2+}]_{cyt}$) is in the region of 100 nM, whereas the extracellular Ca^{2+} concentration ($[Ca^{2+}]_e$) is around 2 mM—10,000-fold greater. To maintain Ca^{2+} homeostasis after entry into the cytosol, the Ca^{2+}-magnesium (Mg^{2+})-ATPase and the sarco/endoplasmic reticulum Ca^{2+}-ATPase (SERCA) are two predominant transporters that expend energy in the form of ATP to extrude Ca^{2+} ions from the cytosol against their electrochemical gradient, the former to extrude Ca^{2+} from the cell and the latter to replenish SR Ca^{2+} stores.

Another homeostatic mechanism to maintain the Ca^{2+} distribution across the VSMC membrane is the Na^+/Ca^{2+} exchanger (NCX). The NCX is an electrogenic pump that, when the $[Ca^{2+}]_{cyt}$ increases, extrudes one Ca^{2+} ion in exchange for three Na^+ ions, generating a net inward current. Along with store-operated Ca^{2+} entry (SOCE), NCX is important in SR refilling via the sarco-endoplasmic reticulum ATPase (SERCA) after store depletion (Lemos et al., 2007).

In reverse mode, the NCX extrudes Na^+ ions from the cytosol in exchange for the entry of Ca^{2+}. An increase in the $[Na^+]_{cyt}$ converts the NCX into reverse mode, where it extrudes Na^+ ions from the cytosol in exchange for the entry of Ca^{2+} ions into the cytosol. Reverse mode NCX is a key contributor to an increase in the $[Ca^{2+}]_{cyt}$ after Na^+ influx through the non-selective TRPC channels.

Store-operated Ca^{2+} entry and the subsequent increase in the $[Ca^{2+}]_{cyt}$ activate the Ca^{2+}-activated chloride (Cl^-) channel in pulmonary VSMCs (Angermann et al., 2006; Forrest et al., 2010; Wiwchar et al., 2009). The $[Cl^-]_{cyt}$ is ~50mM, which is relatively high compared to the $[Cl^-]_e$. Thus, the equilibrium potential for Cl^- (E_{Cl-}) is less negative than the resting membrane potential (E_m) (LeBlanc et al., 2005 - Regulation of calcium-activated chloride channels) and upon activation of Ca^{2+}-activated Cl^- channels, there is an efflux of Cl^- (inward current). This inward current causes membrane depolarisation, which activates VDCCs, and further increases the $[Ca^{2+}]_{cyt}$ in pulmonary VSMCs.

The functional interactions outlined above that occur in normal pulmonary VSMCs to maintain Ca^{2+} homeostasis incorporate multiple Ca^{2+}-permeable channels including ROC channels, SOC channels and VDCCs. The above ion channel interactions are not exhaustive but offer some insight into the complexity of Ca^{2+} regulation within pulmonary VSMCs. It follows that any change in the expression of any of these components can affect Ca^{2+} homeostasis.

Changes in Ca^{2+} distribution across the VSMC membrane occur via activation of a range of ion channels that allow influx of Ca^{2+} ions from the extracellular milieu

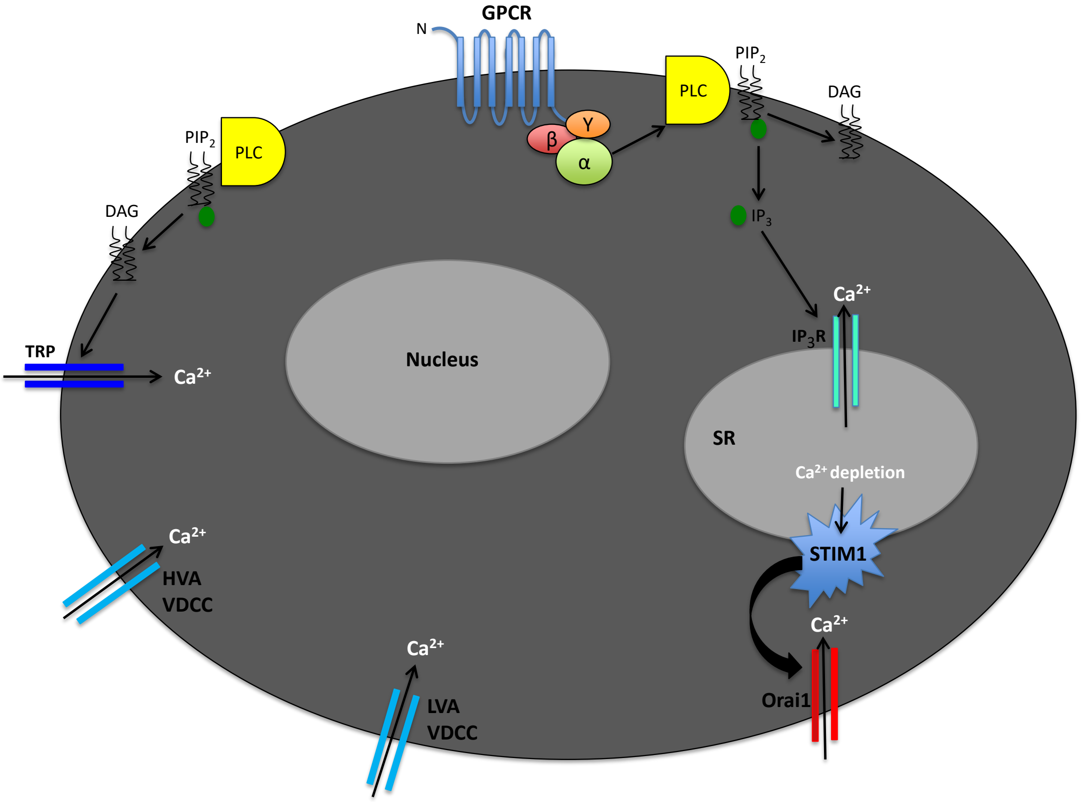

Figure 1.5. A simplified representation of Ca^{2+} entry pathways in pulmonary VSMCs.

Orai1-mediated SOCE, TRPC-mediated Ca^{2+} entry and voltage-dependent Ca^{2+} entry allow influx of Ca^{2+} ions from the extracellular milieu into the cytosol down their electrochemical gradient. PLC, phospholipase C; GPCR, G protein-coupled receptor; PIP_2, phosphatidylinositol 4,5 bisphosphate; IP_3, inositol 1,4,5-trisphosphate; ROCE, receptor-operated Ca^{2+} entry; SOCE, store-operated Ca^{2+} entry; SR, sarcoplasmic reticulum; STIM1, stromal interaction molecule 1; TRPC, transient receptor potential canonical; LVA VDCC, low-voltage-activated voltage-dependent Ca^{2+} channel; HVA VDCC, high-voltage-activated voltage-dependent Ca^{2+} channel.

into the cytosol down their electrochemical gradient. Thus, upon channel opening, the $[Ca^{2+}]_{cyt}$ rises without the expense of energy. Of particular interest in this thesis are the VDCCs, ROC channels and SOC channels (Figure 1.5).

1.5.1 Voltage-dependent Ca^{2+} channels

The VDCCs are a family of membrane proteins. The central building block of all VDCCs is the voltage-sensitive pore, which is formed by α1-subunits (Figure 1.6). The α1-subunits are encoded by 10 genes, which depending on the isoform, form high- (HVA/Ca_v1.x), mid- (Ca_v2.x) or low-voltage-activated (LVA/Ca_v3.x) channels (Striessnig et al., 2014). Mid-voltage-activated channels will not be discussed further in this thesis.

1.5.1.1 High-voltage-activated (L-type) Ca^{2+} channels

The HVA VDCCs, herein referred to as L-type Ca^{2+} channels, are encoded by four genes: *CACNA1S* (Ca_v1.1), *CACNA1C* (Ca_v1.2), *CACNA1D* (Ca_v1.3) and *CACNA1F* (Ca_v1.4) (Striessnig, 1999; Bourinet et al., 2004; Dolphin, 2006). Ca_v1.1 is exclusively found in skeletal muscle, while Ca_v1.4 is localised to retinal tissue (Striessnig et al., 2014). Thus, these channel isoforms are not relevant to this thesis.

The α1-subunit is the pore-forming subunit and provides the Ca^{2+} permeability characteristics of all L-type Ca^{2+} channel isoforms. The α1-subunits of L-type Ca^{2+} channels form multimers with auxiliary subunits to function as plasma membrane Ca^{2+} channels. These auxiliary subunits are non-covalently linked to the pore-forming α1-subunit. This auxiliary subunit interaction enables trafficking of L-type Ca^{2+} channels to the plasma membrane and modifies the biophysical properties of the channels (Bodi et al., 2005).

L-type Ca^{2+} channels are activated by large depolarisations that increase the resting membrane potential (E_m) of normal pulmonary VSMCs (-40 mV to -60 mV) (Firth et al., 2011) to a more positive potential of around -20 mV, with a maximal current amplitude observed at 0 mV to +10 mV. As well as depolarisation-dependent activation, L-type Ca^{2+} channels are indirectly activated by a multitude of cellular second messenger systems. For example, activation of GPCRs by agonists including endothelin, noradrenaline, angiotensin II and serotonin (Kuhr et al., 2012) can result in secondary activation of L-type Ca^{2+} channels.

L-type Ca^{2+} channels undergo slow voltage-dependent inactivation, giving rise to their long-lasting (L-type) classification. Voltage-dependent inactivation limits ion entry in the presence of persistent depolarising stimuli (Kuo et al., 2011). In addition, L-type Ca^{2+} channels are sensitive to block by dihydropyridines such as nifedipine, verapamil and diltiazem, making these compounds valuable experimental tools to investigate the effect of L-type Ca^{2+} channels on cellular processes such as VSMC contraction. The reliability of these compounds as L-type Ca^{2+} channel blockers also justifies their clinical use in the treatment of multiple vascular diseases and thus are an excellent example of an ion channel blocker being translated to clinical practice.

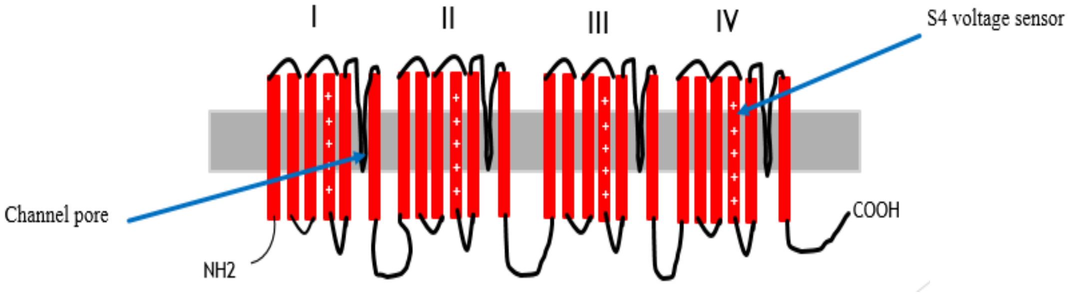

Figure 1.6. A simplified schematic of the VDCC α1 pore-forming subunit.

The VDCC α1-subunit is comprised of four domains (I–IV), each with six transmembrane segments (S1–S6). The S4 segment contains charged residues that form the voltage-sensor, and the hydrophobic loops between the S5 and S6 segments form the channel pore. VDCC, voltage-dependent Ca^{2+} channel.

1.5.1.2 Low-voltage-activated (T-type) Ca^{2+} channels

The LVA VDCCs, herein referred to as T-type Ca^{2+} channels, were characterised by electrophysiology on voltage-clamped dorsal root ganglion neurons (Carbone and Lux, 1984). The pore-forming α1-subunits of T-type Ca^{2+} channels are encoded by three genes, *CACNA1G* ($Ca_v3.1$), *CACNA1H* ($Ca_v3.2$), and *CACNA1I* ($Ca_v3.3$). $Ca_v3.3$ is not considered further in this thesis due to its predominant expression in neuronal tissue. T-type Ca^{2+} channels can localise to the plasma membrane of VSMCs as a functional α1-subunit, which comprises both the voltage-sensor and channel pore (Figure 1.6). Unlike L-type Ca^{2+} channels, T-type Ca^{2+} channels do not require multimerisation with auxiliary subunits for functional membrane expression (Dolphin, 2016).

T-type Ca^{2+} channels are activated by small depolarisations that increase the resting E_m of normal pulmonary VSMCs (-60 mV to -40 mV) to around -40 mV. Unlike L-type Ca^{2+} channels, T-type Ca^{2+} channels inactivate rapidly (giving rise to their transient [T-type] classification) and deactivate slowly (Perez-Reyes, 2003).

Like L-type Ca^{2+} channels, T-type Ca^{2+} channels undergo voltage-dependent inactivation. They are also sensitive to block by nickel (Ni) (Fox et al., 1987; Hagiwara et al., 1988). The IC_{50} of Ni varies dependent on T-type Ca^{2+} channel isoform, making it a useful experimental tool to investigate the functional effects of T-type Ca^{2+} channel inhibition on cellular processes.

T-type Ca^{2+} channel mRNA, protein and functionality were confirmed in early passage cultured human pulmonary VSMCs and human lung tissue using RT-PCR, immunostaining and electrophysiology, respectively (Rodman et al., 2005). Specifically, RT-PCR was used to detect $Ca_v3.1$ and $Ca_v3.2$ mRNA in cultured human pulmonary VSMCs and human lung tissue. Immunostaining demonstrated SMC α-actin (α-SMA) and $Ca_v3.1$ co-expression in the tunica media of pulmonary vessels from human lung tissue, while $Ca_v3.2$ was not detected. It is of note that α-SMA is not a sufficient standalone marker of VSMCs as it is also expressed in fibroblasts (Ng et al., 1998; Sousa et al., 2007). To confirm T-type Ca^{2+} channel functionality in human pulmonary VSMCs, whole-cell patch clamp revealed a rapidly inactivating inward current reaching peak density at -40mV (typical of T-type Ca^{2+} channels) and a sustained inward current reaching peak density at +10 mV (typical of L-type Ca^{2+} channels). Nifedipine, an L-type Ca^{2+} channel blocker, abolished the L-type Ca^{2+} channel current-voltage relationship, revealing the remaining transient inward current consequent of T-type Ca^{2+} channels (Rodman et al., 2005).

Although a number of T-type Ca^{2+} channel blockers are available for experimental purposes, they have been classed as sub-optimal research tools due to their poor selectivity. Where T-type Ca^{2+} channels have been ascribed a role in disease pathogenesis, lack of T-type Ca^{2+} channel inhibitors make selective targeting of this channel problematic.

1.5.1.3 Mibefradil

Mibefradil (brand name Posicor) was brought to market in 1997 as a T-type Ca^{2+} channel blocker with vasodilatory properties that was equally as effective as amlodipine, and more effective than diltiazem for the treatment of mild-to-moderate hypertension and angina pectoris (Brogden and Markham, 1997). The inhibitory effect of mibefradil on the cytochrome P450 enzymes, CYP2D6 and CYP3A4, was soon realised (Ernst and Kelly, 1998; Wandel et al., 2000). Since these enzymes are responsible for drug metabolism, their inhibition increases the plasma concentration of potentially toxic substances (Veronese et al., 2003). In 1998, mibefradil was discontinued from clinical use because the large number of contraindicated drugs meant that the risks from mibefradil were too high.

It is estimated that mibefradil blocks T-type Ca^{2+} channels with a 10- to 15-fold greater selectivity than for L-type Ca^{2+} channels (Martin et al., 2000). Although it is recognised for its role as a T-type Ca^{2+} channel blocker, mibefradil also affects other channels with micromolar affinity, including sodium (Na^+) channels, $K_v1.5$ (Perchenet and Clement-Chomienne, 2000), delayed-rectifier potassium (K^+) channels, inward rectifier K^+ channels (Liu et al., 1999), hERG K^+ channels (Chouabe et al., 2000) and Ca^{2+}-activated chloride (Cl^-) channels (Nilius et al., 1997). The identified targets of mibefradil are similar in their voltage-gated characteristics, raising the possibility of a common binding motif (McNulty and Hanck, 2004). Given the extent of cross-reactivity, it is possible that the effects of T-type Ca^{2+} channel inhibition observed upon application of mibefradil might result from its promiscuity at other ion channel targets.

1.5.1.4 NNC55-0396

In 2004, the non-hydrolysable analogue, NNC55-0396, was synthesised by modification of the structure of mibefradil (Li et al., 2005), which is shown in Figure 1.7. Bui et al. (2008) investigated the inhibitory effect of NNC55-0396 on the cytochrome P450 enzymes, CYP2D6 and CYP3A4. The group found that NNC55-0396 had a 10-fold lower inhibitory effect on CYP3A4 (IC_{50} = 300 ± 30 nM) than mibefradil (IC_{50} = 33 ± 3 nM) and Ro40-5966 (IC_{50} = 30 ± 7.8 nM). However, NNC55-0396 had a greater inhibitory activity towards CYP2D6 (IC_{50} = 29.1 ± 2 nM) than mibefradil (IC_{50} = 129 ± 21 nM). Hence, the risks associated with mibefradil also exist with NNC55-0396, preventing the use of this compound in the clinic.

Although it is not safe for clinical applications, NNC55-0396 is superior for experimental uses because substitution of the side chain of NNC55-0396 avoids production of a metabolite that has the capacity to block L-type Ca^{2+} channels. Accordingly, NNC55-0396 has no discernible effects on L-type Ca^{2+} channels up to 100 µM in INS-1 cells (Huang et al., 2004). However, to my knowledge, the selectivity of NNC55-0396 for T-type Ca^{2+} channels over other Ca^{2+} channels in VSMCs has not been stringently verified. This should be clarified when investigating the influence of T-type Ca^{2+} channel inhibition on cellular processes.

1.5.1.5 TTA-A2

TTA-A2 was discovered by Barrow et al. (2007) and is a potent, highly selective T-type Ca^{2+} channel blocker (Kraus et al., 2010) used for experimental purposes. TTA-A2 is equipotent for inhibition of all three isoforms of the T-type Ca^{2+} channel: $Ca_v3.1$, $Ca_v3.2$, and $Ca_v3.3$. In HEK293 cells stably overexpressing $Ca_v3.1$, TTA-A2 preferentially interacts with inactivated channels (IC_{50} = 89 nM at an E_m of -80 mV) compared to closed/deactivated channels (IC_{50} = 4.1 µM at a more hyperpolarised E_m of -100 mV). Hence, TTA-A2 is 40-fold more potent for inhibition of inactivated channels (Kraus et al., 2010). Kraus et al. (2010) demonstrated a 300-fold greater selectivity of TTA-A2 for T- over L-type Ca^{2+} channels—a vast improvement to the 10- to 15-fold preferential selectivity of mibefradil. The selectivity of TTA-A2 has also been probed in 170 binding and fluorescent assays to cover numerous voltage-activated Ca^{2+} and K^+ channels. There was not a single target that demonstrated modulation by TTA-A2 at an IC_{50} below 10 µM (Uebele et al., 2009).

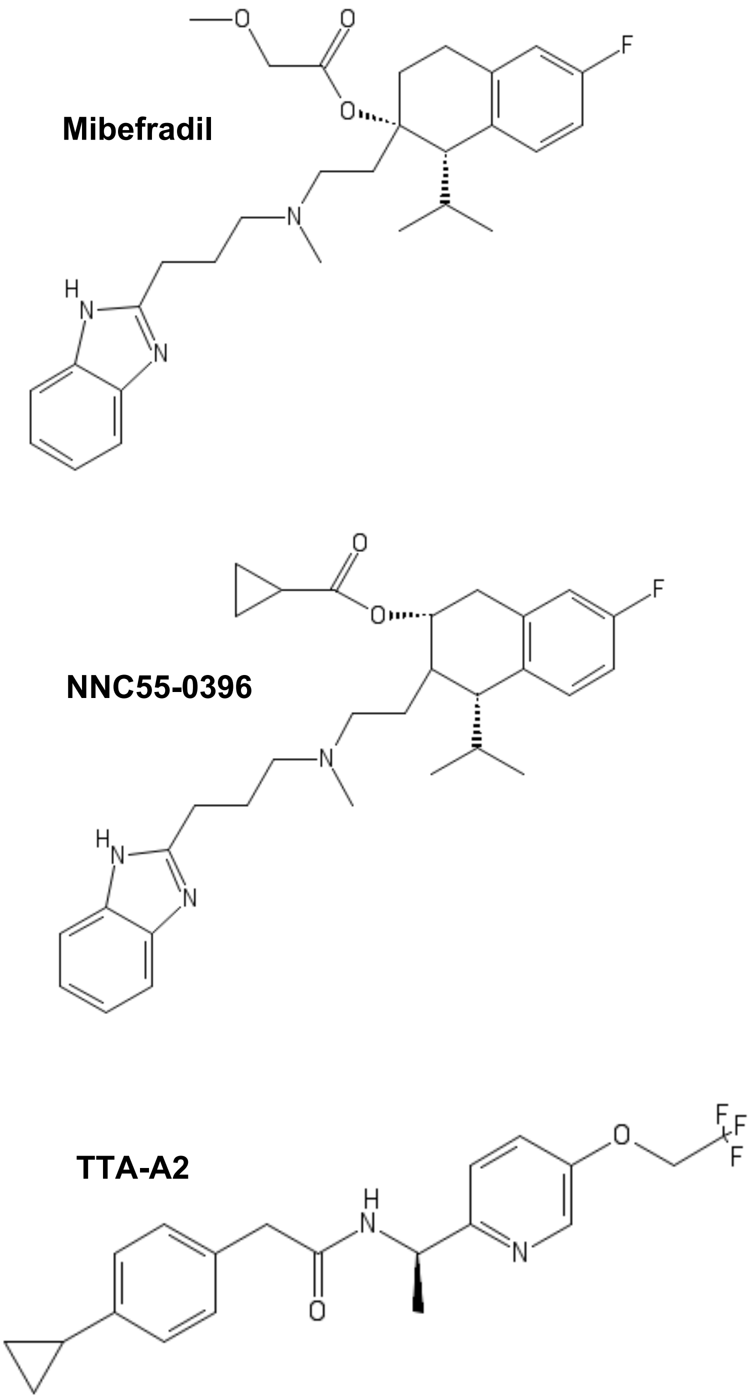

Figure 1.7. Chemical structure of widely used T-type Ca^{2+} channel inhibitors, mibefradil, NNC55-0396 and TTA-A2.

The non-hydrolysable analogue, NNC55-0396, was synthesised by modification of the structure of mibefradil by substitution of the methoxyacetate side chain with cyclopropanecarboxylate. The solubility limit of mibefradil and NNC55-0396 in dH_2O are 50 mM and 25 mM, respectively (Tocris BioScience, Bristol, UK). TTA-A2 is structurally unrelated to mibefradil and NNC55-0396, and is a potent, selective T-type Ca^{2+} channel blocker. TTA-A2 is soluble in DMSO to 100 mM (Abcam, Cambridge, UK). DMSO, dimethyl sulfoxide.

1.5.2 Transient receptor potential (canonical) proteins

The transient receptor potential (TRP) protein family comprises 28 members (Figure 1.8) divided into six structural subfamilies, one of which is the transient receptor potential canonical (TRPC) subfamily. The TRPC protein family are encoded by seven genes (*TRPC1–7*), which were identified after it was realised that the TRP gene from *Drosophila melanogaster* photoreceptors encoded a Ca^{2+}-permeable channel activated by PLC (Wes et al., 1995; Zhu et al., 1995).

A common topology is observed between the members of the TRPC family (Vannier et al., 1998). The N- and C- termini reside in the cytoplasm and are separated by six transmembrane (TM) domains (TM1–6), with the pore region residing between TM5 and TM6. Both the N- and C-termini of the TRPC proteins contain a predicted coiled-coil region, which is thought to influence homo- and heteromultimerisation to form TRPC ion channels with distinct characteristics (Owsianik et al., 2006). The C-terminus of TRPC channels contains calmodulin- and IP_3-binding sites (Clapham, 2003).

TRPC1 was the first TRPC family member to be cloned (Wes et al., 1995; Zhu et al., 1995) and was characterised as a Ca^{2+}-permeable cation channel activated by either IP_3 or thapsigargin (TG) in Chinese hamster ovary cells (Zitt et al., 1996). From these observations, TRPC1 current was described as bearing resemblance to Ca^{2+} release-activated Ca^{2+} current (ICRAC) (Hoth and Penner, 1992), though it is not Ca^{2+} selective.

Given the resemblance of TRPC1 current to ICRAC, considerable research suggests a role for TRPC1 as a component of SOCE. Expression of TRPC1 resulted in both non-selective (Zitt et al., 1996) and Ca^{2+}-selective currents (Liu et al., 2000) that were activated by TG-induced store depletion in multiple cell types. Antisense oligonucleotides against TRPC1 reduced SOCE in pulmonary

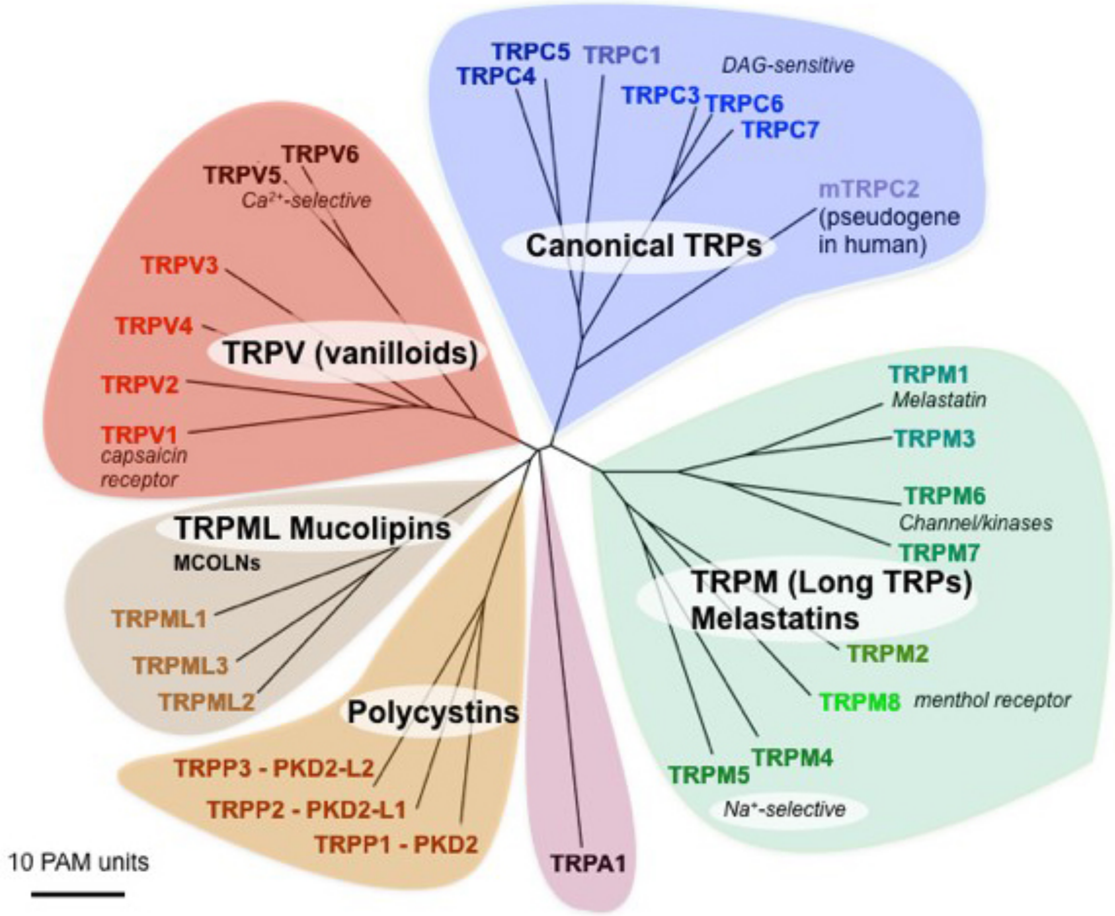

Figure 1.8. The TRP protein family.

The TRP protein family comprises 28 members, divided into six subfamilies. The TRPC subfamily comprises seven members (TRPC1–7). Taken from Clapham (2003).

VSMCs (Sweeney et al., 2002).

Cell surface expression of TRPC1 depends on its interaction with TRPC4 (Hofmann et al., 2002). Thus, TRPC1 is unlikely to form functional homomeric channels (Xu et al., 2006b; Beech, 2013) but likely heteromultimerises with TRPC4 and TRPC5 to form functional channels (Beech et al., 2003). Although both TRPC4 and TRPC5 are able to form functional channels in the absence of TRPC1, this is unlikely to occur because of the high level of TRPC1 expression (Wes et al., 1995; Abramowitz and Birnbaumer, 2009).

TRPC4 and TRPC5 were cloned in 1996 and 1998, respectively. When expressed in mammalian cells, TRPC4 produced a novel Ca^{2+}-selective current that, like TRPC1, was activated by IP_3 or TG-induced store depletion. There has been some controversy regarding this observation, since TRPC4 and TRPC5 currents are *potentiated* by lanthanides (Schaefer et al., 2000), whereas lanthanides *attenuate* SOC current. Like TRPC4, TRPC5 has demonstrated characteristics of a SOC channel (Philipp et al., 1998), but others claim that its characteristics resemble a ROC channel (Okada et al., 1998; Schaefer et al., 2000). An agonist of TRPC4 and TRPC5 that can be used to study these channels experimentally is englerin A (EA). However, this compound is lethal in animals at concentrations required to activate TRPC4 (Carson et al., 2015). Thus, to investigate the functional effects of TRPC4 and TRPC5 modulation *in vivo*, alternative agents should be considered (Minard et al., 2018).

It is well documented that TRPC3, TRPC6 and TRPC7 are activated by 1-oleoly-2-acetyl-*sn*-glycerol (OAG), a DAG analogue. These channels are also activated by DAG lipase and DAG kinase inhibitors, which suggests a mechanism of activation that is independent of IP_3 receptor activation or store depletion, but one that involves GPCR activation and PLC production (Vazquez et al., 2001; Trebak et al., 2003).

Thus, TRPC channels are most often recognised for their role in ROCE, and controversy exists as to whether they also play a role as pore-forming subunits for SOCE in certain cell types including pulmonary VSMCs (Huang et al., 2006; Ong et al., 2007). It is likely that certain TRPC isoforms play a role in SOCE, but that they are not critically required.

1.5.3 Orai proteins

ICRAC was first recognised during studies to elucidate the trigger for activation of T lymphocytes by antigens (Lewis and Cahalan, 1989). It was at this time that SOCE gained acceptance (Penner et al., 1988; Lewis and Cahalan, 1989), and ICRAC has since become a well-established physiological phenomenon. Seventeen years later, the Orai1 protein was characterised as the CRAC protein (Feske et al., 2006; Prakriya et al., 2006; Vig et al., 2006; Yeromin et al., 2006), largely concluded from the observation that Orai1 and STIM1 overexpression in HEK293 cells increased SOCE and Ca^{2+}-selective current by 20-fold (Mercer et al., 2006; Peinelt et al., 2006). These findings were supported by the observation that ICRAC was not observed in T lymphocytes from severe combined immunodeficiency patients with a R91W mutation in the *ORAI1* gene, demonstrating the importance of the gene product as a CRAC protein. Strengthening these observations, expression of WT Orai1 in T lymphocytes restored ICRAC (Feske et al., 2006). Thus, Orai1 is now generally accepted as the pore-forming unit that underpins ICRAC and as the critical contributor to SOCE, enabling refilling of ER/SR Ca^{2+} stores after depletion in most cell types (Hogan and Rao, 2015).

The Orai protein family are encoded by three genes: *ORAI1, ORAI2*, and *ORAI3*. Mammals are the only species that express all three isoforms (Spinelli and Trebak, 2016). Where SOC channels comprise Orai1 subunits, a pentameric arrangement of Orai1 and Orai3 subunits forms the arachidonic acid-regulated Ca^{2+} (ARC) channels. Unlike SOC channels, which are store-dependent and thus require interaction with the ER Ca^{2+} sensor, stromal interaction molecule 1 (STIM1) (1.5.4) for activation, ARC channels are store-independent and instead interact with a plasma membrane pool of STIM1 (Thompson and Shuttleworth, 2012). The function of Orai2 is relatively less well understood, but recent evidence suggests a role for Orai2 in fine-tuning SOCE by forming heteromers with Orai1 (Vaeth et al., 2017).

As depicted in Figure 1.9, Orai1 monomers are cell surface proteins that comprise four TM helices, with TM helix 1 forming the channel pore. Substitution of glutamic acid for aspartic acid at position 106 alters ion selectivity of the Orai1 pore, rendering this residue crucial for Ca^{2+} selectivity (Prakriya et al., 2006). The N- and C-termini are localised to the cytosolic side of the cell. The C-terminus of Orai1 is necessary for relocalisation of the ER Ca^{2+} sensor, STIM1 (Muik et al., 2008; Park et al., 2009), while the N-terminus of Orai1 permits ionic conductance (Muik et al., 2008).

Controversy exists as to whether Orai1 forms the CRAC pore as a hexamer or a tetramer in humans (Liao et al., 2008; Demuro et al., 2011). *Drosophila melanogaster* Orai1 (Hou et al., 2012) is hexameric, and extensive similarity between *Drosophila* Orai and human Orai1 favours the hexameric theory. Orai1 mRNA, protein and functionality were confirmed in murine pulmonary VSMCs using RT-PCR, western blot and Ca^{2+} imaging, respectively (Ng et al., 2010).

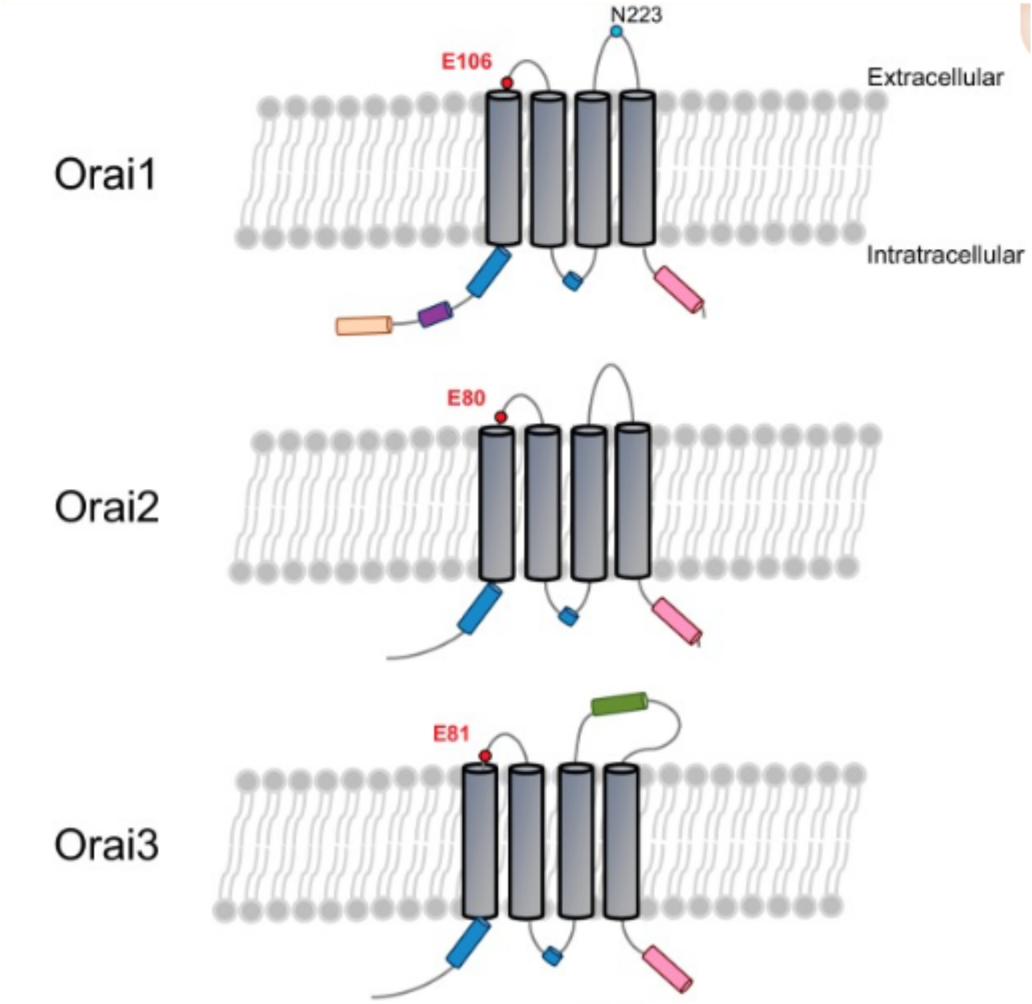

Figure 1.9. The basic structure of the Orai proteins.

The highly conserved 'E' residue of each Orai protein forms the selectivity filter (red). The C-terminus contains a coiled-coil domain required for STIM1 binding and gating of Orai channels (pink). The N-terminus of Orai1 also consists of a proline-rich binding domain (peach) and a caveolin-binding domain (purple). Modified from Spinelli and Trebak (2016).

RT-PCR demonstrated that Orai1 and STIM1 were expressed in mouse pulmonary VSMCs, while western blot demonstrated protein expression. Due to the difficulty in designing ion channel antibodies with high specificity (demonstrated by multiple bands in western blot), functional studies can often provide useful information. For example, Ca^{2+} imaging techniques revealed both a transient and a sustained component of SOCE in mouse pulmonary VSMCs. Knockdown approaches revealed that Orai1 was responsible for the transient component of SOCE (Ng et al., 2010), while TRPC1 was responsible for the sustained component (Ng et al., 2009), further supporting a role for TRPC1 as a contributor to SOCE. It is suggested that upon Ca^{2+} store depletion, relocalisation and aggregation of STIM1 to the plasma membrane facilitate recruitment of Orai1 and TRPC1 to these sites, where STIM1 interacts with and gates these proteins (Luik et al., 2006; Xu et al., 2006a).

1.5.4 STIM proteins

The STIM proteins are encoded by two genes: *STIM1* and *STIM2*. *STIM1* was first identified as a tumour suppressor gene (Parker et al., 1996) localised to a chromosomal region associated with multiple cancers (Williams et al., 2001). The second member of the STIM gene family, *STIM2*, was first described by screening for similar cDNA sequences to STIM1 (Williams et al., 2001). Both STIM1 and STIM2 are ubiquitously expressed in different cell types, although STIM1 is expressed to a greater extent in most tissues (Williams et al., 2001).

In 2005, the STIM proteins were characterised for their role as ER Ca^{2+} sensors during efforts to identify candidates for SOCE (Liou et al., 2005; Roos et al., 2005). The STIM proteins localise to the ER membrane and comprise a single TM region with a cytosolic C-terminus, which differs largely between isoforms; and a luminal N-terminal Ca^{2+}-binding domain (Lewis, 2011).

In the functional protein, a decrease in the luminal Ca^{2+} concentration, which can decline from around 1 mM to 300 μM after IP_3 receptor activation, causes Ca^{2+} to dissociate from the N-terminal Ca^{2+}-binding domain (EF-hand) (Stathopulos et al., 2008). It is widely accepted that dissociation of Ca^{2+} from the EF-hand triggers translocation and accumulation of STIM proteins at the ER-plasma membrane junction in structures called *punctae*, where STIM1 interacts with Orai1 on the plasma membrane to activate Ca^{2+} entry (Roos et al., 2005). However, recent evidence suggests that this interaction is more complex than originally thought. Specifically, relocalisation and co-clustering of Orai1 and STIM1 only occurs under conditions of extreme store depletion, where there is a possibility of the cell being compromised. For example, such clustering is observed in response to extreme store depletion by TG, but is not observed in response to physiological store depletion induced by platelet-derived growth factor (PDGF) in saphenous vein VSMCs (McKeown et al., 2012). Importantly, TG severely depletes Ca^{2+} stores, while physiological PDGF stimulation does not. Therefore, PDGF-induced SOCE does not result in Orai1/STIM1 clustering.

The exact mechanism by which STIM translocates to the plasma membrane in response to store depletion is unknown (Kuhr et al., 2012). However, the sterile α-motif (SAM) of STIM is critical to the above process, such that mutations in the SAM prevent punctae formation in response to Ca^{2+} store depletion (Baba et al., 2006). Conversely, mutations in the EF-hand cause STIM to possess an impaired capacity to sense and bind Ca^{2+} such that punctae formation and CRAC activation occur even in the absence of Ca^{2+} store depletion (Liou et al., 2005). When the C-terminal region of STIM1 is expressed alone, constitutive

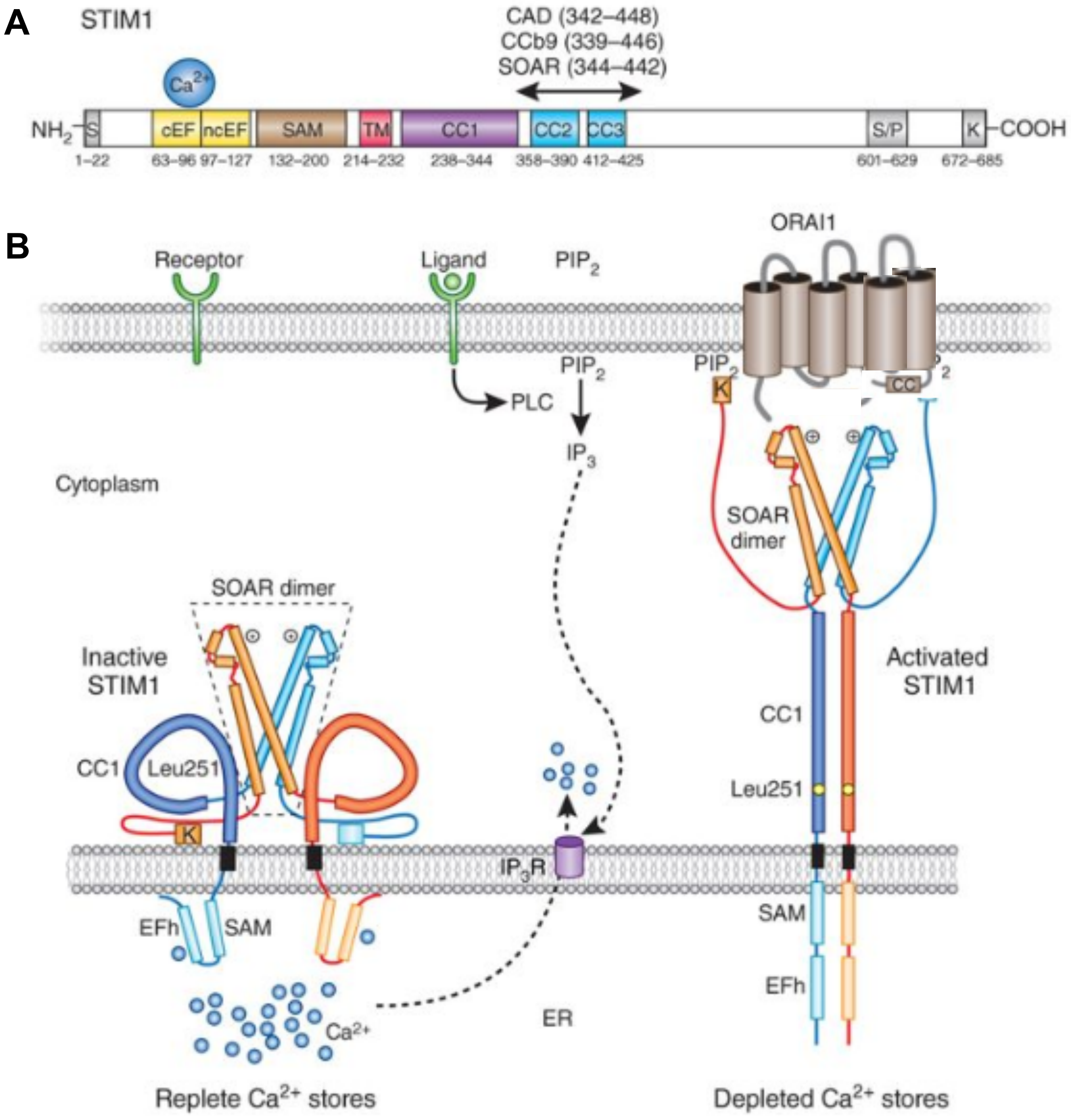

Figure 1.10. Schematic of STIM1 domain organisation and mechanism of STIM1 and Orai1 activation.

Upon ligand binding to a GPCR or PDGF receptor activation, IP_3 is produced and Ca^{2+} is released from the ER/SR. Upon severe store depletion, STIM1 interacts with Orai1 to form discrete punctae (right). When Ca^{2+} stores are repleted (left), STIM1 returns to its ER/SR-localised formation and dissociates from Orai1. GPCR, G protein-coupled receptor; PDGF, platelet-derived growth factor; cEF, canonical EF-hand; ncEF, non-canonical EF hand; SAM, sterile α-motif; TM, transmembrane; CC1–3, coiled-coil domains; STIM1, stromal interaction molecule 1; PIP_2, phosphatidylinositol 4,5-bisphosphate; IP_3(R), inositol 1,4,5 trisphosphate (receptor); SOAR, STIM1-ORAI activating region. Image modifed from Feske and Prakriya (2013).

ICRAC occurs, independent of Ca^{2+} store depletion (Cahalan, 2009). It is suggested that an interaction between the cytosolic C-terminus of STIM1 and the C-terminal coiled-coil domain of Orai1, traps Orai1 and activates SOCE (Spinelli and Trebak, 2016).

Kuhr et al. (2012) claim that STIM1 acts as an effector, with an element of promiscuity in its interaction with plasma membrane pore-forming channels, and in doing so, mediates Ca^{2+} influx thorough multiple pathways.

1.6 Regulation of VSMC contraction

Contraction of VSMCs is dependent on an increase in the intracellular Ca^{2+} concentration ($[Ca^{2+}]_i$), which occurs secondary to activation of the above Ca^{2+} entry pathways. Ca^{2+} interacts with calmodulin to form the Ca^{2+}/calmodulin complex, which in turn activates myosin light chain kinase (MLCK). Myosin light chain kinase converts adenosine triphosphate (ATP) into adenosine diphosphate (ADP) and free phosphate (P_i). The regulatory light chain of myosin is then phosphorylated at serine 19 (Ikebe and Hartshorne, 1985), enabling cross-bridge formation between the two fundamental contractile proteins in differentiated VSMCs: myosin and α-actin. This interaction between myosin and α-actin underpins VSMC contraction. According to their role as contractile proteins, VSMCs are characterised by expression of α-actin and smooth muscle myosin heavy chain (SMMHC), which are early markers of VSMC differentiation (Babij et al., 1992; Rodriguez et al., 2006).

A second mechanism of VSMC contraction is Ca^{2+} sensitisation. Ca^{2+} sensitisation is a Ca^{2+}-independent mechanism that is underpinned by a change in the sensitivity of the MLC to $Ca^{2+.}$ This mechanism allows fine-tuning of VSMC contraction and ensures that it can be sustained even after the Ca^{2+}

transient has terminated (Kuo and Ehrlich, 2015). This mechanism of VSMC contractile regulation is mediated by the DAG-PLC-PKC pathways and a RhoA pathway (Kuo and Ehrlich, 2015).

To terminate VSMC contraction, the regulatory light chain of myosin is dephosphorylated by myosin light chain phosphatase (MLCP), causing VSMC relaxation (Hartshorne et al., 1998; Somlyo and Somlyo, 2003). To restore Ca^{2+} homeostasis, the Ca^{2+}-Mg^{2+}-ATPase and SERCA expend energy to extrude Ca^{2+} ions from the cytosol against their electrochemical gradient, the former to extrude Ca^{2+} from the cell, and the latter to replenish SR Ca^{2+} stores.

1.7 VSMC phenotypic switching

Unlike cardiac and skeletal muscle cells, VSMCs are not terminally differentiated. Instead, VSMCs retain plasticity, which enables them to modulate their phenotype in response to changing local environments (Rzucidlo et al., 2007). Thus, VSMCs are able to re-enter the cell cycle and dedifferentiate from their quiescent, contractile phenotype to a synthetic, proliferative and migratory phenotype—often as a maladaptive attempt at vascular repair after injury or insult (House et al., 2008; Alexander and Owens, 2012). Platelet-derived growth factor is a potent mitogen that is released at the site of injury by SMCs and other cell types associated with the vessel wall (Heldin and Westermark, 1999; Raines, 2004). The role of PDGF in promoting the SMC phenotypic transition from contraction to proliferation is well-established in conditions such as restenosis (Bilder et al., 1999; Sihvola et al., 1999), atherosclerosis (Kozaki et al., 2002), abdominal aortic aneurysm (Vorkapic et al., 2016) and PH (Barst, 2005; Antoniu, 2012; Xiao et al., 2017; Perros et al., 2008; Tannenberg et al., 2018).

Phenotypic switching in VSMCs is accompanied by an altered transcriptional profile (specific reference to which is made in the following sections), which manifests as a change in the expression of multiple ion channels and proteins. Downregulation of proteins associated with the contractile apparatus is observed. For example, conventional smooth muscle myosin II is downregulated during VSMC phenotypic switching from a contractile to a proliferative phenotype, resulting in a slower rate of contraction (Rensen et al., 2007). Downregulation of the VSMC contractile apparatus during this phenotypic transition accounts for experimental difficulty detecting VSMCs in *in-vivo* models of vascular disease using classic immunohistochemical approaches. These challenges can be overcome using lineage tracing technology.

To provide insight into the benefits of this approach, all VSMCs, whether they are differentiated or dedifferentiated, express the SMMHC promoter, which is specific to SMCs (Miano et al., 1994). Lineage tracing technology makes use of the Cre recombinase enzyme under the control of the SMMHC promoter. Thus, when the SMMHC gene is transcribed, Cre recombinase excises a floxed stop codon and membrane tomato (mT) reporter, revealing the downstream membrane-targeted green fluorescent protein (mGFP) reporter. This process occurs in VSMCs upon differentiation, thus mGFP is already expressed even after VSMCs transition from their differentiated to their dedifferentiated (proliferative) phenotype. This circumvents the issues of downregulation of the SMMHC protein as a contractile marker upon phenotypic switching. The benefits of lineage tracing technology are discussed in further detail by Shankman et al. (2015).

Accompanying transcriptional/translational adaptations to the contractile apparatus in dedifferentiated VSMCs, upregulation of apparatus associated with the synthetic/proliferative phenotype is also observed. For example, synthetic VSMCs exhibit ribosomal upregulation and a dense Golgi apparatus, contributing to protein synthesis. Of particular relevance to this thesis, VSMC phenotypic switching is associated with changes in the expression of Ca^{2+} channels and signalling proteins that occur downstream of mitogenic activation. Since Ca^{2+} is an abundant second messenger and contributes to so many functions within pulmonary VSMCs, changes in the expression of Ca^{2+} channels have the capacity to modulate a number of cellular processes, including the VSMC phenotypic transition from contraction to proliferation (House et al., 2008).

1.8 Pulmonary VSMC proliferation is a Ca^{2+}-dependent process

In pulmonary VSMCs, both cytosolic Ca^{2+} and intracellular Ca^{2+} stores influence phenotypic switching, cell-cycle progression and proliferation, evidenced by the observation that removal of these Ca^{2+} sources abolished proliferation even in the presence of serum and growth factors (Golovina et al., 2001). Ca^{2+} is required for activation of transcription factors such as c-Fos, nuclear factor of activated T-cells (NFAT), and cAMP response element-binding protein (CREB); Ca^{2+}-dependent kinases such as Ca^{2+}/calmodulin-dependent protein kinases (CaMKs); cyclins and cyclin-dependent kinases; and immediate early genes. These influence all stages of cell division including cell growth, the G_0 to G_1 transition (cell-cycle entry), progression from G_1 to S (DNA replication), through to G_2 (growth and protein synthesis) and mitosis itself (Kuhr et al., 2012). Therefore, Ca^{2+} is indispensable in the VSMC proliferative process and any change in the expression of Ca^{2+} channels and signalling proteins can disrupt Ca^{2+} homeostasis, influencing the transition of VSMCs from a contractile to a proliferative phenotype—a hallmark of many vascular diseases, including atherosclerosis, neo-intimal hyperplasia and PH.

1.9 Pulmonary hypertension

Pulmonary hypertension is a syndrome of progressive pulmonary vasculopathy clinically defined by an elevated PAP of ≥25 mmHg at rest and ≥30 mmHg upon exertion (Badesch et al., 2009; Voelkel et al., 2012).

The prevalence of PH ranges from 5–52 per million adults and the incidence of PH is approximately 2.5–7.1 cases per million adults (Humbert et al., 2006; Peacock et al., 2007). The mean age of patients with PH in the Western world is 45–65 years (Prins and Thenappan, 2016). Pulmonary hypertension is predominant in females with a ratio of 1.7–4.8:1 (Rich et al., 1987; Frost et al., 2011; Moon et al., 2014), the reason for which is unclear, but may be due to use of hormone replacement therapy. Although awareness of PH is increasing, there is still a delay between diagnosis and symptomatic onset. To put this into context, the mean duration between symptomatic onset and diagnosis of PH in the modern era is around 18–32 months (Brown et al., 2011; Ling et al., 2012). This is thought to be due to the co-morbidities associated with PH, including diabetes, coronary artery disease and metabolic syndrome, which can mask PH and therefore result in inaccurate diagnosis (Prins and Thenappan, 2016).

Group 1 PH encompasses pulmonary arterial hypertension (PAH). Group 1 PH is sub-classified into idiopathic, heritable, drug/toxin-induced and PAH secondary to other diseases including the human immunodeficiency virus (Schermuly et al., 2011). Heritable PAH can result from a mutation or single nucleotide polymorphism (SNP) in a given gene. Associated mutations include an inactivating mutation in *BMPR2*, the gene encoding the superfamily of bone morphogenetic protein receptors, which normally function to regulate proliferation of VSMCs (Morrell, 2006). Also, in Group 1 PH is idiopathic PAH (iPAH), which occurs in the absence of any identifiable risk factor. While Group 1 PH is characterised by those conditions that encompass disease specifically in the pulmonary arteries, all other groups are categorised as PH—a general term used to define high pressure in the lungs.

Group 2 PH owing to left heart disease can occur due to left ventricular (LV) systolic or diastolic dysfunction, valvular disease, congenital cardiomyopathies and left heart inflow/outflow obstruction. Group 3 PH may occur secondary to lung disease or hypoxia, such as that observed in chronic obstructive pulmonary disease (COPD), emphysema or pneumonia. The estimated prevalence of PH as a consequence of obstructive sleep apnoea is 15%–20% (Kessler et al., 1996), and in patients with any sleep-related breathing disorder is 17%–53% (Roux et al., 2000; Houtchens et al., 2011). Group 4 chronic thromboembolic PH can occur as a result of numerous disorders ranging from systemic sarcoidosis, glycogen storage disease or chronic haemolytic anaemia.

Although the above list is not exhaustive it demonstrates the multi-factorial aetiology of PH and gives some insight into the complexity of the syndrome. Due to the relative ease of reproducing experimental chronic hypoxia (CH)-induced PH, the findings of this thesis are understood in the context of Group 3 PH. The benefits and limitations of widely used *in-vivo* models of CH-induced PH are discussed in Section 1.15 and were used to inform the choice of *in-vivo* model in this thesis.

1.10 Pulmonary VSMC phenotypic switching in CH-induced PH

1.10.1 Hypoxic pulmonary vasoconstriction

Hypoxia occurs when the partial pressure of O_2 (PO_2) falls below ~50 mmHg (normal alveolar PO_2 is ~100 mmHg at sea level) (Lumb and Slinger, 2015). The initial response of the pulmonary vascular system to hypoxia is hypoxic pulmonary vasoconstriction (HPV), which is mediated by pulmonary VSMCs in the medial layer of the vessel wall. Hypoxic pulmonary vasoconstriction underpins the physiological phenomenon of ventilation–perfusion matching, which aims to achieve an optimum ratio between the volume of air that reaches the alveoli and the volume of blood that is available at the capillaries for gas exchange. Ventilation–perfusion matching promotes haemoglobin saturation to utilise the maximal O_2 carrying capacity of the blood. Hypoxic pulmonary vasoconstriction temporarily reduces the intraluminal radius of pulmonary vessels in poorly ventilated regions of the lung and diverts blood away from areas of the lung with localised hypoxia. Blood is diverted to more well-ventilated areas to support regional blood flow and maintain efficient gas exchange. The reduction in the intraluminal radius of blood vessels that occurs during HPV increases PVR as a consequence of the relationship: $PVR \propto 1/r^4$. Since CO stays the same and PVR is increased, PAP is also increased according to the relationship: $CO \times PVR = PAP$.

The cellular and molecular mechanisms that underpin HPV are elusive but are thought to involve various Ca^{2+} channels associated with VSMC contraction. One well-accepted explanation is that hypoxia increases intracellular reactive O_2 species (ROS) in pulmonary VSMCs (Marshall et al., 1996; Killilea et al., 2000; Liu et al., 2003; Paddenberg et al., 2003; Jernigan et al., 2004), which directly modulate the activity of K_v channels. Since K_v channels maintain the resting E_m, inhibition of these channels by ROS initiates membrane depolarisation and activates VDCCs, leading to Ca^{2+} entry and VSMC contraction. A second explanation is that ROS activate the ryanodine receptor to induce release of Ca^{2+} from internal stores, specifically the SR, which triggers SOCE and VSMC contraction (Lin et al., 2007; Pourmahram et al., 2008). Thus, it is clear that Ca^{2+} channels are fundamental in the regulation of HPV. A review describing the mechanisms of HPV is provided by Dunham-Snary et al. (2017).

Although HPV serves benefit as a physiological mechanism in the short term, when the lungs are subject to sustained hypoxia on a global scale such as in disease states like COPD, emphysema, bronchitis and pneumonia (Group 3 PH), development of CH-induced PH occurs due to a transition from sustained HPV to vascular remodelling—a shift that is underpinned at the cellular level by VSMC phenotypic switching from a contractile to a proliferative phenotype.

1.10.2 Vascular remodelling

Vascular remodelling is a term used to describe a multitude of adaptations within the vessel wall including thickening of the intimal and medial layers of small muscular arteries and arterioles, development of occlusive lesions within pulmonary vessels and proliferation and migration of VSMCs down to precapillary arterioles (distal muscularisation) (Voelkel and Tuder, 2000; Humbert et al., 2004; Stenmark et al., 2009).

Many of these vascular remodelling processes are consequent of VSMC phenotypic switching from a quiescent, contractile phenotype to a synthetic, proliferative, migratory phenotype in response to an insult—in this instance, CH. Phenotypic switching in VSMCs and the consequent gross morphological adaptation of the vessels reduce the intraluminal radius and impede blood flow.

Since PVR $\propto 1/r^4$, PVR is increased, thereby increasing PAP—the clinically defining feature of PH.

1.11 Therapeutic approaches to PH

Although vascular remodelling and vasoconstriction are two fundamental and well-established pathologies in PH, no treatment is currently available in the clinic with an anti-proliferative primary mechanism of action. Thus, there is concerning unmet clinical need for anti-proliferative therapeutics.

On the other hand, the pathology of vasoconstriction is extensively targeted by existing therapies. In theory, excessive vasoconstriction can be counteracted using agents that either directly cause vasodilation or inhibit vasoconstriction (Archer et al., 2010).

1.11.1 Prostacyclin analogues

Prostacyclin is a predominantly endothelial cell-derived prostaglandin that inhibits platelet aggregation and induces vasodilation. Justifying the use of prostacyclin analogues such as beraprost, epoprostenol, iloprost and treprostinil for the treatment of PH is the finding that prostacyclin synthase expression is reduced in the pulmonary arteries of PH patients (Christman et al., 1992; Galie et al., 2003). In addition to its potent vasodilatory properties, prostacyclin also appears to exhibit mild anti-proliferative effects (Jones et al., 1995), although this is not the primary mechanism of action of prostacyclin analogues.

1.11.2 Phosphodiesterase type-five inhibitors

Phosphodiesterase type-five (PDE5) inhibitors such as sildenafil and tadalafil prevent the breakdown of cyclic guanosine monophosphate (cGMP); and soluble guanylate cyclase (sGC) stimulators (riociguat) increase cGMP production, which in turn potentiates the action of nitric oxide (NO) leading to vasodilation. These agents are useful because NO synthesis and signalling are impaired in PH. In addition to the vasodilatory effects of these drug classes, pre-clinical studies using sGC stimulators and PDE5 inhibitors have demonstrated some anti-proliferative and anti-remodelling properties in animal models of PH (Galie et al., 2013), although this is not the primary mechanism of action of these agents.

1.11.3 Endothelin receptor blockers

To inhibit vasoconstriction, endothelin (ET) receptor blockers including bosentan and ambrisentan are used. ET causes vasoconstriction by acting as an agonist at ET-A and ET-B receptors in pulmonary VSMCs. Although ET-B receptors are also expressed in endothelial cells, and activation causes release of vasodilators such as NO and prostacyclin, the efficacy of dual ET-A and ET-B receptor blockers versus selective ET-A blockers is comparable (Galie et al., 2013). Although it is unclear whether the increase in plasma ET is a cause or consequence of PH, activation of this system has been demonstrated in plasma and lung tissues from PH patients (Giaid et al., 1993).

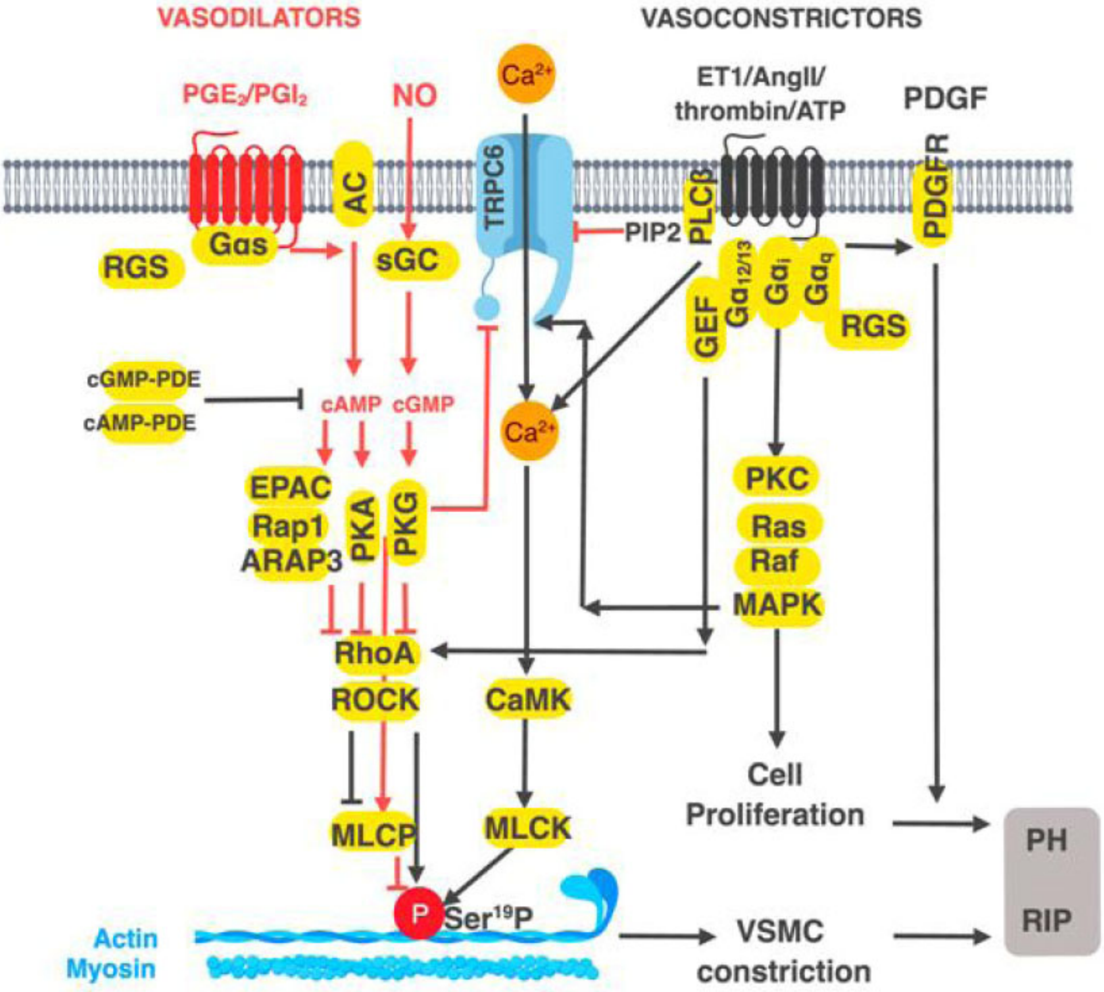

Figure 1.11. Regulation of vascular tone and VSMC proliferation by GPCRs.

Therapeutic management options for PH primarily target GPCRs to either promote vasodilation or inhibit vasoconstriction. Although these agents produce mild anti-proliferative effects, this is not their primary mechanism of action. Anti-proliferative therapeutics could be pivotal in PH management. PGE$_2$, prostaglandin E2; PGI$_2$, prostaglandin I2; NO, nitric oxide; ET1, endothelin-1; AngII, angiotensin II; PDGF(R), platelet-derived growth factor (receptor); AC, adenylate cyclase; sGC, soluble guanylate cyclase; cAMP, cyclic adenosine monophosphate; cGMP, cyclic guanosine monophosphate; PKA, protein kinase A; PKG, protein kinase G; PKC, protein kinase C; MLCP, myosin light chain phosphatase; MLCK, myosin light chain kinase; CaMK, Ca^{2+}/calmodulin-dependent protein kinase; PIP$_2$, phosphatidylinositol 4,5-bisphosphate; PLCβ, phospholipase C-β; MAPK, mitogen-activated protein kinase. Image taken from Strassheim et al. (2018).

1.11.4 L-type Ca^{2+} channel blockers

L-type Ca^{2+} channels are widely recognised for their role in vasoconstriction, justifying the use of L-type Ca^{2+} channel blockers (nifedipine, diltiazem, nicardipine, amlodipine) as a therapeutic approach for PH. However, in VSMC phenotypic switching, L-type Ca^{2+} channel expression is reduced (Gollasch et al., 1998; Clunn et al., 2010). Thus, these approaches may be effective in the initial phases of the condition where HPV predominates but may account for poor responsiveness to such therapies in advanced PH after the transition from sustained HPV to vascular remodelling.

1.11.5 PDGF receptor inhibitors

Since 2003, another target of therapeutic interest is the PDGF receptor due to substantial upregulation in small pulmonary arteries of patients with PH and its contribution to pulmonary vascular remodelling (Humbert et al., 1998; Perros et al., 2008a) and VSMC remodelling in general (1.7). Thus, PDGF receptor blockers were speculated to be therapeutically beneficial for PH patients (Balasubramaniam et al., 2003). The PDGF receptor blocker, imatinib, showed promise in reversing elevated pulmonary pressure and pulmonary vascular remodelling in the monocrotaline (MCT)-induced PH rodent model (Schermuly et al., 2005). Further, a combination of imatinib with an ET receptor blocker, a PDE5 inhibitor and a prostanoid led to an extraordinary improvement in multiple markers associated with PH (Ghofrani et al., 2005).

Numerous studies have demonstrated promise for imatinib as a therapeutic agent for PH. Specifically, patients administered imatinib exhibited improved exercise capacity and haemodynamics (Ghofrani et al., 2010), reduced PVR (Ghofrani et al., 2005) and improved quality of life and functional class (Speich et al., 2015).

Despite significant improvements in multiple parameters of PH in phase II and III clinical trials, a phase III clinical study (Imatinib in Pulmonary Arterial Hypertension, a Randomised, Efficacy Study [IMPRES]) demonstrated that 4.2% of patients enrolled in the trial developed subdural haematoma after imatinib treatment, the mechanism for which was unknown. Thus, the sponsors of the trial withdrew the approval application. The occurrence of subdural haematoma in patients administered imatinib was corroborated by a study conducted in Zurich, in which two out of a total of 15 patients presented with subdural haematoma (Speich et al., 2014).

Although PDGF receptor inhibition improves parameters associated with PH, it is possible that the number of divergent downstream pathways affected by direct PDGF receptor inhibition is too widespread, resulting in detrimental off-target effects. Research to identify the specific downstream targets of the PDGF receptor that mediate the protective effects of PDGF receptor inhibition would be beneficial. At present, expert opinion suggests that imatinib is only recommended for patients whose existing therapeutic regime is ineffective, and in those patients whose only remaining options are organ transplantation or death (Hoeper et al., 2013).

1.12 Unmet clinical need for anti-proliferative therapeutics

It is widely accepted that the hallmarks of all forms of PH are sustained pulmonary vasoconstriction and vascular remodelling (Shimoda and Laurie, 2013). Despite existing therapeutic management options, which primarily target the pathology of vasoconstriction, PH mortality rates are high with only around 55% of patients surviving past three years of diagnosis (Humbert et al., 2010). The mortality rate within one year of diagnosis is around 15% (Thenappan et al., 2007). This figure is variable when accounting for specific patient comorbidities (Archer et al., 2010). In paediatric patients, current therapeutic approaches are effective. However, only 15% of adult patients are classed as *responders* (Rich et al., 1992; Montani et al., 2010; Solik et al., 2013), and even then, there is a risk that these patients will become resistant to therapies (Morrell et al., 2009). In responders, current therapeutic strategies are palliative rather than curative, are reasonably costly, and as is clear from the above statistics, are only effective in a small proportion of patients (Archer et al., 2010; Baliga et al., 2011). One explanation for this poor patient response is that the vascular remodelling associated with advanced PH is accompanied at the cellular level by a downregulation in genes currently targeted by existing vasoregulatory therapeutics, such as L-type Ca^{2+} channel blockers, which could account for the poor clinical response to such agents.

Since PH is an umbrella term used to describe a potentially diverse range of diseases, the heterogeneity of disease is large. Thus, instead of taking a *one-size-fits-all* approach, a personalised medicine approach may be beneficial. To improve existing options, which primarily provide symptomatic management for patients, research should aim to identify prophylactic interventions and cures. Since vascular remodelling is the pathology that underpins the development and progression of PH, lack of anti-proliferative therapeutics means that a whole area of clinical possibility remains untargeted. Identification of viable anti-proliferative targets could be pivotal in the clinical management of PH. Multiple ion channel proteins are currently the subject of extensive research as anti-proliferative targets for PH.

1.13 Potassium channels as modulators of Ca^{2+} entry

As well as direct modulation of Ca^{2+} entry pathways in PH (1.14), Ca^{2+} entry pathways are modulated secondary to changes in K^+ channels. Specifically, patients with PH display a downregulation in $K_v1.5$ (Yuan et al., 1998b) and SNPs in the gene encoding $K_v1.5$ (*KCNA5*) have been identified in iPAH patients (Remillard et al., 2007). The mRNA and protein expression of K_v channels and the amplitude of whole-cell K^+ current were significantly lower in pulmonary VSMCs from iPAH patients compared to normotensive patients, and the resting E_m of pulmonary VSMCs was more depolarised (Yuan et al., 1998a). Similarly, changes in K^+ channel activity and expression have been noted in acute HPV. Acute hypoxia inhibits numerous K_v channels including $K_v1.5$, $K_v1.2$, $K_v2.1$ and $K_v3.1b$, which causes membrane depolarisation and activation of VDCCs (Joshi et al., 2006; Joshi et al., 2009). Chronic hypoxia downregulates K^+ channels (Wang et al., 1997) and decreases whole-cell K^+ current in pulmonary VSMCs (Smirnov et al., 1994; Platoshyn et al., 2001). Importantly, adenoviral transfection to restore $K_v1.5$ expression in a rodent model reduced experimental CH-induced PH (Pozeg et al., 2003).

The electrochemical gradient for K^+ enables its efflux from the cell upon channel opening, causing hyperpolarisation (Burg et al., 2008). Thus, the consequence of $K_v1.5$ downregulation is membrane depolarisation, triggering an increase in the $[Ca^{2+}]_{cyt}$ via VDCCs, and altering the electrochemical driving force for Ca^{2+}, promoting Ca^{2+} entry via non-voltage-dependent pathways. It follows that the resting $[Ca^{2+}]_{cyt}$ and resting E_m are elevated in proliferating compared to growth-arrested cells. A sustained increase in the $[Ca^{2+}]_{cyt}$ contributes to VSMC proliferation and PH progression (Wang et al., 1997; Archer et al., 1998).

1.14 Calcium channels

Chelation of extracellular Ca^{2+} abolishes cell growth (Platoshyn et al., 2000), evidencing the importance of Ca^{2+} arising from the extracellular space in proliferation of pulmonary VSMCs. Plasma membrane Ca^{2+} channels of specific interest are the VDCCs, ROC channels and SOC channels. To gain clear insight into the Ca^{2+} channels that play a role in VSMC proliferation in CH-induced PH, candidate genes should be collectively screened under comparable conditions, because as is clear from the literature, changes in the expression of Ca^{2+} channel genes are variable depending on the experimental model used and the class of PH under investigation. Herein, this thesis focuses on hypoxia-induced changes in Ca^{2+} channel subunit expression.

1.14.1 L-type Ca^{2+} channels in CH-induced PH

Under physiological conditions, the resting E_m of -60 to -40 mV in pulmonary VSMCs is maintained by K_v channels. Thus, the resting E_m is more negative than the membrane potential required for L-type Ca^{2+} channel activation (-20 mV). Thus, at the resting E_m, there is very little activation of these channels, evidenced by the absence of any effect of L-type Ca^{2+} channel blockers on basal $[Ca^{2+}]_i$ or vascular tone (Somlyo and Somlyo, 1994).

As described earlier, hypoxia-induced downregulation of K_v channels (Smirnov et al., 1994; Wang et al., 1997; Yuan et al., 1998b; Platoshyn et al., 2001) is sufficient to depolarise pulmonary VSMCs to an extent appropriate to trigger activation of L-type Ca^{2+} channels, supporting these channels as a component of early HPV. The involvement of L-type Ca^{2+} channels in early HPV provides the rationale for use of L-type Ca^{2+} channel blockers as important therapeutic tools in early PH.

There is extensive literature dedicated to understanding the role of L-type Ca^{2+} channels in the development of CH-induced PH. Acute hypoxia (60 hours) increased the basal $[Ca^{2+}]_{cyt}$, which was reversed with L-type Ca^{2+} channel blockers in pulmonary VSMCs (Wang et al., 2005). Like acute hypoxia, CH (two and three weeks) showed similar increases in basal $[Ca^{2+}]_{cyt}$ in pulmonary VSMCs from rats and mice (Salvaterra and Goldman, 1993; Peng et al., 2013). However, in CH the L-type Ca^{2+} channel blockers, verapamil and nifedipine, were ineffective in blocking this increase in basal $[Ca^{2+}]_{cyt}$, despite appropriate concentrations (Salvaterra and Goldman, 1993). In CH rats, the increase in basal $[Ca^{2+}]_{cyt}$ was maintained even after hypoxia ceased, suggesting that it was not due to activation of L-type Ca^{2+} channels by vasoconstrictive factors, but rather due to transcriptional and translational adaptations (Kuhr et al., 2012).

A further consideration is that L-type Ca^{2+} channels are downregulated as PH progresses (Gollasch et al., 1998; Clunn et al., 2010). This means that the time spent in hypoxia may determine the effectiveness of L-type Ca^{2+} channel blockers on the development of CH-induced PH, reflecting the reduced sensitivity to L-type Ca^{2+} channel blockers that is observed in the clinic, and that they are unlikely to play a role in the remodelling processes of advanced PH.

Thus, while L-type Ca^{2+} channels may be early players in the development of HPV, it is likely that transcriptional and translational adaptations are required to sustain the elevated basal $[Ca^{2+}]_{cyt}$ in response to hypoxia. Downregulation of L-type Ca^{2+} channels as PH progresses from HPV to vascular remodelling suggests that L-type Ca^{2+} channels are unlikely to play a role in the vascular remodelling processes that underpin the progression of CH-induced PH.

1.14.2 T-type Ca^{2+} channels in CH-induced PH

T-type Ca^{2+} channels have been associated with proliferation due to the observation that small interfering RNA (siRNA) against $Ca_v3.1$ in human pulmonary VSMCs reduced cell proliferation compared to scrambled control siRNA (Rodman et al., 2005). Although this group used western blot and electrophysiology to validate T-type Ca^{2+} channel knockdown in both HEK293 cells stably overexpressing $Ca_v3.1$ and human pulmonary VSMCs to validate these findings, they did not test for off-target effects on Ca^{2+} channels that are also natively expressed in both wild type (WT) HEK293 cells and human pulmonary VSMCs, such as Orai1 and STIM1 (Fukushima et al., 2012).

Duckles et al. (2015) showed a raised $[Ca^{2+}]_{cyt}$ and increased proliferation of HEK293 cells overexpressing $Ca_v3.2$ when compared to non-transfected cells. The increase in the $[Ca^{2+}]_{cyt}$ and proliferation observed here may not be solely attributable to $Ca_v3.2$ overexpression. Given that Orai1 and STIM1 are natively expressed in WT HEK293 cells and have been associated with VSMC proliferation in multiple cell types (1.14.4), it is possible that the presence of Orai1 is necessary to observe the increase in the $[Ca^{2+}]_{cyt}$ and proliferative effects of $Ca_v3.2$. This is similar to the regulation of TRPC1 by Orai1 and STIM1, which facilitates the contribution of TRPC1 to SOCE (Cheng et al., 2011).

The rationale for this speculation is the observation that knockdown of STIM1 modulated the peak amplitude and current density of T-type Ca^{2+} channels and shifted the E_m to more negative values in the cardiac muscle cell line, HL-1 (Nguyen et al., 2013). Knockdown of STIM1 also modulated the surface expression of T-type Ca^{2+} channels, and coimmunoprecipitation assays demonstrated a direct interaction between T-type Ca^{2+} channels and STIM1 (Nguyen et al., 2013).

The complex functional interactions between Ca^{2+} entry pathways highlighted above mean that the influence of native gene expression should be considered when deciding a suitable cell type for a particular observation. For example, WT

HEK293 cells would be a suitable system to investigate the roles of Orai1 that are independent of T-type Ca^{2+} channels, as this cell type do not natively express the latter. When using cell types that express multiple Ca^{2+} channels, suitable tools should be utilised to investigate the relative contribution of each candidate Ca^{2+} channel gene to a particular cellular process. One way to achieve this is by use of inhibitors that have undergone selectivity verification.

Observations on the effect of T-type Ca^{2+} channels in proliferation of pulmonary VSMCs are heavily based on the use of the T-type Ca^{2+} channel blockers, mibefradil and NNC55-0396. It is noteworthy that off-target effects of mibefradil and NNC55-0396 are well recognised in the literature (1.5.1.3–1.5.1.5), justifying withdrawal of mibefradil from the market and the restriction of NNC55-0396 for experimental use only. It would be beneficial to verify the anti-proliferative effects of these compounds in pulmonary VSMCs using the newly established T-type Ca^{2+} channel inhibitor, TTA-A2.

Other evidence in support of a role for T-type Ca^{2+} channels in proliferation is the observation that as VSMCs differentiate and lose their ability to proliferate, the expression of T-type Ca^{2+} channels declines (Cribbs, 2006). Richard et al. (1992) reported that T-type Ca^{2+} channel function reappears in cultured rat aortic myocytes compared to freshly isolated (differentiated) cells, suggesting an important role for T-type Ca^{2+} channels in proliferation. Whether or not this T-type Ca^{2+} channel upregulation is also observed in pulmonary VSMCs in the context of CH-induced PH should be clarified.

Interestingly, in a CH-induced PH mouse model, $Ca_v3.2$ expression was increased in pulmonary artery compared to mesenteric artery (Wan et al., 2013). Similarly, Sellak et al. (2014) demonstrated increased $Ca_v3.2$ mRNA after 12 hours of hypoxic exposure, followed by increased $Ca_v3.2$-mediated T-type Ca^{2+} channel current after 24 and 48 hours, evidencing a hypoxia-induced upregulation on a transcriptional, translational and functional level in rat pulmonary VSMCs. It is fundamental to highlight that the threshold for activation (-40 mV) and rapidly inactivating nature of T-type Ca^{2+} channels mean that they are highly unlikely to be active at the resting E_m of CH pulmonary VSMCs (around -20 mV) (Cribbs, 2006), which prompts us to reconsider their contribution to pulmonary VSMC proliferation in CH-induced PH.

Perhaps the most convincing evidence linking T-type Ca^{2+} channels to PH is that treatment of CH rats with TTA-A2; or $Ca_v3.1$ deletion, inhibited right cardiac hypertrophy, pulmonary artery remodelling and CH-induced PH (Chevalier et al., 2014). TTA-A2 appears to be one of the most selective T-type Ca^{2+} channel inhibitors available for research purposes and should be utilised when investigating the T-type Ca^{2+} channel as an anti-proliferative target in CH-induced PH.

1.14.3 TRPC proteins in CH-induced PH

Research suggests that proliferation of pulmonary VSMCs is attributable, at least in part, to an increased $[Ca^{2+}]_{cyt}$ related to TRPC upregulation. Upregulated TRPC1 expression and a greater SOCE amplitude are observed in pulmonary VSMCs when compared to growth-arrested cells, supporting TRPC1 as a contributor to SOCE in pulmonary VSMCs. Antisense oligonucleotides against TRPC1 inhibited proliferation by 50% and markedly reduced SOCE (Sweeney et al., 2002).

In pulmonary VSMCs, an increase in the mRNA and protein expression of TRPC1 and TRPC6 was paralleled by an increase in proliferation (Golovina et al., 2001). Similarly, Lin et al. (2004) reported a two- to three-fold increase in TRPC1 and TRPC6 expression in hypoxic rat pulmonary VSMCs. Exposure of human pulmonary VSMCs to hypoxia increased SOCE-dependent basal $[Ca^{2+}]_{cyt}$ that was accompanied by an increase in TRPC1 expression (Lin et al., 2004).

Similarly, mRNA for TRPC1 and SOCE were increased in proliferating compared to growth-arrested human pulmonary VSMCs (Golovina et al., 2001), supporting a role for TRPC1 in SOCE-mediated pulmonary VSMC proliferation. Malczyk et al. (2013) revealed that upregulation of TRPC1 mRNA was observed in murine pulmonary VSMCs maintained in 1% O_2 for 72 hours, and that hypoxia-induced proliferation of these cells was reduced when subjected to siRNA against TRPC1. Similarly, TRPC1-/- mice presented with less vascular muscularisation, albeit a similar degree of RV hypertrophy, compared with WT animals. Yang Xia et al. (2013) also observed reduced muscularisation in small pulmonary arteries of TRPC1-/- and TRPC6-/- mice exposed to CH compared to WT animals.

It appears that TRPC1, which has been heavily ascribed a role as a contributor to SOCE in pulmonary VSMCs (albeit not critically required), plays a role in the development and progression of CH-induced PH and could be a useful anti-proliferative target. However, the well-established non-selective cation selectivity of TRPC channels means that less focus was placed on investigating their role as anti-proliferative targets in pulmonary VSMCs in this thesis, since the predominant interest was on Ca^{2+}-selective cation channels. However, that is not to rule out TRPC channels as key players in CH-induced VSMC proliferation, rather evidence shows that these channels are worthy of further research.

1.14.4 Orai and STIM proteins in CH-induced PH

Evidence linking Orai proteins to the development of CH-induced PH include the observation that in rats exposed to CH for three weeks, a significant increase in both Orai1 and Orai2 mRNA and protein expression was observed in distal pulmonary arteries compared to normoxic controls. Orai3 was unaffected (Hou et al., 2013; Smith et al., 2015; Chen et al., 2017; Wang et al., 2017b; He et al., 2018). Since arachidonic acid-regulated (ARC) channels are formed by Orai1 and Orai3 heteromultimers, and no hypoxia-induced upregulation in Orai3 was observed, it is unlikely that ARC channels play a role in CH-induced pulmonary VSMC proliferation. However, changes in the expression of all Orai isoforms in the context of CH-induced PH will be clarified in this research.

Wang et al. (2017) demonstrated that knockdown of hypoxia-inducible factor 1α (HIF1α) in mice, and siRNA against HIF1α in pulmonary VSMCs prevented the hypoxia-induced upregulation of Orai2, but not Orai1, suggesting that Orai2 upregulation is a direct response to low O_2 conditions. These findings are in support of earlier studies that also demonstrated a hypoxia-induced upregulation of Orai1 and Orai2 proteins in the pulmonary vasculature of hypoxic rats (Lin et al., 2004; He et al., 2018). Upregulation of Orai1 and Orai2 is corroborated by the observation that SOCE is increased in hypoxia. Importantly, Orai upregulation translates to an increase in basal $[Ca^{2+}]_{cyt}$ and increased SOCE as demonstrated by a reduction in both these parameters upon Orai1, Orai2 and STIM1 silencing (Wang et al., 2017).

Although no upregulation of STIM1 was observed in the pulmonary vasculature of hypoxic rats (Lin et al., 2004; He et al., 2018), which would be expected due to the close functional association between Orai1 and STIM1, other groups have demonstrated a hypoxia-induced upregulation of STIM1 (Hou et al., 2013). Discrepancies may exist here due to the passage of pulmonary VSMCs used (primary cultures versus passage 2–8 cells, respectively). While primary cultures are more likely to resemble a differentiated, contractile phenotype, later passages adopt a synthetic, proliferative phenotype due to the conditions to which they are exposed to sustain culture. Importantly, the extent of this synthetic phenotype is exacerbated by hypoxia. Thus, the expression of STIM isoforms in the context of CH-induced PH will be clarified in this research.

Lu et al. (2009) demonstrated that knockdown of STIM1 abolished the increase in SOCE observed in response to acute hypoxia (4%, 15 minutes) in pulmonary VSMCs. Thus, STIM1 has been described as a stress-sensor, due to its capacity to respond to changing local environments such as hypoxic stress (Wang et al., 2017).

In both aortic and pulmonary VSMCs, Orai1-dependent SOCE is mediated by PDGF via IP_3 generation and release of Ca^{2+} from internal stores. Platelet-derived growth factor-induced VSMC migration and proliferation are also Orai1-dependent in both aortic (Bisaillon et al., 2010) and airway SMCs (Spinelli et al., 2012; Suganuma et al., 2012). As earlier described, the PDGF receptor blocker, imatinib, slowed PH progression and improved multiple pathological parameters of PH. However, imatinib demonstrated detrimental off-target effects such as subdural haematoma, possibly due to the widespread consequences of direct PDGF receptor inhibition, which affects a multitude of divergent second messenger pathways. Orai1 is just one downstream target of PDGF, and selective Orai1 inhibition reduces PDGF-induced VSMC proliferation and migration, showing promise in targeting Orai1 as an anti-proliferative therapeutic approach for CH-induced PH.

1.14.4.1 CM4620

There are currently no Orai1 inhibitors available for clinical use. However, the CRAC channel inhibitor, CM4620, has been approved for clinical trials for the treatment of acute pancreatitis (Waldron et al., 2019) and selective inhibition of Orai channels has been suggested to treat inflammation, cancer (Mo and Yang, 2018) and cardiovascular disease. These findings, combined with the ongoing research to identify novel, soluble, selective Orai1 blockers, make Orai1 an interesting Ca^{2+}-selective ion channel worthy of further investigation in the context of CH-induced PH. Two potent, highly selective experimental Orai1 inhibitors have been developed and can be used to investigate the anti-proliferative effects of Orai1 inhibition in pulmonary VSMCs.

1.14.4.2 Synta66

Synta66 (Figure 1.12) is a potent, selective inhibitor of TG-induced store depletion in human VSMCs with an IC_{50} of 26 nM (Li et al., 2011b). The selectivity of Synta66 was confirmed from the observation that the compound had no off-target effects when screened against 50 targets including receptors, enzymes and ion channels (Di Sabatino et al., 2009). The selectivity of Synta66 provides confidence that any anti-proliferative effects observed in the presence of this compound can be directly attributed to inhibition of Orai1-mediated SOCE.

Orai proteins are relatively understudied in the context of CH-induced PH, and Synta66 has never been used to investigate the anti-proliferative effects of Orai1 inhibition in the context of CH-induced PH. However, VSMC proliferation and migration are key pathologies in a number of occlusive diseases of the vasculature, including abdominal aortic aneurysm, atherosclerotic arterial stenosis, angioplasty-induced neointimal hyperplasia and vascular remodelling in hypertension. In common with CH-induced PH, these diseases also possess hypoxia as a key risk factor.

Liang et al. (2016) demonstrated that inhibition of Orai1-dependent SOCE or knockdown of Orai1 reduced foam cell formation in atherosclerosis. In addition, inflammatory gene expression in atherosclerotic plaques of the aortic sinus was decreased after inhibition of Orai1 signalling. Thus, Orai1 appears to have a role in foam cell formation and vascular inflammation in atherosclerosis. To support these findings, Synta66 inhibited VEGF-evoked Ca^{2+} entry and vessel growth in an *in-vivo* model of angiogenesis (Li et al., 2011a). Selective inhibition of Orai1 with Synta66 has also shown promise as an anti-proliferative approach to treat various types of cancer (Mo and Yang, 2018), confirming Orai1 as an interesting target worthy of further investigation. Although Synta66 is a reliable experimental tool, it is limited for *in-vivo* applications due to its poor solubility and difficulty in achieving high enough concentrations to infuse into rodents.

1.14.4.3 JPIII

Our laboratory have recently designed a novel compound, JPIII (Figure 1.12), which demonstrated selective inhibition of Orai1 in a selectivity screen. The selectivity screen was outsourced to a commercial research organisation (Eurofins Panlabs), and permission was sought to present the JPIII CEREP Safety-44 selectivity screen data in this thesis with appropriate acknowledgement (Figure 4.21). Although slightly less potent than Synta66 in VSMCs with an IC_{50} of 360 nM (unpublished data from Bailey lab), JPIII has superior pharmacokinetics, culminating in improved solubility. JPIII is also highly plasma protein-bound, meaning that high enough concentrations can be achieved to infuse into rodents to observe its effects in the context of disease. Accordingly, recent evidence demonstrates that Orai1 inhibition with JPIII

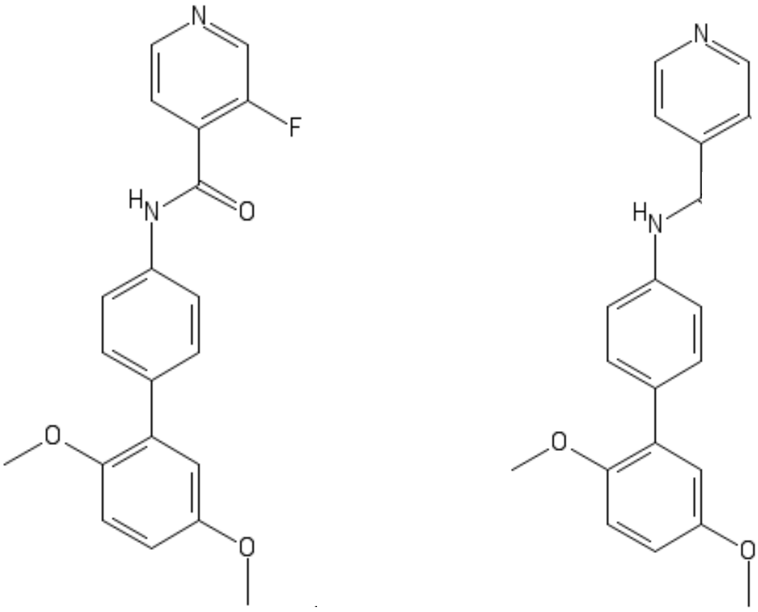

Figure 1.12. Chemical structure of Synta66 and JPIII.

JPIII was synthesised using the Synta66 scaffold with the aim of improving its pharmacokinetics for *in-vivo* studies.

reduced VSMC proliferation and migration in three mouse models of abdominal aortic aneurysm with nanomolar potency (Bailey, 2016). As demonstrated by histology and *in-vivo* ultrasound, respectively, JPIII reduced aortic remodelling and luminal dimensions in rodent models of abdominal aortic aneurysm.

The development of a potent, selective, soluble Orai1 inhibitor—JPIII, means that the tools to investigate the effects of selective Orai1 inhibition on CH-induced VSMC proliferation both *in vitro* and *in vivo* are now available.

1.15 *In-vivo* models of PH

Although many PH animal models exist and go some way to informing on certain aspects of PH, the two most widely used models do not completely recapitulate the histology of human PH, particularly the presence of plexiform lesions (Humbert et al., 2004; Archer et al., 2010). Two modern and widely published techniques are MCT and chronic hypoxia (CH) (Sztuka and Jasinska-Stroschein, 2017). Each of these approaches has its benefits and limitations.

1.15.1 Monocrotaline-induced PH

Monocrotaline is a toxic pyrrolizidine alkaloid that is activated by mixed function oxidases present in the liver *in vivo*. This process leads to production of the reactive compound, MCT pyrrole (MCTP) (Wilson et al., 1992; Cooper and Huxtable, 1999), which induces vascular injury (Sztuka and Jasinska-Stroschein, 2017) and subsequent remodelling (Rosenberg and Rabinovitch, 1988).

Despite resemblances between the MCT-induced PH model and human PH, this model has off-target effects on other organs such and the heart and liver. For example, hepatic veno-occlusive disease, and left- and right-sided myocarditis are observed in MCT-induced rats (Miyauchi et al., 1993). Animals treated with MCT can present with liver damage, kidney damage or cardiac damage (Schermuly et al., 2011). These comorbidities increase animal mortality and complicate the analysis of RV hypertrophy and failure consequent of PH. As a stimulus for PH, MCT also lacks the complex vascular remodelling processes (Ciuclan et al., 2011). Some rat strains also present with systemic hypertension, which is not typically associated with PH in humans (Sato et al., 1992; Nagaoka et al., 2001).

The MCT-induced rodent model is also limiting as it is restricted to rats due to the inability of mice to convert MCT into its active form (Gomez-Arroyo et al., 2012). It has been suggested that the metabolism of MCT into MCTP by the cytochrome P450 enzymes in the liver may differ between species. When infused into mice, MCT results in liver damage (Miranda et al., 1983), immunotoxicity (Deyo et al., 1994) and dose-dependent mortality (Dumitrascu et al., 2008).

1.15.2 CH-induced PH

In the aim of utilising genetically modifiable mice to investigate the mechanisms of PH, the CH models of PH are also widely used, and can be used as a rodent comparison to CH-induced PH in humans associated with conditions such as COPD and emphysema. However, like the MCT-induced PH rodent model, CH alone does not recapitulate the complex vascular remodelling processes of human PH.

Although Ciuclan et al. (2011) noted a subtle phenotype in mice exposed to CH, they found that weekly injections of the VEGF blocker, SU5416, combined with three weeks of CH (10%) recapitulated the pathological processes of CH-induced PH, such as vascular remodelling and cardiac indices, to a greater extent than CH alone. A marked increase in RV systolic pressure and RV hypertrophy were observed compared to the vehicle-treated hypoxic cohort. Importantly, this group demonstrated a variable degree of occluded pulmonary arterioles immediately after three weeks of hypoxia and SU5416, but these lesions were not quantified.

The means by which SU5416 worsens the CH-induced PH phenotype is not well understood, but some suggest that it is due to endothelial cell apoptosis as a consequence of VEGF receptor inhibition (Taraseviciene-Stewart et al., 2001). Another possibility is that block of the VEGF receptor precludes formation of new blood vessels, preventing the pulmonary system from adapting to CH by undergoing angiogenesis, worsening the phenotype compared to mice exposed to CH alone. The relative ease of reproducing the SuHx mouse model of CH-induced PH, combined with its capacity to reproduce pathological vascular remodelling, make the SuHx mouse model a useful tool to study the anti-remodelling effects of selective Ca^{2+} channel inhibition *in vivo*.

1.16 Summary of the present study

The phenotypic transition of VSMCs from a contractile to a proliferative phenotype is a pathological hallmark of multiple occlusive diseases of the vasculature, including CH-induced PH. This phenotypic transition underpins the vascular remodelling that supports progression of this fatal syndrome. There is a concerning unmet clinical need for anti-proliferative therapeutics, limiting patient prognosis. The VSMC phenotypic transition is influenced by changes in Ca^{2+} signalling in proliferative VSMCs. Thus, Ca^{2+} channels as anti-proliferative therapeutic targets in CH-induced PH are an area worthy of further research. Both T-type Ca^{2+} channels and Orai1 are Ca^{2+}-selective ion channels that show promise as anti-proliferative targets in CH-induced PH, but lack of highly selective inhibitors against the T-type Ca^{2+} channel; and complete lack of T-type Ca^{2+} channel blockers in the clinic, may limit the potential of T-type Ca^{2+} channels as anti-proliferative targets. One selective Orai1 inhibitor is currently being tested in clinical trials, and the novel selective Orai1 inhibitor, JPIII, has shown promise in *in-vivo* models of abdominal aortic aneurysm. Availability of this tool makes Orai1 an anti-proliferative target worthy of further investigation in the context of CH-induced PH.

Hypothesis: T-type Ca^{2+} channels and Orai1 are viable anti-proliferative targets in hypoxia-induced pulmonary VSMC proliferation and CH-induced PH.

Aim: Investigate the anti-proliferative effects of selective T-type Ca^{2+} channel and Orai1 inhibition in an *in-vitro* model of hypoxia-induced pulmonary VSMC proliferation and an *in-vivo* model of CH-induced PH.

Objectives:

1. Validate commercially available HPASMCs as an *in-vitro* model to study hypoxia-induced VSMC proliferation
2. Investigate the ability of widely used T-type Ca^{2+} channel inhibitors to reduce hypoxia-induced VSMC proliferation *in vitro*
3. Investigate the ability of the novel Orai1 inhibitor, JPIII, to reduce hypoxia-induced VSMC proliferation *in vitro*
4. Reproduce the SuHx mouse model of CH-induced PH
5. Investigate the effect of selective Orai1 inhibition on parameters of CH-induced PH

Chapter 2

Methods and materials

2.1 Cell culture

Normoxia is a term used to infer a normal O_2 concentration. For *in-vitro* experiments, cell culture conditions of 37ºC, 95% air and 5% carbon dioxide (CO_2) (equating to a ~20% O_2 environment) were used. *Hypoxia* is defined as a reduction in O_2 availability in one condition compared to another (Prabhakar and Semenza, 2012). For *in-vitro* experiments, hypoxia was defined as culture conditions of 37ºC, 1% O_2 (supplemented with nitrogen [N_2]) and 5% CO_2.

2.1.1 Preparation and culture of HPASMCs

Smooth muscle basal medium (SmBM™) (Lonza, Basel, Switzerland) was stored at 4ºC and SingleQuots™ (Lonza, Basel, Switzerland) at -20ºC. For medium preparation, SingleQuots™ (0.5 ml human epidermal growth factor [hEGF], 1.0 ml human fibroblast growth factor [hFGF-B], 0.5 ml gentamicin/amphotericin-B and 0.5 ml insulin) and 25 ml foetal bovine serum (FBS) were thawed before being transferred to 500 ml SmBM™ to make SmGM™-2 (complete medium), which was stored at 4ºC.

SmGM™-2 was warmed to 37ºC for one hour before use. HPASMCs (ATCC® PCS-100-023™) were obtained from the European Collection of Authenticated Cell Cultures (ECACC, Public Health England, UK) and stored in liquid N_2. These cells were sourced from normal pulmonary artery of Homo sapiens under informed consent and Health Insurance Portability and Accountability (HIPAA) standards to protect the privacy of the donor's personal health information. Age, gender and ethnicity are batch-specific. Despite this, this cell type have been widely used as an *in-vitro* model to study hypertension, arterial disease, organ-specific drug screening, and vascular differentiation (Liu et al., 2013; Kim et al., 2016; Wei et al., 2016; Chakraborty et al., 2017; Cheng et al., 2017; Hao et al., 2017; Labrousse-Arias et al., 2017). Cells were cryopreserved in the second passage to ensure optimal viability and plating efficiency. A cryovial was thawed in a 37ºC water bath, cells resuspended in 1 ml/5-cm^2 SmGM™-2, transferred to a 75-cm^2 flask and stored in either a normoxic or a hypoxic incubator. SmGM™-2 was replaced with fresh SmGM™-2 24 hours after seeding and a half medium change performed every 48 hours thereafter until 70%–80% confluent. The volume of SmGM™-2 was adjusted according to percentage confluence as follows: <25% = 1 ml/5-cm^2; 25%–45% = 1.5 ml/5-cm^2; >45% = 2 ml/5-cm^2.

2.1.2 Preparation and culture of WT HEK293 cells

Dulbecco's Modified Eagle Medium (DMEM) (Thermo Fisher, USA) was stored at 4ºC and FBS at -20ºC. For medium preparation, 50 ml FBS was thawed before being transferred to 500 ml DMEM, which was stored at 4ºC.

DMEM containing 10% FBS was warmed to 37ºC for one hour before use. WT HEK293 cells were obtained from the liquid N_2 stores of Professor Chris Peers' research group, originally sourced from the ECACC (Public Health England, UK). A cryovial was thawed in a 37ºC water bath, cells resuspended in 1 ml/5-cm^2 DMEM containing 10% FBS, transferred to a 75-cm^2 flask and stored in a normoxic incubator. DMEM containing 10% FBS was replaced with fresh DMEM containing 10% FBS 24 hours after seeding and a half medium change performed every 48 hours thereafter until 70%–80% confluent.

2.1.3 Preparation and culture of HEK293 cells stably overexpressing rat *CACNA1G*

Minimum Essential Medium (MEM) (Thermo Fisher, USA) was stored at 4ºC. For medium preparation, 50 ml FBS was thawed before being transferred to 500 ml MEM. Next, 0.22 g of the selection antibiotic, G418 (Thermo Fisher, USA), and 1.3 ml of 1M sodium hydroxide (NaOH) were combined with 10 ml MEM, filter sterilised and added to MEM. Five millilitres of antibiotic/antimycotic and 5 ml non-essential amino acids (NEAAs) were added to MEM (each at a final concentration of 1%), along with 500 µl gentamicin (at a final concentration of 0.1%). Complete medium was stored at 4ºC until use.

Complete MEM was warmed to 37ºC for one hour before use. HEK293 cells stably overexpressing rat *CACNA1G* were obtained from the liquid N_2 stores of Professor Chris Peers' research group and were derived from the original cells of Peres-Reyes' research group (Shcheglovitov et al., 2008). A cryovial was thawed in a 37ºC water bath, cells resuspended in 1 ml/5-cm^2 complete MEM and transferred to a 75-cm^2 flask and stored in a normoxic incubator. Complete MEM was replaced with fresh MEM 24 hours after seeding and a half medium change performed every 48 hours thereafter until 70%–80% confluent.

2.1.4 Preparation and culture of tetracycline-inducible HEK293 cells overexpressing TRPC isoforms

DMEM (Thermo Fisher, USA) was stored at 4ºC and FBS at -20ºC. For medium preparation, 50 ml FBS was thawed before being transferred to 500 ml DMEM. Next, 0.5 ml blasticidin (final concentration of 10 µg/ml), 2.2 ml zeocin (final concentration of 400 µg/ml) were added to DMEM. Complete medium was stored at 4ºC until use.

Complete DMEM was warmed to 37ºC for one hour before use. HEK293 cells stably overexpressing TRPC isoforms were obtained from the liquid N_2 stores of Professor David Beech's research group (Rubaiy et al., 2017). A cryovial was thawed in a 37ºC water bath, cells resuspended in 1 ml/5-cm^2 complete DMEM and transferred to a 75-cm^2 flask and stored in a normoxic incubator. Complete DMEM was replaced with fresh MEM 24 hours after seeding and a half medium change performed every 48 hours thereafter until 70–80% confluent.

2.1.5 Subculture

Cell culture medium was aspirated, and cells washed with 10 ml Dulbecco's phosphate-buffered saline (DPBS) before adding 2 ml of TrypLe Express (a direct trypsin replacement) (Thermo Fisher, USA). Cells were incubated at 37ºC for either 6 minutes (HPASMCs) or 2 minutes (WT HEK293, and HEK293 cells stably overexpressing rat *CACNA1G, TRPC4, TRPC5, TRPC1/4 and TRPC1/5*) to facilitate cell detachment. Eight millilitres of the appropriate medium was added to the cell suspension to neutralise TrypLe Express and the cell suspension was centrifuged at either 600 rcf for 6 minutes (HPASMCs) or 100 rcf for 6 minutes (all HEK293 variants) to pellet cells. Supernatant was discarded, and appropriate cell culture medium was added to perform a range of dilutions for subculture.

2.2 Proliferation assay

2.2.1 Cell plating

The same population of HPASMCs was maintained in SmGM™-2, passaged weekly and cultured in either normoxia (37ºC, 95% air, 5% CO_2) or hypoxia (37ºC, 1% O_2 [supplemented with N_2], 5% CO_2) until 70%–80% confluent. HPASMCs were prepared as described in 2.1.5 and resuspended in 1 ml

SmGM™-2. A 50 µl sample was mixed with an equal volume of 0.4% trypan blue (Thermo Fisher, USA) to indicate percentage viability, and counted in a TC10™ Automated Cell Counter (Biorad, UK) to calculate volume required for plating at 1 x 10^4 cells/ml in 24-well plates or 4 x 10^3 cells/100 µl in 96-well plates. Cells were plated in SmGM™-2 in triplicate for each intervention and stored in either a normoxic or hypoxic incubator for six hours to allow adherence, before being subjected to serum-free medium (SFM) overnight to arrest growth and synchronise cells to the same phase of the cell cycle. The cell counting experiments were then performed in one of two ways as detailed below (one manual and one semi-automated method) using the same overall experimental conditions.

2.2.2 Direct cell counting

The following day (day 0), SFM was removed from each well of the 24-well plate, cells washed with 1 ml DPBS, 200 µl of TrypLe Express added and the plate incubated (37ºC, 6 minutes). Cell suspension with 800 µl of SmGM™-2 was centrifuged (600 rcf*,* 6 minutes), 950 µl of supernatant discarded and the remaining 50 µl resuspended with 50 µl of 0.4% trypan blue to indicate percentage viability. Medium from one well of each intervention was processed in the same way as the cell samples as an additional means of viability quantification. As the cell suspension was diluted 2x (by mixing with trypan blue stain), cells were counted within both chambers of a haemocytometer. After counting, SFM was removed and cells washed with 1 ml DPBS before adding 1 ml of SmGM™-2 to each well, either alone (control) or in the presence of an appropriate concentration of experimental compound (2.2.4). Experimental compounds were replenished every 48 hours. Plates were maintained in either a normoxic (control) or hypoxic (experimental) incubator until day 3 counts were performed with the above protocol.

2.2.3 IncuCyte® Live Cell Analysis Imaging System

Experiments were performed as described in 2.2.2 but instead, 96-well plates were used and counts were performed by staining the cells with Vybrant® DyeCycle™ Green Stain at an optimum final concentration of 10 µM, which was applied to each well of the 96-well plate and incubated at 37ºC for 30 minutes to allow the dye to permeate the cells, bind to double-stranded DNA and emit a green fluorescent signal upon imaging. For imaging, the 96-well plate was loaded into the IncuCyte Live Cell Analysis Imaging system and the automated cell counting algorithm in the IncuCyte ZOOM 2016A software was used to count cells. Objects below 50 µm were filtered out to avoid detection of small cellular debris. Within each biological replicate, four images per well across three technical replicates were captured in the green fluorescent channel for each intervention. All images were added to an image collection for processing. The cell counts from four images per well were averaged, and a subsequent average of the three technical replicates was taken to represent the number of cells present at that particular time point. After day 0 counts, SFM was removed and cells washed with 100 µl DPBS before adding 100 µl of SmGM™-2 to each well, either alone (control) or in the presence of an appropriate concentration of experimental compound (2.2.4).

Experimental compounds were replenished every 48 hours. Plates were maintained in either a normoxic or hypoxic incubator and counts performed on days 1, 2 and 3 with the above protocol. All IncuCyte settings were kept consistent throughout the remainder of the experiment.

2.2.4 Experimental compound concentrations

Table 2.1. Concentrations of experimental inhibitors for proliferation assays. T-type Ca^{2+} channel and Orai1 inhibitors used to investigate the role of these Ca^{2+} channel subunits as anti-proliferative targets in an *in-vitro* model of hypoxia-induced pulmonary VSMC proliferation.

Compound	**Supplier**	**Target**	**Final conc.**	**Solvent**	**Protocol number**
Mibefradil	Tocris Bioscience, Bristol, UK	T-type Ca^{2+} channel inhibitor	0.3, 1, 3, 10 µM	dH_2O	1.2.2
NNC55-0396	Sigma-Aldrich, Missouri, USA	T-type Ca^{2+} channel inhibitor	0.3, 1, 3, 10 µM	dH_2O	1.2.2
TTA-A2	Abcam, Cambridge, UK	T-type Ca^{2+} channel inhibitor	3, 10, 30, 100, 300, 1000 nM	DMSO	1.2.2
JPIII	In-house	Orai1 inhibitor	3, 10, 30 µM	DMSO	1.2.3

2.3 HPASMC morphology

2.3.1 IncuCyte Live Cell Analysis Imaging System

HPASMCs were maintained in 75-cm^2 flasks in either normoxia or hypoxia for 72 hours or 19 days before being plated into 96-well plates according to 2.2.1. In this instance, cells were not subjected to SFM, but were subjected to SmGM™-2 and allowed to attach for 24 hours. After 24 hours, the 96-well plate was loaded into the IncuCyte Live Cell Analysis Imaging System and the IncuCyte ZOOM 2016A settings adjusted to eliminate detection of small cellular debris below 50 µm. Four images per well were captured in phase contrast to obtain representative images of HPASMC morphology in normoxia and hypoxia at 72 hours and 19 days.

2.3.2 EVOS™ FL Auto 2 digital microscope

HPASMCs were prepared as described in 2.1.5. After being exposed to hypoxia or normoxia for 19 days, 75-cm^2 flasks containing HPASMCs were imaged in phase contrast using the EVOS FL Auto 2 digital microscope to assess morphology characteristics.

2.4 Quantitative polymerase chain reaction (qPCR)

2.4.1 RNA isolation

To determine mRNA transcript levels of Ca^{2+} channel subunits *in vitro* and *in vivo*, HPASMCs were cultured in 25-cm^2 flasks to 70%–80% confluence in either a normoxic or a hypoxic incubator for 72 hours, 7 days, 14 days, 19 days, 21 days or 28 days, and whole lungs were maintained in either normoxia or hypoxia for 28 days *in vivo.* The next steps depended on the RNA isolation method used.

Using the Bio-Rad Aurum™ Total RNA Mini Kit, SmGM™-2 was aspirated and HPASMCs washed with 3 ml DPBS, 1 ml TrypLe Express was added and flasks were incubated at 37ºC for 6 minutes. Cell suspension with 5 ml SmGM™-2 was centrifuged (600 rcf, 6 minutes). The supernatant was discarded, and cells were resuspended in 1 ml RNA Later (Thermo Fisher, Massachusetts, USA) before being stored at 4ºC overnight (to allow RNA Later to penetrate cells) and subsequently at -80ºC. Cell samples were thawed on ice before performing RNA isolation using the Aurum™ Total RNA Mini Kit (Bio-Rad, UK) following the manufacturer's instructions.

Using the TRIzol® reagent/glycogen method to isolate RNA from HPASMCs, SmGM™-2 was aspirated and cells washed with 3 ml DPBS before adding 1 ml of TRIzol reagent (Thermo Fisher, Massachusetts, USA) to lyse cells directly in the culture flask. The flask contents were transferred to a 1.5 ml Eppendorf and kept at RT for five minutes before freezing at -80ºC until RNA isolation.

Using the TRIzol reagent/glycogen method to isolate RNA from whole lungs, after being snap frozen and stored at -80ºC, lungs were thawed and 200 µl of TRIzol reagent (Thermo Fisher, Massachusetts, USA) was added before homogenizing 50x by hand using a pipette. A further 400 µl of TRIzol reagent was added and tissue homogenized using a Polytron (2x 60–90s maximum speed). A further 400 µl of TRIzol reagent was added to the tissue mixture before storing at -80ºC until RNA isolation.

Using the TRIzol reagent/glycogen method for RNA isolation, cell samples and lung tissue samples were thawed at RT for five minutes. Fresh 75% ethanol (E7148-500 ml) was prepared using RNase-free water (Molecular Biology Grade Water 443847D VWR) and kept on ice. Samples were centrifuged at 13000 rpm (4ºC) for 10 minutes to pellet large debris and DNA. Supernatant was transferred to a fresh 1.5 ml Eppendorf and 100 µl of bromochloropropane (BCP, B9673-200 ml) and 12.5 µl glycogen (G1767-1VL from Mytilus edulis) were added. Eppendorfs were vortexed thoroughly before centrifuging at 13000 rpm (4ºC) for 15 minutes to obtain three layers: RNA in the top, aqueous layer; DNA in the middle, white layer; and protein in the bottom, pink layer. RNA was transferred to a fresh 1.5 ml Eppendorf and 100 µl of ice-cold isopropanol (I9516-500ml, propran-2-ol) was added. RNA was vortexed 2–3x (5–10 seconds each) and left on ice for 15 minutes before centrifuging at 13000 rpm (4ºC) for 20 minutes. Isopropanol was removed using a P1000 pipette, being careful not to disturb the RNA pellet. The RNA pellet was washed by adding 750 µl of 75% ethanol and the pellet centrifuged at 13000 rpm (4ºC) for five minutes before removing the ethanol. The RNA pellet was air dried for five minutes to yield a white RNA pellet. Ten microlitres of RNase-free water was added to the pellet and the RNA resuspended and stored at (-20ºC) until cDNA preparation.

2.4.2 DNase digestion

For DNAse digestion, 1.2 µl of 10x reaction buffer and 0.5 µl DNase were added to the 10 µl RNA sample and the sample incubated at 37ºC for one hour. The RNA sample was bench centrifuged, 2 µl of stop reagent was added and the sample incubated at RT for five minutes before bench centrifuging for one minute. The clear supernatant RNA solution was transferred to another Eppendorf and the white pellet discarded. The RNA concentration was quantified using the Nanodrop 2000 and stored at -80ºC until cDNA preparation.

2.4.3 cDNA preparation

The reverse transcriptase reaction was prepared on ice and included (for a 10 µl reaction volume): 5 µl 2x RT buffer, 0.5 µl 20X RT enzyme mix, appropriate volume of RNA to achieve a final concentration of 500 ng (up to 4.5 µl RNA), and nuclease-free water (quantity sufficient to 10 µl). The reverse transcription programme was then run in either the Eppendorf PCR machine with a reaction profile of: 1) 37ºC for one hour; 2) 95ºC for five minutes; 3) hold at 4ºC; OR in the TECHNE3PRIME thermal cycler (Cole-Parmer Illinois, USA) with a reaction profile of: 1) 25ºC for five minutes; 2) 42ºC for 30 minutes; 3) 85ºC for five minutes; 4) hold at 4ºC. cDNA concentrations were measured using the NanoDrop2000 spectrophotometer (Thermo Fisher, Massachusetts, USA) and stored at –20ºC. For a 20 µl reaction, the volume of all RT components was doubled and 1000 ng RNA was used.

2.4.4 Quantitative PCR

Pre-designed and cited Taqman probes for *CACNA1G* (human: Hs00367969_m1; mouse: Mm00486572_m1), *CACNA1H* (human: Hs01103527_m1; mouse: Mm00445382_m1), *ORAI1* (human: Hs03046013_m1; mouse: Mm00774349_m1*), ORAI2* (human:

Hs00259863_m1; mouse: Mm04214089_s1)*,* *ORAI3* (human: Hs00743683_s1; mouse: Mm01612888_m1)*,* *STIM1* (human: Hs00963373_m1; mouse: Mm01158413_m1)*,* *STIM2* (human: Hs00957788_m1; mouse: Mm01223103_m1), *TRPC1* (human: Hs00608195_m1; mouse: Mm00441975_m1)*,* *TRPC3* (human: Hs00162985_m1; mouse: Mm00444690_m1), *TRPC4* (human: Hs01077392_m1; mouse: Mm00444280_m1), *TRPC5* (human: Hs00202960_m1; mouse: Mm00437183_m1), *TRPC6* (human: Hs00175753_m1; mouse: Mm01176083_m1) and the endogenous reference gene, *B2M* (human: Hs00187842_m1; mouse: Mm00437762_m1) were used. Pre-designed and cited human Taqman probes for common reference genes were also used to optimise PCR: *GAPDH* (Hs092786624_g1); *18S* (Hs99999901_s1); *TIMP3* (Hs00165949_m1); *BACE1* (Hs04232267_s1); and *ACTB* (Hs01060665_g1). All Taqman probes are quality controlled in-house at ThermoFisher, and those with the most citations and highest sequence coverage were chosen for this research. For a 10 µl reaction volume in a 384-well plate (Applied Biosystems, Cambridge, UK), 9.5 µl of PCR reaction mix comprising Taqman Universal PCR Mastermix (5 µl), Taqman primer (0.25 µl) and nuclease-free water (4.25 µl) were added to the appropriate well of a 384-well plate (Applied Biosystems, Cambridge, UK) followed by an appropriate volume of sample cDNA (for a final concentration of 500 ng). For a 20 µl reaction volume, the above volumes were doubled for a final concentration of 1000 ng. All samples were processed in triplicate. Quantitative PCR was performed in either:

- Bio-Rad C1000 Touch™ Thermal Cycler, CFX96 Real-Time System

Reaction profile: 1) 50ºC for two minutes; 2) 95ºC for 10 minutes; 3) 95ºC for 15 seconds; 4) 60ºC for one minute; 5) plate read; 6) Go to 3. 50X; 7) hold at 4ºC, and data analysed using Bio-Rad CFX Manager™ and Microsoft Excel 2013.

- Roche LightCycler 480

The pre-set mono-dye hydrolysis protocol was used for Taqman probes with a reaction profile of: 1) 95ºC for 10 minutes; 2) 95ºC for 10 seconds; 3) 60ºC for 30 seconds; 4) 72ºC for one second; 5) plate read; 6) Go to 3. 35X; 7) 40ºC for 30 seconds; 8) hold at 4ºC. Data were exported into a PDF and analysed using Microsoft Excel 2013.

2.5 Immunocytochemistry

HPASMCs were prepared at 7, 14, 21 or 28 days as described in 2.1.5 and plated at a density of 1 x 10^4 cells/well onto coverslips in a 6-well plate. Plates containing HPASMCs were maintained in either a normoxic or a hypoxic incubator for a further 24 hours before immunocytochemistry was performed. For WT HEK293 cells, poly-d-lysine-coated coverslips were used. Plates containing HUVECs and WT HEK293 cells were maintained in a normoxic incubator until ~70% confluent.

Each step of fixing, permeabilising and antibody application (performed in the dark at RT) was followed by washing 3 x 5 minutes at RT with 3% bovine serum albumin (BSA) in DPBS. Cells were fixed in 4% paraformaldehyde (PFA) for 20 minutes and stored in 3 ml/well DPBS at 4ºC until permeabilisation (0.2% Triton X100 for 20 minutes at RT). Twenty percent BSA was applied for 30 minutes as a protein blocking buffer. Primary antibodies at appropriate concentrations (Table 2.2) made up in 3% BSA were applied and coverslips stored at 4ºC overnight. Cells were exposed to the appropriate secondary antibody at a dilution of 1:500 in 3% BSA and left at RT for one hour. The primary and secondary antibody application steps were repeated the following day if multiple targets were stained per sample. DAPI at 4 µg/ml in DPBS was applied for 20 minutes. Cover slips were mounted using 50–70 µl

of ProLong™ gold antifade reagent (Thermo Fisher, USA) and left in the dark at RT until set, before refrigerating at 4ºC in an opaque box to minimise bleaching. Samples were imaged with a laser scanning confocal microscope (Zeiss LSM700 or LSM880) and scale bar added using ZEN Black imaging software.

2.5.1 Antibody concentrations

Table 2.2. Details of primary and secondary antibodies employed throughout immunocytochemistry optimisation.

Black = all antibodies and concentrations tested during optimisation; **blue** = antibodies for which data is presented in this thesis. IC, immunocytochemistry; IH, immunohistochemistry.

Primary	Supplier	Effective conc.	Secondary
Rabbit anti-Ca$_v$3.1 (IC)	Alomone Labs, Israel	5 µg/ml (1:170)	AF 555 goat anti-rabbit
Mouse anti-Ca$_v$3.1 (IC)	Neuromab, California, USA	10 µg/ml (1:100) 20 µg/ml (1:50) 30 µg/ml (1:33)	AF 555 donkey anti-mouse
Rabbit anti-Ca$_v$3.1 (IC)	Proteintech, Chicago, USA	2.5 µg/ml (1:140) 5 µg/ml (1:70)	AF 555 goat anti-rabbit
Rabbit anti-Ca$_v$3.2 (IC)	Alomone Labs, Jerusalem, Israel	5 µg/ml (1:180)	AF 555 goat anti-rabbit
Mouse anti-Ca$_v$3.2 (IC)	Neuromab, California, USA	1 µg/ml (1:1000) 2.5 µg/ml (1:400) 5 µg/ml (1:200)	AF 555 donkey anti-mouse
Rabbit anti-Ca$_v$3.2 (IC)	GeneTex, California, USA	2.5 µg/ml (1:400) 5 µg/ml (1:200) 20 µg/ml (1:50)	AF 555 goat anti-rabbit
Rabbit anti-Ca$_v$3.2 (IC)	SantaCruz, Texas, USA	0.5 µg/ml (1:400) 1 µg/ml (1:200)	AF 555 goat anti-rabbit
Rabbit anti-α-SMA (IC)	Proteintech, Chicago, UK	2 µg/ml (1:250) 5 µg/ml (1:100)	AF 488 goat anti-rabbit
Mouse anti-α-SMA (IC)	Sigma-Aldrich, Missouri, USA	1:300 from aliquots provided	AF 488 donkey anti-mouse
Rabbit anti-α-SMA (IH)	Abcam, Cambridge, UK	1:100 from aliquots provided	AF 647 goat anti-rabbit
Rabbit anti-SMMHC (IC)	Abcam, Cambridge, UK	1:50 from aliquots provided	AF 514 goat anti-rabbit
Mouse anti-CD31 (IC)	Jackson Labs, USA	1:300 from aliquots provided	AF 555 donkey anti-mouse
Rat anti-ki67 (IC)	ThermoFisher, Massachusetts, USA	1:100 from aliquots provided	AF 647 chicken anti-rat

2.6 Calcium microfluorimetry

Fura-2-acetoxylmethyl ester (Fura-2-AM) is a membrane-permeable ratiometric Ca^{2+} imaging dye. Acetoxylmethyl groups are removed by intracellular esterases to produce Fura-2, which is not membrane-permeable, trapping it inside the cell where it can produce Ca^{2+}-induced fluorescence at both 340 and 380 nm. Fura-2 ratiometrics provides an internal control that normalises for differences in cell thickness and dye loading. The benefits and limitations of different Ca^{2+} indicators are reviewed by Paredes et al. (2009).

2.6.1 Store-operated Ca^{2+} entry

WT HEK293 cells were plated in poly-d-lysine coated 96-well plates (Corning, New York, USA) and HPASMCs were plated in 96-well plates (Applied Biosciences) at 90% confluence 24 hours before experimentation (after optimisation to ensure a confluent monolayer was present on the day of the experiment). Cells were incubated with 2 µM Fura-2-AM (Thermo Fisher, Massachusetts, USA) and 0.01% pluronic acid (Thermo Fisher, Massachusetts, USA) to facilitate Fura-2-AM loading, in standard bath solution (SBS) for one hour at 37ºC. Cells were washed three times with 100 µl SBS followed by pre-incubation with Ca^{2+}-free SBS, TG (final concentration of 1 µM) to deplete Ca^{2+} stores, and appropriate concentrations of experimental compounds (2.6.3) were applied for 30 minutes at RT. Experimental compounds were maintained throughout the remainder of the experiment. During the experiment, Ca^{2+} add-back was performed at a final concentration of 0.3 mM to trigger the SOCE response. Measurements were made at RT on a 96-well fluorescence plate reader (FlexStation III, Molecular Devices, California, USA) controlled by Softmax Pro software v5.4.5. The change (Δ) in intracellular Ca^{2+} was indicated as the ratio of Fura-2-AM emission (510 nm) intensities for 340 and 380 nm excitation wavelengths. The SBS contained (in mM): 130 NaCl, 5 KCl, 8 D-glucose, 10 HEPES, 1.2 $MgCl_2$, 1.5 $CaCl_2$ and the pH was titrated to 7.4 with NaOH. The composition of the Ca^{2+}-free SBS was the same as SBS, but Ca^{2+}-free SBS also contained 0.4 mM EGTA and did not contain $CaCl_2$.

2.6.2 TRPC1/4-dependent Ca^{2+} entry

Tetracycline-inducible HEK293 cells stably overexpressing TRPC1/4 (Rubaiy et al., 2017) were plated in poly-d-lysine-coated 96-well plates (Corning, New York, USA) at 90% confluence (in the presence of tetracycline at a final concentration of 1 µg/ml) 24 hours before experimentation to ensure a confluent monolayer. Cells were incubated with 2 µM Fura-2-AM (Thermo Fisher, Massachusetts, USA) and 0.01% pluronic acid (Thermo Fisher, Massachusetts, USA) in SBS for one hour at 37ºC. Cells were washed three times with 100 µl SBS followed by pre-incubation with SBS and appropriate concentrations of experimental compound (2.6.3) for 30 minutes at RT. Experimental compounds were maintained throughout the remainder of the experiment. During the experiment, 1000 nM EA was applied to trigger TRPC-dependent Ca^{2+} entry. Measurements were made at RT on a 96-well fluorescence plate reader (FlexStation III, Molecular Devices, California, USA) controlled by Softmax Pro software v5.4.5. The change (Δ) in intracellular Ca^{2+} was indicated as the ratio of Fura-2-AM emission (510 nm) intensities for 340 and 380 nm excitation wavelengths. The SBS contained (in mM): 130 NaCl, 5 KCl, 8 D-glucose, 10 HEPES, 1.2 $MgCl_2$, 1.5 $CaCl_2$ and the pH was titrated to 7.4 with NaOH.

2.6.3 Experimental compound concentrations

Table 2.3. Dose-response concentrations of experimental compounds in Ca^{2+} microfluorimetry.

Details of T-type Ca^{2+} channel inhibitors used to investigate off-target effects on Orai1-mediated SOCE and TRPC1/4-dependent Ca^{2+} entry. Details of JPIII used to demonstrate inhibition of Orai1-mediated SOCE. SOCE, store-operated Ca^{2+} entry.

Compound	Supplier	Target	Final conc.	Solvent	Protocol number
Mibefradil	Tocris Bioscience, Bristol, UK	T-type Ca^{2+} channel inhibitor	0.3, 1, 3, 10, 30, 100 µM	dH_2O	2.6.1 2.6.2
NNC55-0396	Sigma-Aldrich, Missouri, USA	T-type Ca^{2+} channel inhibitor	0.3, 1, 3, 10, 30 µM	dH_2O	2.6.1 2.6.2
TTA-A2	Abcam, Cambridge, UK	T-type Ca^{2+} channel inhibitor	30, 100, 300, 1000, 3000, 100000 nM	DMSO	2.6.1 2.6.2
JPIII	In-house	Orai1 inhibitor	0.1, 1, 10, 100, 1000, 10000 nM	DMSO	2.6.1

2.7 Whole-cell patch clamp electrophysiology

WT HEK293 cells and HEK293 cells stably overexpressing rat *CACNA1G* were prepared as described in 2.1.5 and plated at a density of 5 x 10^4 cells/well onto coverslips in 6-well plates. Plates were maintained in a normoxic incubator for 24 hours to achieve a confluent monolayer. Electrophysiology was performed by Dr Jian Shi according to the following protocol. Whole-cell patch clamp recordings were achieved using Axopatch-200B (Axon Instruments, Inc., USA) equipped with Digidata 1550B and pCLAMP 10.6 software (Molecular Devices, California, USA) at RT. The recording glass pipettes had a tip resistance of 3–5 MΩ. The currents were sampled at 20 kHz and filtered at 2 kHz.

For SOCE recordings in WT HEK293 cells, the external solutions consisted of (in mM): 140 NaCl, 4 CsCl, 10 $CaCl_2$, 2 $MgCl_2$ and 10 Na-HEPES and the pH was titrated to 7.4 with NaOH. The pipette solution contained (in mM):

130 caesium glutamate, 4 $CaCl_2$, 1 MgATP, 5 $MgCl_2$, 10 EGTA and 10 Na-HEPES and the pH was titrated to 7.2 with NaOH.

For T-type Ca^{2+} channel whole-cell recordings in HEK293 cells stably overexpressing rat *CACNA1G*, the extracellular solution was composed of (in mM): 95 NaCl, 5 CsCl, 0.6 $MgCl_2$, 15 $CaCl_2$, 20 tetraethylammonium (TEA)-Cl, 5 HEPES, and 10 glucose and the pH was titrated to 7.4 with NaOH. The pipette solution consisted of (in mM): 120 CsCl, 2 $MgCl_2$, 10 HEPES, 10 EGTA, 20 TEA-Cl, 2 Na-ATP and 2 Mg-ATP and the pH was titrated to 7.2 with CsOH.

2.8 CH-induced PH *in vivo*

2.8.1 SMMHC.Cre^{ERT2}-mTmG mouse line

The SMMHC.Cre^{ERT2}-mTmG mouse line was produced by crossing the SMMHC.Cre^{ERT2} line (Figure 2.1, A) with floxed mTmG reporter mice (Figure 2.1, B), both obtained from Jackson Labs (stock numbers: 019079 and 007676, respectively).

In the SMMHC.Cre^{ERT2} mouse line, Cre is expressed specifically in smooth muscle cells (SMCs) under the control of a SMMHC promoter. In the floxed mTmG reporter mice, the ROSA26 locus contains the mT (membrane tomato) component of the fluorescent reporter and a STOP codon are floxed by lox p sites (Figure 2.1, B). The mG (membrane GFP) component of the fluorescent reporter is located downstream of the STOP codon, external to the lox p sites. After crossing and prior to Cre recombination (which is induced with tamoxifen), plasma membrane-localised mT fluorescence is expressed constitutively in cells, upstream of a STOP codon (Figure 2.1, B). Upon Cre recombination, which occurs only in SMCs due to the positioning of Cre downstream of the

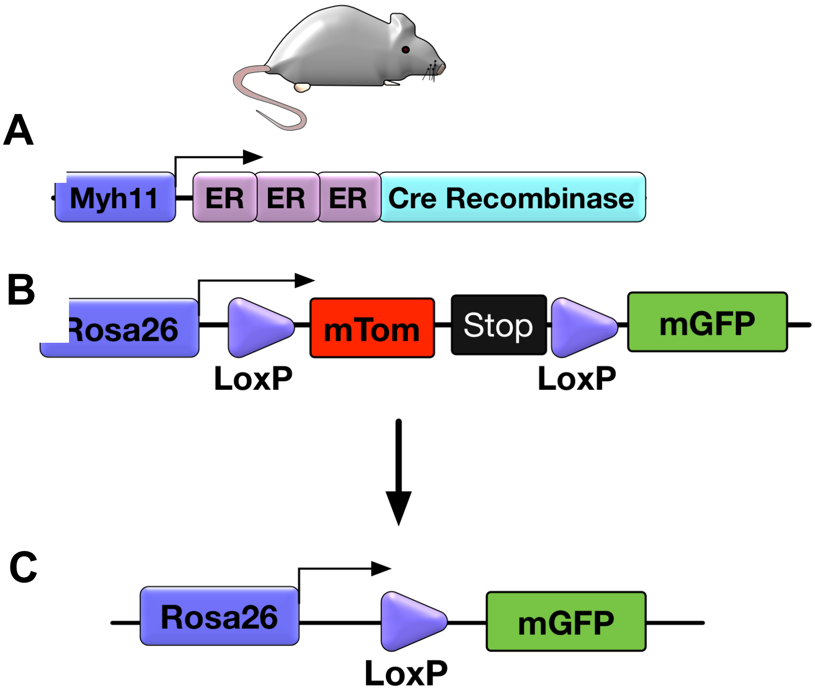

Figure 2.1. Producing the SMMHC.Cre^{ERT2}-mTmG mouse line.

Cre recombinase, under the control of a SMMHC promoter, catalyses the excision of the mT and STOP codon at lox p sites, revealing downstream mGFP fluorescence in SMCs. mT, membrane tomato; mGFP, membrane green fluorescent protein; SMC, smooth muscle cell.

SMMHC promoter, the mT and STOP codon are excised, revealing downstream green fluorescence (mGFP) (Figure 2.1, C).

2.8.2 Validation of SMMHC.Cre^{ERT2}-mTmG mouse line

To validate the specificity of Cre recombination in the SMMHC.Cre^{ERT2} mice, males were crossed with ROSA26.*LacZ*.floxed STOP females. Offspring (SMMHC^{ERT2}*LacZ*$^{+/-}$) were given 2 mg of tamoxifen (Δ) by intraperitoneal injection for five consecutive days at eight weeks of age. Two weeks later, a range of organs were stained with BluGal for 24 hours and examined using bright field microscopy. Positive staining was apparent in vessels and in smooth muscle of the bowel. Positively stained vessels within tissues are arrowed (Figure 2.3). These mice were validated by the Bailey laboratory according to the above protocol prior to use in this research project.

2.8.3 SuHx mouse model standard experimental protocol

SMMHC.Cre^{ERT2}-mTmG (herein referred to as SM-mTmG-Cre) mice were provided by the Bailey lab as part of a parallel British Heart Foundation-funded project grant. C57BL6/J mice were purchased either from the University of Leeds' in-house colony or from the commercial supplier, Charles River. Animals were allowed to acclimatise to their surroundings and reach eight weeks of age before the beginning of the experiment. As demonstrated in Figures 2.4 and 2.5, SM-mTmG-Cre mice were injected with tamoxifen (2.8.4) for five consecutive days and kept in quarantine for one further week before the beginning of the experiment. During the experiment, all cohorts were maintained in either normoxia (RT, 95% air, 5% CO_2) (control) or hypoxia (RT, 10% O_2 [supplemented with N_2]) for four weeks. Animals were monitored daily

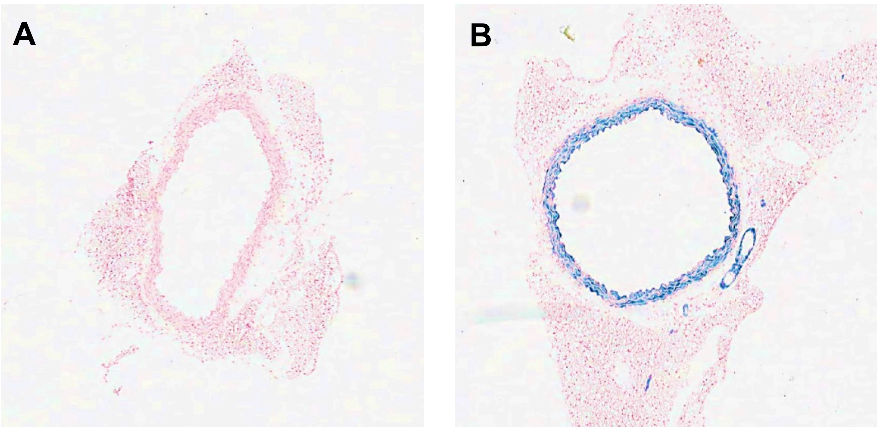

Figure 2.2. Validation of Cre recombination.

Crossing SMMHC.Cre^{ERT2} males with ROSA26.*LacZ*.floxed STOP females produced a mouse line in which Cre was expressed downstream of the SMMHC promoter. The β-galactosidase gene, *LacZ*, was positioned within the ROSA26 locus, downstream of a floxed STOP codon. Upon Cre recombination (which occurs only in SMCs due to the presence of the SMMHC promoter), the floxed STOP codon is excised, revealing downstream LacZ. The LacZ stain, BluGal, revealed specific staining in aortic SMCs in the medial layer in SMMHC^{+}.LacZ^{+} mice induced with tamoxifen (B), while no blue staining was observed in aortae of SMMHC^{+}.LacZ^{-} mice (A).

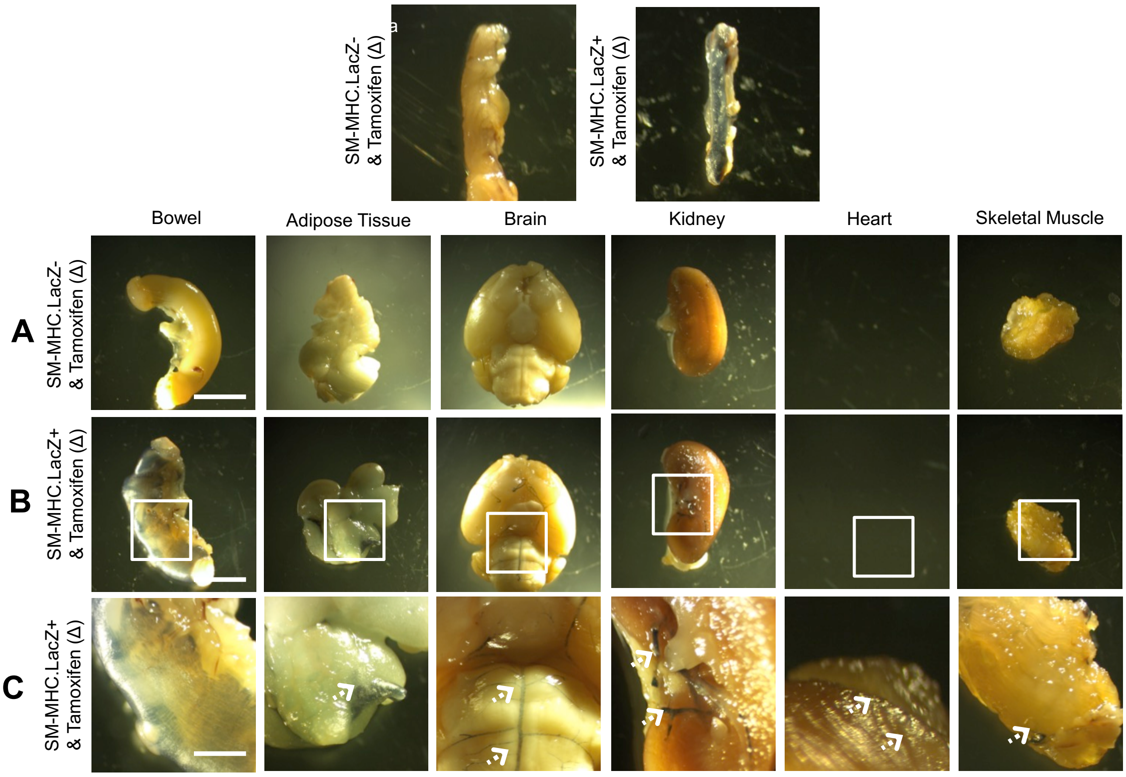

Figure 2.3. Validation of Cre recombination.

Crossing SMMHC.Cre^{ERT2} males with ROSA26.*LacZ*.floxed STOP females produced a mouse line in which Cre was expressed downstream of the SMMHC promoter. The β-galactosidase gene, *LacZ*, was positioned within the ROSA26 locus, downstream of a floxed STOP codon. Upon Cre recombination (which occurs only in SMCs due to the presence of the SMMHC promoter), the floxed STOP codon is excised, revealing downstream LacZ. The LacZ stain, BluGal, revealed specific staining in small vessels from SMMHC^{+}.LacZ^{+} tissues induced with tamoxifen (B), while no blue staining was observed in SMMHC^{+}.LacZ^{-} tissues (A). Zoomed in images of SMMHC^{+}.LacZ^{+} tissues are demonstrated (C). Arrows indicate BluGal-stained small vessels.

for their body condition score. Cages were cleaned once per fortnight and food was available *ad libitum*. In the first series of experiments to reproduce the CH-induced PH mouse model, mice maintained in hypoxia were either administered weekly injections of the VEGF blocker, SU5416, at a final concentration of 20 mg/kg according to previously published studies (Ciuclan et al., 2011); or in the vehicle-treated hypoxic cohorts, an equivalent volume of vehicle (carboxymethylcellulose sodium [CMC Na^+]). Mice maintained in normoxia were also administered weekly injections of CMC Na^+. The different experimental groups for this investigation are herein referred to as: *Hx* + *SU5416, Hx* + *veh, and Nx* + *veh.*

In the second series of experiments, the *Hx* + *SU5416* mouse model of CH-induced PH was used to examine the anti-proliferative potential of selective Orai1 inhibition using JPIII. In this instance, **all** mice maintained in hypoxia were administered weekly injections of SU5416 at a final concentration of 20 mg/kg (2.8.6) as well as a continuous infusion of either the experimental Orai1 inhibitor, JPIII, at 750 ng/kg/min (2.8.7), or DMSO as a vehicle-treated negative control. A vehicle-treated negative control was also employed in these experiments, specifically a DMSO-treated normoxic cohort. The different experimental groups for this investigation are herein referred to as: *Hx* + *SU5416* + *DMSO, Hx* + *SU5416* + *JPIII,* and *Nx* + *veh* + *DMSO.*

2.8.4 Preparation and administration of tamoxifen

Tamoxifen injection was performed on animals after eight weeks of age to induce recombination. Tamoxifen was dissolved in corn oil as it is not water soluble. In SM-mTmG-Cre mice, a 200 µl intraperitoneal injection of tamoxifen at a final concentration of 20 mg/ml was administered to each animal for five consecutive days. Intraperitoneal injection was performed by scruffing the animal and turning the animal into the palm of the hand, securing the tail. To prevent organ puncture upon injection, the animal was positioned cranium down to allow internal organs to fall towards the cranial end with gravity. The injection site was alternated each day to avoid irritation.

2.8.5 Preparation and administration of CMC Na^+

Carboxymethylcellulose Na^+ comprised 0.5% w/v (5 g per litre) CMC Na^+ powder, 0.9% w/v (9 g per litre) NaCl, 0.4% v/v (4 ml per litre) polysorbate 80, and 0.9% v/v (9 ml per litre) benzyl alcohol (all sourced from Sigma-Aldrich, Missouri, USA) in deionized water. Solids were mixed with liquids on a warming plate with a stir bar for one hour to produce a clear, viscous vehicle.

2.8.6 Preparation and administration of SU5416

SU5416 (Sigma-Aldrich, Missouri, USA) was mixed with CMC Na^+, and sonicated for 15 minutes (30 seconds on, 30 seconds off). SU5416 does not dissolve but forms a suspension. The SU5416 suspension was vortex mixed and drawn up into syringes before administering to animals once per week via subcutaneous injection at a final concentration of 20 mg/kg.

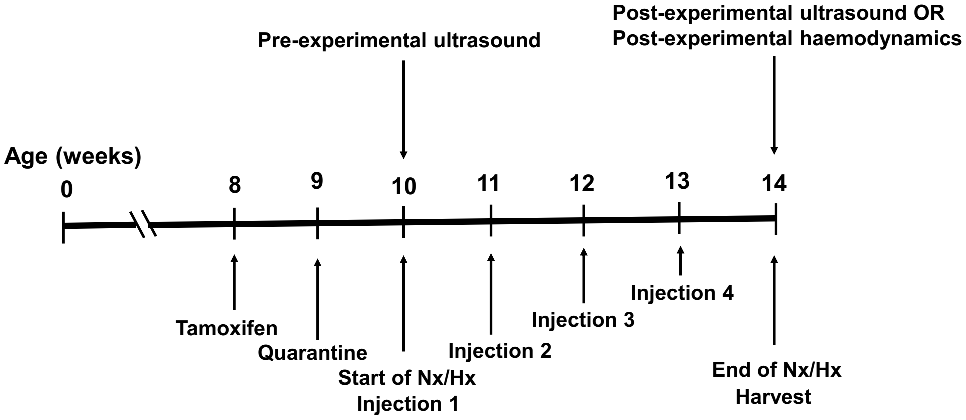

Figure 2.4. Timeline for *in-vivo* experiments to reproduce CH-induced PH.

Animals were allowed to reach eight weeks of age before undergoing tamoxifen injection for five consecutive days and kept in quarantine for one week (SM-mTmG-Cre only). C57BL6/J mice did not required tamoxifen injection. At 10 weeks of age, all animals were subjected to either hypoxia or normoxia for four weeks with weekly injections of either vehicle (CMC Na^+) or SU5416 to induce CH-induced PH using either CH alone or CH in combination with SU5416. At the end of the experimental period, tissues were harvested for analysis. For mice that underwent echocardiography, animals were subject to the protocol outlined in 2.8.11 at 10 weeks (pre-experimental) and 14 weeks (post-experimental). Animals that underwent PV monitoring, were subject to the protocol outlined in 2.8.12 at 14 weeks (post-experimental) only since this was a terminal procedure. PV, pressure volume.

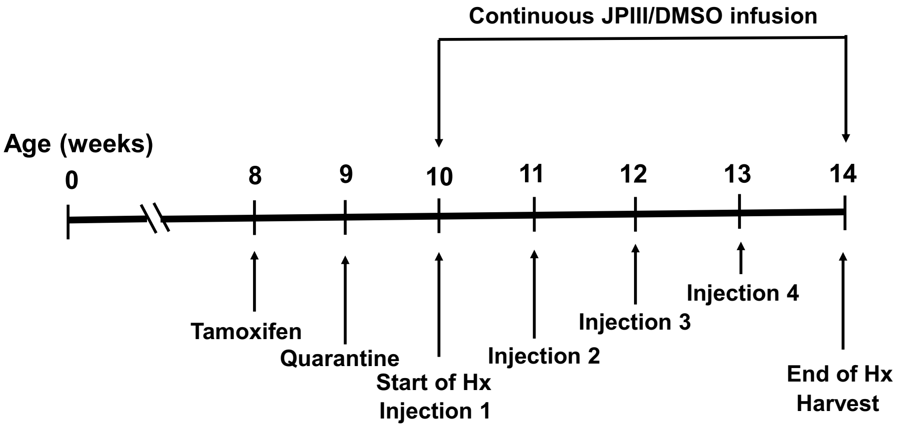

Figure 2.5. Timeline for *in-vivo* experiments to test the effect of JPIII on morphological cardiac indices and distal muscularisation.

Animals were allowed to reach eight weeks of age before undergoing tamoxifen injection for five consecutive days and kept in quarantine for one week (SM-mTmG-Cre only). C57BL6/J mice did not required tamoxifen injection. At 10 weeks of age, all animals were subjected to either hypoxia or normoxia for four weeks with weekly injections of either vehicle (CMC Na^+) or SU5416 to induce CH-induced PH using either CH alone or CH in combination with SU5416. At the end of the experimental period, tissues were harvested for analysis.

2.8.7 Preparation and administration of ALZET® osmotic pumps

ALZET osmotic pumps were used to deliver JPIII or vehicle (DMSO) to the systemic circulation of mice at a continuous, controlled rate for four weeks. Osmotic pumps were prepared using a 30 mM (9.6 µg/µl) JPIII stock made up in DMSO. The total volume of JPIII to be infused per animal was 100 µl. Since the JPIII stock concentration was 9.6 µg/µl and the desired total volume was 120 µl (to account for dead space volume of loading syringes), the stock concentration was considered to calculate the final volume of JPIII stock required. The pump volume was made up with DMSO to achieve a total volume of 100 µl.

Mice were anaesthetised with inhaled isoflurane (5% for induction, 2% for maintenance) in 2 L/min O_2. A small patch of hair was shaved between the scapulae and cleaned with Vetasept® (disinfectant and antiseptic, active ingredient = chlorhexidine gluconate). A small (sub-1 cm) incision was made and a pouch created in the left flank by blunt dissection. The primed pump was inserted into the pouch with the flow moderator facing inwards. The wound was closed with a continuous 4-0 Vicryl® (Ethicon) suture. Animals were administered 100 µl of 0.1 mg/ml Vetergesic® (analgesic, active ingredient = buprenorphine) at the end of the procedure before recovery. JPIII was administered to the animals at a final concentration of 750 ng/kg/min.

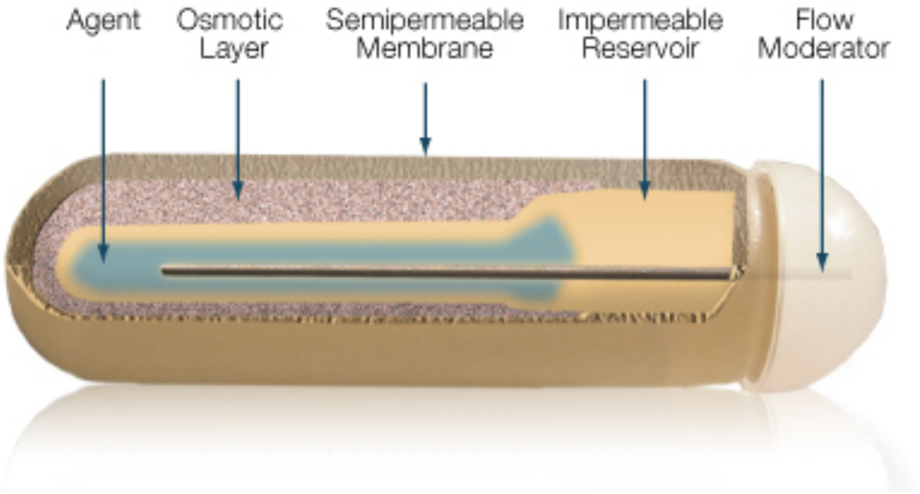

Figure 2.6. The components of the ALZET® osmotic mini pump.

Osmotic pumps are useful to avoid frequent injections and to reduce the need for animal handling. The high osmolality of the osmotic layer causes water from surrounding tissues to permeate the semi-permeable membrane, which in turn compresses the impermeable reservoir and displaces the test solution from the pump at a pre-determined rate. The compressed reservoir cannot be refilled, thus the appropriate volume of JPIII solution was loaded at the beginning of the experimental period. Image taken from DURECT Corporation (2019).

2.8.8 OxyCycler

To expose mice to hypoxia, an OxyCycler attached to a chamber and controlling PC was used. To set up and calibrate the OxyCycler, the OxyCycler software was opened and *new calibration* option selected. To set the parameters of the chamber, the *lower boundary* was set at 0% O_2 and the *upper boundary* at 95% O_2 (to account for the 5% CO_2 in atmospheric air). The chamber O_2 delivery percentage was then adjusted to 10% by accessing the *chamber 1 setpoint* option, and N_2 cylinders used as a supplement for the reduced O_2. Data logging was carried out to ensure the percentage O_2 in the chamber remained stable throughout the experimental period. A weekly calibration was performed by David Myers/Simon Futers.

2.8.9 Body weight

The first mouse cohort, SM-mTmG-Cre, was weighed once a week for three weeks before the beginning of the experimental period to examine normal weight fluctuations at baseline and the mean body weight (n=4 per group) plotted at each time point. During the experimental period, all animals were weighed at regular intervals to monitor weight changes closely to adhere to project license restrictions. If weight loss exceeded 15%, animals were culled using a method listed under Schedule 1 of the UK Scientific Procedures Act.

2.8.10 Heart and lung weights

At the end of the four-week experimental period, mice were perfusion-fixed, and the lungs and heart harvested, stored in 4% PFA for two hours, before being transferred to DPBS and stored at 4ºC. Whole uncleaned hearts were massaged to clear DPBS, dried and weighed before further dissection. The left lung was also cleared of DPBS, dried and weighed. From the whole uncleaned

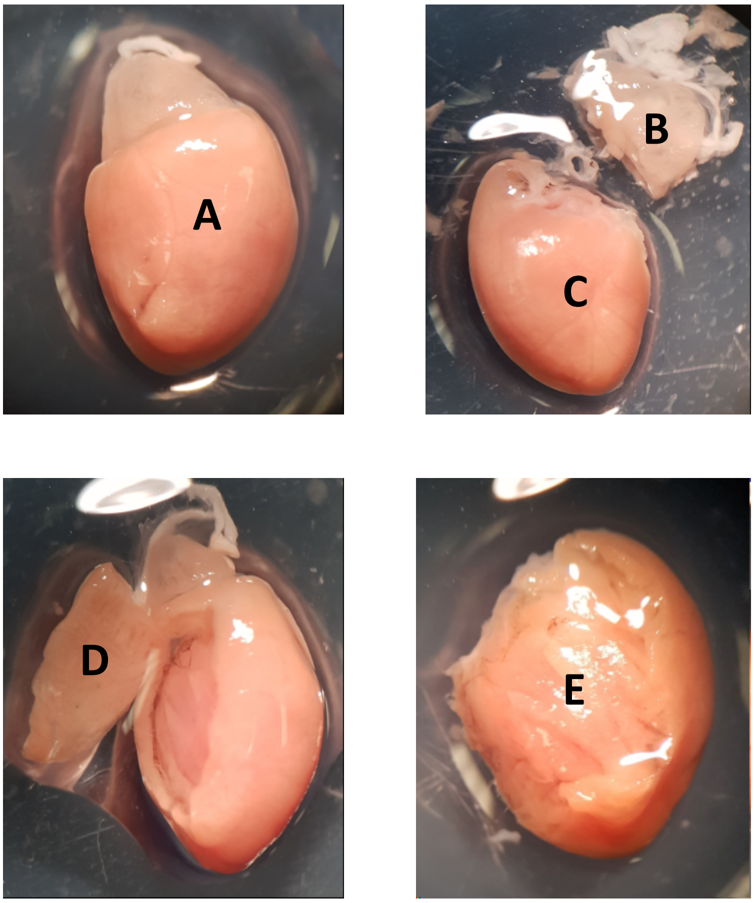

Figure 2.7. Representative images of mouse heart dissection steps.

At the four-week experimental period, animals were perfusion-fixed and the lungs and heart harvested, stored in 4% PFA for two hours, before being transferred to DPBS and stored at 4°C. Whole uncleaned hearts (A) were massaged to clear DPBS and weighed before removal of the atria/appendices/fat (B). The remaining tissue was classed as the cleaned heart (C), which was normalised to total body weight to identify true differences. Subsequently, the RV free wall (D) was dissected and weighed, and expressed relative to LV + S (E) for Fulton’s index. PFA, paraformaldehyde; DPBS, Dulbecco’s phosphate-buffered saline; RV, right ventricular; LV, left ventricular; S, septum.

heart (Figure 2.7, A), the atria, appendices and fat were removed (Figure 2.7, B) and weighed. The remaining cleaned heart (Figure 2.7, C) comprising LV, RV and septum (S) was weighed. The RV was then dissected (Figure 2.7, D) and weighed, and expressed relative to LV + S for Fulton’s index (Figure 2.7, E).

2.8.11 Echocardiography

After the four-week experimental period, LV ejection fraction (EF) and fractional shortening (FS) measurements were obtained using left-sided cardiac echocardiography. Although CH-induced PH presents with right-sided heart failure, we did not have the expertise to perform reliable right-sided echocardiography. At the end of the four-week experimental period, animals were anaesthetised with 5% isoflurane and maintained under 1.5% isoflurane. Hair was removed from the thoracic region and body temperature maintained using a warming plate. Echocardiography was performed on the left side of the heart in both the short and longitudinal axes in M-mode using the Vevo2100 (FujiFilm Visualsonics) micro-ultrasound imaging system and the associated Vevo® LAB software. These experiments were performed with help from Dr Mark Drinkhill (Senior Lecturer).

From the M-mode traces, five separate measurements for each of interventricular S (IVS) thickness, LV internal diameter (LVID) and LV posterior (free) wall (LVPW) thickness were made in both systole and diastole according to Figure 2.8. These measurements were made across five M-mode traces per animal to gain an average and standard deviation for each parameter. From this, measurements of EF and FS were made. Data were normalised to pre-experimental EF and FS values to identify *true* differences.

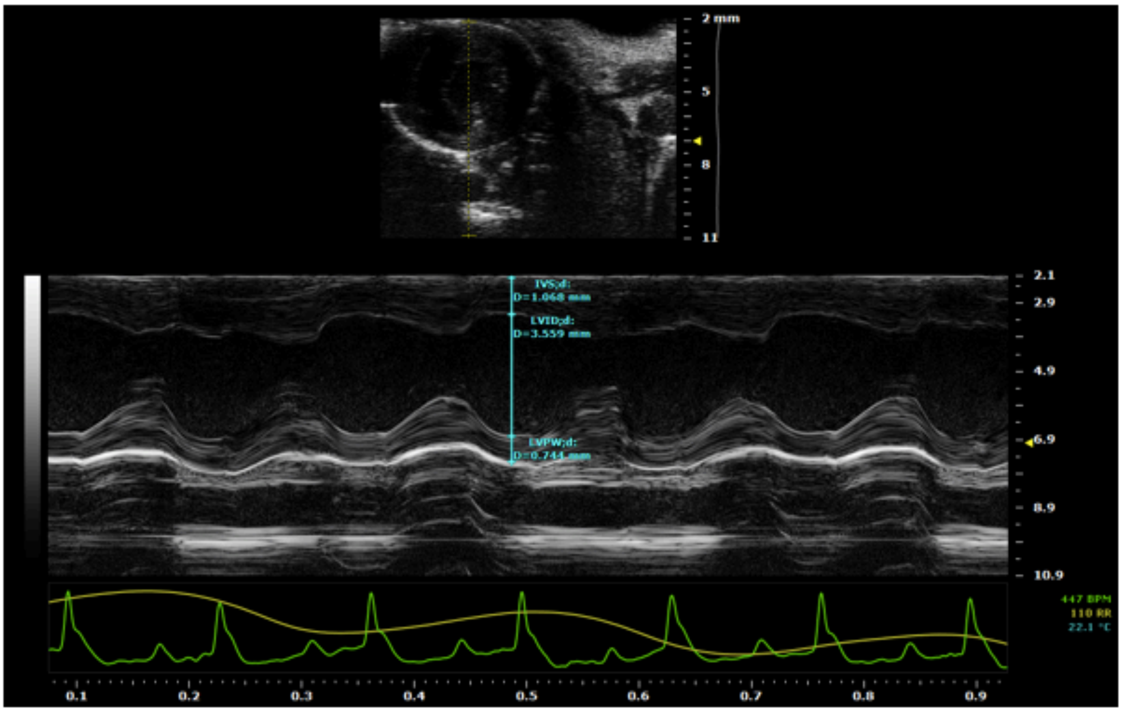

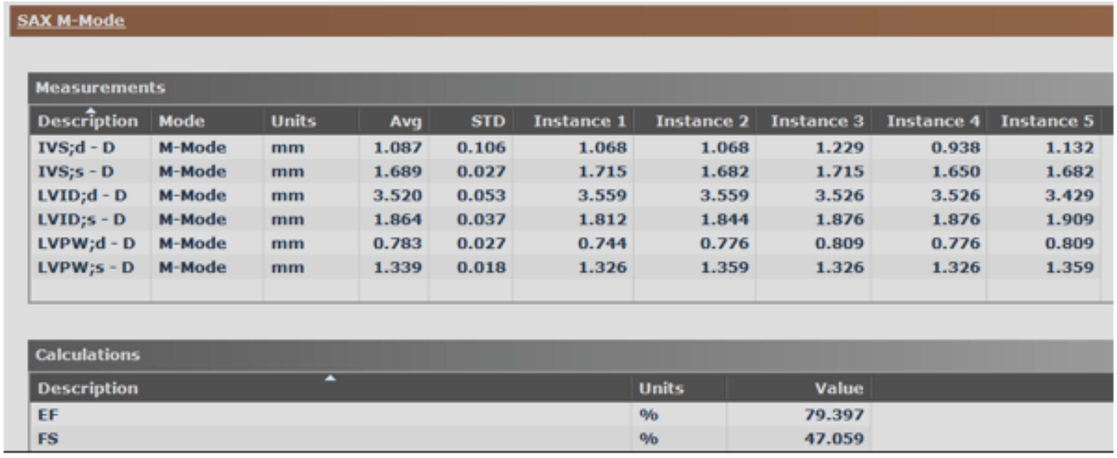
SAX M-Mode

Measurements

Description	Mode	Units	Avg	STD	Instance 1	Instance 2	Instance 3	Instance 4	Instance 5
IVS;d - D	M-Mode	mm	1.087	0.106	1.068	1.068	1.229	0.938	1.132
IVS;s - D	M-Mode	mm	1.689	0.027	1.715	1.682	1.715	1.650	1.682
LVID;d - D	M-Mode	mm	3.520	0.053	3.559	3.559	3.526	3.526	3.429
LVID;s - D	M-Mode	mm	1.864	0.037	1.812	1.844	1.876	1.876	1.909
LVPW;d - D	M-Mode	mm	0.783	0.027	0.744	0.776	0.809	0.776	0.809
LVPW;s - D	M-Mode	mm	1.339	0.018	1.326	1.359	1.326	1.326	1.359

Calculations

Description	Units	Value
EF	%	79.397
FS	%	47.059

Figure 2.8. Example view in M-mode, short axis view was taken at the beginning and end of the experimental period.

Measurements for all parameters (below) were made in both systole and diastole. Five separate instances of each parameter were measured across three M-mode traces per animal to gain an average for each parameter measured. IVS, interventricular septum in systole and diastole; LVID, left ventricular internal diameter in systole and diastole; LVPW, left ventricular posterior wall (free wall) in systole and diastole. Each of these parameters was measured on five occasions and an average and standard deviation automatically calculated using the Vevo® LAB software. From this, measurements of ejection fraction (EF) and fractional shortening (FS) were made.

2.8.12 Pressure volume loops

At the end of the four-week experimental period, animals were placed in an induction chamber and anaesthetised with 5% isoflurane for induction and 1.5% for maintenance. A depilatory was applied to the chest and fur removed. A tracheotomy was performed, and the manifold adjusted to supply isoflurane to the ventilator. After steady respiration was accomplished, the chest was opened, and a cardiac catheter inserted into the RV using a 25-gauge needle. Fine adjustments in catheter position were performed until a box-shaped pressure volume (PV) trace was achieved (Figure 2.9). The animal was allowed to stabilise for 10 minutes to allow recovery from acute surgical stress and PV loops monitored continuously for 10 minutes using LabChart software. The volume component of the signal measured by the catheter is comprised of conduction through the blood (which varies with ventricular volume) and conduction though the wall of the cardiac ventricle (parallel conductance). To determine the absolute ventricular volume, parallel conductance was determined and accounted for by injecting 5–10 µl of hypertonic saline solution. The injection of hypertonic saline transiently changes the conductivity of the blood in the ventricle, while the conductivity of the wall remains constant. From this, the blood conductance can be isolated from the wall conductance, giving a true value for volume. Blood was also collected using a heparinised syringe to prevent clotting and placed into cuvettes of known volume, and the catheter used to measure conductance, which related to the volume component of the PV loop. This measurement, along with the volume measured by the catheter, is used to determine the absolute volume. A detailed protocol is provided by Townsend (2016). These experiments were performed with help from Dr Mark Drinkhill (Senior Lecturer).

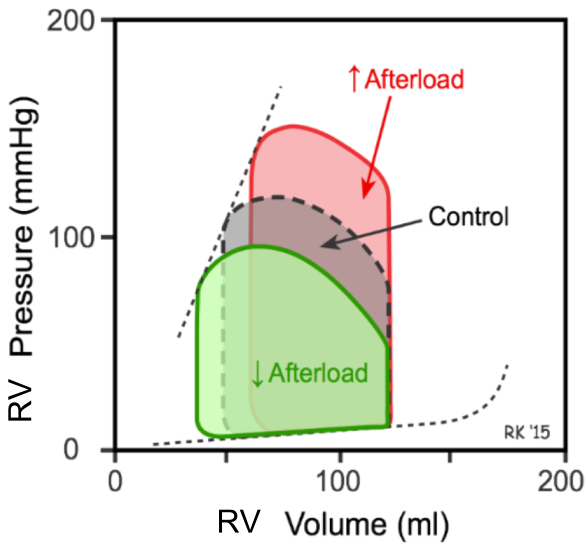

Figure 2.9. Example PV loop.

An example PV loop is demonstrated. The horizontal portion of the trace represents diastolic filling (represented by the increase in volume) and closing of the tricuspid valve. Closing of the tricuspid valve and isovolumic contraction causes an increase in pressure (bottom right to top right). The pulmonary valve opens (top right), blood is ejected into the pulmonary artery and RV volume declines (top right to top left). The pulmonary valve closes, isovolumic relaxation occurs and pressure declines (top left to bottom left). The tricuspid valve opens and the cycle repeats. The area within the PV loop represents the ventricular stroke work. Thus, the larger the area within the PV loop, the more work is being carried out by the ventricle to eject blood. Over long periods, the increased work culminates in RV hypertrophy, which leads to heart failure—a characteristic feature of PH. PV, pressure volume.

2.8.13 Histology and imaging

At the end of the four-week experimental period, SM-mTmG-Cre animals were perfusion-fixed, and lungs fixed in 4% PFA for two hours before being transferred to DPBS and stored at 4ºC. Lungs were dissected into three parasagittal regions (lateral parasagittal, mid-parasagittal, and medial parasagittal [closest to the heart]) using a scalpel, embedded in OCT, sectioned to 10 µm and stored at -80ºC. Sections were either allowed to thaw and imaged with a LSM700 at 63x magnification or further stained with antibodies before imaging with a LSM880 at 63x magnification.

For immunofluorescent staining of frozen tissue sections, sections were allowed to thaw at RT for 10 minutes before washing with 100 µl DPBS to remove OCT residue. Sections were permeabilised in 0.2% Triton X-100 for 30 minutes. Sections were then blocked in 20% BSA at RT for one hour. One hundred microlitres of primary antibody for α-SMA at a concentration of 1:100 made up in 3% BSA was added to each section and incubated at RT for one hour. Sections were washed 3 x 5 minutes with 3% BSA at RT. Secondary antibody was then applied for 90 minutes made up in 3% BSA before washing 3 x 5 minutes in DPBS. Sections were allowed to air dry for 5 minutes before mounting using ProLong™ Gold Antifade Reagent with DAPI. Antibody-stained mTmG lung sections were imaged with a LSM880 confocal microscope due to the number of channels required.

For both mTmG sections and mTmG sections stained with antibodies, Z-stacks (63x magnification) were performed on three lateral parasagittal sections per animal to capture smooth muscle in small arterioles (furthest from bronchioles), with four animals per condition. Slices were examined to identify small vessels.

2.8.14 Mean fluorescence intensity analysis

Three Z-stacks per animal, across four animals per condition were analysed using ImageJ to gain data about mean fluorescence intensity (MFI). For this analysis, out-of-focus edge slices were deleted from each end of the Z-stack. The number of remaining slices was the same in all samples. Using ImageJ, the central slice of each Z-stack (the most in-focus slice) was analysed for MFI in the green fluorescent channel. The MFI measurement was obtained by automatic averaging of the pixels in that particular slice and reflects the staining intensity in arbitrary units. An analysis of MFI is semi-quantitative and was performed as a preliminary analysis before detailed quantification by direct cell counting.

2.8.15 Direct cell counting

ImageJ was used to perform direct cell counting on histology sections. Images were opened in ImageJ and all fluorescent channels merged. Out-of-focus edge slices were removed, and the final number of slices analysed was the same in each sample. All channels were switched off except the blue channel (DAPI) and total cell number was determined, followed by the number of GFP+, tomato+ and α-SMA-stained cells. The number of cells that were both GFP+ and α-SMA-stained, and tomato+ and α-SMA-stained were then determined. The number of cells that expressed each marker was expressed as a percentage of the total DAPI count in each condition. This analysis was performed on three sections per animal with four animals per condition.

2.9 Data analysis

Statistical analysis was performed using Origin 2018. Data are presented as mean ± standard error of the mean (SEM).

For qPCR data. the mean threshold cycle for detection (Ct) was calculated for each gene. The mean Ct of each target gene was normalised to the mean Ct of the reference gene, *B2M*, providing ΔCt values for all target genes in both normoxia and hypoxia. The ΔCt values were manipulated using either the $2^{-\Delta Ct}$ calculation, giving values that represent target gene expression relative to *B2M* in both normoxia and hypoxia, or the $2^{-\Delta\Delta Ct}$ calculation to obtain values for fold change in gene expression in hypoxia relative to normoxia. The latter approach was used when several genes were screened to prevent over complication in data presentation. In both cases, statistics were used to identify differences in gene expression in hypoxia relative to normoxia at each time point tested.

When comparing two groups, a t-test was used. A one-tailed t-test was used when the direction of change was predictable, while a two-tailed t-test was used when the direction of change was uncertain. For comparison between three or more levels across one factor (e.g. the effect of multiple doses of a compound on proliferation, the effect of three conditions on ejection fraction), a one-way ANOVA was used with either Tukey's, Sidak's, or the Bonferonni-Holme multiple comparison test as appropriate. For comparisons between three or more variables across more than one factor (e.g. effect of multiple doses of a compound on proliferation over several days), a two-way ANOVA was used with Tukey's post-hoc analysis.

Chapter 3

Characterisation of commercially available HPASMCs as an *in-vitro* model of hypoxia-induced pulmonary VSMC proliferation

3.1 Introduction

In excess of 400 widely used cell lines have been subject to misidentification since the 1960s (Capes-Davis et al., 2010). Despite this, the necessity to validate the identity of cell lines does not appear to be widely recognised by researchers (Lorsch et al., 2014). Mistakes can be made because cells from different sources can be morphologically similar. Further, changes in cell morphology can occur over time. Cultured cells can also undergo a number of chromosomal modifications such as duplications, rearrangements, mutations and epigenetic fluctuations that result in a changing phenotype (Lorsch et al., 2014). Thus, to avoid misidentification, cells should be reliably sourced and for extra precaution, an assessment of cell type-specific gene expression, growth characteristics and morphology should be carried out.

In VSMCs, α-SMA is the predominant actin isoform and is thus a commonly used marker to confirm VSMC identity. However, α-SMA is not a reliable standalone marker to confirm VSMC identity because of its expression in myofibroblasts (Ng et al., 1998; Sousa et al., 2007). This is important because myofibroblasts look phenotypically similar to VSMCs and are readily cultured from the adventitial layer of blood vessels. One way to clarify VSMC identity is to demonstrate expression of a second VSMC marker such as SMMHC. Miano et al. (1994) justified SMMHC as a marker that provides the best definition of a contractile VSMC phenotype because it has never been detected in non-SMCs *in vivo.* Expression of SMMHC is also absent in myofibroblasts in models of arterial injury (Christen et al., 2001). Thus, expression of both α-SMA and SMMHC as contractile markers is suitable to confirm the identity of differentiated VSMCs.

3.1.1 Assessing the growth characteristics of pulmonary VSMCs

Patel et al. (2016) explained that VSMCs modulate their phenotype, which may be contractile or synthetic. However, this does not mean that VSMCs are *either* contractile or synthetic. Rather, these descriptions represent the two extremities of a spectrum of SMCs with intermediate phenotypes (Rensen et al., 2007). As mentioned previously, proliferation of pulmonary VSMCs is not observed in healthy human blood vessels but is a disease response contributing to the pathogenesis of PH (Cooper and Beasley, 1999). Although cells in culture most often favour a proliferative phenotype because of the conditions to which they are exposed to sustain healthy cultures, hypoxia shifts VSMCs even further to favour a proliferative phenotype. It seems counterintuitive for VSMC proliferation to increase in hypoxia since an increased cell number and concomitant reduction in O_2 availability would worsen hypoxic stress (Hubbi and Semenza, 2015). Accordingly, in many cell types proliferation *is* reduced in hypoxia. Conversely, CH consequent of diseases such as COPD and sleep apnoea is a leading cause of CH-induced PH, for which pulmonary VSMC proliferation is a key pathological feature (House et al., 2008). It follows that CH is a valuable tool to understand the hypoxia-induced pulmonary VSMC proliferation that underpins PH development and progression, further confirming the identity of pulmonary VSMCs. It is important to note that the relatively loose definition of *hypoxia* (a reduction in O_2 availability in one condition compared to another) means it is easy to mimic hypoxic conditions in cell culture experiments. Hypoxia is commonly defined as 1% O_2 in *in-vitro* studies in the literature (Pak et al., 2007; Pugliese et al., 2015; Evans et al., 2016).

When deciding on the time-course of hypoxic exposure, it is important to consider that primary cell lines cannot be cultured indefinitely due to changes in both their genotype and phenotype as passage number increases and the eventual onset of replicative senescence sets in. For *in-vivo* studies, 10% O_2 for three weeks is common when using the SuHx mouse model of CH-induced PH (Ciuclan et al., 2011; Vitali et al., 2014). To establish a comparable *in-vitro* model, observations should be made over the same period, both in normoxia (control condition) and hypoxia (experimental condition). Thus, a growth profile of HPASMCs cultured in either normoxia or hypoxia for at least three weeks would be useful to establish the onset of senescence in these primary cells and to assess the potential of these cells as a suitable *in-vitro* model to investigate the mechanisms of hypoxia-induced pulmonary VSMC proliferation.

3.1.2 Morphology characteristics of pulmonary VSMCs

It is noted in the literature that human aortic VSMCs cultured in normoxia adopt an elongated and flattened morphology, while those cultured in hypoxia maintain a rhomboid shape (Minamino et al., 2001) commensurate with a shift towards a synthetic, proliferative phenotype. Thus, an assessment of pulmonary VSMC morphology is useful to assist in confirming the identity of commercially available HPASMCs and may signify hypoxia-induced phenotypic switching.

3.1.3 Identifying VSMC phenotypic switching

As demonstrated previously, contractile VSMCs can be recognised using the marker proteins, α-SMA and SMMHC. However, markers that are upregulated in the synthetic phenotype of SMCs are rare (Rensen et al., 2007). Thus, a reduction in the expression of markers associated with the contractile phenotype are generally accepted as characteristics of the synthetic phenotype. However, contractile marker protein expression also gradually decreases as VSMCs are cultured, and the extent of this decrease varies between markers. Thus to avoid ambiguity, Christen et al. (1999) conclude that an assessment of at least two proteins associated with a particular phenotype is necessary to conclude a synthetic VSMC, and this data should be supplemented with an assessment of morphology and proliferation characteristics. To confirm a shift towards a synthetic phenotype in hypoxic HPASMCs *in vitro,* an assessment of SMMHC and α-SMA expression as contractile markers, and ki67 as a proliferative marker is suitable when considered alongside morphology and proliferation characteristics. Ki67 is a nuclear protein that is strictly used as a cellular marker for proliferation. Ki67 is present during all active phases of the cell cycle (G_1, S, G_2 and mitosis), but is absent in the quiescent phase (G_0) (Bruno and Darzynkiewicz, 1992).

To verify the identity of commercially available HPASMCs and to establish a suitable *in-vitro* model of hypoxia-induced pulmonary VSMC proliferation, an assessment of: 1) contractile and proliferative VSMC marker expression; 2) the growth characteristics of HPASMCs; and 3) cell morphology were performed in both normoxia and hypoxia.

3.2 Results

3.2.1 Confirming VSMC-specific gene expression

Basic immunocytochemistry was carried out to confirm the identity of commercially available HPASMCs by staining for smooth muscle genes. Figure 3.1 and Figure 3.2 demonstrate positive staining for α-SMA (A and C) using primary antibodies from either Proteintech or Sigma. The two main cell types most closely associated with HPASMCs in the vessel wall are endothelial cells and fibroblasts. Figures 3.1 and 3.2 confirm negative staining for the endothelial marker, CD31 (A and B), using the antibody from Jackson Labs. Since both HPASMCs and myofibroblasts express α-SMA, the two cell types were distinguished by demonstrating positive staining for the SMC-specific marker, SMMHC (Figures 3.1 and 3.2, B and C) using the primary antibody from Abcam. Overall, immunocytochemistry indicates positive expression of α-SMA and SMMHC in HPASMCs cultured in normoxia and hypoxia for 72 hours, confirming the VSMC identity.

The selectivity of primary antibodies was also confirmed to provide confidence in immunocytochemistry observations. To confirm the selectivity of the CD31 primary antibody from Jackson labs, Figure 3.3 (A) demonstrates positive CD31 staining in HUVECs. Figure 3.3 (A) also confirms negative expression of SMMHC in HUVECs, clarifying the VSMC-specific nature of this marker, and acting as a negative control for the SMMHC primary antibody from Abcam. However, HUVECs were not a suitable control to confirm the selectivity of the α-SMA primary antibody, as α-SMA expression is observed in this cell type. Therefore, WT HEK293 cells were used to confirm absent α-SMA staining, acting as a negative control for the α-SMA primary antibodies from Sigma (Figure 3.3, B) and Proteintech (data not shown).

Appropriate controls were also implemented for all secondary antibodies used (Figure 3.4) and are relevant throughout the remainder of this thesis. To confirm the specificity of secondary antibodies, cells were processed in the same way as experimental samples, and appropriate concentrations of secondary antibody were applied to HPASMCs in the absence of primary antibody to confirm negative staining. Where weak background staining was visible, the LSM700 microscope settings (specifically the laser power, gain and saturation) were adjusted to ensure that any staining observed in experimental samples was *true* and was consequent of an interation between the primary and secondary antibodies, rather than due to a non-specific background signal.

Positive staining for both α-SMA and SMMHC, and negative staining for CD31 confirm the VSMC identity, ruling out the possibility of misidentification of this cell type with two closely associated cell types within the vessel wall, myofibroblasts and endothelial cells. These observations also suggest that a 72-hour exposure to hypoxia is not sufficient to observe a phenotypic transition towards a proliferative phenotype, concluded from the observation that no obvious downregulation in contractile proteins was observed when HPASMCs were cultured in hypoxia for 72 hours, although this was not quantified.

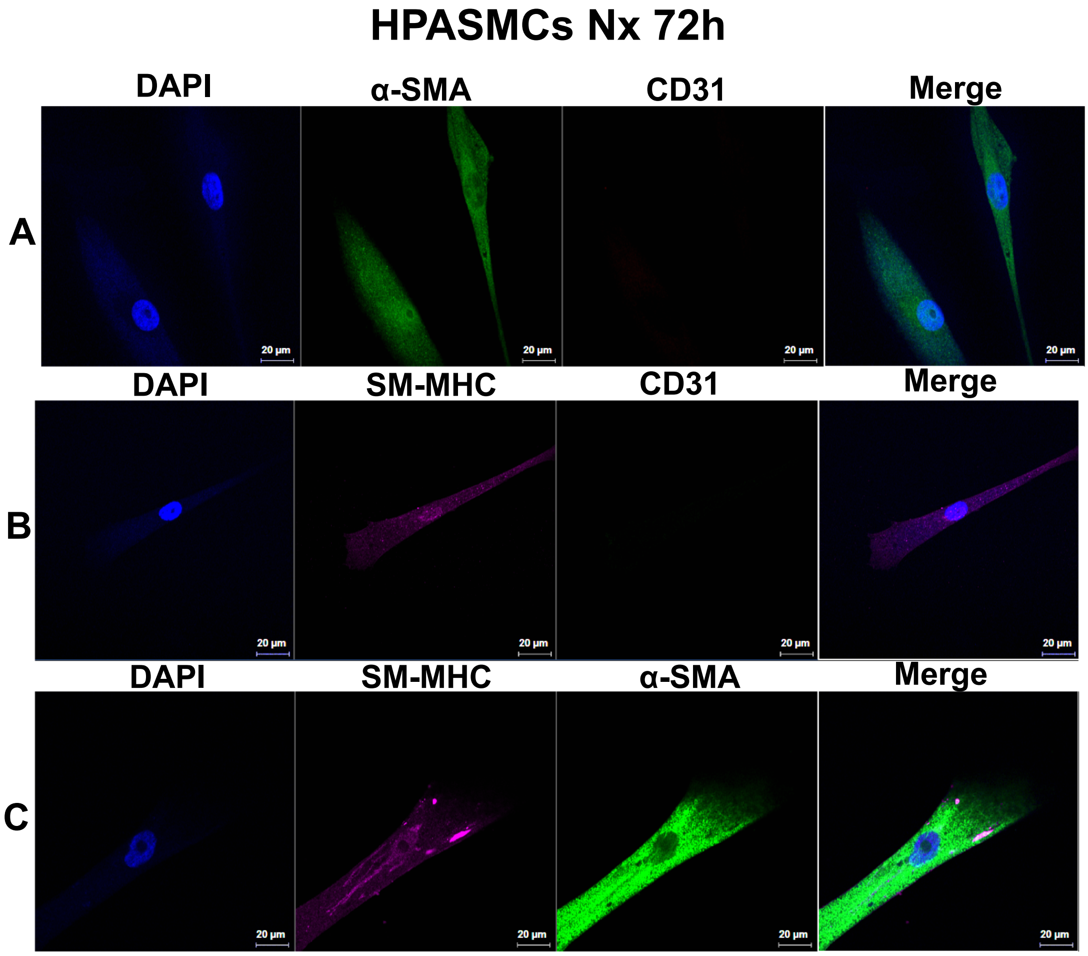

Figure 3.1. HPASMCs cultured in normoxia for 72 hours demonstrate positive staining for the SMC markers, α-SMA and SMMHC.

Representative image demonstrating smooth muscle markers, α-SMA (A and C) and SMMHC (B and C); and negative staining for the endothelial marker, CD31 (A and B) in commercially available HPASMCs cultured in normoxia (37ºC, 95% air, 5% CO_2) for 72 hours. A merged image is represented in each panel. Four images per well with three batches of cells were obtained (n=4/N=12) and representative images shown. Images were obtained with an inverted confocal laser scanning microscope (LSM700). Scale bar = 20 µm. α-SMA, α-smooth muscle actin; SMMHC, smooth muscle-myosin heavy chain 11; CD31, cluster of differentiation 31; HPASMC, human pulmonary artery smooth muscle cell.

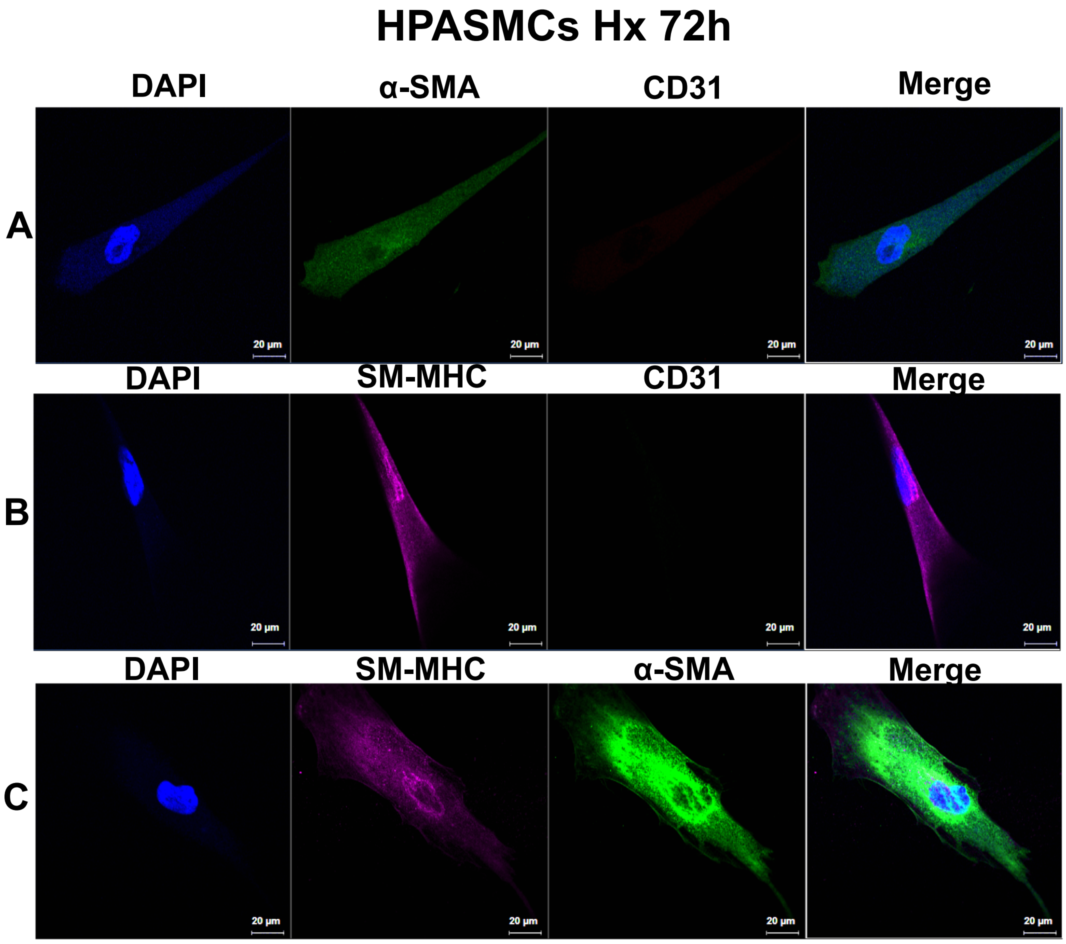

Figure 3.2. HPASMCs cultured in hypoxia for 72 hours demonstrate positive staining for the SMC markers, α-SMA and SMMHC.

Immunocytochemistry was carried out to confirm expression of smooth muscle markers, α-SMA (A and C) and SMMHC (B and C); and negative staining for the endothelial marker, CD31 (A and B), in commercially available HPASMCs cultured in hypoxia (37ºC, 1% O2 [supplemented with N_2], 5% CO_2) for 72 hours. A merged image is represented in each panel. Four images per well with three batches of cells were obtained (n=4/N=12) and representative images shown. Images were obtained with an inverted confocal laser scanning microscope (LSM700). Scale bar = 20 µm. α-SMA, α-smooth muscle actin; SMMHC, smooth muscle-myosin heavy chain 11; CD31, cluster of differentiation 31; HPASMC, human pulmonary artery smooth muscle cell.

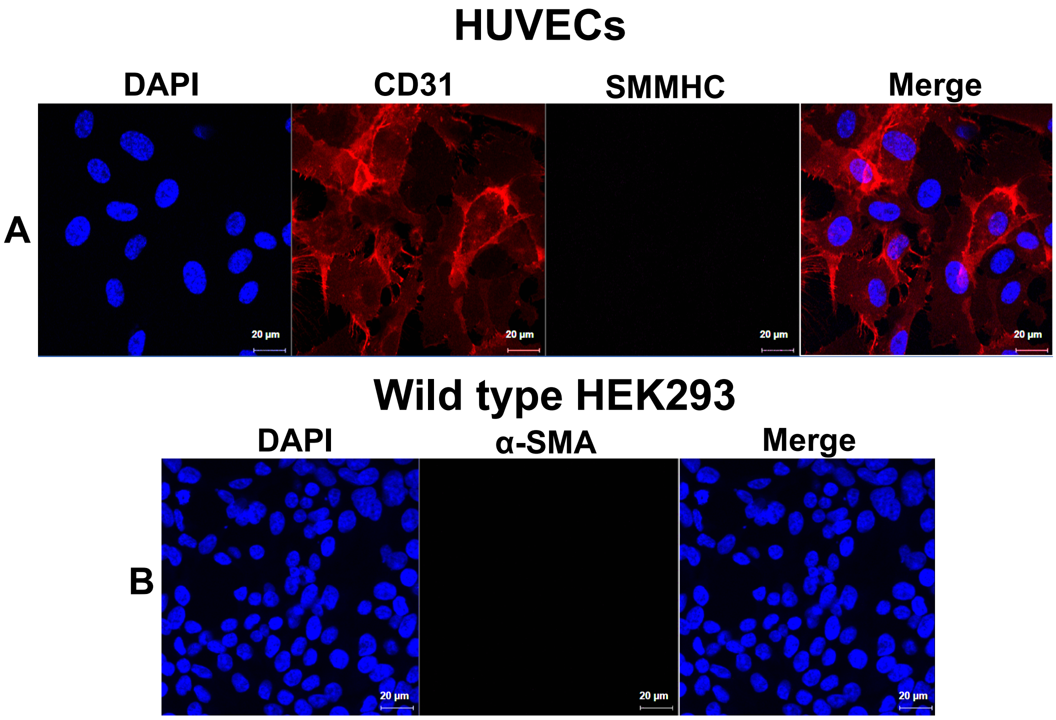

Figure 3.3. HUVECs and WT HEK293 cells confirm selectivity of SMMHC and α-SMA primary antibodies.

To validate selectivity of antibodies, immunocytochemistry was carried out to confirm negative expression of smooth muscle markers in HUVECs and WT HEK293 cells. Negative staining for SMMHC (A) and α-SMA (B); and positive staining for the endothelial marker, CD31 (A) are observed. Merged images are represented in each panel. Images were obtained with an inverted confocal laser scanning microscope (LSM700). Scale bar = 20 µm. α-SMA, α-smooth muscle actin; SMMHC, smooth muscle-myosin heavy chain 11; CD31, cluster of differentiation 31; HUVECs, human umbilical vein endothelial cells; WT HEK293, wild type human embryonic kidney 293.

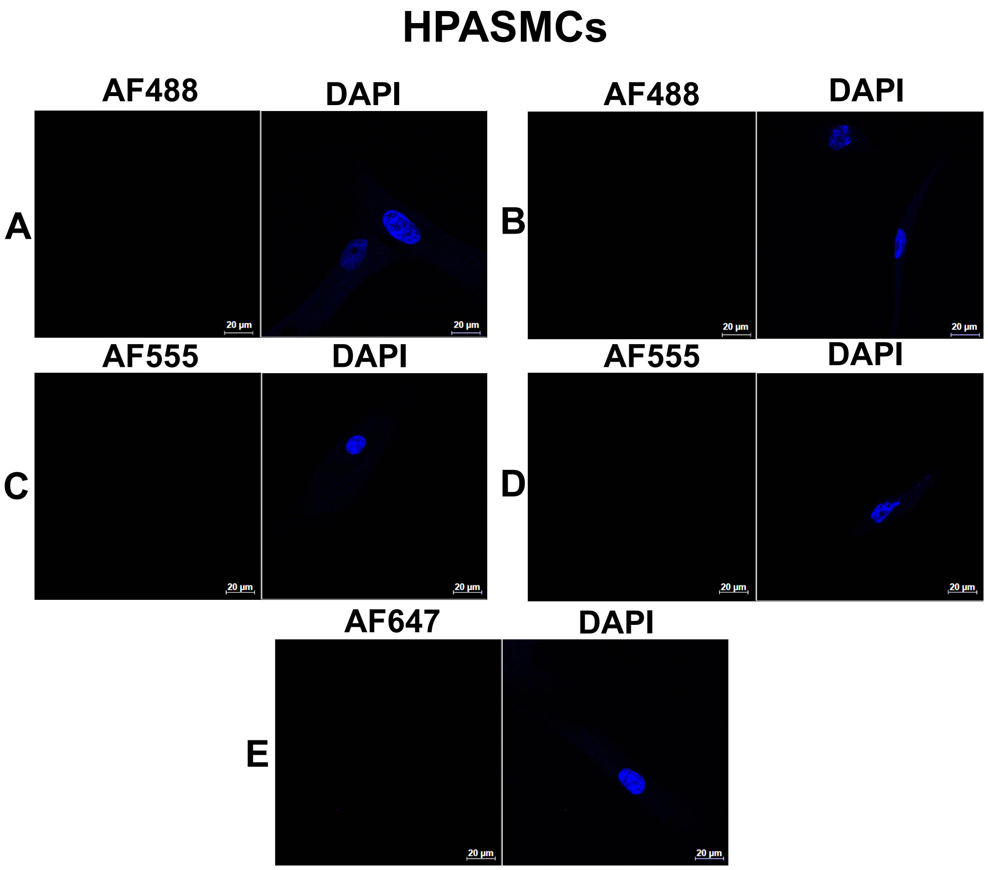

Figure 3.4. HPASMCs demonstrate selectivity of secondary antibodies.

Alexa Fluor® secondary antibodies were applied to HPASMCs in the absence of primary antibody to confirm negative staining. Images were obtained with an inverted confocal laser scanning microscope (LSM700). Scale bar = 20 µm. HPASMC, human pulmonary artery smooth muscle cell.

3.2.2 Growth characteristics of HPASMCs cultured in normoxia

The predictability of primary cells to senesce after a certain number of divisions warranted a growth profile to assess the proliferative behaviour of commercially available HPASMCs maintained in standard cell culture conditions.

Figure 3.5 demonstrates the growth profile of HPASMCs cultured in normoxia for 7 (A), 14 (B), 21 (C) or 28 days (D). After culturing in normoxia for the durations specified, HPASMCs were plated at 10000 cells/well (day 0) and the degree of proliferation was quantified in a three-day assay. At each time point, a paired, one-tailed t-test was used to identify statistically significant differences in HPASMC proliferation in a three-day assay when compared to the number of cells plated at the beginning of the experiment (day 0).

A significant degree of proliferation was observed in HPASMCs that had initially been cultured in normoxia for 14 (B) and 21 days (C) when proliferation in a three-day assay was compared with the number of cells plated at day 0 ($p<0.05$). In HPASMCs initially cultured in normoxia for 14 days, proliferation was increased by 325% ± 66% when day 3 counts were compared to day 0 counts. In HPASMCs cultured in normoxia for 21 days, proliferation at day 3 was increased by 455% ± 91% compared with day 0. Although not statistically significant, a three-day proliferation assay demonstrated an increase in HPASMC proliferation in cells initially cultured in normoxia for 7 days (A) in a three-day assay (396% ± 187%).

Proliferation of HPASMCs cultured in normoxia for 28 days appears to decline, demonstrated by the observation that in a three-day assay, proliferation only increased by 169% ± 130% when compared with day 0 (D), indicating the onset of senescence. Copious cell debris was also observed in HPASMCs cultured in normoxia for 28 days. Since the onset of senescence in HPASMCs cultured in normoxia appears to occur by the 28-day time point, this was taken as the limit at which a suitable *in vitro* normoxic control for hypoxia-induced VSMC proliferation could be established.

Although trypan blue was incorporated into the proliferation assay method as an additional measure of cell viability, no dead cells were detected with this method in this particular dataset, likely due to the cells being washed away during the DPBS washing step of the protocol.

Collectively, these data show that HPASMCs are proliferative in culture for up to 21 days when cultured in normoxia and start to reach senescence after this point.

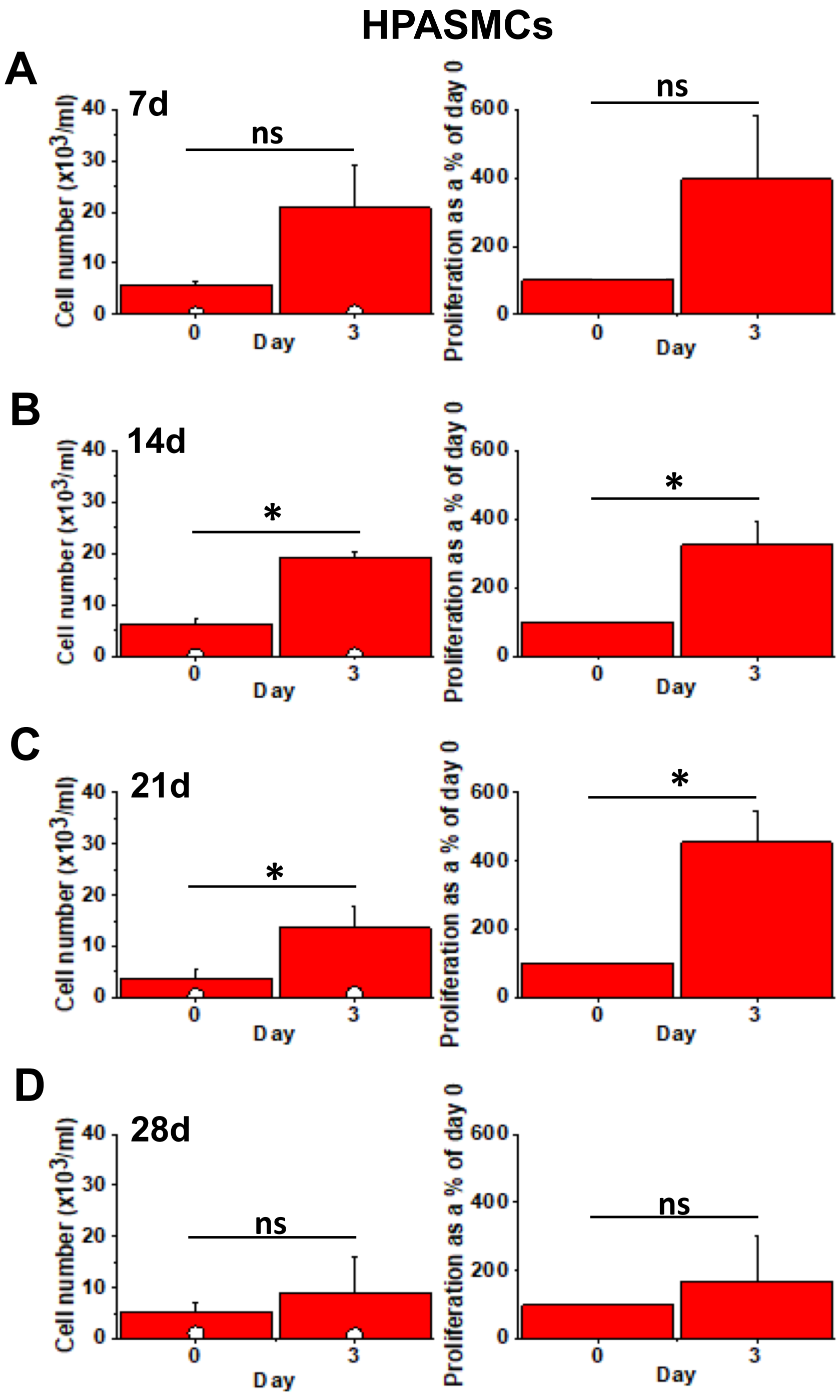

Figure 3.5. Growth profile of HPASMCs cultured in normoxia.

Proliferation of HPASMCs cultured in normoxia (37ºC, 95% air, 5% CO_2) for 7 (A), 14 (B), 21 (C) or 28 (D) days. Left: Cell number was determined on day 0 and day 3. Trypan blue stain was also used as an additional measure of cell viability (white circles). Right: Day 3 data are normalised to day 0 counts to account for variability in cell number during plating. The mean ± SEM of independent experiments (n=6, 7 and 14 days; n=5, 21 days; n=4, 28 days) are plotted. Data analysed via paired, one-tailed t-test. * = $p<0.05$. HPASMCs, human pulmonary artery smooth muscle cells.

3.2.3 Growth characteristics of HPASMCs cultured in hypoxia

Culturing HPASMCs in hypoxia is a useful *in-vitro* tool to study the mechanisms that underpin hypoxia-induced pulmonary VSMC proliferation.

To ensure 75-cm^2 cell culture flasks maintained in both normoxia and hypoxia were sufficiently confluent to carry out proliferation assays in parallel at each time point, a range of dilutions were utilised to account for the expectation that HPASMCs proliferate faster in hypoxia. This minimised any error that could have been introduced by carrying out experiments on different days. Hence, each independent biological replicate encompassed observations from both normoxic and hypoxic cultures performed in parallel. Figure 3.6 demonstrates the growth profile of HPASMCs cultured in either normoxia or hypoxia for 7 (A), 14 (B), 21 (C) or 28 days (D). After culturing in normoxia and hypoxia for the durations specified, HPASMCs were plated at 10000 cells/well (day 0) and the degree of proliferation was quantified in a three-day assay. At each time point, a two-way analysis of variance (ANOVA) was used to identify statistically significant differences.

In a three-day assay, proliferation of hypoxic HPASMCs was 374% ± 126% (14 days), 472% ± 58% (21 days) and 547% ± 57% (28 days) of proliferation at day 0, which represents a statistically significant increase in proliferation. Although not statistically significant due to the large standard error, a three-day proliferation assay also demonstrated an increase in proliferation of 293% ± 114% in HPASMCs initially cultured in hypoxia for 7 days (A) when compared to the number of cells plated on day 0.

HPASMC proliferation appears to amplify with time spent in hypoxia (Figure 3.6, A–D). Although senescence of primary cells is expected, HPASMCs cultured in hypoxia maintained rapid proliferation for around 10 weeks when passaged weekly (equating to a total culture time of ~70 days in hypoxia) (data not shown). Also, HPASMCs cultured in hypoxia did not exhibit the cell debris indicative of apoptotic events, and susceptibility to infection was greatly reduced compared to HPASMCs cultured in normoxia. Thus, commercially available HPASMCs responded better to 1% O_2 (hypoxia) than the hyperoxic environment of a standard cell culture incubator (Minamino et al., 2001).

Figure 3.6 also confirms that HPASMCs cultured in hypoxia proliferated faster than HPASMCs cultured in normoxia. At 14 days, HPASMC proliferation increased by 374% ± 126% in hypoxia, compared to 164% ± 45% in normoxia ($p<0.05$). At day 21, proliferation increased by 472% ± 58% in hypoxia, compared to 228% ± 49% in normoxia ($p<0.01$). At 28 days, proliferation increased by 547% ± 57% in hypoxia, compared to 198% ± 47% in normoxia ($p<0.01$).

These observations confirm that hypoxia has the capacity to shift HPASMCs to favour a proliferative phenotype—an observation that further clarifies the identity of commercially available HPASMCs, since this behaviour is expected in this cell type. In a three-day assay, no significant difference was observed between HPASMC proliferation in hypoxia versus normoxia at the 7-day time point (Figure 3.6, A), where proliferation was increased by 293% ± 114% in hypoxia and 219% ± 70% in normoxia when compared to day 0. It is possible that at a short time point of 7 days, HPASMCs have not yet undergone the hypoxia-induced phenotypic transition to favour a proliferative phenotype.

Taken together, the hypoxia-induced increase in HPASMC proliferation and the amplification of this response with time spent in hypoxia confirm the identity of commercially available HPASMCs and justify 1% O_2 as a suitable *in-vitro* model to investigate the mechanisms of hypoxia-induced VSMC proliferation.

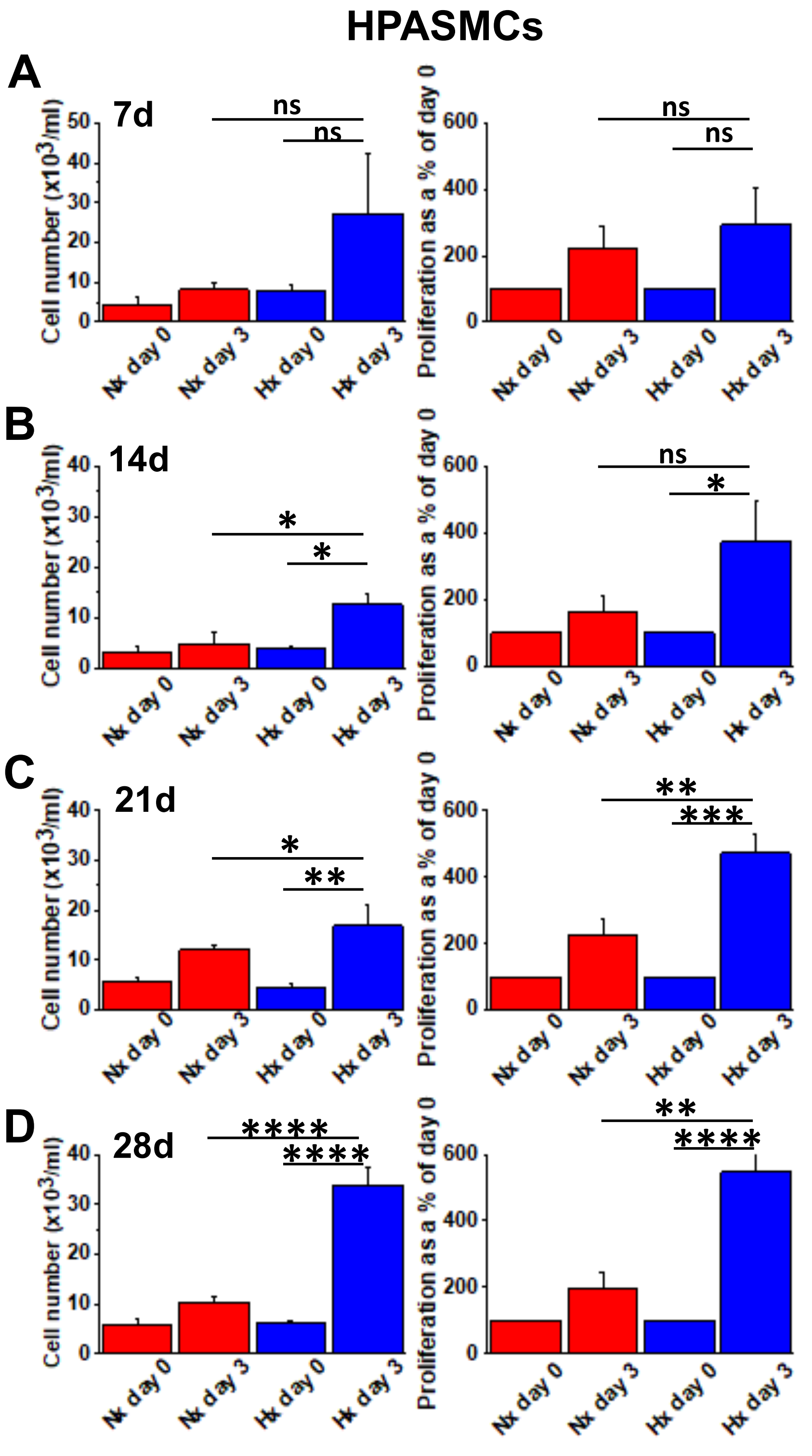

Figure 3.6. Hypoxia increases proliferation of HPASMCs.

Proliferation of HPASMCs cultured in hypoxia (37ºC, 1% O2 [supplemented with N_2], 5% CO_2) and normoxia (37ºC, 95% air, 5% CO_2) for 7 (A), 14 (B), 21 (C) or 28 (D) days. Left: Cell number was determined on day 0 and day 3. Trypan blue stain was also used as an additional measure of cell viability (white circles). Right: Day 3 data are normalised to day 0 counts to account for variability in cell number during plating. The mean ± SEM of independent experiments (n=3 for each time point) are plotted. Data analysed via repeated measures two-way ANOVA followed by Sidak's multiple comparison test. * = p<0.05; ** = p<0.01; **** = p<0.0001.

3.2.4 HPASMC morphology in normoxia and hypoxia

It is noted in the literature that human aortic VSMCs cultured in normoxia adopt an elongated and flattened morphology, while those cultured in hypoxia maintain a rhomboid morphology (Minamino et al., 2001), the latter of which is consistent with a more synthetic phenotype.

The IncuCyte Live Cell Analysis Imaging System (Figure 3.7, A) and EVOS FL Auto 2 digital microscope (Figure 3.7, B) were used to obtain representative images of the morphology of HPASMCs cultured in normoxia and hypoxia for equivalent time points. To avoid background interference from the copious cell debris observed at the 28-day time point in HPASMCs cultured in normoxia, HPASMCs were imaged at 19 days in both conditions.

Figure 3.7 demonstrates that commercially available HPASMCs demonstrate an elongated and spindle-like morphology when cultured in normoxia for 19 days, and a rhomboid morphology when cultured in hypoxia for 19 days. This phenomenon is also observed in HPASMCs cultured in hypoxia for 72 hours, albeit to a lesser extent. A morphological shift from elongated to rhomboid by the 19-day time point is consistent with a hypoxia-induced transition to a synthetic, proliferative pulmonary VSMC phenotype.

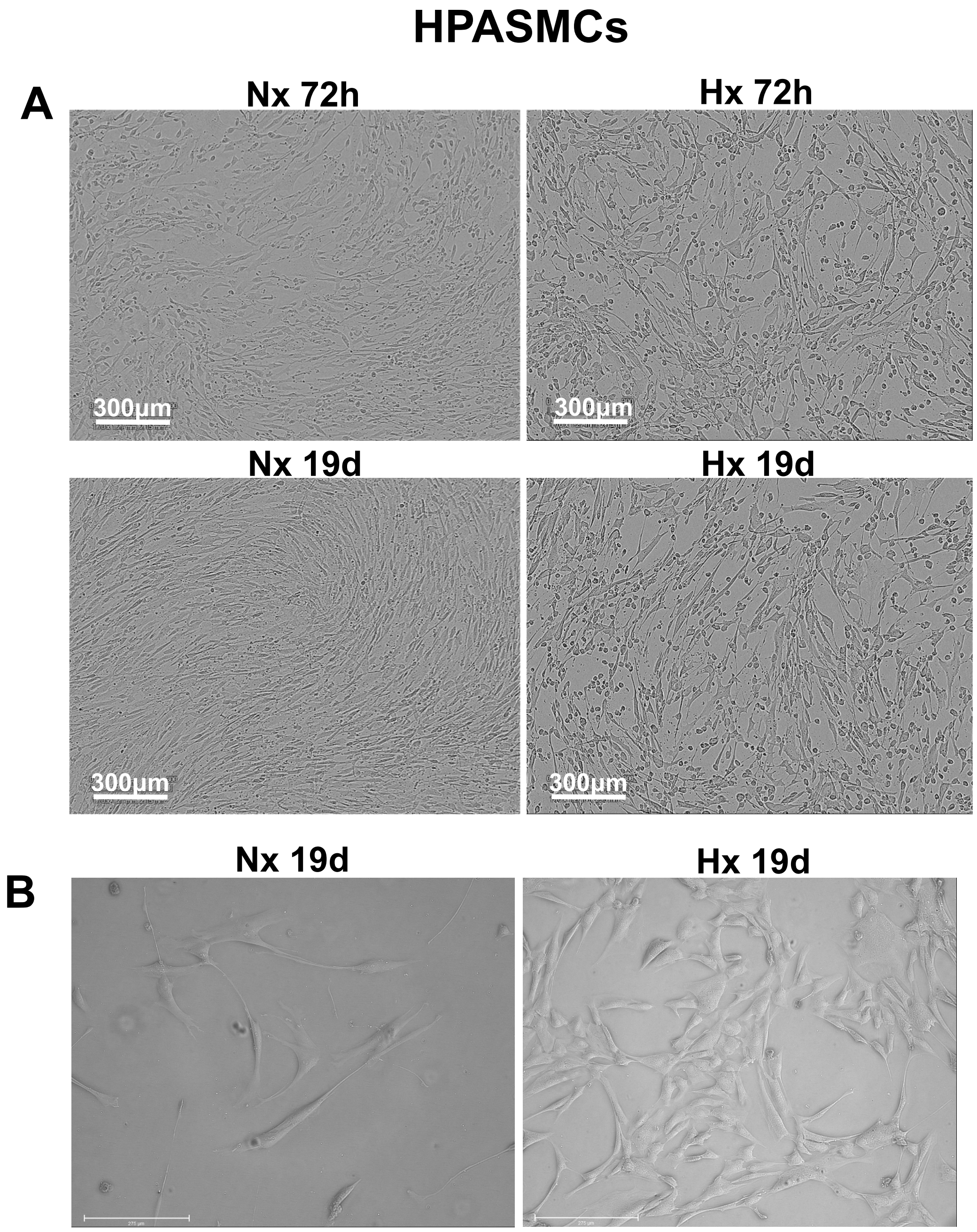

Figure 3.7. HPASMCs cultured in hypoxia for 19 days adopt a rhomboid morphology, consistent with a synthetic, proliferative VSMC phenotype.

HPASMCs were cultured in either normoxia (37ºC, 95% air, 5% CO_2) or hypoxia (37ºC, 1% O_2 [supplemented with N_2], 5% CO_2) for 72 hours or 19 days before being plated into 96-well plates and imaged in phase contrast using the IncuCyte Live Cell Analysis Imaging System to observe cell morphology (A). Digital images were also taken using the EVOS FL Auto 2 in phase contrast to demonstrate elongated morphology in normoxia at 19 days. Representative images are illustrated (n=3). HPASMC, human pulmonary artery smooth muscle cell; VSMC, vascular smooth muscle cell.

According to Rensen et al. (2007), markers that are upregulated in the VSMC synthetic phenotype are rare. Thus, a reduction in the expression of markers associated with the VSMC contractile phenotype is generally accepted as characteristic of a synthetic VSMC phenotype. To confirm a phenotypic transition in HPASMCs, the expression of α-SMA and SMMHC as contractile markers, and ki67 as a proliferative marker were assessed at 72 hours and 28 days in HPASMCs cultured in either normoxia or hypoxia.

Figure 3.8 confirms earlier observations that α-SMA and SMMHC are expressed in HPASMCs cultured in both normoxia and hypoxia at 72 hours, supporting the observation that a 72-hour hypoxic exposure is not sufficient to observe any obvious downregulation in the contractile markers, α-SMA and SMMHC. This is consistent with the observation that 7 days was not sufficient to observe any significant hypoxia-induced increase in pulmonary VSMC proliferation (Figure 3.6, A). At the 72-hour time point, Ki67 staining is visible in the nuclei of a subset of HPASMCs cultured in hypoxia (B) (approximately 30%, although this was not directly quantified), suggesting possible initiation of the hypoxia-induced transition to a synthetic, proliferative VSMC phenotype at this time point. Ki67 staining is not present in any cells at the 72-hour time point in HPASMCs cultured in normoxia (A).

Figure 3.9 demonstrates that in HPASMCs cultured in hypoxia for 28 days (B), α-SMA and SMMHC (B) staining are less intense than in HPASMCs cultured in normoxia for an equivalent time period (A). These immunocytochemistry observations were not quantified due to time limitations, but downregulation of α-SMA and SMMHC has also been demonstrated in previous literature (Rensen et al. 2007; Shankman et al. 2015). To provide confidence in these observations, the concentrations of primary and secondary antibodies used and the application times were comparable and samples were imaged at the same time.

The reduced staining intensity could indicate downregulation of these contractile markers in HPASMCs cultured in hypoxia for 28 days and a shift of these cells towards a synthetic phenotype, which is consistent with previous literature. In support of this phenotypic transition, Ki67 staining is also visible in a subset of HPASMCs cultured in hypoxia for 28 days (B), but it is not present in HPASMCs cultured in normoxia for 28 days (A). Collectively, possible downregulation of α-SMA and SMMHC, and positive ki67 staining in HPASMCs cultured in hypoxia for 28 days suggest a possible hypoxia-induced phenotypic transition towards a proliferative phenotype.

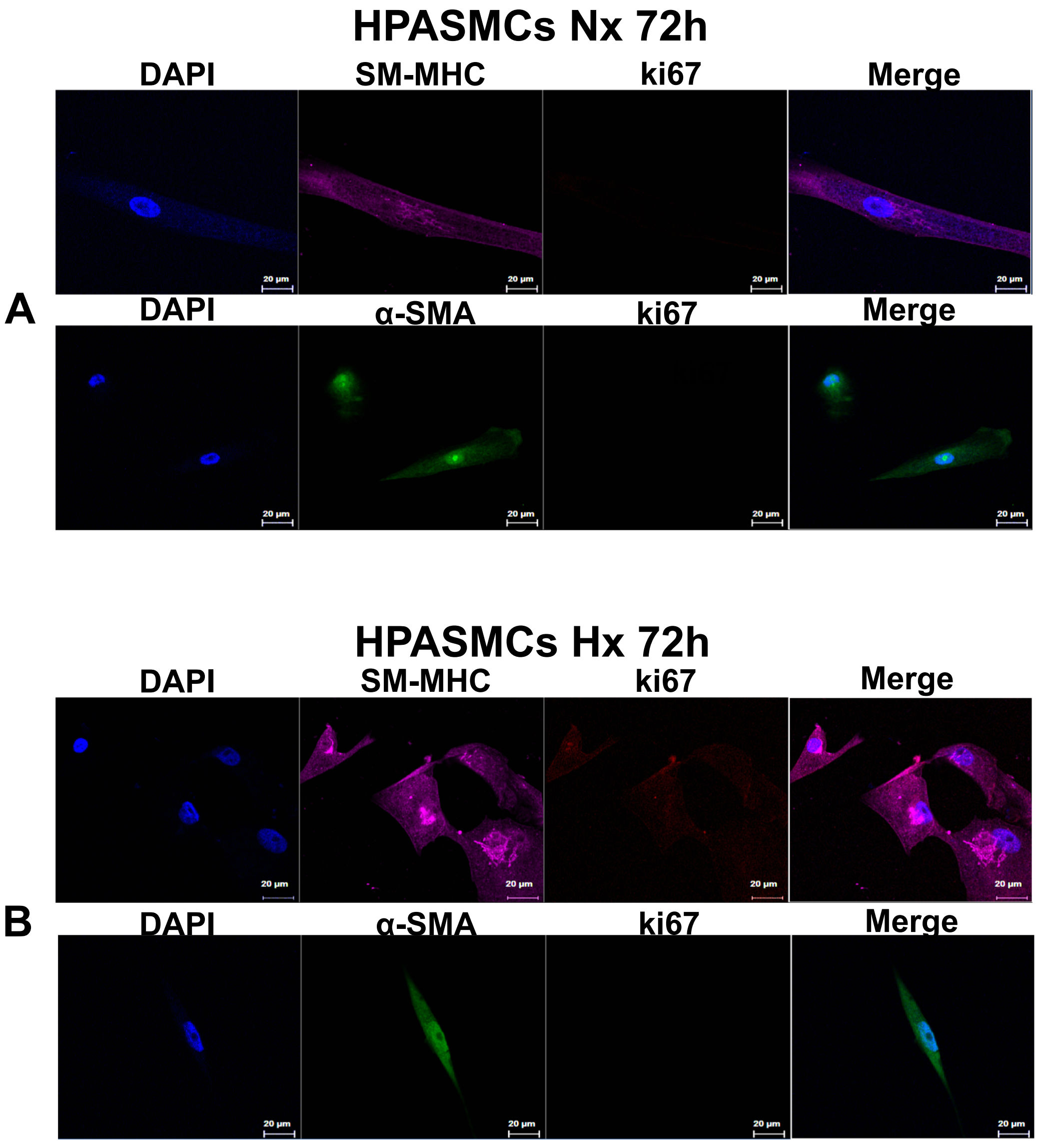

Figure 3.8. No obvious change is observed in the expression of the contractile markers, α-SMA and SMMHC, in HPASMCs cultured in hypoxia for 72 hours.

Immunocytochemistry was carried out to identify changes in the expression of smooth muscle markers, SMMHC and α-SMA; and the proliferative marker, ki67 in commercially available HPASMCs cultured in either normoxia (37ºC, 95% air, 5% CO_2) or hypoxia 37ºC, 1% O_2 [supplemented with N_2], 5% CO_2) for 72 hours and representative images demonstrated (n=3). A merged image is represented in each panel. Images were obtained with an inverted confocal laser scanning microscope (LSM700). Scale bar = 20 µm. α-SMA, α-smooth muscle actin; SMMHC, smooth muscle myosin heavy chain 11; HPASMC, human pulmonary artery smooth muscle cell.

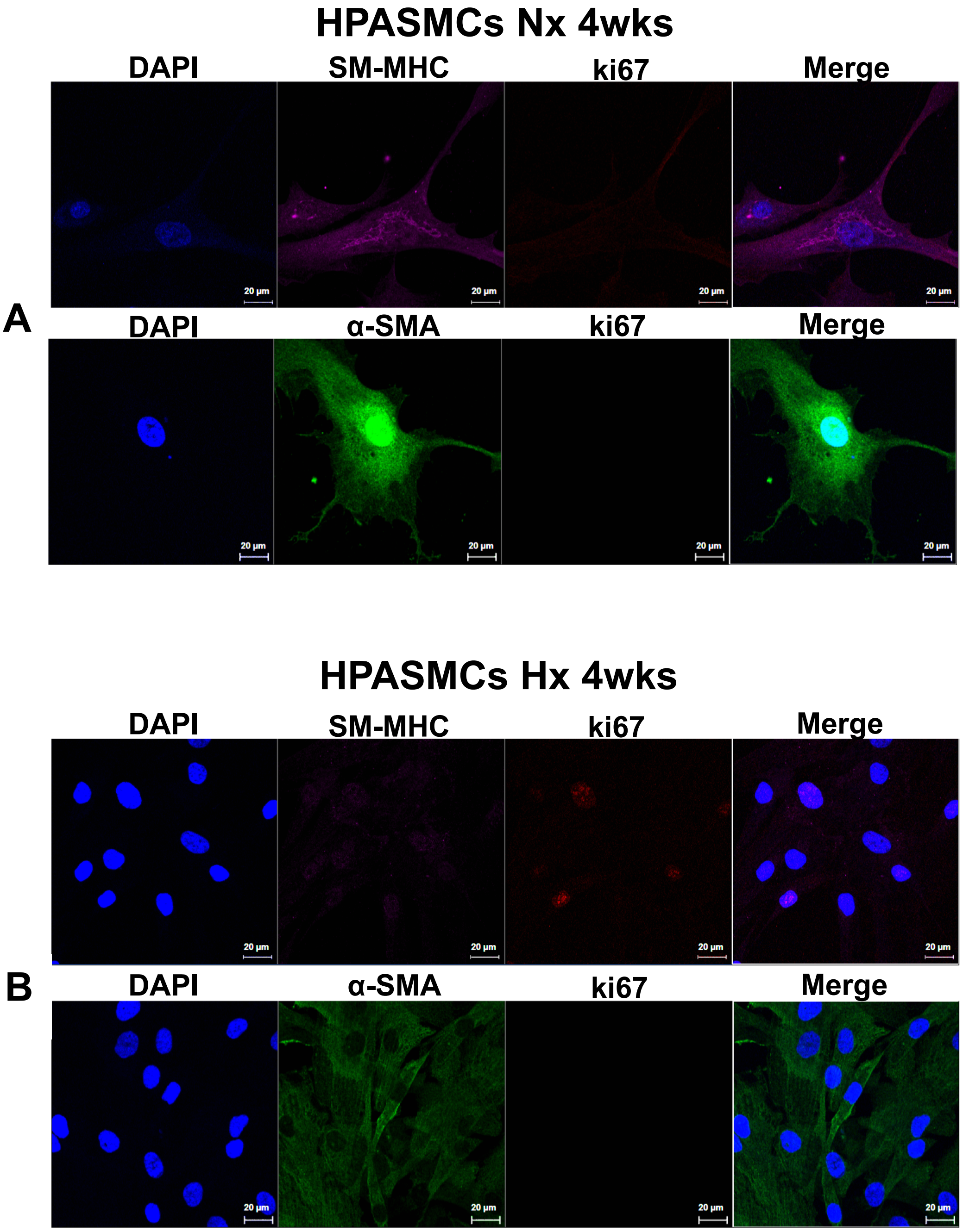

Figure 3.9. α-SMA and SMMHC are downregulated in HPASMCs cultured in hypoxia for 28 days, and ki67 expression is increased.

Immunocytochemistry was carried out to identify changes in the expression of smooth muscle markers, SMMHC and α-SMA; and the proliferative marker, ki67 in commercially available HPASMCs cultured in either normoxia (37ºC, 95% air, 5% CO_2) or hypoxia 37ºC, 1% O_2 [supplemented with N_2], 5% CO_2) for 28 days and representative images demonstrated (n=3). A merged image is represented in each panel. Images were obtained with an inverted confocal laser scanning microscope (LSM700). Scale bar = 20 µm. α-SMA, α-smooth muscle actin; SMMHC, smooth muscle myosin heavy chain 11; HPASMC, human pulmonary artery smooth muscle cell.

3.3 Summary of aims and key findings

To verify the identity of commercially available HPASMCs and to establish a suitable *in-vitro* model of hypoxia-induced VSMC proliferation, an assessment of: 1) contractile and proliferative VSMC marker expression; 2) the growth characteristics of HPASMCs; and 3) cell morphology were performed in HPASMCs cultured in normoxia and hypoxia.

It is of note that *normoxia* refers to a standard cell culture environment of ~20% O_2—a level at which most cells in the human body, especially pulmonary VSMCs, would not be exposed (Prabhakar and Semenza, 2012). Thus, standard cell culture conditions of ~20% O_2 are supraphysiological and represent *hyperoxia*. Due to limitations with laboratory equipment (multiple laboratory users maintaining cells in the same incubator under standard culture conditions), it was not possible to adapt the O_2 percentage to resemble the physiological conditions of pulmonary VSMCs *in situ.* However, this did not pose a major issue given that a 20% O_2 environment is widely accepted as standard in research. This limitation is addressed further in Section 6.1.

The proliferative profile of HPASMCs cultured in normoxia presented in Figures 3.5 and 3.6 demonstrates variability, possibly because of batch-specific differences in age, gender and ethnicity (Section 2.1.1). It could be suggested that the significant hypoxia-induced increase in HPASMC proliferation in Figure 3.6 would not be observed if HPASMCs cultured in normoxia proliferated to a similar degree as was observed in Figure 3.5. Batch-specific variability poses uncertainty about how the results could be extrapolated to larger populations; thus, greater sample sizes would help to clarify the extent to which hypoxia increases HPASMC proliferation.

The proliferative capacity of HPASMCs cultured in hypoxia was maintained for around 10 weeks—substantially longer than HPASMCs cultured in normoxia, which became susceptible to infection, emitted debris, and had higher dead cell counts. It is logical to suggest that commercially available HPASMCs respond better to 1% O_2 (hypoxia) than the hyperoxic environment of a standard cell culture incubator (Minamino et al., 2001). Thus, as well as being a useful model to study the mechanisms that underpin hypoxia-induced pulmonary VSMC proliferation, hypoxia may be a useful tool for pulmonary VSMC culture more generally.

No significant hypoxia-induced increase in proliferation was observed at 7 days when compared to HPASMCs cultured in normoxia, suggesting that at a time point of 7 days, cultured HPASMCs have not yet undergone the hypoxia-induced phenotypic transition to favour a proliferative phenotype. The first indication of a hypoxia-induced increase in HPASMC proliferation was at the 14-day time point. Thus, it was hypothesised that the transcriptional and translational adaptations that accompany pulmonary VSMC phenotypic switching were likely to be noticeable from around the 14-day time point, justifying immunocytochemistry to assess contractile and proliferative gene expression at a later time point of 28 days.

Although immunocytochemistry was not directly quantified, care was taken to ensure that antibody concentrations, application times, and imaging settings were consistent. Thus, it was concluded that any variation in staining intensity at time points of 72 hours and 28 days semi-quantitatively reflected a variation in expression. Although immunocytochemistry is semi-quantitative, SM-MHC staining was absent at 28 days. This could be due to reduced expression of SM-MHC as a contractile protein, supporting a shift away from expression of contractile markers, and towards a synthetic phenotype. In support of this phenotypic transition, nuclear ki67 staining was also observed. Although ki67 staining was only observed in a subset of cells, detection to any extent is promising given the difficulty various group members had in detecting ki67 in other proliferative cell types with ki67 antibodies.

It is possible that the marked reduction in SM-MHC staining in HPASMCs cultured in hypoxia indicates dedifferentiation into some other cell type, such as myofibroblasts. Dedifferentiation of VSMCs into myofibroblasts is a common phenomenon seen in response to vascular injury as the vessels attempt repair. Positive expression of α-SMA would support this speculation, since α-SMA is also expressed in fibroblasts. A closer look at Figure 3.9 (B) reveals spindle-like structures throughout the cell, which resemble the pattern of α-SMA staining in cytoskeletal stress fibres in high tension fibroblasts (Shinde, Humeres and Frangogiannis, 2017). Myofibroblasts appear during injury or wound healing, where they initiate substantial contractile activity (Hinz, Dugina and Ballestrem, 2003). Despite this speculation, the hypoxia-induced increase in HPASMC proliferation would not be accompanied by a concomitant increase in contractile activity, since these phenotypes represent opposite ends of the phenotypic spectrum. Although dedifferentiation into myofibroblasts is unlikely, this could be investigated in the future by co-staining for myofibroblast markers such as vimentin or desmin.

Although differences in morphology between HPASMCs cultured in normoxia versus HPASMCs cultured in hypoxia are visible to some (Figure 3.7), the data would have benefited from quantification of cell dimensions, since it is well-established that proliferative VSMCs adopt a rhomboid morphology, while contractile VSMCs adopt an elongated morphology (Minamino et al., 2001). To strengthen these findings, measurements of contractile shortening in VSMCs would have also been useful to distinguish the contractile phenotype of normoxic HPASMCs from the proliferative phenotype of hypoxic HPASMCs. Contractile shortening could be measured using either muscle-on-a-chip approaches or by loading the cells with a fluorescent indicator and measuring Ca^{2+} waves upon application of a contractile stimulus (Grosberg et al. 2012). In addition to the above, VSMC migration assays such as the scratch wound assay would have been useful to distinguish contractile HPASMCs from proliferative HPASMCs, since migration is closely associated with proliferation and remodelling of VSMCs in PH.

Taken together, the results presented in Chapter 3 go some way to confirming that commercially available HPASMCs undergo a hypoxia-induced increase in proliferation (Figure 3.6), adopt a rhomboid morphology (Figure 3.7) and demonstrate an apparent reduction in contractile VSMC marker expression (and an increase in proliferative marker expression) (Figure 3.9), supporting the published observation that HPASMCs cultured in hypoxia adopt a proliferative phenotype that is more pronounced than that observed in normoxia (Cooper and Beasley, 2009; Voelkel and Tuder, 2000; Humbert et al., 2004; Stenmark et al., 2009).

Although there were limitations in the data presented, HPASMCs were deemed a suitable *in-vitro* model to study the mechanisms of hypoxia-induced VSMC proliferation. In chapter 4, this *in-vitro* model is used to study the role of Ca^{2+}-selective ion channels in hypoxia-induced pulmonary VSMC proliferation, and to determine the potential of T-type Ca^{2+} channels and Orai1 as anti-proliferative targets in hypoxia-induced pulmonary VSMC proliferation.

Chapter 4

T-type Ca^{2+} channels and Orai1 as targets in hypoxia-induced pulmonary VSMC proliferation

4.1 Introduction

Since pulmonary VSMC proliferation and vascular remodelling underpin the development and progression of PH, lack of anti-proliferative therapeutics means that a whole area of clinical possibility remains untargeted. In this chapter, the *in-vitro* model of hypoxia-induced pulmonary VSMC proliferation established in Chapter 3 is used to study the potential of Ca^{2+}-selective ion channels, specifically T-type Ca^{2+} channels and Orai1, as anti-proliferative targets in CH-induced PH.

4.1.1 Revisiting the anti-proliferative role of T-type Ca^{2+} channels

Although T-type Ca^{2+} channels show some promise as anti-proliferative targets, existing research mainly relies on the use of small-molecule inhibitors. However, the selectivity of these inhibitors is questionable. Mibefradil has received criticism due to its off-target effects on other ion channels (Nilius et al., 1997; Liu et al., 1999; Chouabe et al., 2000; Perchenet and Clement-Chomienne, 2000; Wu et al., 2000). Although the structural analogue of mibefradil, NNC55-0396, does not inhibit L-type Ca^{2+} channels at biologically relevant concentrations (Huang et al., 2004), it has not been tested for off-target effects on other Ca^{2+} channel subtypes that might also drive hypoxia-induced pulmonary VSMC proliferation. TTA-A2 has been described as a highly specific and potent T-type Ca^{2+} channel inhibitor with no off-target effects at an IC_{50} below 10 μM (Uebele et al., 2009). Despite this, there is no data in the public domain demonstrating a lack of off-target effects at other potentially relevant Ca^{2+} channel targets that are also associated with hypoxia-induced VSMC proliferation.

Thus, the anti-proliferative effects of widely used T-type Ca^{2+} channel inhibitors should be clarified in a biologically relevant in-*vitro* model of hypoxia-induced pulmonary VSMC proliferation before determining whether any anti-proliferative effects are attributable to T-type Ca^{2+} channel inhibition as opposed to off-target effects at other Ca^{2+} channels that are also associated with hypoxia-induced pulmonary VSMC proliferation, such as Orai1 or TRPC channels.

4.1.2 Revisiting the anti-proliferative role of Orai1

Promise has been demonstrated for the Orai proteins as anti-proliferative targets in CH-induced PH. Of particular interest in this thesis is Orai1, since Orai1-dependent SOCE is mediated by PDGF and PDGF receptor inhibition slowed PH progression and improved multiple pathological parameters of PH but did not translate to clinical practice due to off-target effects (Ghofrani et al., 2005; Schermuly et al., 2005; Speich et al., 2015).

Orai1 is just one downstream target of PDGF, which when inhibited with the novel inhibitor, JPIII (developed in Leeds), has reduced VSMC proliferation in the context of abdominal aortic aneurysm in *in-vivo* models in the Bailey lab (unpublished observations). The superior pharmacokinetic properties of JPIII compared to the widely published Orai1 inhibitor, Synta66, make it a suitable tool to investigate the anti-proliferative potential of Orai1 inhibition in pulmonary VSMCs in *in-vivo* models of CH-induced PH. Before proceeding to investigate the anti-proliferative effects of JPIII *in vivo*, the potential of Orai1 as an anti-proliferative target should be investigated in a biologically relevant model of CH-induced PH, such as the *in-vitro* model of hypoxia-induced VSMC proliferation established in Chapter 3.

This chapter aims to reproduce the anti-proliferative effects of widely used T-type Ca^{2+} channel inhibitors in an appropriate *in-vitro* model of hypoxia-induced VSMC proliferation and confirm lack of any off-target modulation on other Ca^{2+} entry pathways associated with hypoxia-induced pulmonary VSMC proliferation. The hypoxia-induced upregulation of T-type Ca^{2+} channels that is reported in the literature will also be clarified, specifically in HPASMCs.

This chapter will also clarify the hypoxia-induced increase in Orai1 expression that is reported in the literature, specifically in HPASMCs, as well as confirm lack of off-target modulation by JPIII on T-type voltage-dependent Ca^{2+} entry. JPIII will be used to examine the anti-proliferative effects of Orai1 inhibition in an appropriate *in-vitro* model of hypoxia-induced VSMC proliferation.

4.2 Results

4.2.1 The anti-proliferative effect of T-type Ca^{2+} channel inhibitors in an *in-vitro* model of hypoxia-induced VSMC proliferation

Despite previous evidence demonstrating a role for T-type Ca^{2+} channels in pulmonary VSMC proliferation (Rodman et al., 2005), opposing findings from two studies using HEK293 cells overexpressing T-type Ca^{2+} channels (Chemin et al., 2000; Duckles et al., 2015) prompted me to seek confirmation of the anti-proliferative effects of widely-used T-type Ca^{2+} channel inhibitors in a biologically relevant cell type—HPASMCs.

Pilot investigations revealed that in a three-day dose-response investigation, mibefradil at concentrations of 0.3 and 1 µM had no anti-proliferative effect in HPASMCs, and 10 µM mibefradil caused toxicity (data not shown), which was indicated by a large number of floating cells and cells stained positive for trypan blue. A concentration of 3 µM mibefradil was tested further based on previous data evidencing this concentration as effective in reducing proliferation of the rat aortic smooth muscle cell line, A7r5, without causing toxicity (Duckles et al., 2015).

Accordingly, a proliferation assay was carried out to observe the anti-proliferative effects of 3 µM mibefradil in HPASMCs cultured in normoxia (Figure 4.1) for 7 (A), 14 (B), 21 (C) or 28 (D) days. At the 14-day time point (Figure 4.1, B), the degree of HPASMC proliferation over three days was significantly reduced by 3 µM mibefradil (151% ± 35%) without loss of cell viability when compared to HPASMCs exposed to SmGM™-2 only at the 14-day time point (325% ± 66%).

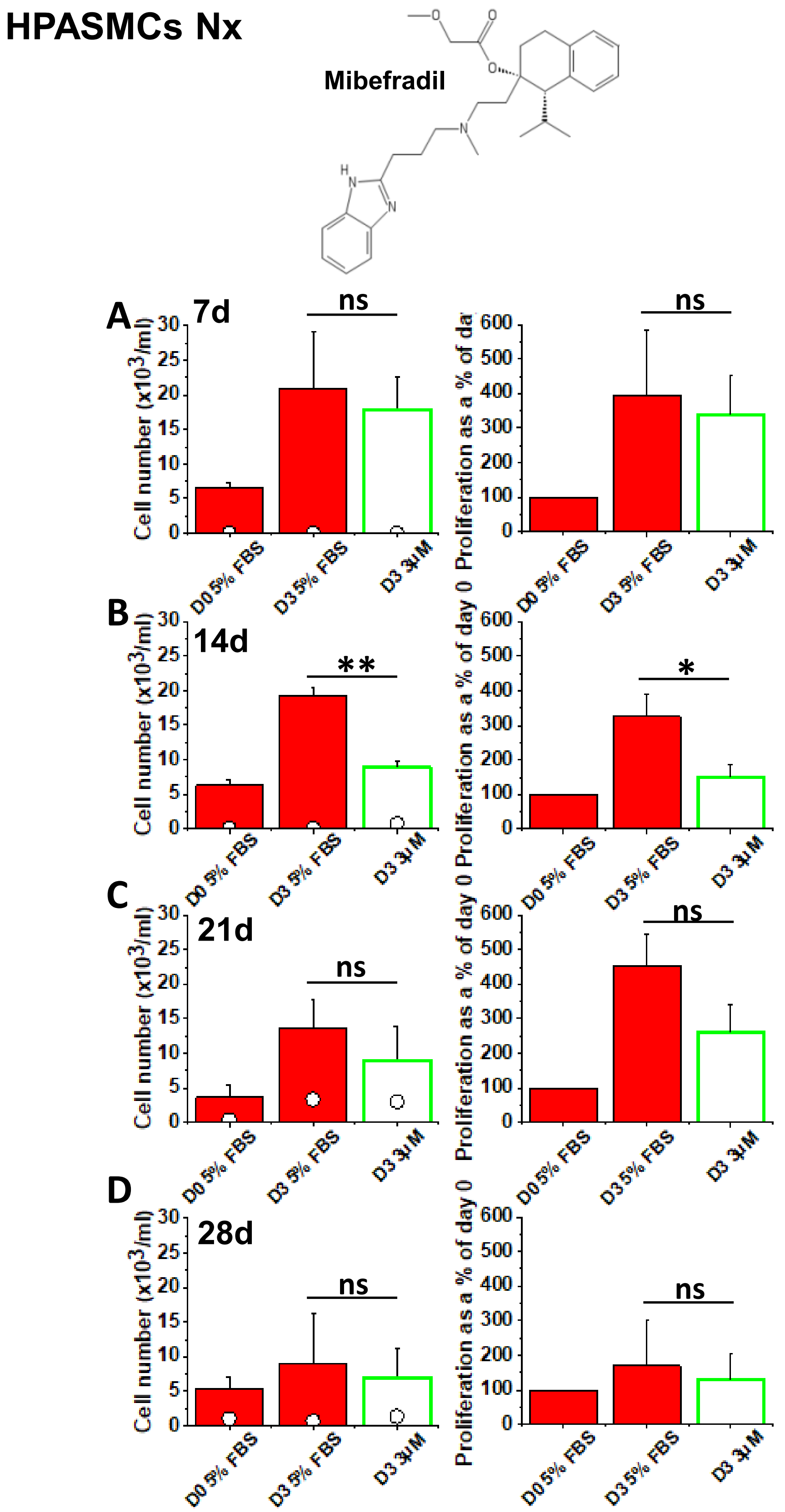

Figure 4.1. 3 µM mibefradil reduces HPASMC proliferation.

Left: Cell number was determined on day 0 and day 3 using a haemocytometer. Trypan blue was used as an additional measure of cell viability (white circles). Right: Day 3 counts are normalised to day 0 to account for variability in cell number during plating. The mean ± SEM of independent experiments (n=3 for each time point) are plotted. Data analysed using a paired two-tailed t-test. * = *p*<0.05; ** = *p*<0.01; ns = non-significant.

The poor selectivity of mibefradil warranted clarification of the anti-proliferative effects of T-type Ca^{2+} channel inhibition with the non-hydrolysable structural analogue, NNC55-0396, which has no inhibitory effect on L-type Ca^{2+} channels (Huang et al., 2004). In keeping with the prior investigation, a three-day dose-response investigation was carried out to observe the anti-proliferative effects of NNC55-0396 in HPASMCs cultured in normoxia (Figure 4.2) for 7 (A) or 28 days (B). The 14- and 21-day time points were excluded here due to time limitations.

In a three-day dose-response investigation, 10 μM NNC55-0396 reduced cell number when compared to cells maintained in SmGM™-2 only at both the 7- (A) and 28-day (B) time points. Floating cells were observed under the microscope prior to processing the wells, and trypan blue as an additional means of viability quantification revealed high dead cell counts. Thus, the significant reduction in cell number in response to 10 μM NNC55-0396 was attributed to cell toxicity rather than an effect on proliferation.

At the 28-day time point (Figure 4.2, B), the degree of HPASMCs proliferation over three days was significantly lower in HPASMCs exposed to 1 μM (181 ± 2%) and 3 μM (197% ± 12%) NNC55-0396 without loss of cell viability when compared to HPASMCs exposed to SmGM™-2 only (226% ± 7%). Although the degree of proliferation was lower in HPASMCs exposed to 3 μM (121% ± 16%) than HPASMCs exposed to SmGM™-2 only (223% ± 45%), variability meant that the data were non-significant.

NNC55-0396 was used to study the anti-proliferative effects of T-type Ca^{2+} channel inhibition in an appropriate *in-vitro* model of hypoxia-induced VSMC proliferation. In keeping with the above investigation, HPASMCs were cultured

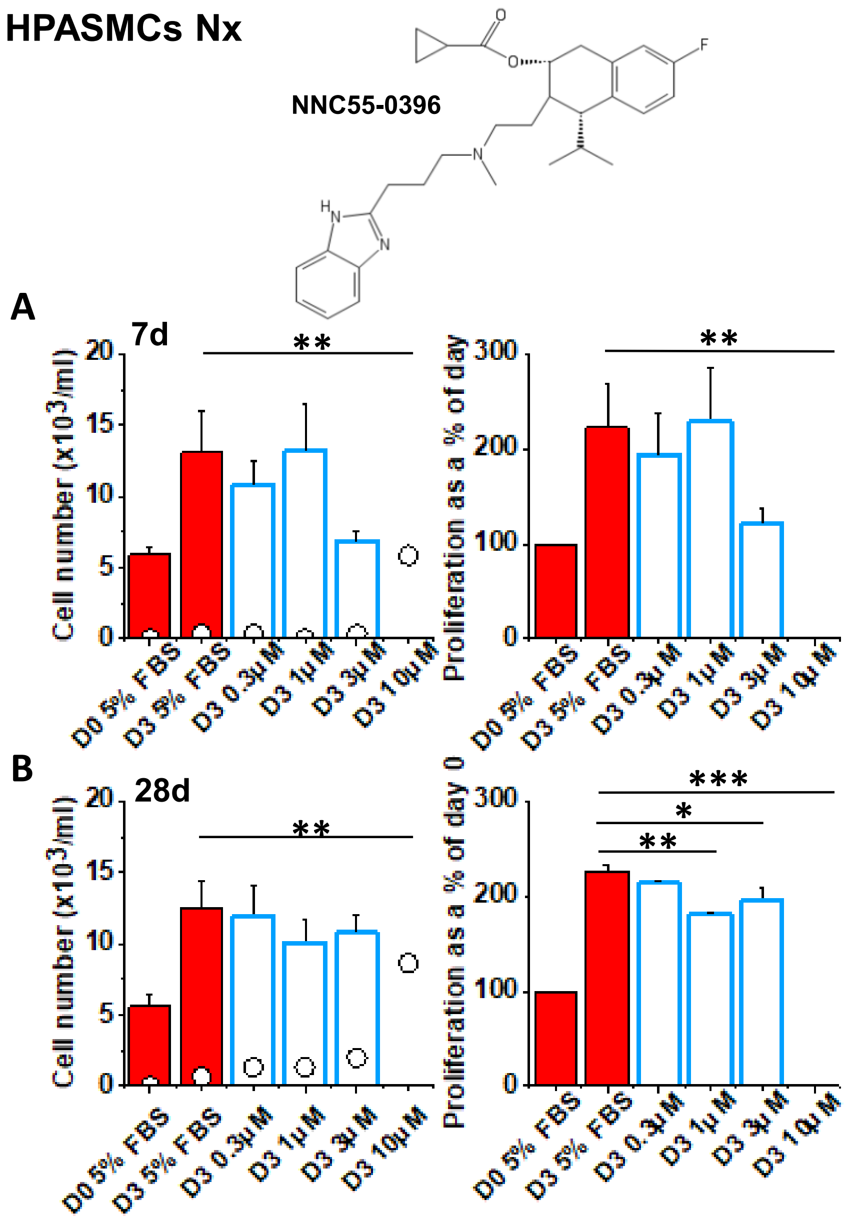

Figure 4.2. NNC55-0396 reduces HPASMC proliferation.

Left: Cell number was determined on day 0 and day 3 using a haemocytometer. Trypan blue stain was also used as an additional measure of cell viability (white circles). Right: Day 3 data are normalised to day 0 counts to account for variability in cell number during plating. The mean ± SEM of independent experiments (n=6 for 7-day time point; n=3 for 28-day time point) are plotted. Data were analysed via one-way ANOVA with Tukey's post-hoc analysis. * = *p*<0.05; ** = *p*<0.01; *** = *p*<0.001.

in hypoxia (Figure 4.3) for either 7 (A) or 28 days (B) prior to a three-day dose response investigation.

At the 7-day time point (Figure 4.3, A), the degree of hypoxic HPASMC proliferation over three days was lower in HPASMCs exposed to 3 µM NNC55-0396 (122% ± 37%) without loss of cell viability when compared to HPASMCs exposed to SmGM™-2 only (218% ± 42 %). This was non-significant, likely due to the large standard error. The large standard error prevented the detection of a significant degree of cell death caused by 10 µM NNC55-0396, which was revealed upon normalisation of the data to day 0 counts.

Conversely, at the 28-day time point (Figure 4.3, B), the degree of hypoxic HPASMC proliferation over three days was significantly lower in HPASMCs exposed to 3 µM NNC55-0396 (50% ± 18%) without loss of cell viability when compared to HPASMCs exposed to SmGM™-2 only (203% ± 13%) at the 28-day time point.

Thus, 3 µM NNC55-0396 reduces proliferation of HPASMCs, but this effect is more pronounced in HPASMCs cultured in hypoxia for 28 days, indicating a hypoxia-induced increase in the sensitivity to the anti-proliferative effects of this experimental compound.

HPASMCs Hx

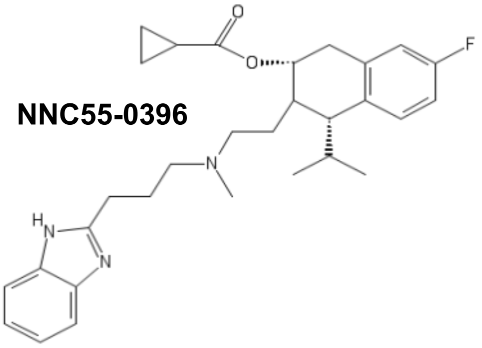

NNC55-0396

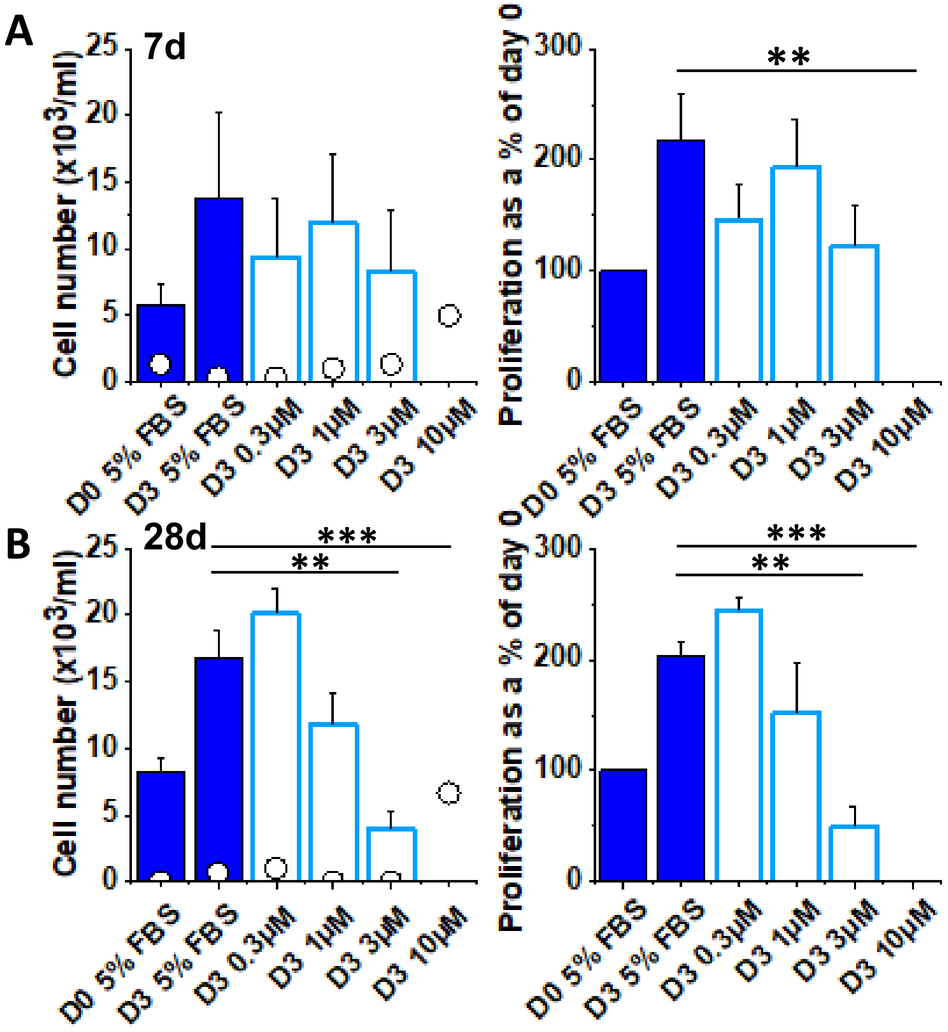

Figure 4.3. The anti-proliferative effects of NNC55-0396 are more pronounced in HPASMCs cultured in hypoxia for 28 days.

Left: Cell number was determined on day 0 and day 3 using a haemocytometer. Trypan blue stain was also used as an additional measure of cell viability (white circles). Right: Day 3 data are normalised to day 0 counts to account for variability in cell number during plating. The mean ± SEM of independent experiments (n=3 for each time point) are plotted. Data were analysed via one-way ANOVA with Tukey's post-hoc analysis. ** = *p*<0.01; *** = *p*<0.001.

As a T-type Ca^{2+} channel inhibitor that appears to exhibit superior selectivity to mibefradil and NNC55-0396, TTA-A2 was used to further clarify the anti-proliferative effect of T-type Ca^{2+} channel inhibition. The concentrations tested (0.001–1 µM) were biologically relevant, since Chevalier et al. (2014) used a final concentration of 1 µM to demonstrate protection from the hypoxia-induced increase in PAP and vascular wall thickness in an *in-vivo* model of CH-induced PH and the published IC_{50} of TTA-A2 for block of T-type Ca^{2+} channels is 0.089 µM (Chevalier et al., 2014). Accordingly, HPASMCs were cultured in normoxia (Figure 4.4) and hypoxia (Figure 4.5) for either 7 (A) or 28 days (B) prior to a three-day dose response investigation.

At the 7-day time point, the degree of normoxic HPASMC proliferation from day 0 was lower in HPASMCs exposed to 0.01 µM (129% ± 11%), 0.03 µM (98% ± 9%) and 0.1 µM (102% ± 10%) TTA-A2 compared to cells exposed to SmGM™-2 only (159% ± 56%). Although a reduction in proliferation was observed, it was non-significant (Figure 4.4, A).

At the 7-day time point, the degree of hypoxic HPASMC proliferation from day 0 was lower in HPASMCs exposed to 0.1 µM TTA-A2 (152% ± 50%) compared to cells exposed to SmGM™-2 only (201% ± 131%), although this was non-significant (Figure 4.5, A).

At the 28-day time point, the degree of normoxic HPASMC proliferation from day 0 was significantly lower in HPASMCs exposed to 0.1 µM TTA-A2 (106% ± 11%) compared to cells exposed to SmGM™-2 only (273% ± 24%, $p<0.05$) (Figure 4.4, B), although significance was only detected upon normalisation of the data to day 0 counts to account for variability in cell number during plating.

The degree of hypoxic HPASMC proliferation from day 0 was also significantly lower in HPASMCs exposed to 0.1 µM TTA-A2 (112% ± 14%) compared to cells exposed to SmGM™-2 only (402% ± 38%, $p<0.05$) (Figure 4.5, B), although significance was only detected upon data normalisation to day 0 counts.

The anti-proliferative effect of 0.1 µM TTA-A2 compared to cells exposed to SmGM™-2 was similar in both normoxia and hypoxia, suggesting no hypoxia-induced change in the sensitivity to the anti-proliferative effects of 0.1 µM TTA-A2.

These data suggest that widely-used T-type Ca^{2+} channel inhibitors including mibefradil, NNC55-0396 and TTA-A2 have the capacity to reduce pulmonary VSMC proliferation, supporting T-type Ca^{2+} channels as anti-proliferative targets in pulmonary VSMCs. In a biologically relevant *in-vitro* model of hypoxia-induced pulmonary VSMC proliferation, the anti-proliferative effects of NNC55-0396 were more marked compared to those observed in HPASMCs cultured in normoxia for an equivalent time period. Conversely, the anti-proliferative effects of TTA-A2 were relatively consistent in HPASMCs cultured in both normoxia and hypoxia at both time points tested.

These discrepancies in the response to two widely used T-type Ca^{2+} channel inhibitors justified an investigation to: 1) clarify any change in Ca^{2+} channel gene expression in hypoxia-induced VSMC proliferation; and 2) investigate the possibility of off-target modulation on other Ca^{2+} entry pathways associated with hypoxia-induced pulmonary VSMC proliferation that could account for the increased sensitivity to NNC55-0396 in hypoxia.

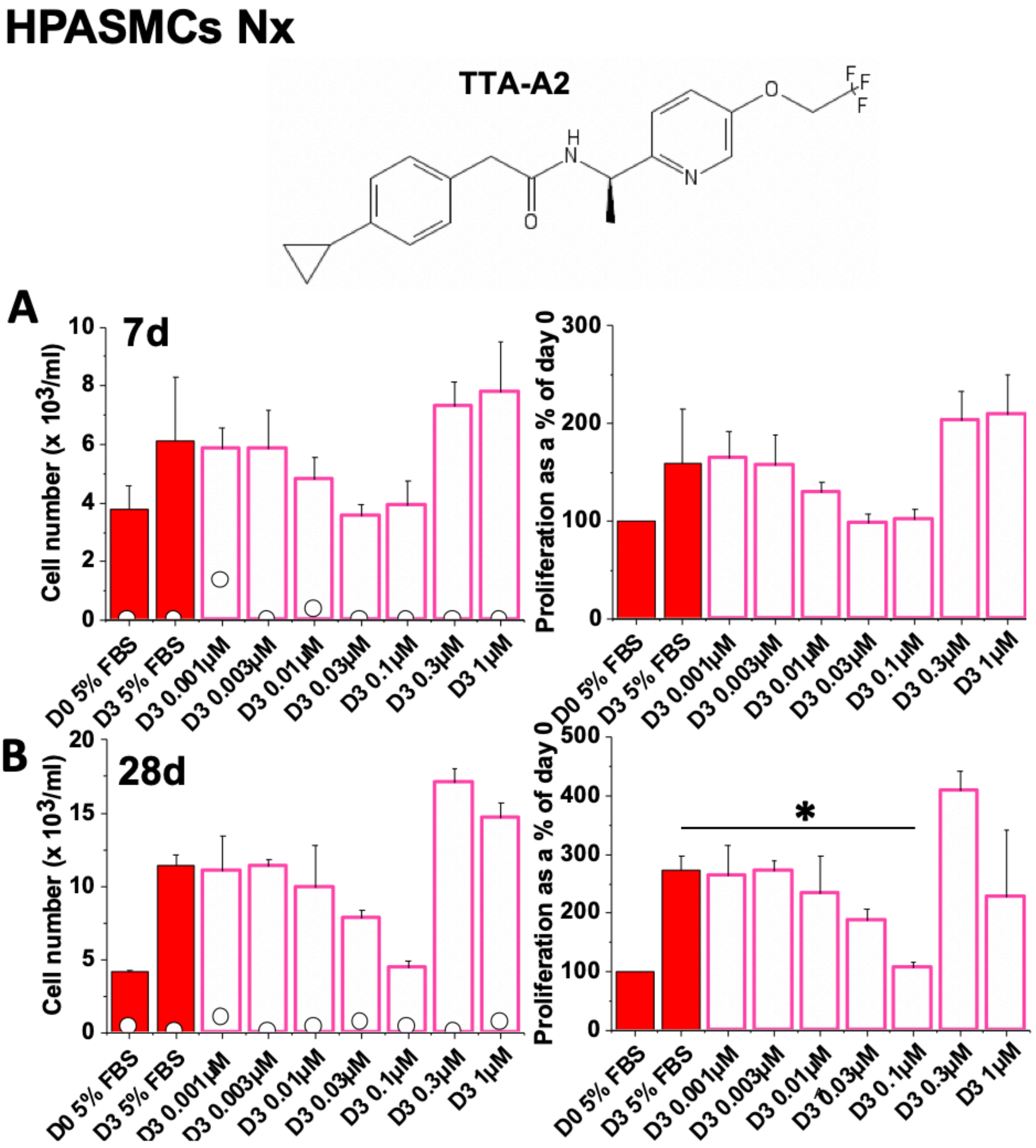

Figure 4.4. 0.1 μM TTA-A2 significantly reduces proliferation of HPASMCs cultured in normoxia for 28 days.

Left: Cell number was determined on day 0 and day 3 using a haemocytometer after maintaining in normoxia for 7 days (A) and 28 days (B). Trypan blue stain was also used as an additional measure of cell viability (white circles). Right: Day 3 data are normalised to day 0 counts to account for variability in cell number during plating. The mean ± SEM of independent experiments (n=3 for each time point) are plotted. Data were analysed via one-way ANOVA with Tukey's post-hoc analysis. Statistical significance: * = *p*<0.05.

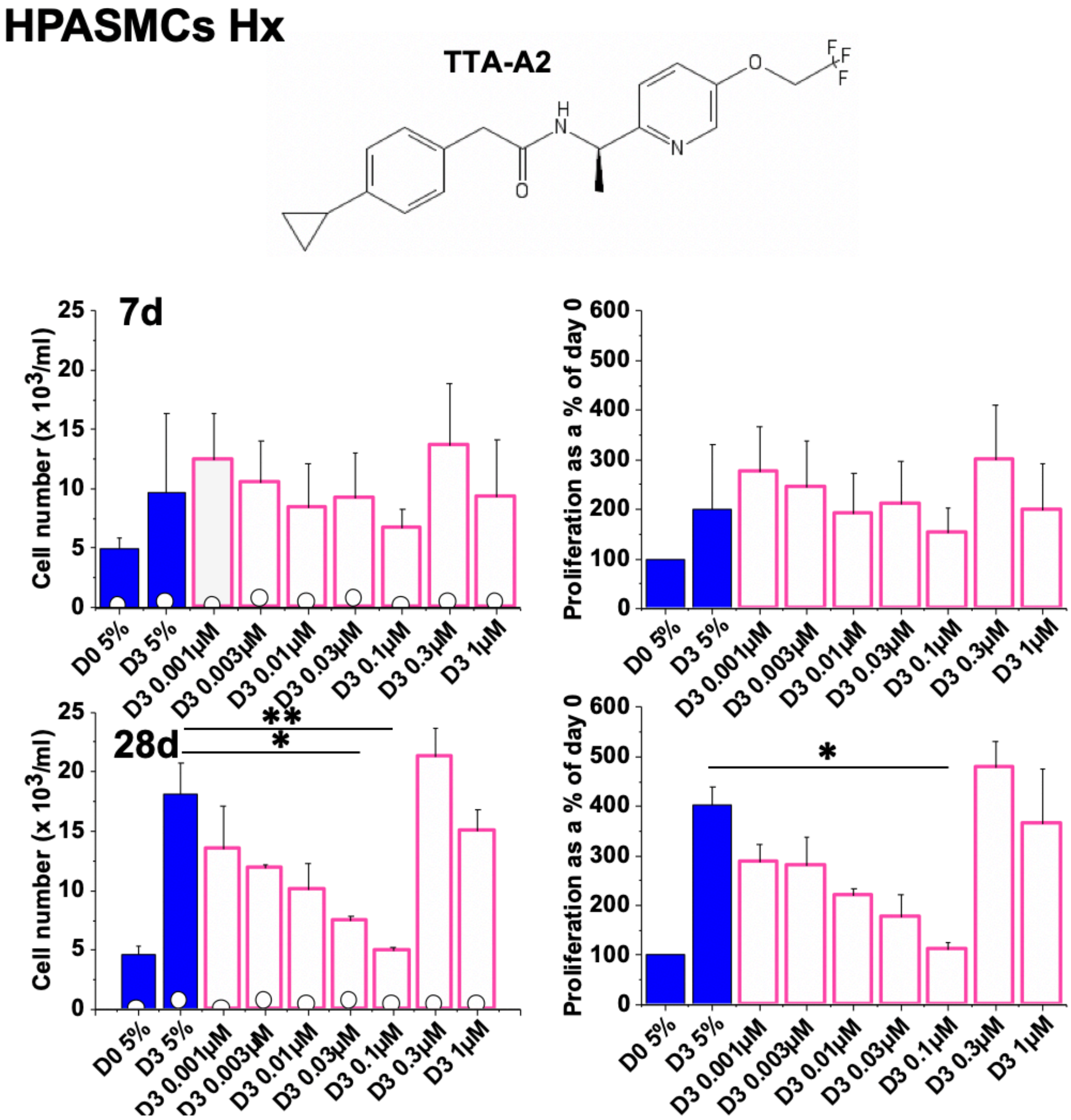

Figure 4.5. 0.1 µM TTA-A2 significantly reduces proliferation of HPASMCs cultured in hypoxia for 28 days.

Left: Cell number was determined on day 0 and day 3 using a haemocytometer after maintaining in normoxia for 7 days (A) and 28 days (B). Trypan blue stain was also used as an additional measure of cell viability (white circles). Right: Day 3 data are normalised to day 0 counts to account for variability in cell number during plating. The mean ± SEM of independent experiments (n=3 for each time point) are plotted. Data were analysed via one-way ANOVA with Tukey’s post-hoc analysis. * = *p*<0.05; ** = *p*<0.01.

4.2.2 Hypoxia-dependent Ca^{2+} channel subunit expression

Previous reports demonstrating hypoxia-induced T-type Ca^{2+} channel upregulation, combined with the hypoxia-induced increase in the sensitivity to the anti-proliferative effects of some of the T-type Ca^{2+} channel inhibitors tested, progressed this study to determine how T-type Ca^{2+} channel transcripts were altered by the hypoxic conditions used in our experiments.

First, we sought to identify a stable reference gene for qPCR experiments. Genes tested included hypoxanthine phosphoribosyltransferase (*HPRT1*), *18S*, β-actin (*ACTB*), glyceraldehyde 3-phosphate dehydrogenase (*GAPDH*), metalloproteinase inhibitor 3 (*TIMP3*), β-secretase 1 (*BACE*-1) and β2-microglobulin (*B2M*) (Figure 4.6). After identifying *B2M* as a stable reference gene in HPASMCs exposed to variable O_2 conditions at a range of time points (only day 7 data are shown), the T-type Ca^{2+} channel genes, *CACNA1G* (Figure 4.7, A) and *CACNA1H* (Figure 4.7, B), were screened using cDNA from HPASMCs cultured in normoxia or hypoxia for 7, 14, 21 or 28 days.

As shown in Figure 4.7 (A), no significant difference in *CACNA1G* ($Ca_v3.1$) mRNA expression was observed in HPASMCs cultured in hypoxia compared to HPASMCs cultured in normoxia at any time point tested. The raw Ct values for $Ca_v3.1$ transcripts were also high (~35 cycles) suggesting low expression levels overall.

Figure 4.7 (B) shows an equivalent experiment for *CACNA1H* ($Ca_v3.2$) mRNA expression in HPASMCs cultured in hypoxia compared to HPASMCs cultured in normoxia. In keeping with the $Ca_v3.1$ data, no significant difference was observed at any time point in the expression of *CACNA1H* between normoxic and hypoxic conditions. Again, the Ct values observed for $Ca_v3.2$ were high (~35 cycles) suggesting low expression levels overall.

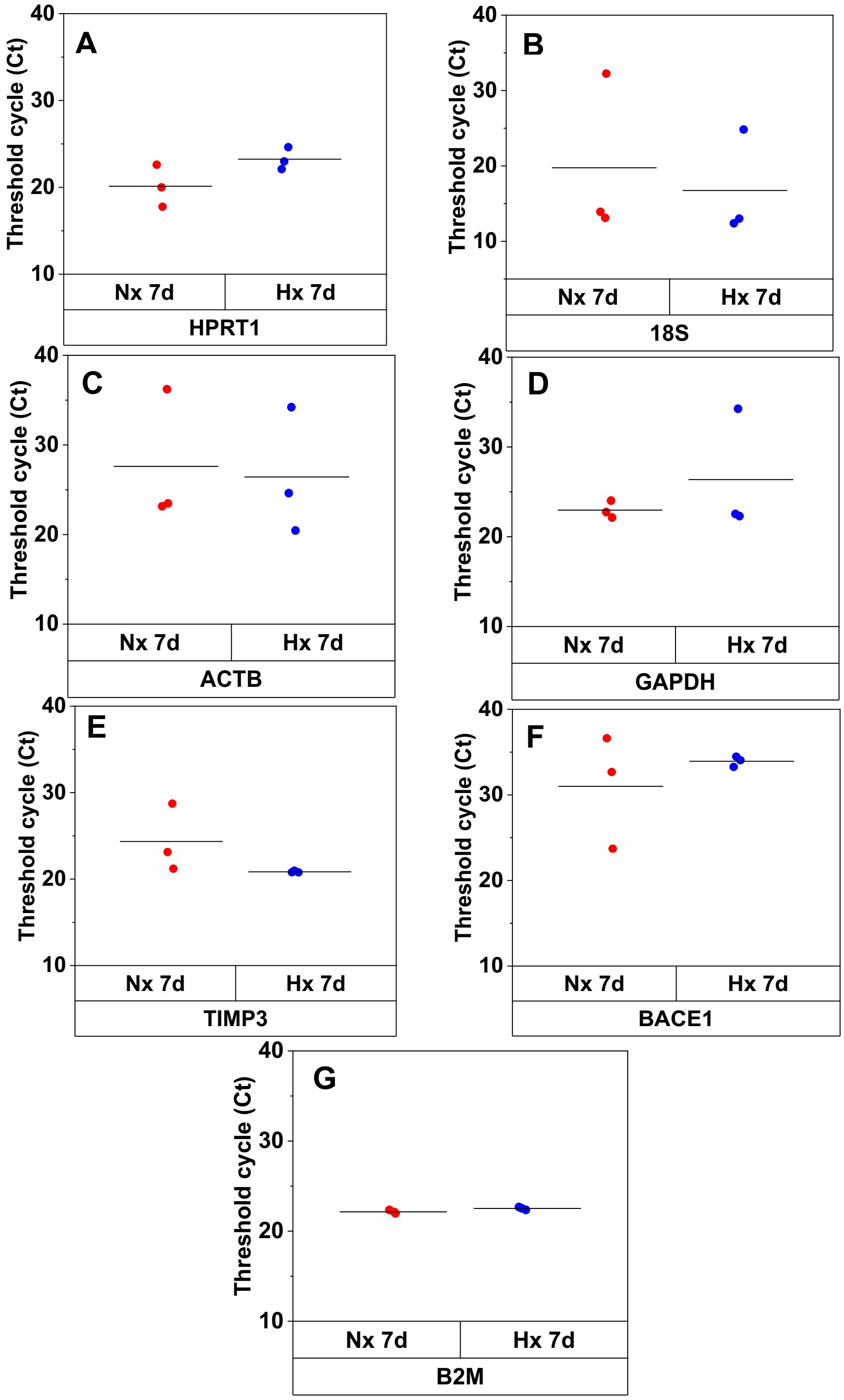

Figure 4.6. *B2M* is a stable housekeeper gene in HPASMCs cultured in variable O_2 conditions.

HPRT1 (A), *18S* (B), *ACTB* (C), *GAPDH* (D), *TIMP3* (E), *BACE1* (F) and *B2M* (G) were screened in triplicate in HPASMCs cultured in either normoxia or hypoxia for 7 days and mean Ct calculated. Three independent experiments (n=3) were performed to identify a stable reference gene for qPCR experiments. HPASMCs, human pulmonary artery smooth muscle cells; O_2, oxygen; HPRT1, hypoxanthine phosphoribosyltransferase; ACTB, β-actin; GAPDH, glyceraldehyde 3-phosphate dehydrogenase; TIMP3, metalloproteinase inhibitor 3; BACE-1, β-secretase 1; B2M, β2-microglobulin.

HPASMCs

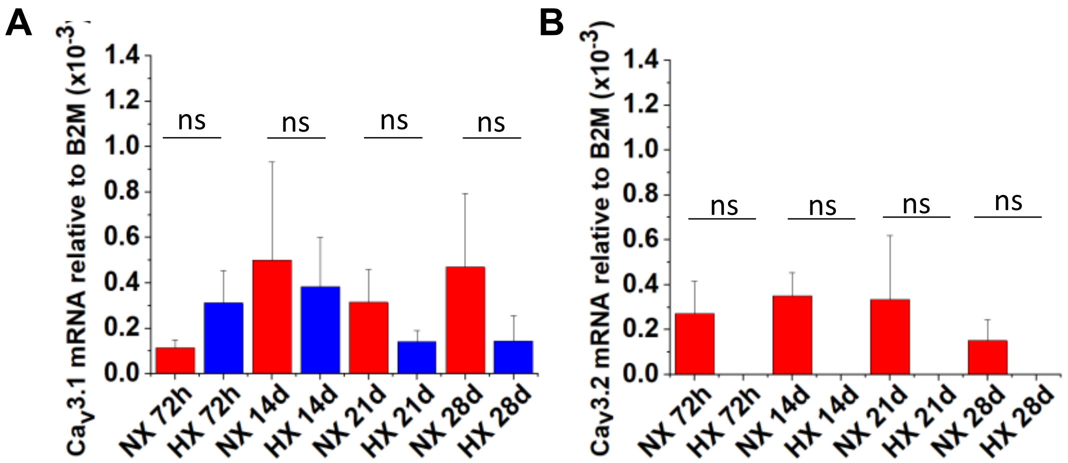

Figure 4.7. qPCR shows no significant change in $\mathrm{Ca_v}$3.1 or $\mathrm{Ca_v}$3.2 mRNA in HPASMCs cultured in hypoxia compared to normoxia.

CACNA1G and *CACNA1H* were screened in triplicate in HPASMCs at each time point and mean Ct calculated. Three independent experiments (n=3) were performed. $\mathrm{Ca_v}$3.1 (A) and $\mathrm{Ca_v}$3.2 (B) mRNA abundance expressed relative to the housekeeper gene, *B2M*, in either normoxia or hypoxia at 72 hours, 14 days, 21 days or 28 days. Data were analysed via the comparative Ct ($2^{-\Delta Ct}$) method. For each independent experiment, the mean Ct of *CACNA1G* and *CACNA1H* was normalised to the mean Ct of *B2M* (ΔCt). Data were analysed by one-way ANOVA to identify differences between normoxia and hypoxia at each time point. This was followed by Tukey's multiple comparison test. ns = non-significant.

These data were initially puzzling. Both $Ca_v3.1$ and $Ca_v3.2$ transcripts were minimally expressed at the limits of detection of the technique and were not impacted by hypoxia at the time points tested. Despite this, a significant anti-proliferative effect of T-type Ca^{2+} channel inhibitors was observed under the same experimental conditions. These two observations seemed superficially at odds.

Given the unexpected findings with regards to hypoxia-induced changes in T-type Ca^{2+} channel mRNA expression, a wide range of potentially relevant Ca^{2+} channel subunits in hypoxic experimental conditions were screened to identify targets that might be more relevant and worthy of further investigation as anti-proliferative targets in hypoxia-induced pulmonary VSMC proliferation.

Figure 4.8 illustrates the mRNA expression of 12 Ca^{2+} channel genes in hypoxia expressed as a percentage of mRNA abundance in normoxia at 72 hours (A) and 19 days (B). These data were analysed using the $2^{-\Delta\Delta Ct}$ approach, where the Ct of the stable reference gene, *B2M*, was the first internal control and the Ct of target gene cDNA from HPASMCs cultured in normoxia was the second internal control. Data were analysed this way to ensure concision in data presentation. Presenting gene expression in hypoxia relative to normoxia eliminated the need to plot mRNA expression in *both* normoxia and hypoxia for all 12 Ca^{2+} channel genes.

At the 72-hour time point (A), no significant differences were observed in the mRNA expression of any gene screened, suggesting that this duration was not sufficient to observe the hypoxia-induced changes in Ca^{2+} channel gene expression that may underpin the transition to a proliferative phenotype. This is in agreement with Figures 3.1 and 3.2, which demonstrate no obvious hypoxia-induced downregulation in the contractile markers, α-SMA and SMMHC, at 72 hours.

In keeping with the observations in Figure 4.6, at the 19-day time point (Figure 4.8, B) no hypoxia-induced upregulation in $Ca_v3.1$ or $Ca_v3.2$ mRNA was observed. Conversely, a significant upregulation in Orai1 (1371% ± 328%), Orai2 (704% ± 218%) and TRPC1 (337% ± 82%) mRNA was observed at 19 days, with non-significant potential increases in Orai3 (550% ± 245%) and STIM1 (523% ± 187%) (Figure 4.8, B).

Upregulation in Orai1, Orai2 and TRPC1 mRNA, with a trend towards an increase in Orai3 and STIM1, suggest possible relevance of SOCE in hypoxic conditions. These findings motivated further studies around Orai1 compared to $Ca_v3.1$ or $Ca_v3.2$, where minimal changes were observed.

Given the increased sensitivity to the anti-proliferative effects of the T-type Ca^{2+} channel inhibitor, NNC55-0396, in HPASMCs cultured in hypoxia for 28 days (Figure 4.3, B), one possibility was off-target effects on Orai1 channels or TRPC1-containing multimeric channels. These widely used T-type Ca^{2+} channel inhibitors have never been evaluated for off-target effects at Orai1 and TRPC1.

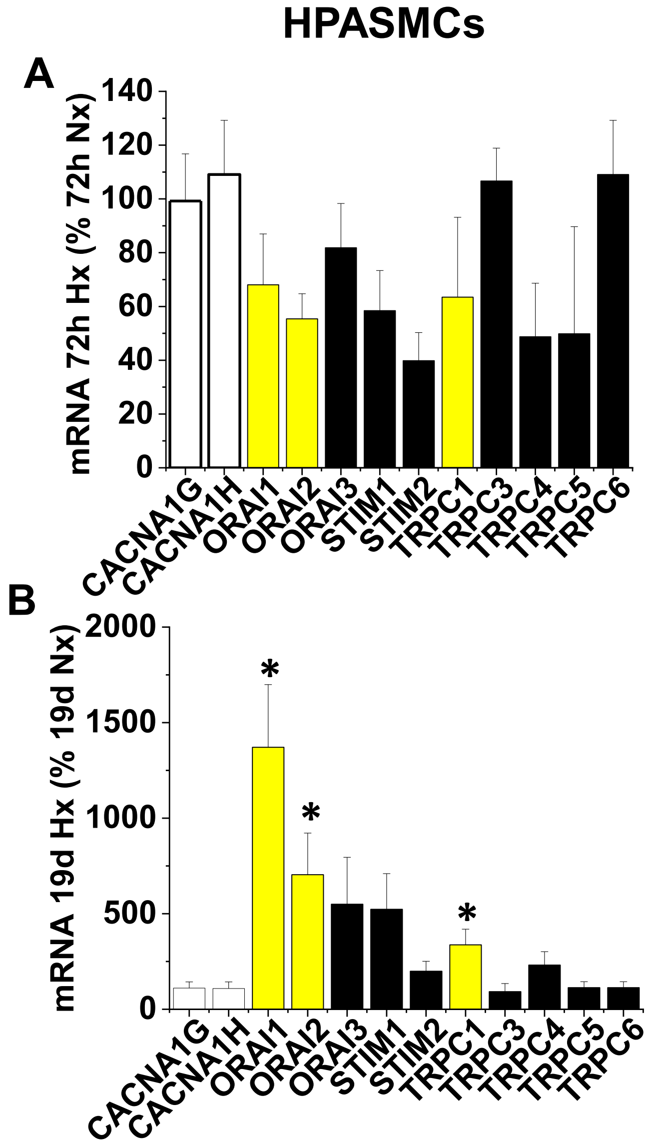

Figure 4.8. qPCR shows significant upregulation of Orai1, Orai2 and TRPC1 mRNA in HPASMCs cultured in hypoxia for 19 days, and no significant change in Ca$_v$3.1 or Ca$_v$3.2 mRNA at either time point.

All genes were screened in triplicate and mean Ct calculated. Three independent experiments (n=3) were performed. Ca^{2+} channel gene mRNA abundance in hypoxia at 72 hours (A) and 19 days (B) are expressed as a percentage of mRNA expression in normoxia. Data were analysed via the comparative Ct ($2^{-\Delta\Delta Ct}$) method. For each independent experiment, the mean Ct of each gene was normalised to the mean Ct of *B2M* (ΔCt). Cells cultured in normoxia were the control to which cells cultured in hypoxia (experimental condition) were compared (ΔΔCt). As gene abundance halves, the Ct value increases by one. This is a logarithm base 2 relationship analysed by $2^{-\Delta\Delta Ct}$ to calculate expression fold change and converted to a percentage relative to normoxia. mRNA expression for each gene was compared between conditions using a two-tailed t-test. Each time point was analysed independently. * = $p<0.05$.

4.2.3 Off-target effects of T-type Ca^{2+} channel inhibitors at Orai1 and TRPC1/4

Mibefradil, NNC55-0396 and TTA-A2 were tested for off-target effects on Orai1-mediated SOCE (in WT HEK293 cells, since they do not natively express T-type Ca^{2+} channels) or TRPC1-mediated Ca^{2+} entry. Since TRPC1 is unlikely to be functional alone (Beech et al., 2003) but rather forms heteromultimers with other TRPC isoforms, tetracycline-inducible HEK293 cells stably overexpressing TRPC heteromultimers were used in this research. Specifically, TRPC4 was the second most highly upregulated TRPC gene after TRPC1 (Figure 4.8) in HPASMCs cultured in hypoxia. Thus, TRPC1/4 heteromultimers were used.

Ca^{2+} microfluorimetry demonstrated that mibefradil (Figure 4.9, A) and NNC55-0396 (Figure 4.10, A) significantly reduce TG-induced SOCE in a dose-dependent manner in WT HEK293 cells (B) with IC_{50} values of 10.38 µM (Figure 4.9, C) and 10.21 µM (Figure 4.10, C), respectively.

Thus, two commonly used T-type Ca^{2+} channel inhibitors, mibefradil and NNC55-0396, have off-target effect on SOCE, which is primary underpinned by Orai1. This effect occurs even in the absence of T-type Ca^{2+} channel expression. This dose-dependent inhibition of SOCE by mibefradil and NNC55-0396 further supports the poor selectivity of these widely used T-type Ca^{2+} channel inhibitors.

Although TTA-A2 appears to increase Orai1-mediated SOCE in the representative trace (Figure 4.11, B), this response was variable between biological replicates. Overall, according to Figure 4.11 (C), TTA-A2 did not significantly affect Orai1-mediated SOCE in WT HEK293 cells at biologically relevant concentrations up to 1000 nM.

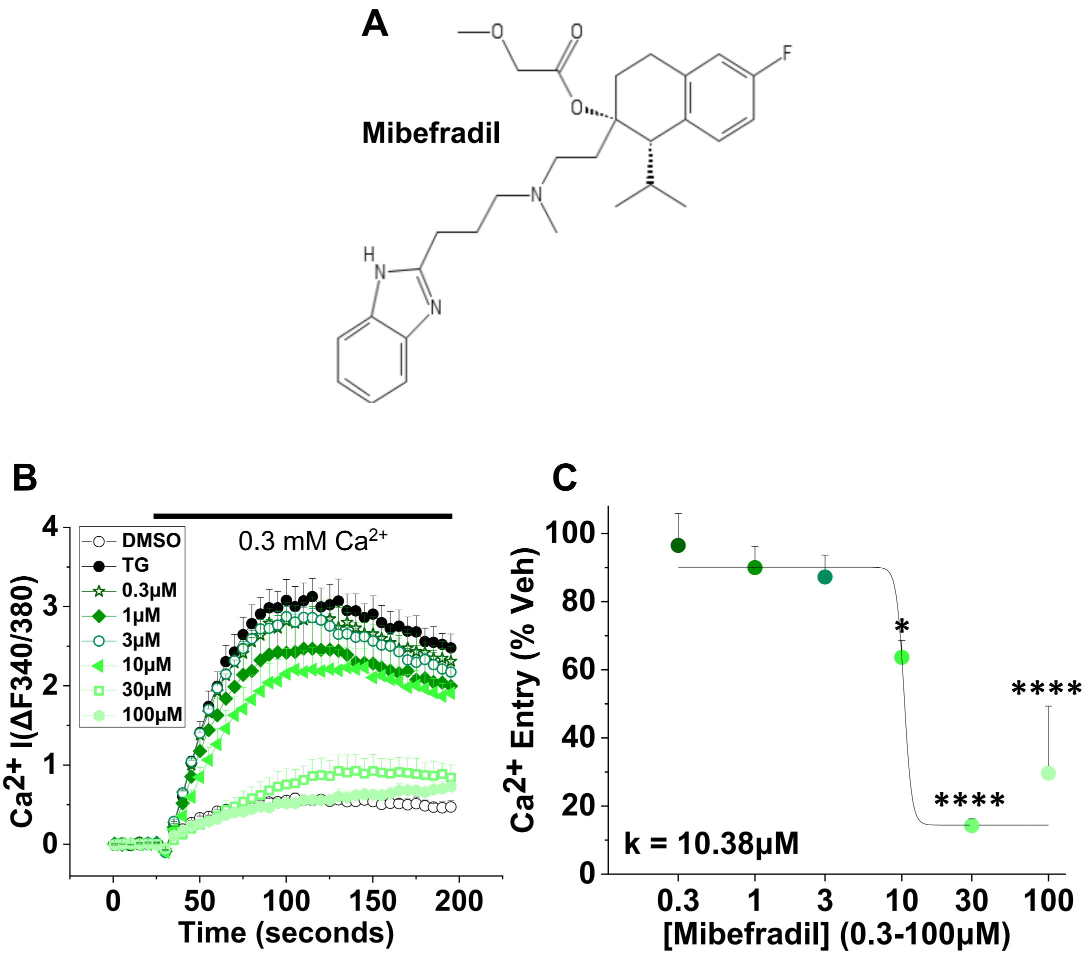

Figure 4.9. Mibefradil reduces TG-induced Orai1-mediated SOCE in a dose-dependent manner.

WT HEK293 cells were incubated with 2 μM Fura-2-AM, in SBS for one hour at 37°C before being pre-incubated with Ca^{2+}-free SBS and TG to deplete Ca^{2+} stores. Cells were also incubated with varying concentrations of the VDCC channel inhibitor, mibefradil (A). Ca^{2+} add-back was performed to trigger the SOCE response. Six biological replicates were performed (n=6), and one representative biological replicate demonstrated (B). A sigmoidal dose-response curve (C) demonstrates an IC_{50} of 10.38 μM for mibefradil against SOCE in WT HEK293 cells. Data analysed using one-way ANOVA with Tukey's post-hoc analysis. * = $p<0.05$; **** = $p<0.0001$. (n=6/N=144). TG, thapsigargin; WT, wild type; SBS, standard bath solution; SOCE, store-operated Ca^{2+} entry, VDCC, voltage-dependent Ca^{2+} channel.

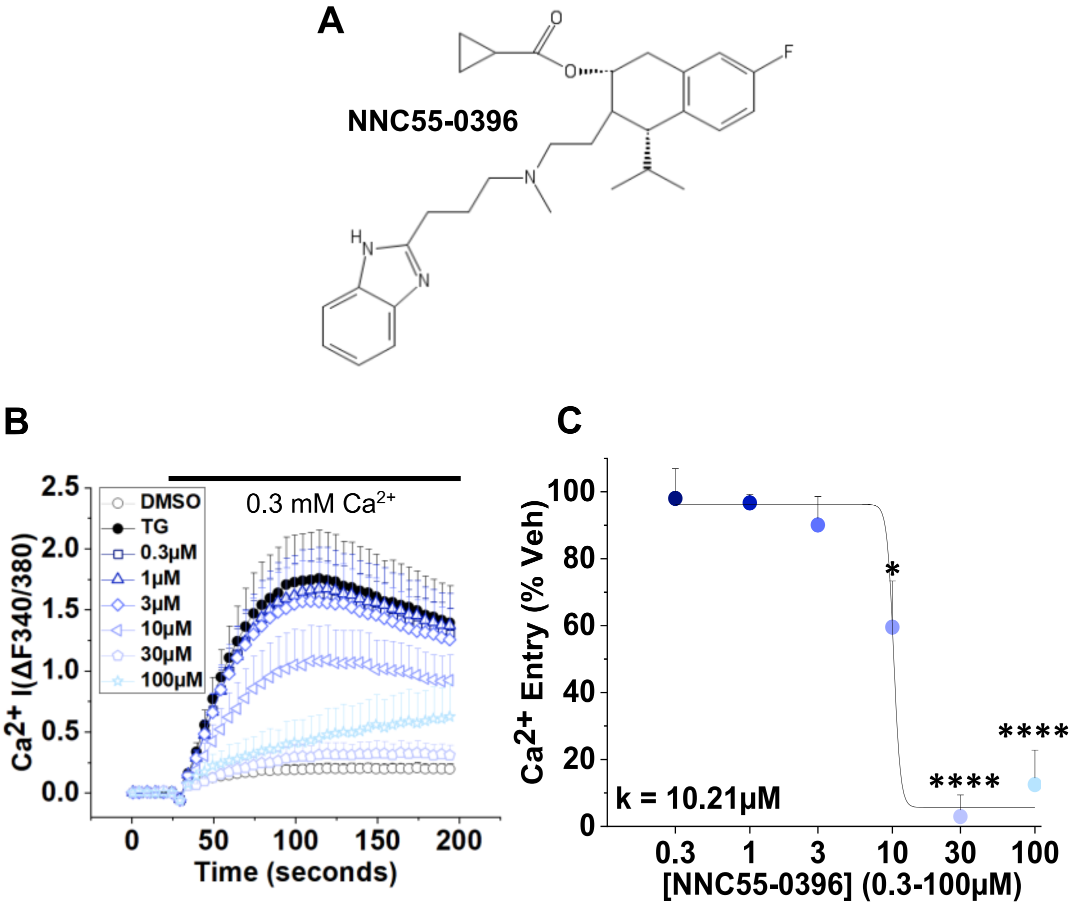

Figure 4.10. NNC55-0396 reduces TG-induced Orai1-mediated SOCE in a dose-dependent manner.

WT HEK293 cells were incubated with 2 μM Fura-2-AM, in SBS for one hour at 37ºC before being pre-incubated with Ca^{2+}-free SBS and TG to deplete Ca^{2+} stores. Cells were also incubated with varying concentrations of the VDCC channel inhibitor, NNC55-0396 (A). Ca^{2+} add-back was performed to trigger the SOCE response. Six biological replicates were performed (n=6), and one representative biological replicate demonstrated (B). A sigmoidal dose-response curve (C) demonstrates an IC_{50} of 10.21 μM for NNC55-0396 against SOCE in WT HEK293 cells. Data analysed using one-way ANOVA with Tukey's post-hoc analysis. * = p<0.05; **** = p<0.0001. (n=6/N=144). TG, thapsigargin; WT, wild type; SBS, standard bath solution; SOCE, store-operated Ca^{2+} entry.

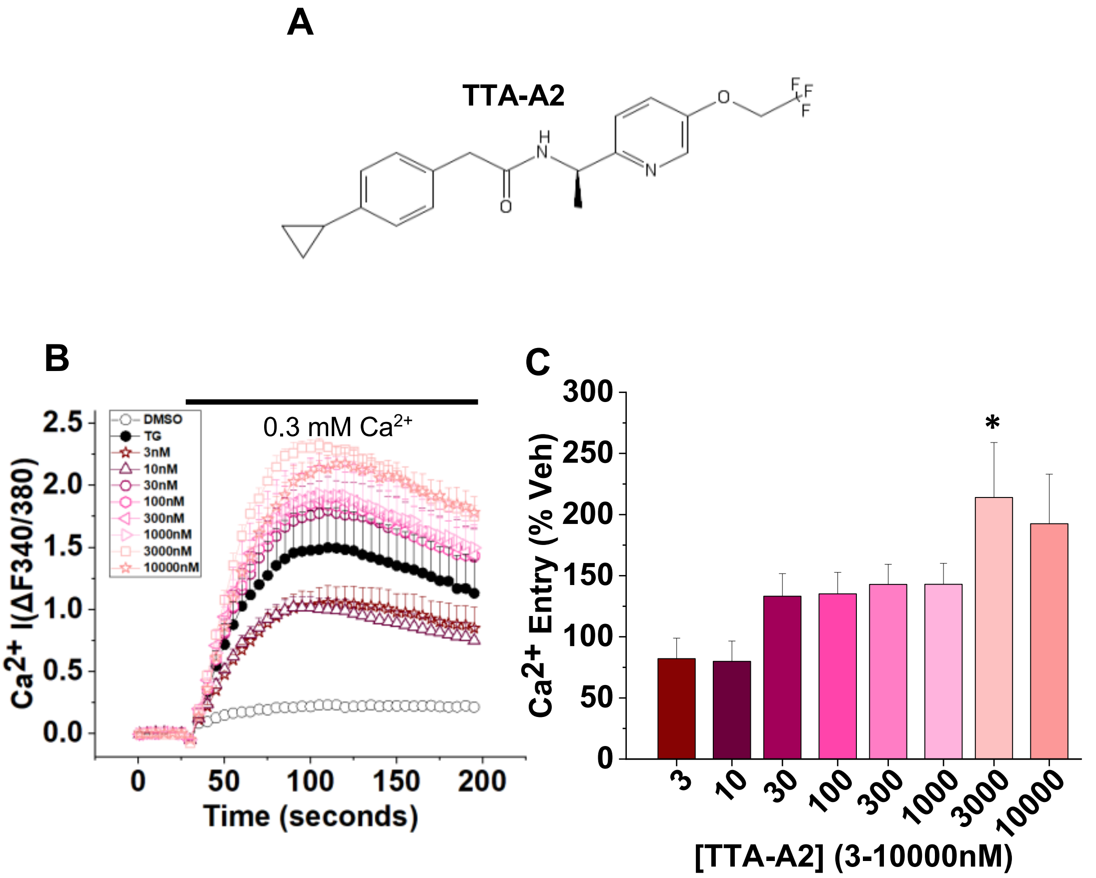

Figure 4.11. TTA-A2 does not significantly affect TG-induced Orai1-mediated SOCE.

WT HEK293 cells were incubated with 2 µM Fura-2-AM, in SBS for one hour at 37°C before being pre-incubated with Ca^{2+}-free SBS and TG to deplete Ca^{2+} stores. Cells were also incubated with varying concentrations of the VDCC inhibitor, TTA-A2 (A). Ca^{2+} add-back was performed to trigger the SOCE response. Four biological replicates were performed (n=4), and one representative biological replicate demonstrated (B). A bar graph (C) demonstrates no significant change in SOCE in WT HEK293 cells at any concentration except 3000 nM. Data analysed using one-way ANOVA with Tukey's post-hoc analysis. * = $p<0.05$. (n=4/N=120). TG, thapsigargin; WT, wild type; SBS, standard bath solution; SOCE, store-operated Ca^{2+} entry.

Ca^{2+} microfluorimetry was also performed to test for off-target effects of mibefradil, NNC55-0396 and TTA-A2 on EA-induced TRPC1/4-mediated Ca^{2+} entry.

Figure 4.12 demonstrates the effect of a range of concentrations of mibefradil on EA-induced TRPC1/4-mediated Ca^{2+} in tetracycline-inducible stably expressing TRPC1/4 HEK293 cells pre-treated in Ca^{2+}-containing SBS. No significant change in EA-induced TRPC1/4-mediated Ca^{2+} entry was observed in the presence of mibefradil at any concentration tested, ruling out off-target effects of mibefradil on TRPC1/4.

The response of TRPC1/4 HEK293 cells to NNC55-0396 is very similar to that of mibefradil, which is expected given that it is a structural analogue. Although Figure 4.13 demonstrates a reduction in TRPC1/4-mediated Ca^{2+} entry in the presence of 100 µM NNC55-0396, the graph only shows the zeroed baseline data. The absolute baseline data (not shown) demonstrates an elevated baseline shift in the presence of 100 µM NNC55-0396. Similarly, in the presence of 100 µM NNC55-0396, the baseline Ca^{2+} amplitude does not change upon addition of EA despite EA being a TRPC1/4 activator, indicating that the Fura-2-AM signal is unreliable in the presence of 100 µM NNC55-0396. At all other concentrations, NNC55-0396 had no effect on TRPC1/4-mediated Ca^{2+} entry.

Figure 4.14 demonstrates that TTA-A2 had no effect on TRPC1/4-mediated Ca^{2+} entry at any concentration tested.

Collectively, Figure 4.12 and Figure 4.13 demonstrate off-target modulation of Orai1-mediated SOCE by mibefradil and NNC55-0396. TTA-A2 does not demonstrate off-target modulation of Orai1-mediated SOCE. Mibefradil, NNC55-0396 and TTA-A2 had no-off target effects on TRPC1/4-mediated Ca^{2+} entry.

Therefore, TTA-A2 appeared to be the only selective T-type Ca^{2+} channel inhibitor. However, since hypoxia-induced T-type Ca^{2+} channel upregulation was not observed in this thesis, it was not logical to continue to progress the study using a T-type Ca^{2+} channel inhibition approach. Instead, we decided to shift the focus of the investigation to Orai1, which was markedly upregulated in hypoxic conditions and was an off-target effector of two of the T-type Ca^{2+} channel blockers used.

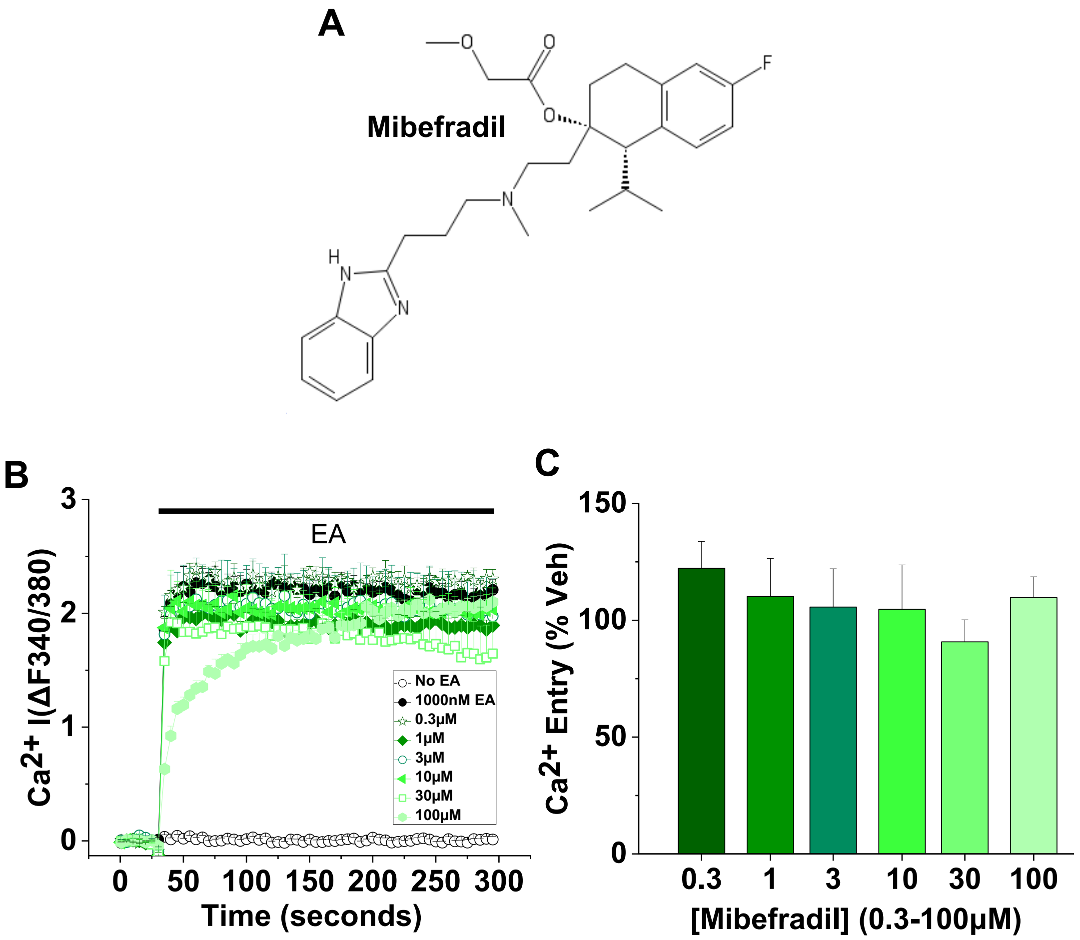

Figure 4.12. Mibefradil has no off-target effect on EA-induced TRPC1/4-dependent Ca^{2+} entry.

Tetracycline-inducible HEK293 cells stably overexpressing TRPC1/4 were incubated with 2 µM Fura-2-AM, in SBS for one hour at 37ºC before being pre-incubated with SBS and varying concentrations of the VDCC inhibitor, mibefradil (A). At the start of the Ca^{2+} measurement, EA was applied to trigger the TRPC1/4-dependent Ca^{2+} response. Four biological replicates were performed (n=4), and one representative biological replicate demonstrated (B). A bar graph (C) demonstrates no significant reduction in TRPC1/4-dependent Ca^{2+} entry by mibefradil. Data analysed using one-way ANOVA with Tukey’s post-hoc analysis. (n=4/N=96). SBS, standard bath solution; EA, englerin A.

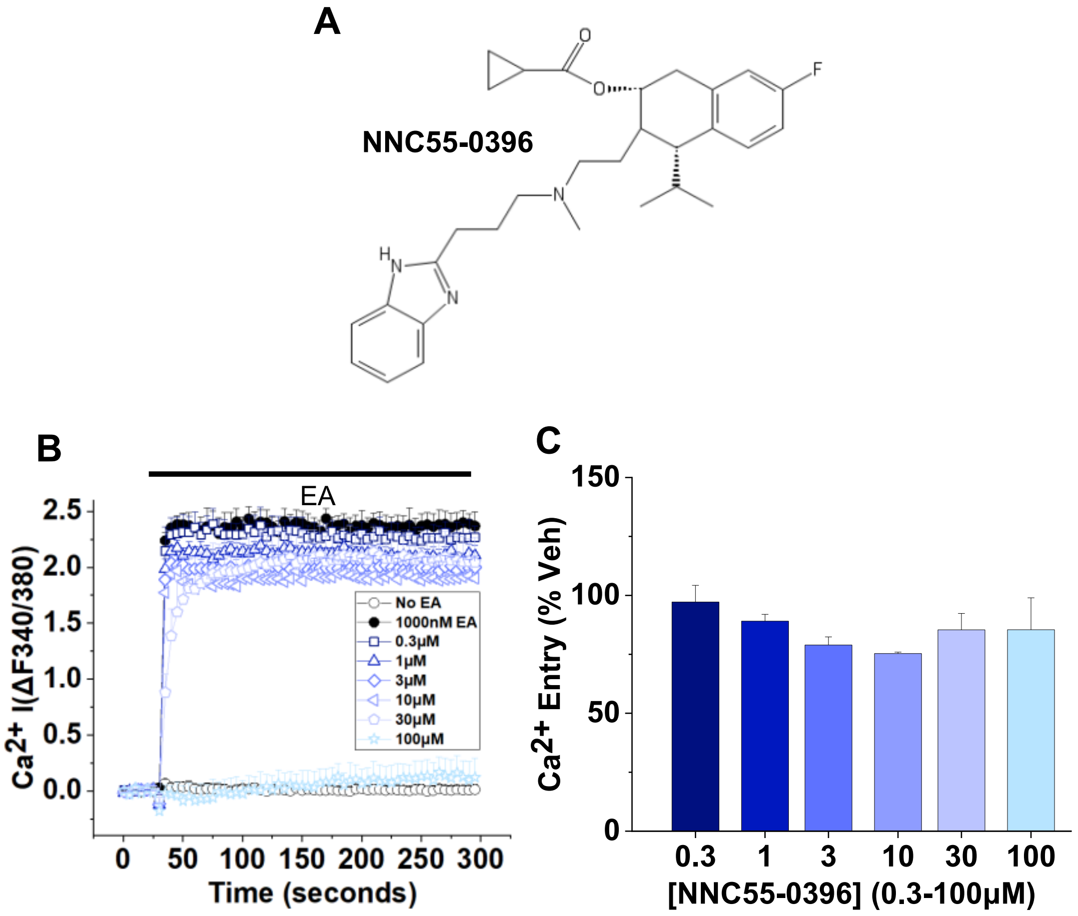

Figure 4.13. NNC55-0396 has no off-target effect on EA-induced TRPC1/4-mediated Ca^{2+} entry.

Tetracycline-inducible HEK293 cells stably overexpressing TRPC1/4 were incubated with 2 µM Fura-2-AM, in SBS for one hour at 37ºC before being pre-incubated with SBS and varying concentrations of the VDCC inhibitor, NNC55-0396 (A). At the start of the Ca^{2+} measurement, EA was applied to trigger the TRPC1/4-dependent Ca^{2+} response. Three biological replicates were performed (n=3), and one representative biological replicate demonstrated (B). A bar graph (C) demonstrates no significant reduction in TRPC1/4-dependent Ca^{2+} entry by NNC55-0396. Data analysed using one-way ANOVA with Tukey's post-hoc analysis. (n=3/N=72). SBS, standard bath solution; EA, englerin A.

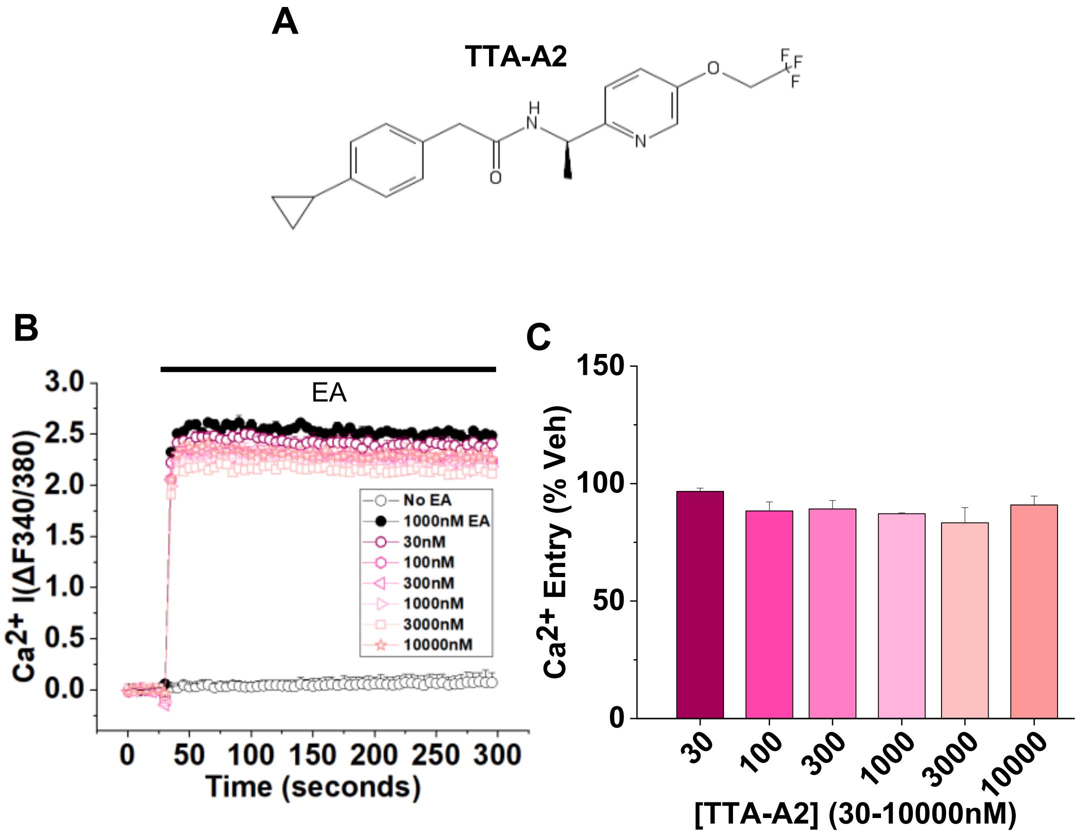

Figure 4.14. TTA-A2 has no off-target effect on EA-induced TRPC1/4-dependent Ca^{2+} entry.

Tetracycline-inducible HEK293 cells stably overexpressing TRPC1/4 were incubated with 2 µM Fura-2-AM, in SBS for one hour at 37°C before being pre-incubated with SBS and varying concentrations of the VDCC inhibitor, TTA-A2 (A). At the start of the Ca^{2+} measurement, EA was also applied to trigger the TRPC1/4-dependent Ca^{2+} response. Four biological replicates were performed (n=4), and one representative biological replicate demonstrated (B). A bar graph (C) demonstrates no significant reduction in TRPC1/4-dependent Ca^{2+} entry by TTA-A2. Data analysed using one-way ANOVA with Tukey's post-hoc analysis. (n=4/N=7=96). SBS, standard bath solution; EA, englerin A.

4.2.4 Confirming the selectivity of JPIII

To begin this investigation, the widely published potent and highly selective Orai1 inhibitor, Synta66, was tested by Ca^{2+} microfluorimetry using the TG-induced SOCE protocol to reproduce published IC_{50} values. Figure 4.15 demonstrates that Synta66 reduces TG-induced SOCE in a dose dependent manner with an IC_{50} of 12.08 nM. This is in keeping with other lab members' data in the same experimental conditions.

Figure 4.16 demonstrates the effect of JPIII on TG-induced SOCE. JPIII is a novel Synta66 analogue developed in Leeds with enhanced solubility to allow functional cell experiments and *in-vivo* dosing. As expected, JPIII was less potent than Synta66, inhibiting TG-induced SOCE with an IC_{50} of 212.46 nM. This is comparable to the IC_{50} results obtained by other lab members.

With the help of Dr Jian Shi, patch clamp electrophysiology experiments were performed to test JPIII against the CRAC current (Figure 4.17). After WT HEK293 cells were pre-treated with 1 µM TG, a 100 ms voltage ramp protocol from -100 to 100 mV was used to induce Orai1-mediated SOCE (Figure 4.17, B). Using the same stimulus, various concentrations of JPIII (Figure 4.17, A) were applied. The inhibitory effect of JPIII on Orai1-mediated SOCE was calculated using the values at -100 mV. Electrophysiology confirmed that JPIII is a potent inhibitor of Orai1 channels with an IC_{50} of 244 nM (Figure 4.17, C).

The selectivity of JPIII for the Orai1 channel has been stringently investigated. A CEREP Safety-44 selectivity screen and associated heat map (Figure 4.18) produced by the commercial research organisation, Eurofins CEREP-Panlabs, demonstrate that JPIII at concentrations up to 10 µM has no significant off-target effects on 42 alternative targets. Significant inhibition of control specific binding was observed against two targets only, 5-HT_{2B} (serotonin receptor) and

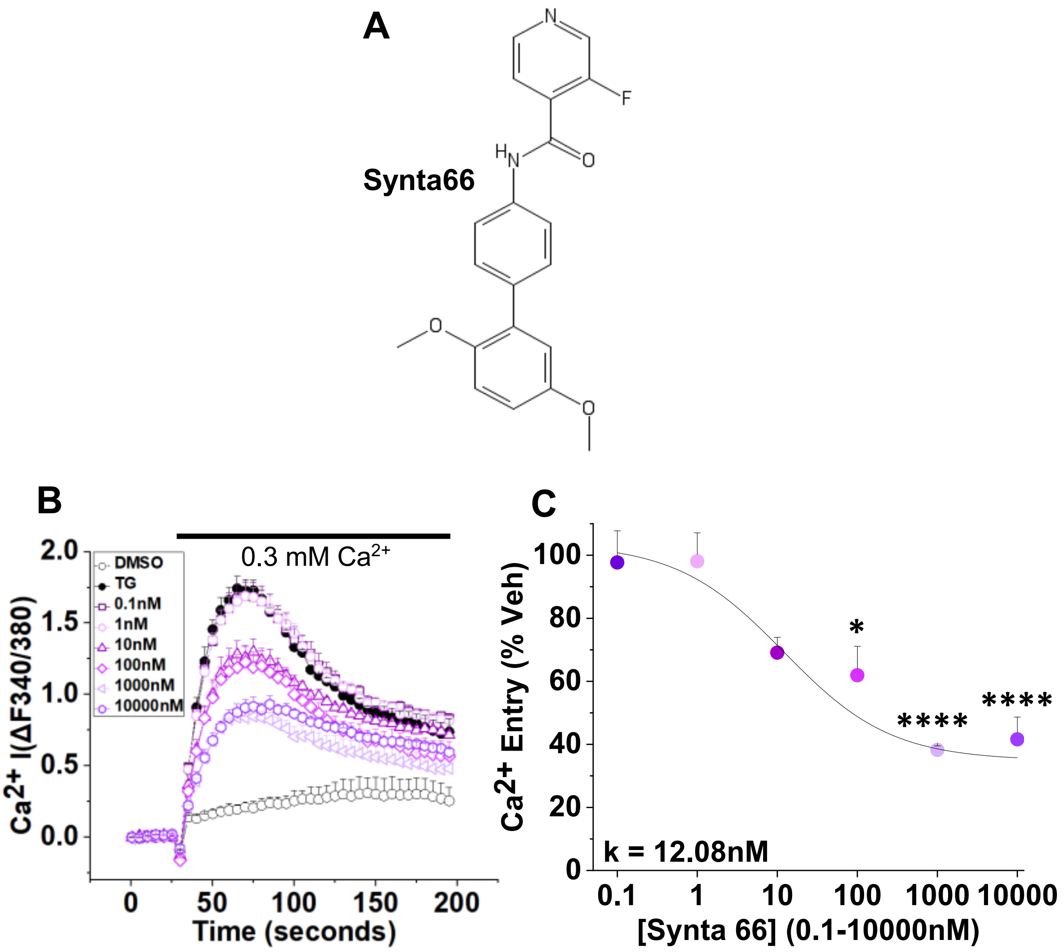

Figure 4.15. Synta66 reduces Orai1-mediated TG-induced SOCE in a dose-dependent manner.

WT HEK293 cells were incubated with 2 μM Fura-2-AM, in SBS for one hour at 37ºC before being pre-incubated with Ca^{2+}-free SBS and TG to deplete Ca^{2+} stores. Cells were also incubated with varying concentrations of the SOCE inhibitor, Synta66 (A). Ca^{2+} add-back was performed to trigger the SOCE response. Three biological replicates were performed (n=3) and one representative biological replicate demonstrated (B). A sigmoidal dose-response curve (C) demonstrates an IC_{50} of 12.08 nM for Synta66 against SOCE in WT HEK293 cells. Data analysed using one-way ANOVA with Tukey's post-hoc analysis. (n=3/N=72). * = p<0.05; **** = p<0.0001. TG, thapsigargin; WT, wild type; SBS, standard bath solution; SOCE, store-operated Ca^{2+} entry.

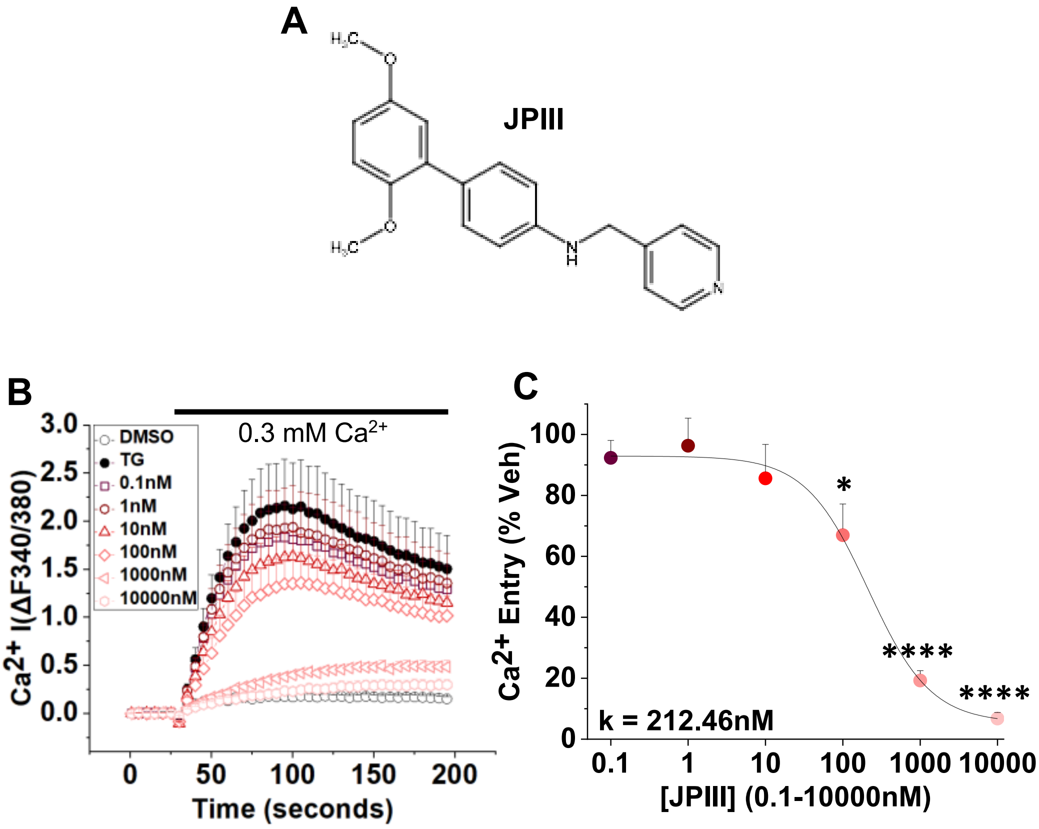

Figure 4.16. JPIII reduces Orai1-mediated TG-induced SOCE in a dose-dependent manner.

WT HEK293 cells were incubated with 2 µM Fura-2-AM, in SBS for one hour at 37ºC before being pre-incubated with Ca^{2+}-free SBS and TG to deplete Ca^{2+} stores. Cells were also incubated with varying concentrations of the SOCE inhibitor, JPIII. Ca^{2+} add-back was performed to trigger the SOCE response. Four biological replicates were performed (n=4) and one representative biological replicate demonstrated (B). A sigmoidal dose-response curve (C) demonstrates an IC_{50} of 212.46 nM for JPIII against SOCE in WT HEK293 cells. Data analysed using one-way ANOVA with Tukey's post-hoc analysis. (n=4/N=96). * = p<0.05; **** = p<0.0001. TG, thapsigargin; WT, wild type; SBS, standard bath solution; SOCE, store-operated Ca^{2+} entry.

CB_2 (cannabinoid receptor), at values of 79.2% and 63.6%, respectively. Although inhibition of control specific binding at values greater than 50% is considered a potential non-specific effect, the binding affinity at these targets was low. Thus, at the functional JPIII IC_{50} for Orai1, it is unlikely that these targets would be impacted. Important to highlight is the observation that JPIII demonstrated inhibition of control specific binding of 49.3% against hERG. hERG is known to be particularly sensitive to drug binding and inhibition of the channel can cause drug-induced long QT syndrome. Because control specific binding was below 50%, this was not classed as a potential off-target effect; however, close attention was paid when employing JPIII in the *in-vivo* model presented in Chapter 5.

In addition to the CEREP Safety-44 selectivity screen, the Bailey and Beech labs have tested JPIII against a range of other Ca^{2+} channel targets at which JPIII has been inactive. T-type Ca^{2+} channels have never been tested. Therefore, patch clamp electrophysiology was carried out to investigate any off-target effects of JPIII on T-type Ca^{2+} channels (Figure 4.19). HEK293 cells stably overexpressing rat *CACNA1G* were used. Rat CACNA1G is 93% homologous to human CACNA1G (Toyota et al., 1999). Immunocytochemistry was used to confirm positive expression of $Ca_v3.1$ in these HEK293 cells (Figure 4.20, A) before proceeding to carry out patch clamp studies. An overexpression system for $Ca_v3.2$ was unavailable for the purpose of this research.

Using patch clamp electrophysiology, T-type Ca^{2+} channels were activated by depolarising voltages from a holding potential of -80 mV (Figure 4.19, B). Subsequently, JPIII at various concentrations from 10 nM to 10 μM was applied.

JPIII did not have any off-target effects on T-type Ca^{2+} channel current at any concentration tested (Figure 4.19, B and C).

Collectively, these data confirm that JPIII is a highly selective Orai1 inhibitor. Combined with the marked upregulation of Orai1 observed in hypoxia, and previous evidence associating Orai1 with hypoxia-induced pulmonary VSMC proliferation, this research proceeded to use the novel, selective Orai1 inhibitor, JPIII, to examine the anti-proliferative effects of Orai1 inhibition in an appropriate *in-vitro* model of hypoxia-induced VSMC proliferation.

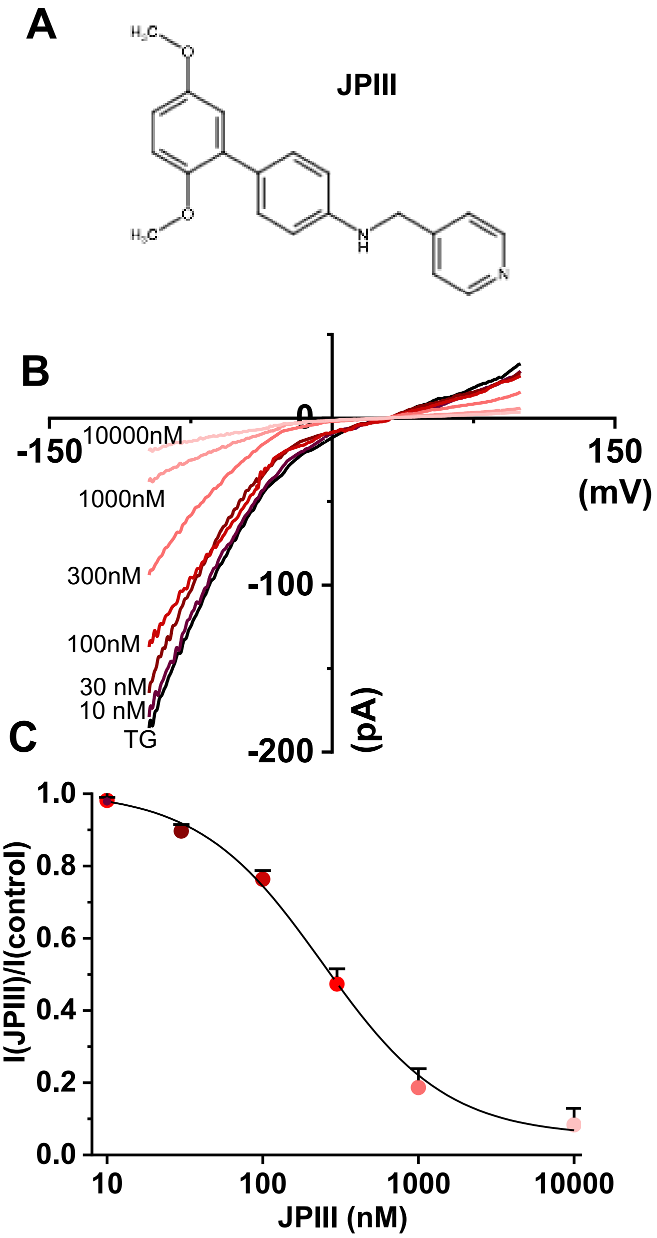

Figure 4.17. JPIII inhibits Orai1-mediated SOCE in a dose-dependent manner.

Patch clamp electrophysiology was carried out to demonstrate dose-dependent inhibition of SOCE by JPIII in WT HEK293 cells. Orai1 currents were significantly inhibited by JPIII. The structure of JPIII is shown (A). Example traces show that JPIII inhibits Orai1 currents induced by 1 μM TG (B). A dose-response curve shows that the IC_{50} of JPIII for SOCE is 244 nM (n=6). This work is credited to Dr Jian Shi. SOCE, store-operated Ca^{2+} entry; WT, wild type; TG, thapsigargin.

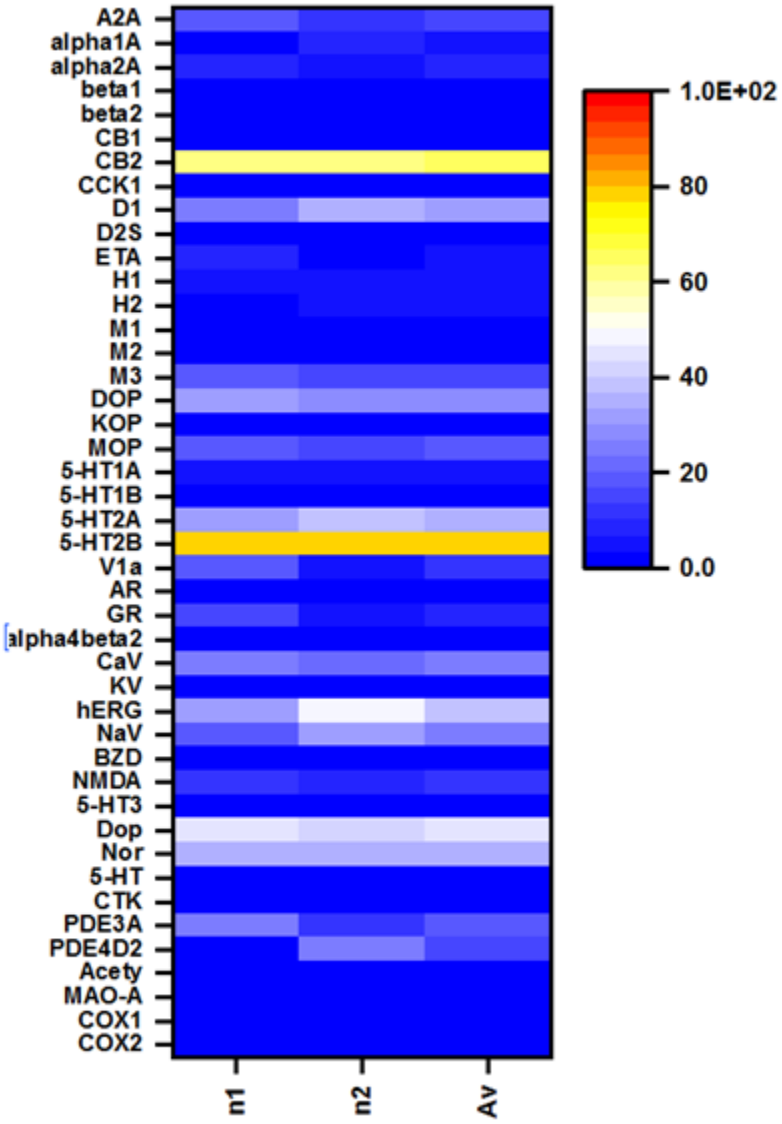

Figure 4.18. Minimal off-target effects of JPIII were observed when tested against 44 other targets.

The final report from a CEREP Safety-44 selectivity screen produced by the commercial research organisation, Eurofins CEREP-Panlabs, on 19th April 2016 (study number: 100027494) demonstrates that JPIII at concentrations up to 10 μM had no significant off-target effects on 42 alternative targets that were recommended by four major pharmaceutical companies (Bowes et al., 2012). Credit for this data goes to Eurofins CEREP-Panlabs and appropriate permission was sought to present the data.

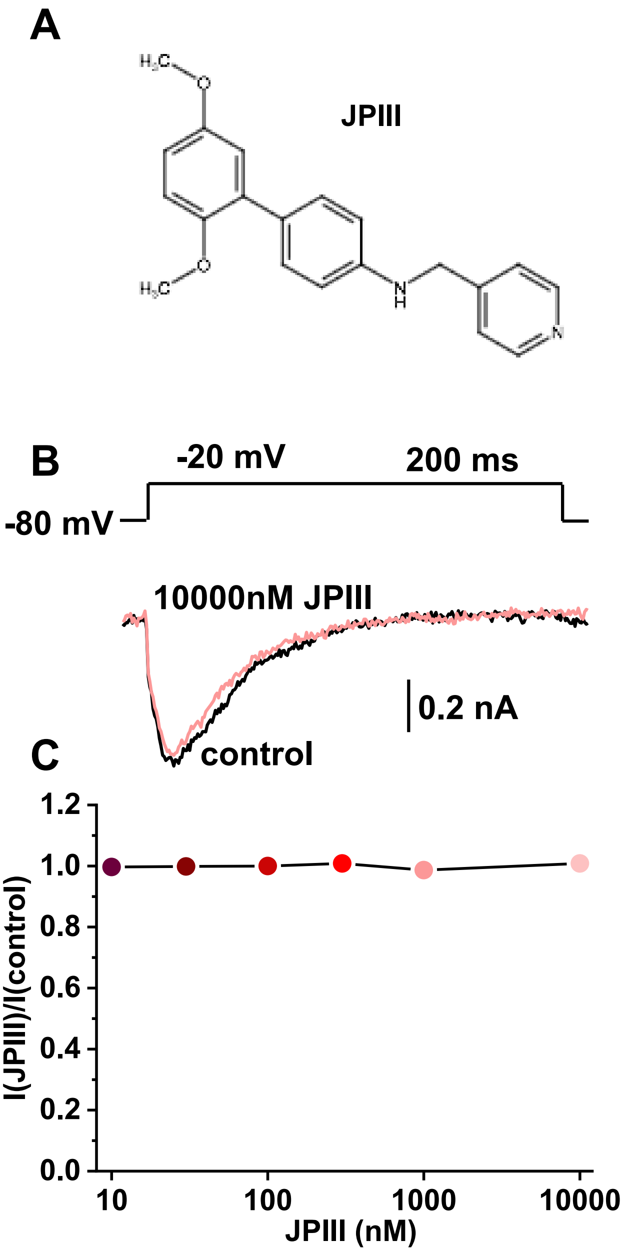

Figure 4.19. JPIII has no off-target effects on T-type Ca^{2+} current.

T-type Ca^{2+} channel activity is not affected by JPIII. Example traces show that T-type Ca^{2+} currents that are activated at -20 mV from a holding potential of -80 mV were unaffected even by 10000 nM (10 μM) JPIII (B). Statistics confirm that T-type Ca^{2+} channels are insensitive to all JPIII concentrations tested (C). (n=6).

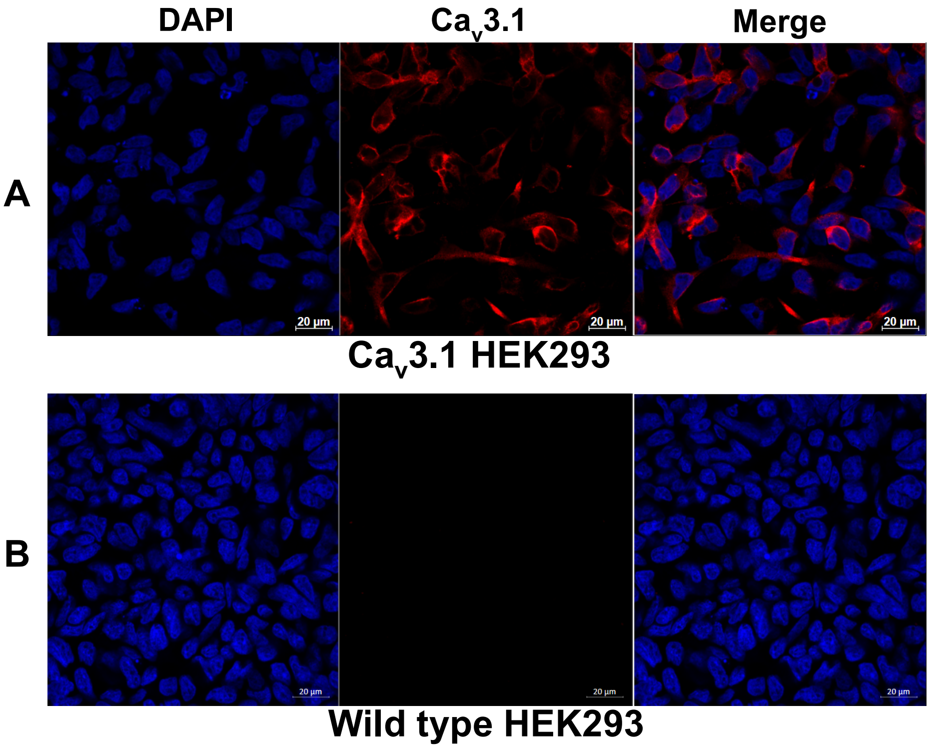

Figure 4.20. Immunocytochemistry confirms positive Ca$_v$3.1 expression in HEK293 cells stably overexpressing rat *CACNA1G*.

Immunocytochemistry was carried out to confirm positive staining in HEK293 cells stably overexpressing rat *CACNA1G* (A) and negative staining in WT HEK293 cells (B) using the Ca$_v$3.1 primary antibody (Proteintech, Chicago, USA). Merged images are represented in each panel. Images were obtained with an inverted confocal laser scanning microscope (LSM700). Scale bar = 20 µm.

4.2.5 The anti-proliferative effect of Orai1 inhibition in an *in-vitro* model of hypoxia-induced pulmonary VSMC proliferation

JPIII was used to study the anti-proliferative effects of Orai1 inhibition in an appropriate *in-vitro* model of hypoxia-induced VSMC proliferation. HPASMCs were cultured in normoxia or hypoxia for 72 hours (Figure 4.22) or 19 days (Figure 4.23) prior to a three-day dose response investigation.

In HPASMCs cultured in normoxia for 72 hours prior to a three-day dose response investigation (Figure 4.22, B and C), cell number was significantly reduced by 30 µM JPIII (2055 ± 45) when compared to HPASMCs exposed to SmGM™-2 only (3298 ± 144). The anti-proliferative effect of JPIII was also significant on day 2 of the assay, where the degree of HPASMC proliferation was significantly reduced by 30 µM JPIII (2126 ± 39) when compared to cells exposed to SmGM™-2 only (2941 ± 132).

In HPASMCs cultured in hypoxia for 72 hours (Figure 4.22, C and D) prior to a three-day dose response investigation, cell number was reduced by 30 µM JPIII (1541 ± 68) when compared to HPASMCs exposed to SmGM™-2 only (1931 ± 84), although this was non-significant.

In HPASMCs cultured in normoxia for 19 days (Figure 4.23, B and C) prior to a three-day dose response investigation, cell number was unaffected by 30 µM JPIII (2618 ± 21) when compared to cells exposed to SmGM™-2 only (2644 ± 18).

Conversely, in HPASMCs cultured in hypoxia for 19 days (Figure 4.23, D and E), 30 µM JPIII significantly reduced cell number (957 ± 48) when compared to HPASMCs exposed to SmGM™-2 only (1279 ± 12). The anti-proliferative effect of 30 µM JPIII (634 ± 17) was also significant at day 2 of the assay when compared to cell number in the presence of SmGM™-2 only (822 ± 15).

In keeping with previous proliferation studies, a negative control (HPASMCs exposed to 0.5% FBS-containing medium) was employed to keep the cells alive and to halt proliferation. These data have been excluded from Figure 4.22 and Figure 4.23 to maintain graph simplicity. Positive control data (HPASMCs exposed to SmGM™-2 only) are shown since these data were used to identity a significant reduction in proliferation in response to JPIII.

Collectively, these data demonstrate that the anti-proliferative effects of JPIII were more pronounced in HPASMCs cultured in hypoxia for 19 days compared to those cultured in normoxia for an equivalent duration. The increased sensitivity to the anti-proliferative effects of JPIII in HPASMCs cultured in hypoxia 19 days exist in parallel with marked upregulation of Orai1 mRNA at an equivalent time point, justifying Orai1 as an interesting anti-proliferative target in hypoxia-induced VSMC proliferation and CH-induced PH.

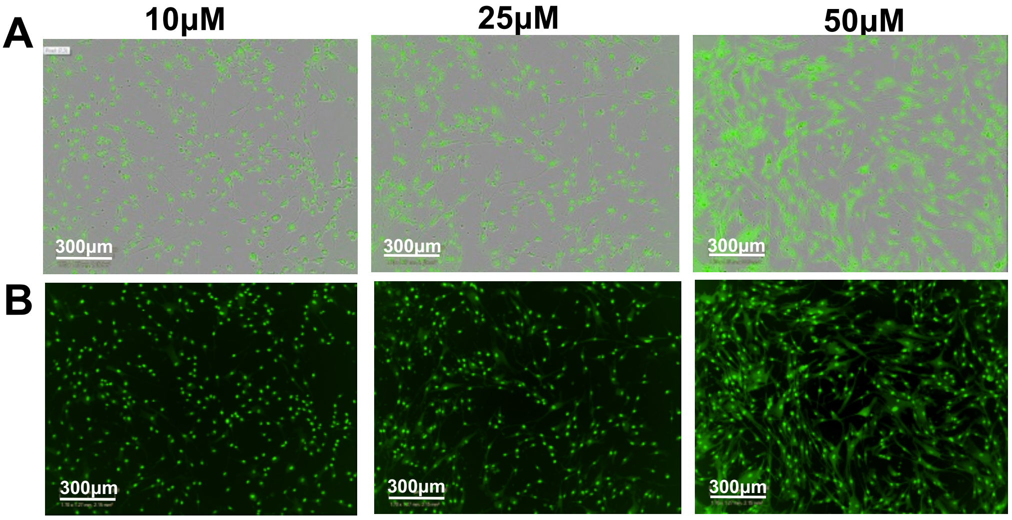

Figure 4.21. 10μM Vybrant® DyeCycle™ Green Stain is optimal for nuclear staining and cell counting.

Vybrant DyeCycle Green Stain is a cell-permeable dye that binds double-stranded DNA, allowing it to emit a fluorescent signal. A concentration of 10 μM was optimal to achieve a homogeneous staining pattern and to minimise background fluorescence as demonstrated in phase contrast (A) and in the green fluorescent channel (B).

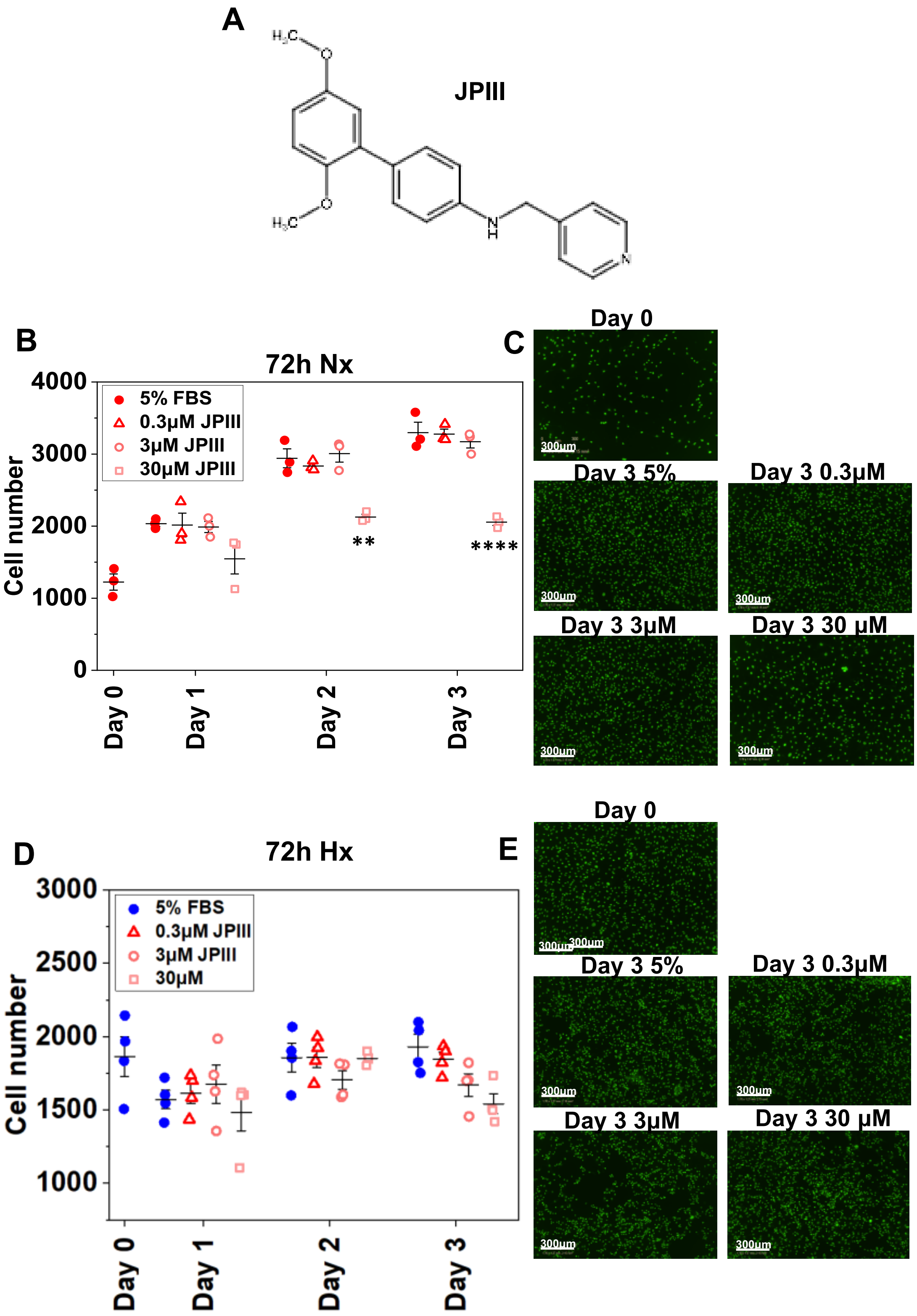

Figure 4.22. JPIII significantly reduces proliferation of HPASMCs cultured in normoxia 72 hours.

In a three-day assay, 30 μM JPIII (A) reduces proliferation of HPASMCs cultured in normoxia (B and C) and hypoxia (D and E) for 72 hours, although this effect was only significant in normoxia. Mean ± SEM are plotted. Data analysed using two-way ANOVA with Tukey's post-hoc analysis. n=3 normoxia; n=5 hypoxia. ** = *p*<0.01; **** = *p*<0.0001. Asterisk indicates significant difference in HPASMC proliferation when compared to proliferation in SmGM^{TM}-2 only on respective day.

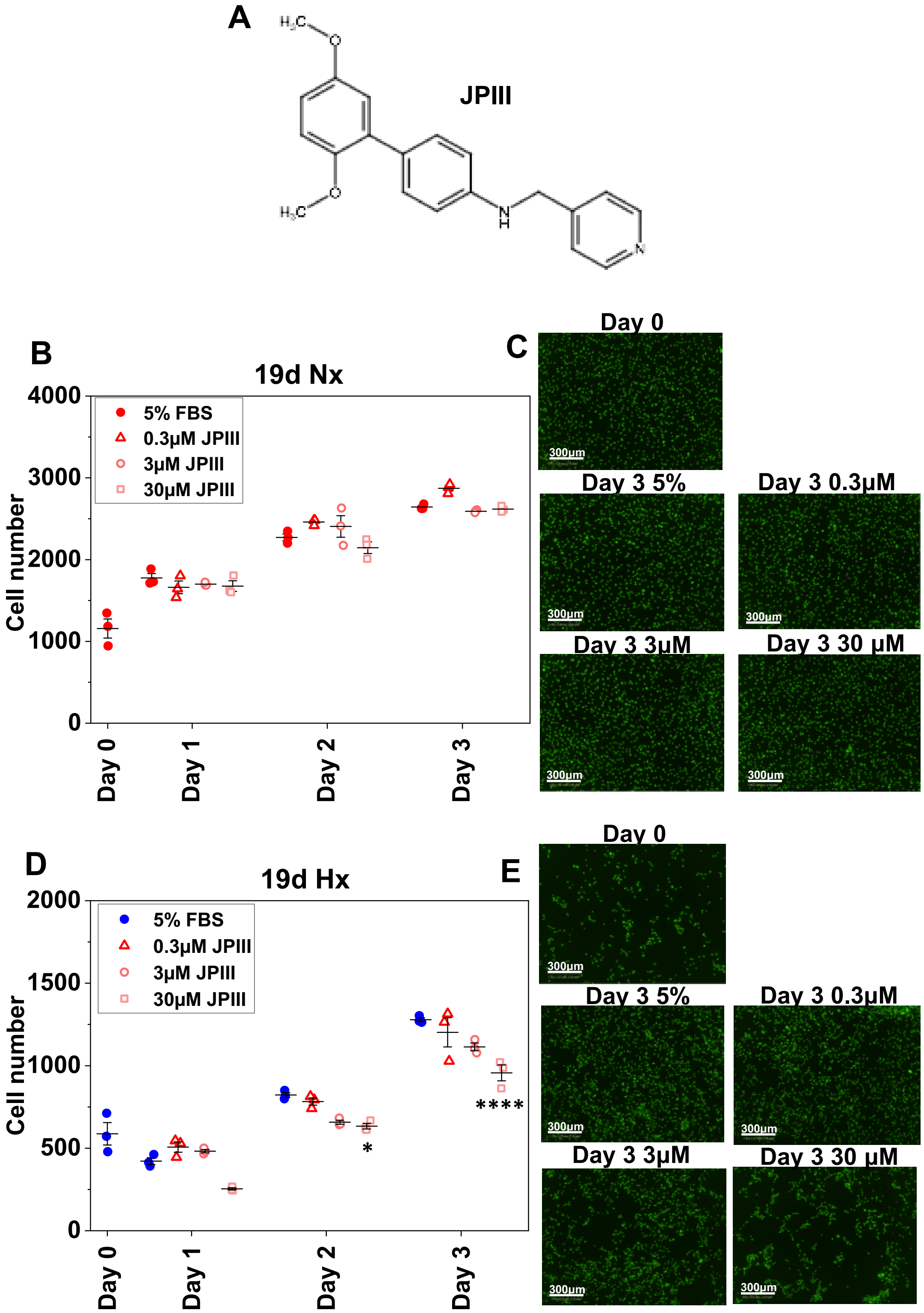

Figure 4.23. JPIII significantly reduces proliferation of HPASMCs cultured in hypoxia for 19 days.

In a three-day assay, 30 µM JPIII (A) reduces proliferation of HPASMCs cultured in hypoxia (D and E) for 19 days. JPIII did not reduce proliferation of HPASMCs cultured in normoxia (B and C) for 19 days. Mean ± SEM are plotted. Data analysed using two-way ANOVA with Tukey's post-hoc analysis. n=3 normoxia and hypoxia. * = $p<0.05$; **** = $p<0.0001$. Asterisk indicates significant difference in HPASMC proliferation when compared to proliferation in SmGM™-2 only on respective day.

4.3 Summary of aims and key findings

The initial aims of this study were to: 1) examine the anti-proliferative effects of widely used T-type Ca^{2+} channel inhibitors in an *in-vitro* model of hypoxia-induced VSMC proliferation; 2) confirm lack of off-target modulation on other Ca^{2+} entry pathways associated with hypoxia-induced VSMC proliferation, including Orai1-mediated SOCE and TRPC1/4-mediated Ca^{2+} entry; and 3) clarify the increase in T-type Ca^{2+} channel expression specifically in the context of hypoxia-induced VSMC proliferation.

First and foremost, it is important to highlight that the sample sizes used in this chapter were small due to time limitations, which led to large standard errors in certain data sets. Despite this limitation, statistics allowed certain conclusions to be drawn from the data presented in this chapter.

The findings from this study demonstrate that in an *in-vitro* model of hypoxia-induced pulmonary VSMC proliferation, widely used T-type Ca^{2+} channel inhibitors, mibefradil, NNC55-0396 and TTA-A2 reduce HPASMC proliferation. A change in the sensitivity to the anti-proliferative effects of NNC55-0396 in hypoxic HPASMCs; combined with the observation that T-type Ca^{2+} channel mRNA was not upregulated in hypoxia, justified an investigation to test for off-target modulation of T-type Ca^{2+} channel inhibitors on other Ca^{2+} channel targets. In the future, it would be beneficial to screen for Ca^{2+} channel proteins using either immunocytochemistry or western blotting approaches. Despite attempts to measure the expression of $Ca_v3.1$ using western blot, the protein size (250 kDa) posed an issue, so no useful results were obtained. Orai1, being the primary focus of this study, was not screened at the protein level due to time limitations and the phenomenon that ion channel antibodies are poorly selective and produce multiple bands due to interactions with other ion channel targets with similar structural characteristics (Hutchings et al., 2019). Screening for Ca^{2+} channel proteins would add value to the mRNA expression data presented in this chapter.

Despite this limitation, no upregulation in T-type Ca^{2+} channel mRNA combined with lack of highly selective inhibitors and complete lack of T-type Ca^{2+} channel blockers in the clinic, limit the potential of these channels as anti-proliferative targets in CH-induced PH. Thus, other Ca^{2+} channel targets that exhibited marked mRNA upregulation, such as Orai1 and TRPC1/4, were investigated.

Ca^{2+} microfluorimetry demonstrated off-target modulation of Orai1-mediated SOCE, but not TRPC1/4-mediated Ca^{2+} entry by mibefradil and its structural analogue, NNC55-0396, raising the possibility that the anti-proliferative effects of these inhibitors could be modulated by Orai1.

Although the IC_{50} of mibefradil and NNC55-0396 against SOCE in wild type HEK293 cells is greater than that used to demonstrate the anti-proliferative effects of these compounds in HPASMCs, it is important to recognise that different cell types have different IC_{50} values. For example, the IC_{50} of NNC55-0396 against T-type Ca^{2+} channels in HEK293 cells stably expressing $Ca_v3.1$ is 6.8 µM (Li et al., 2005). Further, the exposure times differ between Ca^{2+} microfluorimetry, which is a short application; and proliferation assays, which have a long application period. Thus, to provide a direct comparison, the concentrations of mibefradil and NNC55-0396 that inhibit SOCE in wild type HEK293 cells should be tested for their anti-proliferative effects in HEK293 cells overexpressing T-type Ca^{2+} channels. A further improvement would be to determine if the concentrations of mibefradil and NNC55-0396 that inhibit proliferation of HPASMCs also inhibit SOCE in HPASMCs. Attempts were made to carry out the latter, but due to difficulty obtaining Ca^{2+} measurements in primary cells using Ca^{2+} microfluorimetry and the time required to optimise this method, no useful data was obtained. This is a consideration for future work.

Although no off-target effects of T-type Ca^{2+} channels were observed against TRPC1/4-mediated Ca^{2+} entry, it is important to mention that only one dose of the TRPC1/4 agonist, EA, was used in these experiments, which may have prevented any off-target effects from being identified. In future, it would be useful to confirm these observations using a range of EA concentrations. Lower concentrations of EA (i.e. 100 nM) have been shown as effective in inducing TRPC1/4-mediated Ca^{2+} entry in overexpressing HEK293 cells (Rubaiy et al., 2018).

Collectively, these findings support existing evidence that mibefradil and NNC55-0396 are sub-optimal research tools (Nilius et al., 1997; Liu et al., 1999; (Chouabe et al., 2000; Perchenet and Clement-Chomienne, 2000; McNulty and Hanck, 2004). Thus, research employing these inhibitors to investigate the T-type Ca^{2+} channel as an anti-proliferative target should be interpreted with caution.

As earlier mentioned, JPIII exhibits improved pharmacokinetics to Synta66 and can be infused into rodents at high enough concentrations to carry out functional studies. JPIII has previously been infused into mice in models of AAA and was shown to reduce remodelling and intraluminal dimensions (Bailey, 2016). Thus, the tools to investigate the anti-proliferative effects of Orai1 inhibition in *in-vitro* and *in-vivo* models of hypoxia-induced pulmonary VSMC proliferation and CH-induced PH are now available.

These considerations pivoted the study to focus on the potential of Orai1 as an anti-proliferative target in hypoxia-induced VSMC proliferation. To achieve this, research was carried out to: 1) confirm lack of off-target modulation by JPIII on voltage-dependent Ca^{2+} entry; and 2) observe the anti-proliferative effects of JPIII in an appropriate *in-vitro* model of hypoxia-induced VMSC proliferation.

Strengthening the findings of the CEREP Safety-44 selectivity screen, this study confirmed absence of any off-target modulation of JPIII on T-type Ca^{2+} current using patch clamp electrophysiology. Combined with the selectivity screen, these data demonstrate the superior selectivity of JPIII. It should be highlighted that rat CACNA1G was used to test for off-target effects of JPIII. Although rat CACNA1G has 93% protein homology with human CACNA1G (Toyota et al., 1999), a further improvement would be to test for off-target effects of JPIII against either mouse CACNA1G (in line with the *in-vivo* model used in Chapter 5 of this thesis) or human CACNA1G to provide certainty that any off-target effects are consistent between species.

The increased sensitivity to the anti-proliferative effects of JPIII in HPASMCs cultured in hypoxia for 19 days exist in parallel with marked upregulation in Orai1 mRNA at an equivalent time point, justifying Orai1 as an interesting anti-proliferative target in hypoxia-induced VSMC proliferation and CH-induced PH.

In summary, T-type Ca^{2+} channel mRNA is not upregulated in the *in-vitro* model of hypoxia-induced pulmonary VSMC proliferation used in this study and mibefradil and NNC55-0396 have off-target effects on SOCE. Orai1 mRNA is significantly upregulated in hypoxia and selective inhibition of Orai1 with JPIII significantly reduces HPASMC proliferation. JPIII is a selective inhibitor of Orai1 that can be used to investigate the effects of Orai1 inhibition on CH-induced PH *in viv*o, which is performed in Chapter 5.

Chapter 5

Orai1 as an anti-proliferative target in the SuHx model of CH-induced PH

5.1 Introduction

As described earlier, the receptor tyrosine kinase (RTK) blocker with preference for PDGF receptors, imatinib, slowed PH progression and improved multiple pathological parameters of PH in clinical trials (Ghofrani et al., 2005; Schermuly et al., 2005; Ghofrani et al., 2010; Speich et al., 2015). However, imatinib demonstrated detrimental off-target effects, possibly due to such widespread consequences of direct PDGF receptor inhibition or additional effects at other RTKs. Orai1 is just one downstream target of the PDGF receptor, which is also known to control proliferation of VSMCs. Selective Orai1 inhibition using the novel inhibitor, JPIII, reduced hypoxia-induced pulmonary VSMC proliferation in an *in-vitro* model of hypoxia-induced pulmonary VSMC proliferation as shown in Chapter 4.

Promise has been demonstrated for Orai1 as an anti-proliferative target in VSMCs *in vitro* and in the context of atherosclerosis and neo-intimal hyperplasia *in vivo*. Ongoing work (currently unpublished) from the Bailey, Beech and Foster laboratories in Leeds also suggests beneficial effects on pathological remodelling in the context of pressure-induced heart failure and abdominal aortic aneurysm. In common with CH-induced PH, these diseases possess hypoxia as a key clinical risk factor (although in these cases usually as a consequence of smoking), raising the possibility of shared mechanisms and therefore similar potential therapeutic targets. The potential of selective Orai1 inhibition as an anti-proliferative approach in an *in-vivo* model of CH-induced PH has never been examined, providing novelty to this project.

In the aim of utilising genetically modifiable mice to investigate the mechanisms of PH, the CH models of PH are widely used. Although Ciuclan et al. (2011) noted a subtle phenotype in mice exposed to CH, they found that weekly injections of the VEGF blocker, SU5416, combined with three weeks of CH (SuHx) recapitulated the pathological processes of CH-induced PH, such as vascular remodelling and cardiac indices, to a greater extent than CH alone. Since one of the most consistent observations of CH-induced PH in mice is distal muscularisation (Stenmark et al., 2009), Ciuclan et al. (2011) investigated distal muscularisation in the SuHx model and demonstrated a variable degree of occluded pulmonary arterioles after three weeks, but these lesions were not quantified. A marked increase in RV systolic pressure and RV hypertrophy were also observed compared to the vehicle-treated CH cohort.

This chapter will present data on my work establishing the CH and SuHx mouse models of CH-induced PH for the first time at the University of Leeds. To advance earlier studies, the degree of distal muscularisation in small pulmonary arterioles was quantified in mice exposed to CH alone or SuHx for four weeks. Extensive studies on morphological cardiac indices and RV haemodynamics were carried out. In addition, since LV dysfunction can occur secondary to RV dysfunction in CH-induced PH, left-sided echocardiography was performed to measure LV EF and LV FS in these models.

The findings from this investigation justified the remainder of the *in-vivo* studies to focus on the SuHx mouse model. This model was used to study the potential of selective Orai1 inhibition with JPIII on the distal muscularisation and morphological cardiac indices associated with the SuHx model of CH-induced PH. As previous efforts to quantify distal muscularisation have relied on traditional haematoxylin and eosin staining and/or immunohistochemistry with antibodies raised against the contractile proteins found in VSMCs in the differentiated contractile phenotype (which is lost in disease), I took advantage of a VSMC lineage tracing mouse line to overcome these limitations and give confidence in the identification of VSMC remodelling in the pulmonary vasculature.

5.2 Results

5.2.1 Reproducing CH-induced PH *in vivo*

As demonstrated in Figure 5.1, mice were maintained in either normoxia (37ºC, 95% air, 5% CO_2) or hypoxia (37ºC, 10% O_2 [supplemented with N_2]) with weekly injections of either vehicle (CMC Na^+) or SU5416. All mice were weighed at regular intervals throughout the experimental period to adhere to project license restrictions. The project license limited hypoxia-induced weight loss to no greater than 15%. If weight loss exceeded 15%, animals were culled using a method listed under Schedule 1 of the UK Scientific Procedures Act.

In the first series of experiments to reproduce the CH-induced PH mouse model, according to Figure 5.1 (A), mean baseline body weight was reduced by 10.09% in the *Hx* + *SU5416* group by the end of week 1. At the end of week 1, mean body weight in the *Hx* + *SU5416* group was significantly lower ($p<0.05$) than the mean body weight of the *Nx* + *veh* group at the equivalent time point.

In the *Hx* + *veh* group, mean baseline body weight was reduced by 8.27% by the end of week 1. Although mean body weight in the *Hx* + *veh* group was markedly lower than the *Nx* + *veh* group by the end of week 1, this difference was at the borderline of significance ($p=0.053$). The *Nx* + *veh* group demonstrated relatively stable weight throughout the experimental period.

In support of these observations, the second series of experiments to reproduce the CH-induced PH mouse model demonstrated hypoxia-induced weight loss in both the *Hx* + *SU5416* and the *Hx* + *veh* groups within the first week (Figure 5.1, B). Specifically, mean baseline body weight was reduced by 8.15% in the *Hx* + *SU5416* group by the end of day 3, while mean baseline body weight was reduced by 4.15% in the *Hx* + *veh* group. By the end of week 1, mean body

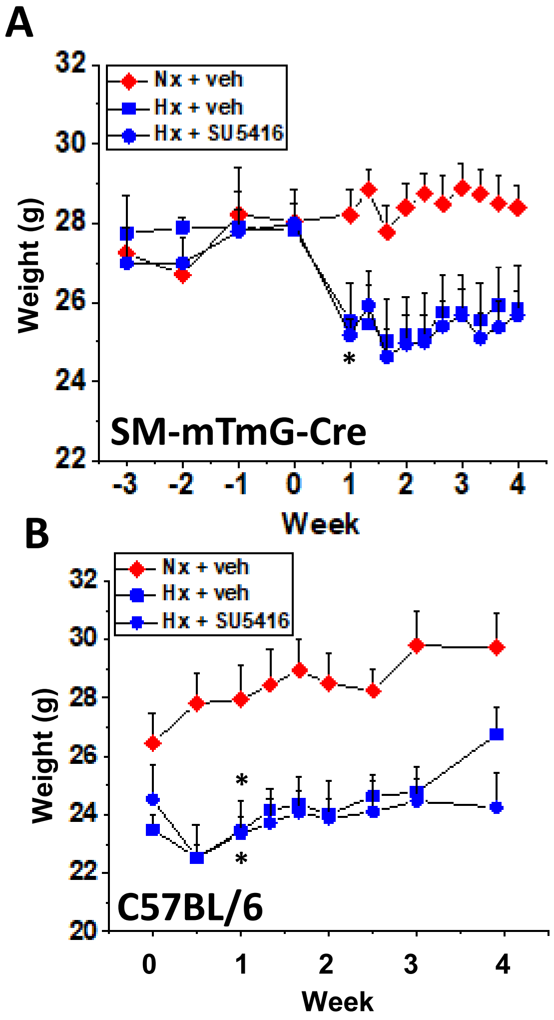

Figure 5.1. Mice exposed to hypoxia present with weight loss within the first week and weigh significantly less than mice exposed to normoxia.

All mice were weighed at regular intervals throughout the experimental period to adhere to project license restrictions (weight loss should not exceed 15% of starting weight). Data analysed by one-way ANOVA followed by Tukey’s multiple comparison test. * = significant difference ($p<0.05$) between *Hx* + *SU5416* group and *Nx* + *veh* group (* below symbol), or between *Hx* + *veh* and *Nx* + *veh* groups (* above symbol). No significant differences in baseline body weight were observed at the start of hypoxia (week 0) between any groups (n=4 per group).

weight was significantly lower in both the *Hx* + *SU5416* group ($p<0.05$) and the *Hx* + *veh* group ($p<0.05$) compared to the *Nx* + *veh* group.

By the end of the experimental period, all animals in both the *Hx* + *veh* group and the *Hx* + *SU5416* group weighed less than their *Nx* + *veh* counterparts, even after accounting for differences in starting weight between groups, which is as expected (Leal et al., 1995; Schols and Westerterp, 2002; Murray and Montgomery, 2014).

The left lungs and whole hearts were harvested, kept in 4% PFA for two hours, before being transferred to DPBS and stored at 4ºC. Tissues were then dissected according to the protocol outlined in 2.8.10 and illustrated in Figure 2.7.

As demonstrated in Figure 5.2 (A), left lung weight was significantly increased by 38.68% in the *Hx* + *veh* group ($p<0.0001$) and 18.11% ($p<0.001$) in the *Hx* + *SU5416* group when compared with the *Nx* + *veh* group.

After removal of the cardiac atria, appendices and fat, the remaining cleaned heart (LV, RV and S) was weighed. Since a greater cleaned heart weight may reflect a greater total body weight (TBW), cleaned heart weight was normalised to TBW to identify true differences (Figure 5.2, B). When normalised to TBW, the cleaned heart represented 0.50% of the TBW in the *Hx* + *SU5416* group compared to 0.39% in the *Nx* + *veh* group, although this difference was non-significant. In the *Hx* + *veh* group, the cleaned heart represented 0.46% of TBW, which was not significantly different from the *Nx* + *veh* group (0.39%).

To establish if this increase in cleaned heart weight was due to RV hypertrophy, the RV was dissected, weighed, and expressed relative to the LV and S

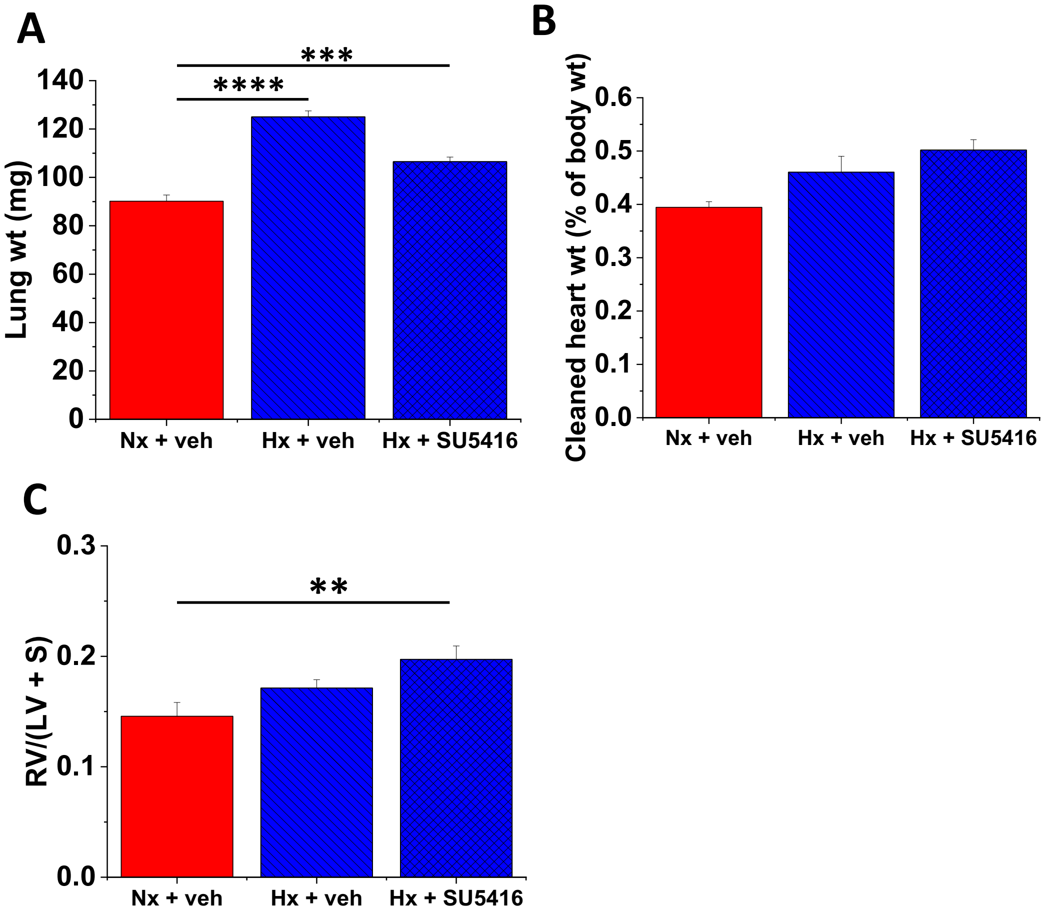

Figure 5.2. Morphological pulmonary and cardiac indices in mice exposed to hypoxia for four weeks.

Mice demonstrated a significant increase in lung weight when exposed to hypoxia (37°C, 10% O_2 [supplemented with N_2], 5% CO_2) with weekly injections of either vehicle (CMC Na$^+$) (*Hx + veh*) or the VEGF blocker, SU5416 (*Hx + SU5416*) when compared to animals exposed to normoxia (37°C, 95% air, 5% CO_2) with weekly injections of CMC Na$^+$ (*Nx + veh*) (A). The *Hx + SU5416* group also demonstrated an increase in cleaned heart weight even after normalisation to TBW (B), albeit not-significant. A significant increase in Fulton's index was observed in the *Hx + SU5416* group (C), consistent with RV hypertrophy. Data were analysed using a one-way ANOVA followed by Tukey's multiple comparison test. ** = $p<0.01$; *** = $p<0.001$; **** = $p<0.0001$. CMC Na$^+$, carboxymethylcellulose sodium; VEGF, vascular endothelial growth factor; TBW, total body weight; RV, right ventricle. (n=8 per group).

(RV/[LV+S]) to calculate Fulton's index (Figure 5.2, C). In the *Hx* + *SU5416* group, Fulton's index was significantly increased by 35.30% when compared to the *Nx* + *veh* group (*p*<0.01). Fulton's index was increased by 17.51% in the *Hx* + *veh* group compared to the *Nx* + *veh* group, but this increase was non-significant. These data suggest that the *Hx* + *SU5416* model reproduces the cardiac indices associated with CH-induced PH to a greater extent than CH alone.

At the beginning and end of the four-week experimental period, LV echocardiography was carried out in M-mode (Figure 5.3) to measure LV EF (Figure 5.4, A) and FS (Figure 5.4, C) as an indicator of LV heart failure. Since a low post-experimental EF and FS may simply reflect a low pre-experimental EF and FS, post-experimental EF and FS data for each animal were normalised to pre-experimental data for each animal to identify *true* differences (Figure 5.4, B and D).

According to Figure 5.4 (B) and Figure 5.4 (D), there was no change in post-experimental EF or FS when normalised to pre-experimental values in either the *Nx* + *veh* group or the *Hx* + *veh* group. Conversely, a reduction in both mean EF (21.46%) and mean FS (27.31%) was observed in the *Hx* + *SU5416* group when post-experimental EF and FS values were normalised to pre-experimental values, although these reductions in EF and FS were non-significant.

These data demonstrate that mice exposed to *Hx* + *SU5416* for four weeks present with a reduced LV EF and FS compared to pre-experimental values, indicative of cardiac dysfunction and heart failure. Since LV failure can occur secondary to RV failure in CH-induced PH, these data suggest that the *Hx* + *SU5416* approach produces more severe cardiac indices than CH alone.

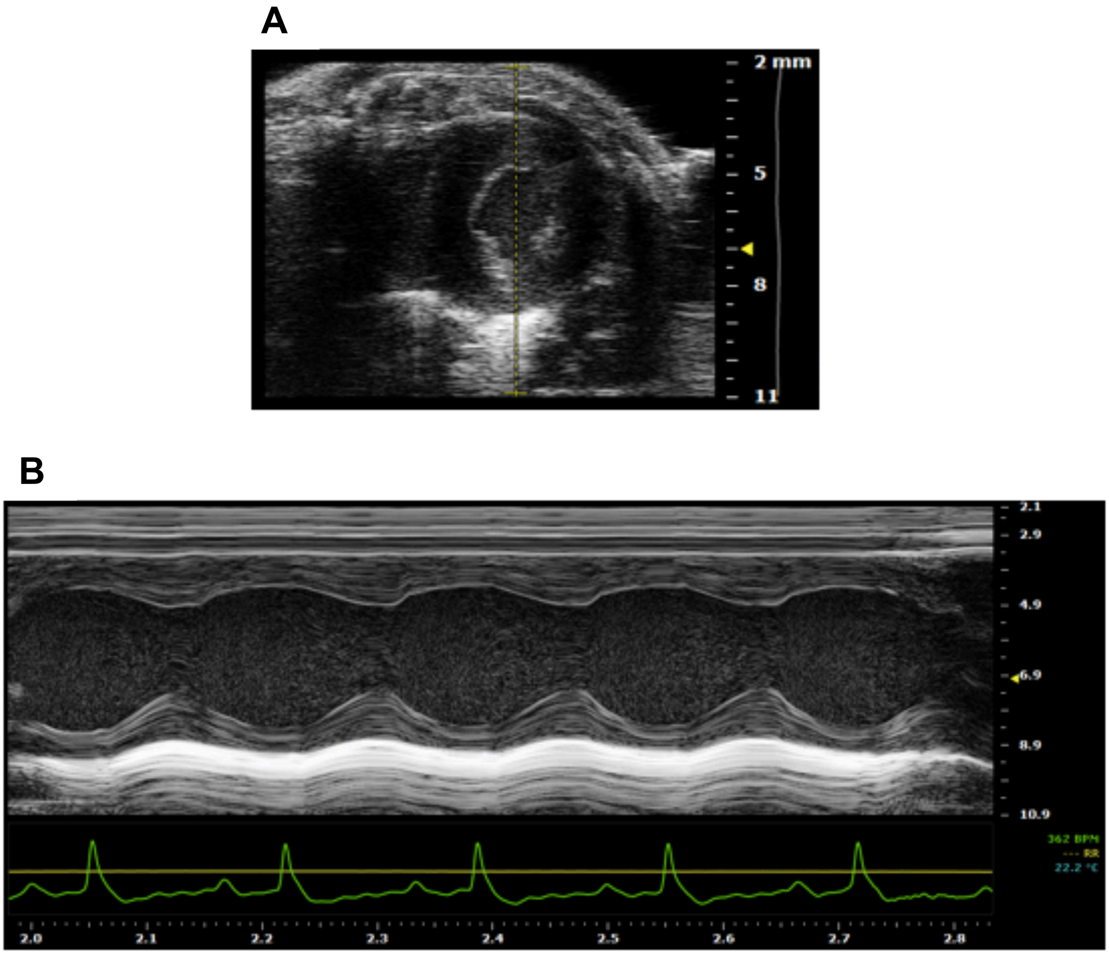

Figure 5.3. Example short axis M-mode echocardiography trace in mice.

Echocardiography was performed in the short cardiac axis (A) using the Vevo2100 (FujiFilm Visualsonics) micro-ultrasound imaging system and the associated Vevo® LAB software at the beginning and end of the experimental period to obtain M-mode echocardiography traces (B). These traces were used to calculate pre- and post-experimental EF and FS as an indicator of cardiac dysfunction and heart failure. EF, ejection fraction; FS, fractional shortening.

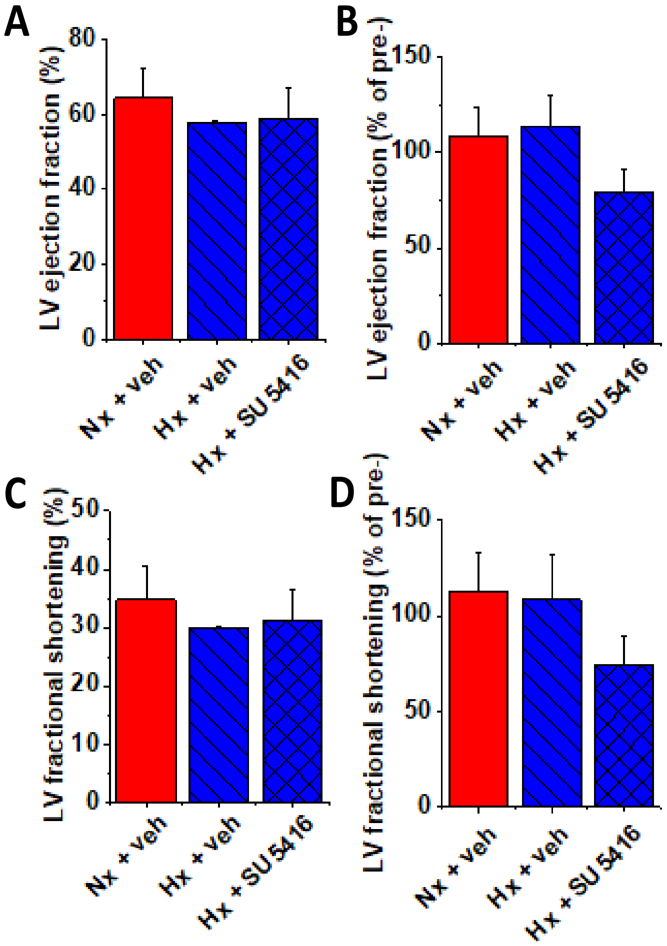

Figure 5.4. LV ejection fraction and fractional shortening are reduced in mice exposed to *Hx* + *SU5416* for four weeks.

Echocardiography was used to measure EF and FS to identify LV cardiac dysfunction and heart failure in mice exposed to either *Hx* + *veh* or *Hx* + *SU5416*. LV EF (A) and LV FS (C) were reduced in the *Hx* + *SU5416* group compared to the *Nx* + *veh* group, albeit non-significant. LV EF (B) and LV FS (D) were normalised to pre-experimental values to identify *true* differences. Data were analysed using a one-way ANOVA followed by a Bonferroni-Holm post-hoc test (n=4 per group). EF, ejection fraction; FS, fractional shortening; LV, left ventricular.

At the end of the four-week experimental period, PV monitoring was carried out to assess changes in right-sided cardiac haemodynamics, specifically end systolic volume (ESV), end systolic pressure (ESP), arterial elastance (E_a), RV ejection fraction (RV EF) and heart rate (HR). Since PV monitoring is a non-recovery procedure, it was not possible to gain pre-experimental values for the purpose of normalisation. Despite this, right-sided cardiac haemodynamics were measured in a *Nx* + *veh* group, which acted as an untreated control. Representative PV loops are demonstrated in Figure 5.5. The representative PV loop from the *Hx* + *veh* group (Figure 5.5, B) demonstrates a RV pressure of 75 mmHg compared to 37 mmHg in the *Nx* + *veh* group. Three of the four mice in the *Hx* + *SU5416* group bled out immediately following cardiac catheterisation (apparently due to very high RV pressure). Thus, only one PV loop (Figure 5.5, C) and associated haemodynamic measurements (Figure 5.6) were obtained from the *Hx* + *SU5416* group.

In addition to an increase in pressure, the total area inside the PV loops is larger in the *Hx* + *SU5416* group when compared with the *Nx* + *veh* group. The area within the PV loop indicates ventricular stroke work (SW), which represents the work carried out by the RV to eject blood into the pulmonary artery. The area within the PV loop is influenced by both the width of the loop (which indicates the difference between the EDV and the ESV [the SV] on the x axis) and the pressure in the ventricle (y axis). Comparing the *Hx* + *SU5416* PV loop with the *Nx* + *veh* PV loop, both the SV and the pressure are greater in the *Hx* + *SU5416* group, which underpins the larger total PV loop area. This indicates that the pressure increase in the RV is achieving ejection of a larger volume (this SV is greater), which is in line with the initial adaptive response of the heart to overcome the increase in afterload that is placed on the RV from the high PAP in the diseased lung.

Comparing the PV loops from the *Hx* + *veh* group with the *Nx* + *veh* group, the pressure is greater but the SV is reduced, which overall produces a PV loop area of approximately the same size. Although it is clear that the RV pressure is increased in the *Hx* + *veh* group when compared with the *Nx* + *veh* group, the total PV loop area is not substantially different due to a reduction in the SV in the Hx + veh group. These observations could indicate that an initial increase in SW, which leads to RV hypertrophy has led to right-sided cardiac failure and an inability of the heart to eject the same volume of blood with each beat, resulting in a reduction in SV.

As demonstrated in Figure 5.6 (A), mean ESV was 81.94% greater in the *Hx* + *veh* group than the *Nx* + *veh* group ($p<0.01$). From a single animal in the *Hx* + *SU5416* group, ESV was 69.66% greater than the mean ESV in the *Nx* + *veh* group, indicating an increase in the volume of blood remaining in the ventricle at the end of systole, which is an indicator of cardiac dysfunction.

The mean ESP was 44.63% greater in the *Hx* + *veh* group compared to the *Nx* + *veh* group ($p<0.05$). From a single animal in the *Hx* + *SU5416* group, ESP was 34.17% greater than the mean ESP in the *Nx* + *veh* group (Figure 5.6, B). Since ESP is closely associated with end PAP (Vonk-Noordegraaf and Westerhof, 2013), this is a good indicator of the CH-induced PH phenotype.

Figure 5.6 (C) demonstrates that mean E_a was 47.36% greater in the *Hx* + *veh group* compared to the *Nx* + *veh* group. In a single animal from the *Hx* + *SU5416* group, E_a was 34.62% greater than the mean E_a in the *Nx* + *veh* group.

Figure 5.6 (E) demonstrates no significant difference in mean heart rate (HR) in the *Hx* + *veh* group when compared to the *Nx* + *veh* group. No difference in HR was observed in a single animal from the *Hx* + *SU5416* group when compared to the mean HR in the *Nx* + *veh* group. The E_a is used as a measure of PVR and is the product of PVR and HR. Since HR was unchanged (Figure 5.6, E) but E_a was increased, PVR must also be increased, which is characteristic of CH-induced PH (Vonk-Noordegraaf and Westerhof, 2013).

A reduction in RV EF of 48.34% in the *Hx* + *veh* group compared to the *Nx* + *veh* group was observed, although this was non-significant. A reduction in RV EF of 21.87% was observed in a single animal from the *Hx* + *SU5416* group compared to the *Nx* + *veh* group (Figure 5.6, D). A reduction in RV EF is an indicator of systolic dysfunction and heart failure, indicative of CH-induced PH.

Overall, these data demonstrate a significant increase in ESV and ESP, an increase in E_a, a reduction in RV EF and no change in HR in the *Hx* + *veh* group, which are all indicative of RV dysfunction and heart failure.

Since n=1 for the *Hx* + *SU5416* group, statistics were not performed. However, the observation that animals bled out due to very high RV pressures upon catheterisation is indicative that changes in RV haemodynamics were severe in the *Hx* + *SU5416* cohort.

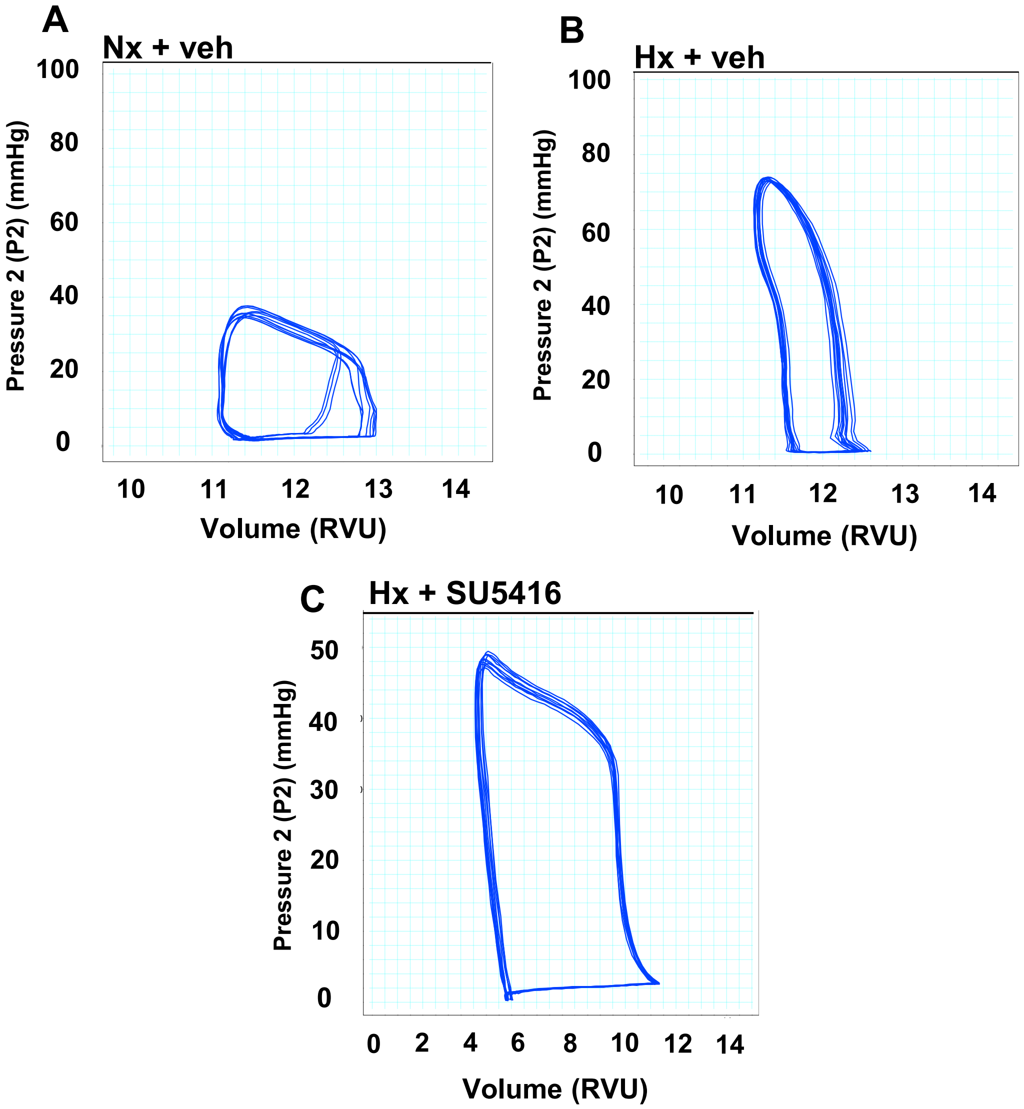

Figure 5.5. Representative RV PV loops.

Animals were intubated, the chest opened, and a cardiac catheter inserted into the RV and pressure monitored continuously for 10 minutes. One representative example of a PV loop is demonstrated for each of the *Nx + veh* group (n=4) (A), the *Hx + veh* group (n=4) (B) and the *Hx + SU5416* group (n=1) (C). PV, pressure volume.

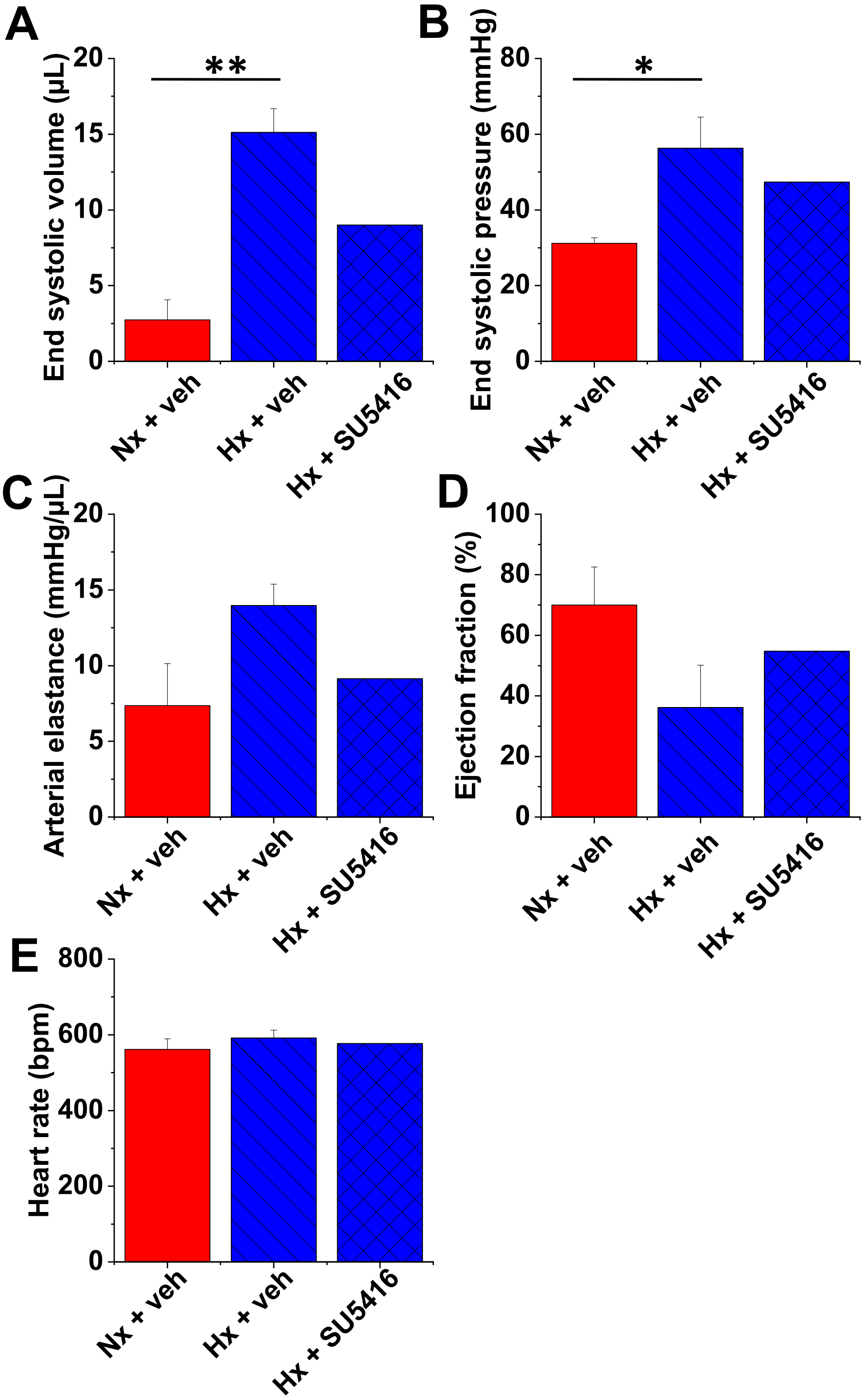

Figure 5.6. Haemodynamic measurements obtained from RV pressure volume monitoring.

In the *Hx* + *veh* group, ESV (A), ESP (B) and E_a (C) were increased. A non-significant reduction in RV EF was also observed (D), while no change in HR was observed (E). Data were analysed using a one-way ANOVA with Tukey's post-hoc analysis. * = p<0.05, ** = *p*<0.01. n=4 *Nx* + *veh, Hx* + *veh*; n=1 *Hx* + *SU5416.* ESV, end systolic volume; ESP, end systolic pressure; E_a, arterial elastance; RV EF, right ventricular ejection fraction; HR, heart rate.

At the end of the four-week experimental period, lungs from SM-mTmG-Cre mice were harvested and kept in 4% PFA for two hours, before being transferred to DPBS and stored at 4ºC. Lungs were then dissected into three parasagittal sections to obtain sections from the lateral parasagittal section (distal to bronchioles) to observe changes in the GFP+ (lineage traced) smooth muscle population as an indicator of distal muscularisation. Small arterioles were located and Z-stacks (63x magnification) performed on small arterioles from three lateral parasagittal sections per animal with four animals per group. Out-of-focus edge slices were removed from each Z-stack and the final number of slices per section was consistent between samples prior to analysis.

Representative three-dimensional Z-stacks are illustrated in Figure 5.7 (A), which demonstrate an increase in the intensity of GFP+ fluorescence within small arterioles. To semi-quantitatively analyse these Z-stacks, MFI was measured. The central slice of each Z-stack (the most in-focus slice) was analysed for the MFI of GFP and a value obtained in arbitrary units (AU). The average MFI values in each of the *Nx* + *veh, Hx* + *veh* and *Hx* + *SU5416* groups are represented in Figure 5.7 (B). The MFI of GFP was significantly greater in the *Hx* + *SU5416* group when compared to the *Nx* + *veh* group (p<0.05) using a one-way ANOVA, warranting a quantitative analysis by direct cell counting.

Figure 5.8 demonstrates representative two-dimensional images of small arterioles obtained from SM-mTmG-Cre mice in the *Nx* + *veh* group (A), the *Hx* + *veh* group (B) and the *Hx* + *SU5416* group (C). Two-dimensional cross sections through small arterioles demonstrate thickening of the GFP+ smooth muscle layer in both the *Hx* + *SU5416* group (Figure 5.8, C) and the

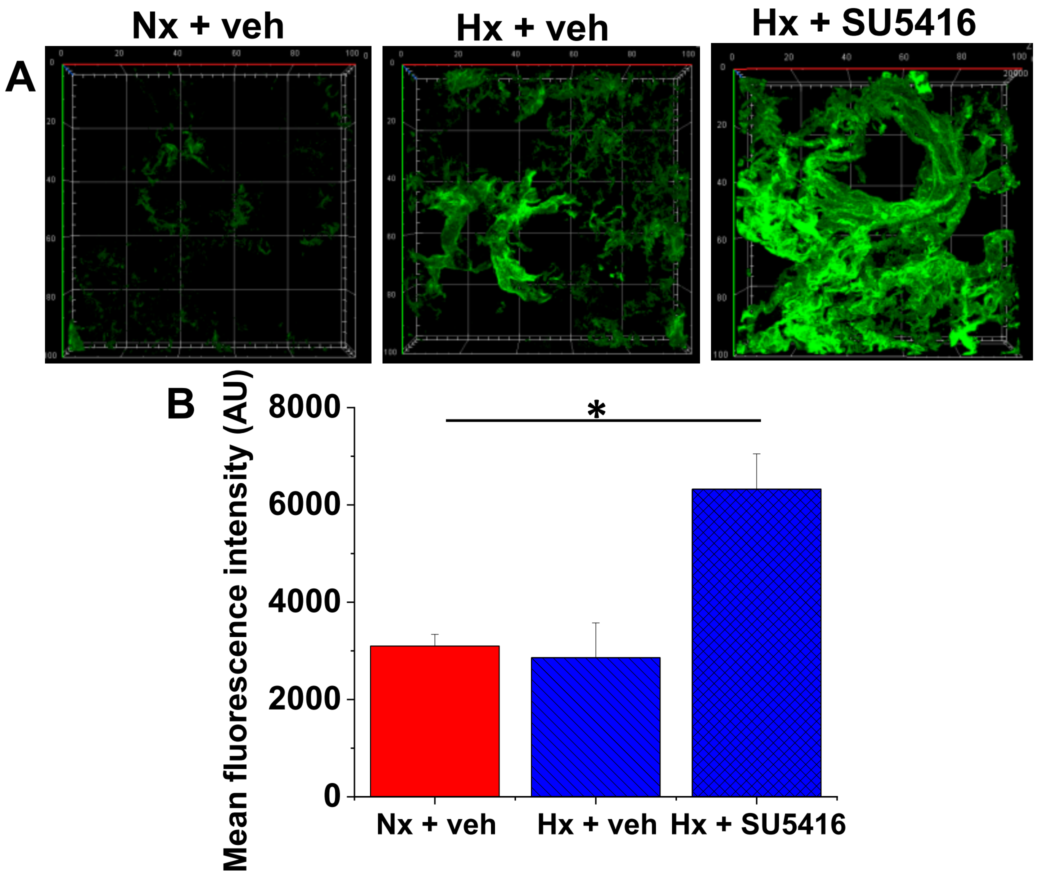

Figure 5.7. Mean fluorescence intensity of GFP in peripheral lung sections from SM-mTmG-Cre mice.

Using a LSM700 confocal microscope, Z-stacks (63x magnification) were performed on three lateral parasagittal sections per animal with four animals per condition to visualise the distribution and abundance of SMCs in small pulmonary arterioles from SM-mTmG-Cre mice exposed to either *Nx + veh* (A), *Hx + veh* (B) or *Hx + SU5416* (C). Mean fluorescence intensity for GFP was quantified and a significant increase observed in the *Hx + SU5416* group compared to the *Nx + veh* group. Data were analysed using a one-way ANOVA with Tukey's post-hoc test. * = $p<0.05$. n=4 per group/N=12 per group. SMCs, smooth muscle cells; GFP, green fluorescent protein.

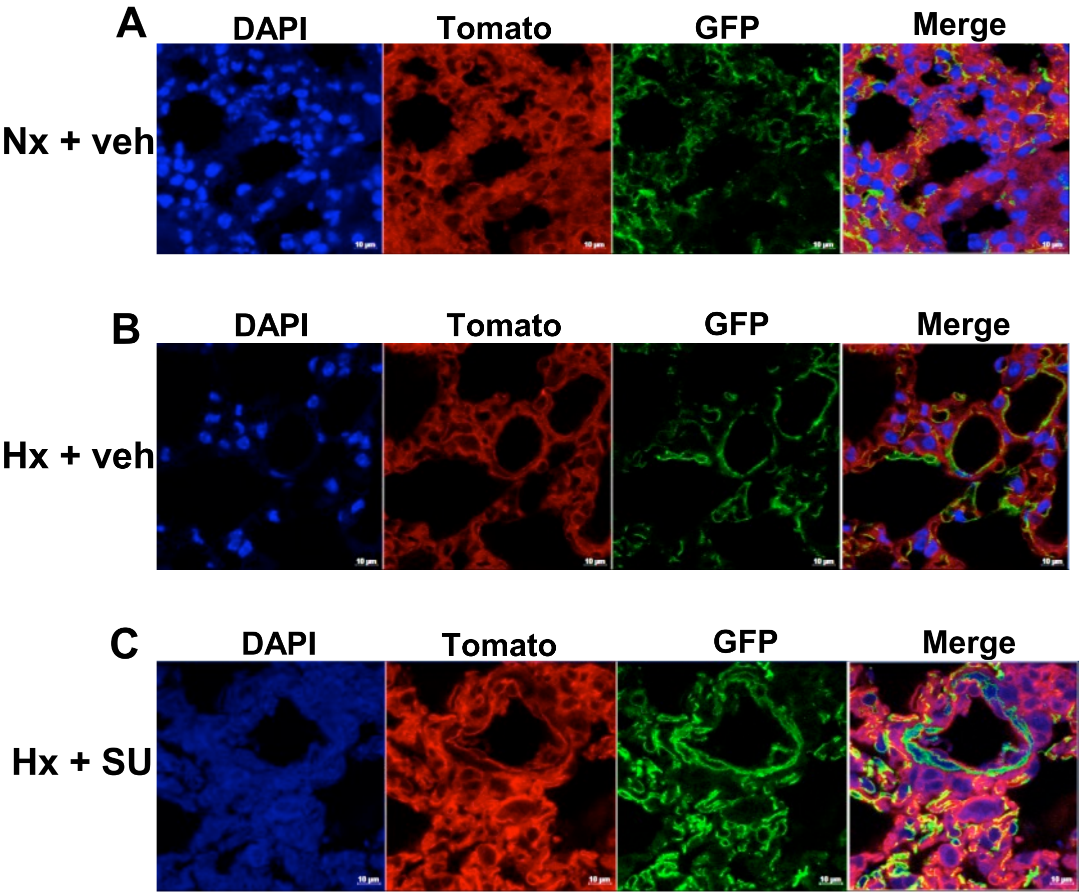

Figure 5.8. Representative fluorescent images of small vessels from SM-mTmG-Cre peripheral lung sections.

Using a LSM700 confocal microscope, Z-stacks (63x magnification) were performed on three lateral parasagittal sections per animal with four animals per condition and slices examined to identify small vessels. One representative image of small vessels from animals maintained in each of *Nx* + *veh* (A), *Hx* + *veh* (B) and *Hx* + *SU5416* (C) is demonstrated. Channels were separated to visualise cell nuclei (DAPI), SMCs (GFP) and all other cell types (tomato) separately, and a merged image presented. Scale bar = 10 um. n=4 per group/N=12 per group. SMCs, smooth muscle cells; GFP, green fluorescent protein.

Hx + *veh* group (Figure 5.8, B) when visually compared to the *Nx* + *veh* group (Figure 5.8, A), although the distal muscularisation is more marked in the *Hx* + *SU5416* group (Figure 5.8, C).

To quantify these observations, direct cell counting was performed on Z-stacks of equal thickness (10 µm, interval 0.26 µm, 40 slices per section) using ImageJ. Figure 5.9 (A) demonstrates a significantly greater percentage of GFP+ cells in the *Hx* + *SU5416* group (47% ± 3%) compared to the *Nx* + *veh* group (33% ± 4%). Although non-significant, the percentage of GFP+ cells in the *Hx* + *veh* group (36% ± 4%) was greater than the *Nx* + *veh* group (33% ± 4%).

Figure 5.9 (B) also demonstrates a significant reduction in the percentage of tomato+ cells in the *Hx* + *SU5416* group (53% ± 4%) compared to the *Nx* + *veh* group (68% ± 4%). Although non-significant, the percentage of tomato+ cells in the *Hx* + *veh* group (61% ± 7%) was reduced compared to the *Nx* + *veh* group (68 ± 4%).

Thus, in animals exposed to *Hx* + *SU5416*, the percentage of GFP+ SMCs was significantly increased, while the percentage of tomato+ cells was significantly reduced when compared to the *Nx* + *veh* group, indicating distal muscularisation in small arterioles. Herein, the *Hx* + *SU5416* model was used to study the CH-induced PH phenotype.

At the end of the four-week experimental period, lungs from SM-mTmG-Cre mice were further stained with the smooth muscle marker, α-SMA, to compare traditional staining methods with lineage tracing approaches.

In keeping with the previous experiment, small arterioles were located and Z-stacks (63x magnification) performed on 10 μm slices from small arterioles from three lateral parasagittal sections per animal with four animals per group.

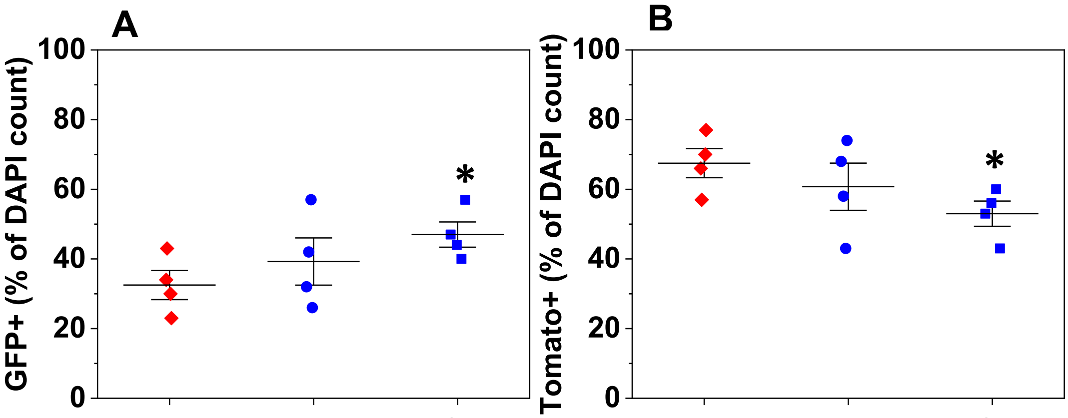

Figure 5.9. The percentage of GFP+ cells was significantly greater in the *Hx + SU5416* group compared to the *Nx + veh* group.

ImageJ software was used to quantify the percentage of total cells that were GFP+ (A) and tomato+ (B) and expressed as a percentage of the total DAPI count in each of *Nx + veh*, *Hx + veh* and *Hx + SU5416*. Data were analysed using one-way ANOVA followed by Tukey's post-hoc analysis. * = *p*<0.05. n=4 per group/N=12 per group.

Out-of-focus edge slices were removed from each Z-stack and the final number of slices per section was consistent between samples prior to analysis.

Figure 5.10 demonstrates representative two-dimensional images of small arterioles obtained from SM-mTmG-Cre mice. Two-dimensional cross sections through small arterioles demonstrate thickening of the GFP+ smooth muscle layer in the *Hx* + *SU5416* group (B) compared to the *Nx* + *veh* group (A), which is in agreement with earlier data (Figure 5.8).

When quantified by direct cell counting, a significant increase in the percentage of GFP+ cells was observed in the *Hx* + *SU5416* group compared to the *Nx* + *veh* group (Figure 5.11, A), which is in agreement with Figure 5.9 (A). Figure 5.11 (B) also demonstrates a reduction in the percentage of tomato+ cells in the *Hx* + *SU5416* group, which is in agreement with Figure 5.9 (B), although the reduction in the percentage of tomato+ cells was non-significant in this data set.

To determine if α-SMA staining is a reliable method to quantify the SMC population, the percentage of cells stained for α-SMA was determined (Figure 5.11, C). In the *Nx* + *veh* group, 82% ± 4% of cells stained positive for α-SMA. The percentage of α-SMA-stained cells was greater in the *Nx* + *veh* group (82% ± 4%) compared to the *Hx* + *SU5416* group (58% ± 11%), supporting downregulation of this contractile marker as the cells transition from a contractile to a proliferative phenotype. This observation is supported in Figure 5.10, where α-SMA staining appears to be less intense in the *Hx* + *SU5416* group (B) than in the *Nx* + *veh* group (A).

The percentage of α-SMA-stained cells was different to the percentage of GFP+ cells. For example, in the *Nx* + *veh* group, 82% ± 4% of cells stained positive for α-SMA, while 27% ± 5% were GFP+, supporting that α-SMA is not a selective marker for SMCs, but is also expressed in other cell types such as myofibroblasts.

Figure 5.11 (D) demonstrates that in the *Nx* + *veh* group, the percentage of GFP+ cells that also stained positive for α-SMA was around 78% ± 4%. This was reduced in the *Hx* + *SU5416* group, where only around 63% ± 10% of cells were positive for both markers. Based on the above data, when using both GFP and α-SMA as markers of SMCs, no significant difference was observed in the SMC population between the *Nx* + *veh* and *Hx* + *SU5416* groups, despite a significant increase in the SMC population already being demonstrated when quantifying GFP+ cells alone (Figure 5.9 and Figure 5.11, A). This is because the *increase* in the percentage of GFP+ cells in the *Hx* + *SU5416* group is counteracted by a concomitant *reduction* in α-SMA staining in this group. Thus, α-SMA staining alone misses a substantial proportion of the VSMC remodelling that occurs in mice exposed to *Hx* + *SU5416.*

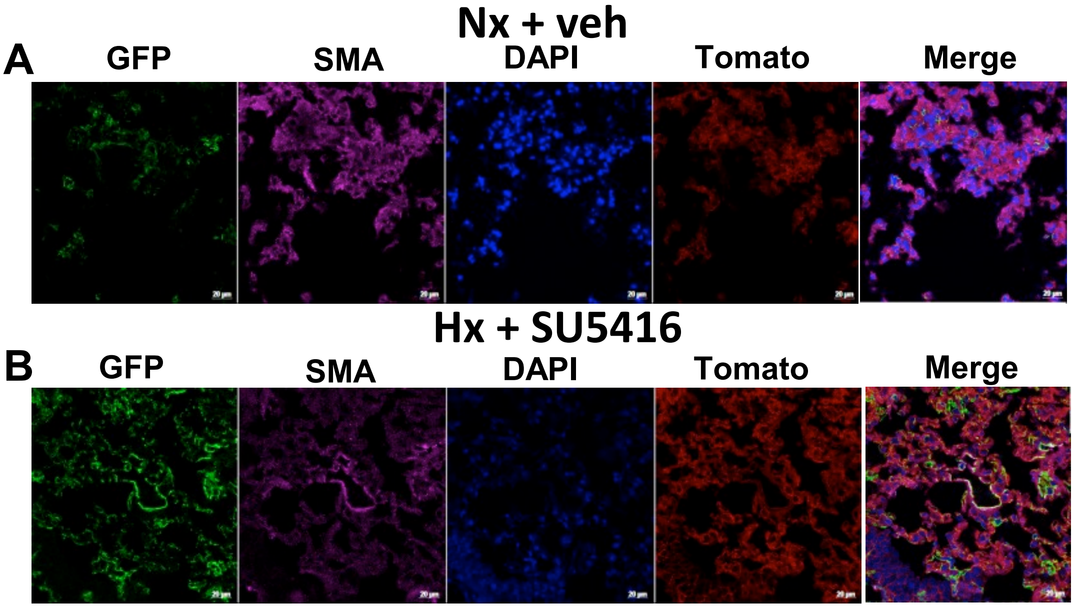

Figure 5.10. Representative fluorescent images of small vessels from SM-mTmG-Cre peripheral lung sections.

Using a LSM880 confocal microscope, Z-stacks (63x magnification) were performed on three lateral parasagittal sections per animal with four animals per condition and slices examined to identify small vessels. One representative image of small vessels from animals maintained in each of *Nx + veh* (A) and *Hx + SU5416* (B) is demonstrated. Channels were separated to visualise SMCs (GFP); the smooth muscle marker, α-SMA; cell nuclei (DAPI); and all other cell types (tomato) separately, and a merged image presented. Scale bar = 10 um. n=4 per group/N=12 per group. SMCs, smooth muscle cells; GFP, green fluorescent protein; α-SMA, α-smooth muscle actin.

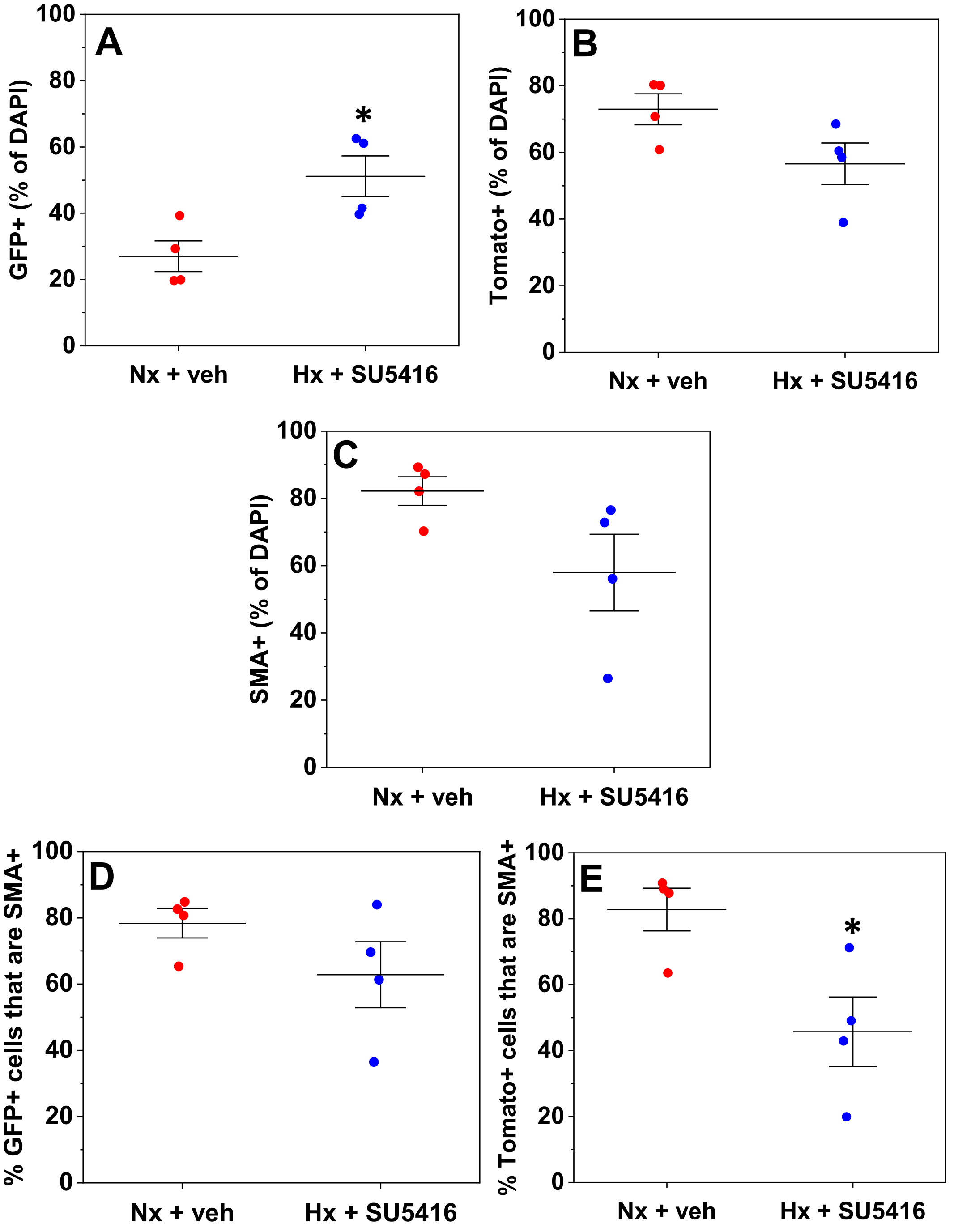

Figure 5.11. α-SMA does not reflect GFP lineage tracing in SM-mTmG-Cre mice.

ImageJ software was used to quantify the percentage of total cells that were GFP+ (A), tomato+ (B) and α-SMA-stained (C) and expressed as a percentage of the total DAPI count in each of *Nx + veh* and *Hx + SU5416*. The percentage of cells that were GFP+ and α-SMA-stained (D) and the percentage of cells that were tomato+ and α-SMA-stained (E) were calculated. Data were analysed using a two-sample t-test. * = $p<0.05$. n=4 per group/N=12 per group. GFP, green fluorescent protein; α-SMA, α-smooth muscle actin.

5.2.2 Orai1 as an anti-proliferative target in the SuHx mouse model of CH-induced PH

At the end of the four-week experimental period, mice were perfusion-fixed, and whole right lungs were harvested, snap frozen and stored at -80ºC before being prepared for RNA isolation and qPCR. The expression of 12 Ca^{2+} channel subunits (target genes) were screened in whole lungs from *Nx* + *veh*, *Hx* + *veh* and *Hx* + *SU5416* groups.

qPCR data were analysed using the comparative Ct ($2^{-\Delta\Delta Ct}$) method. The mean Ct of each target gene was normalised to the mean Ct of *B2M* (ΔCt). mRNA in the *Nx* + *veh* group (control) was the control to which mRNA in the *Hx* + *veh* and *Hx* + *SU5416* groups (experimental conditions) were compared (ΔΔCt). The $2^{-\Delta\Delta Ct}$ calculation was performed to identify expression fold change in hypoxia relative to normoxia and converted to a percentage (Figure 5.12).

Each target gene was analysed independently using a two-tailed t-test to identify significant differences in mRNA expression between *Hx* + *veh* and *Nx* + *veh;* and between *Hx* + *SU5416* and *Nx* + *veh*. The *Hx* + *veh* group demonstrated *ORAI1* upregulation (954% ± 547%), while a more modest upregulation was observed in *TRPC1* (343% ± 190%) (Figure 5.12, A). Similarly, the *Hx* + *SU5416* group demonstrated *ORAI1* and *TRPC1* upregulation (445% ± 342% and 406% ± 187%, respectively). In addition, a modest upregulation in *STIM1* (226% ± 98%), *STIM2* (265% ± 98%) and *ORAI3* (265% ± 103%) was observed (Figure 5.12, B). The above findings are in keeping with the *in-vitro* qPCR data presented in Chapter 4 (Figure 4.8).

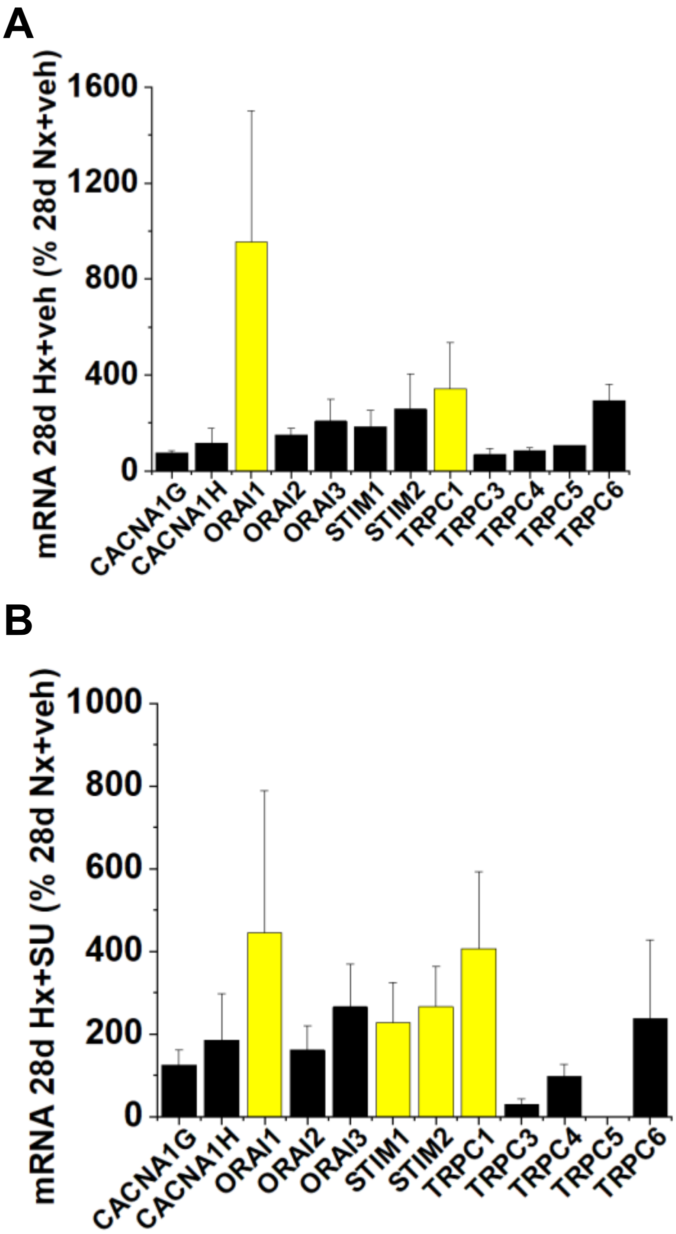

Figure 5.12. mRNA expression of Ca^{2+} channel subunits in whole mouse lung exposed to hypoxia for four weeks.

qPCR was carried out on whole mouse lungs to identify hypoxia-induced changes in Ca^{2+} channel subunit mRNA expression. An increase in *ORAI1* and *TRPC1* was observed in the *Hx* + *veh* and *Hx* + *SU5416* groups when compared to the *Nx* + *veh* group. In the *Hx* + *SU5416* group, an increase in *STIM1*, *STIM2* and *ORAI3* was observed. Data were analysed using a two-sample two-tailed t-test to identify statistically significant differences in each target gene compared to the *Nx* + *veh* group (n=4 per group).

SM-mTmG-Cre mice and C57BL6/J mice were maintained in either normoxia (37ºC, 95% air, 5% CO_2) with weekly injections of CMC Na^+ or hypoxia (37ºC, 10% O_2 [supplemented with N_2]) with weekly injections of SU5416. Animals kept in hypoxia were also administered a continuous infusion of either DMSO (vehicle) or JPIII. Since JPIII demonstrated inhibition of control specific binding against hERG of 49.3% (Chapter 4), and inhibition of hERG can cause drug-induced long QT syndrome, animals were monitored closely. Importantly, no sudden cardiac death or evidence of complications associated with hERG were observed.

In keeping with earlier experiments, all groups (*Nx* + *veh, Hx* + *SU5416* + *DMSO* and *Hx* + *SU5416* + *JPIII*) were weighed at regular intervals throughout the experimental period to adhere to project license restrictions. Hypoxia-induced weight loss exceeded 15% in one animal only from the SM-mTmG-Cre cohort in the *Hx* + *SU5416* + *DMSO* group, and this animal was culled using a method listed under Schedule 1 of the UK Scientific Procedures Act.

According to Figure 5.13 (B), mean baseline body weight was reduced by 6.81% in the *Hx* + *SU5416* + *DMSO* and 5.92% in the *Hx* + *SU5416* + *JPIII* group by the end of week 1.

At the end of week 1, mean body weight in the *Hx* + *SU5416* + *DMSO* group was 14.63% lower than the mean body weight of the *Nx* + *veh* group at the equivalent time point ($p<0.01$). Mean body weight in the *Hx* + *SU5416* + *JPIII* group was 15.64% lower than the *Nx* + *veh* group by the end of week 1 ($p<0.01$). In keeping with previous experiments, the *Nx* + *veh* group demonstrated relatively stable weights throughout the experimental period.

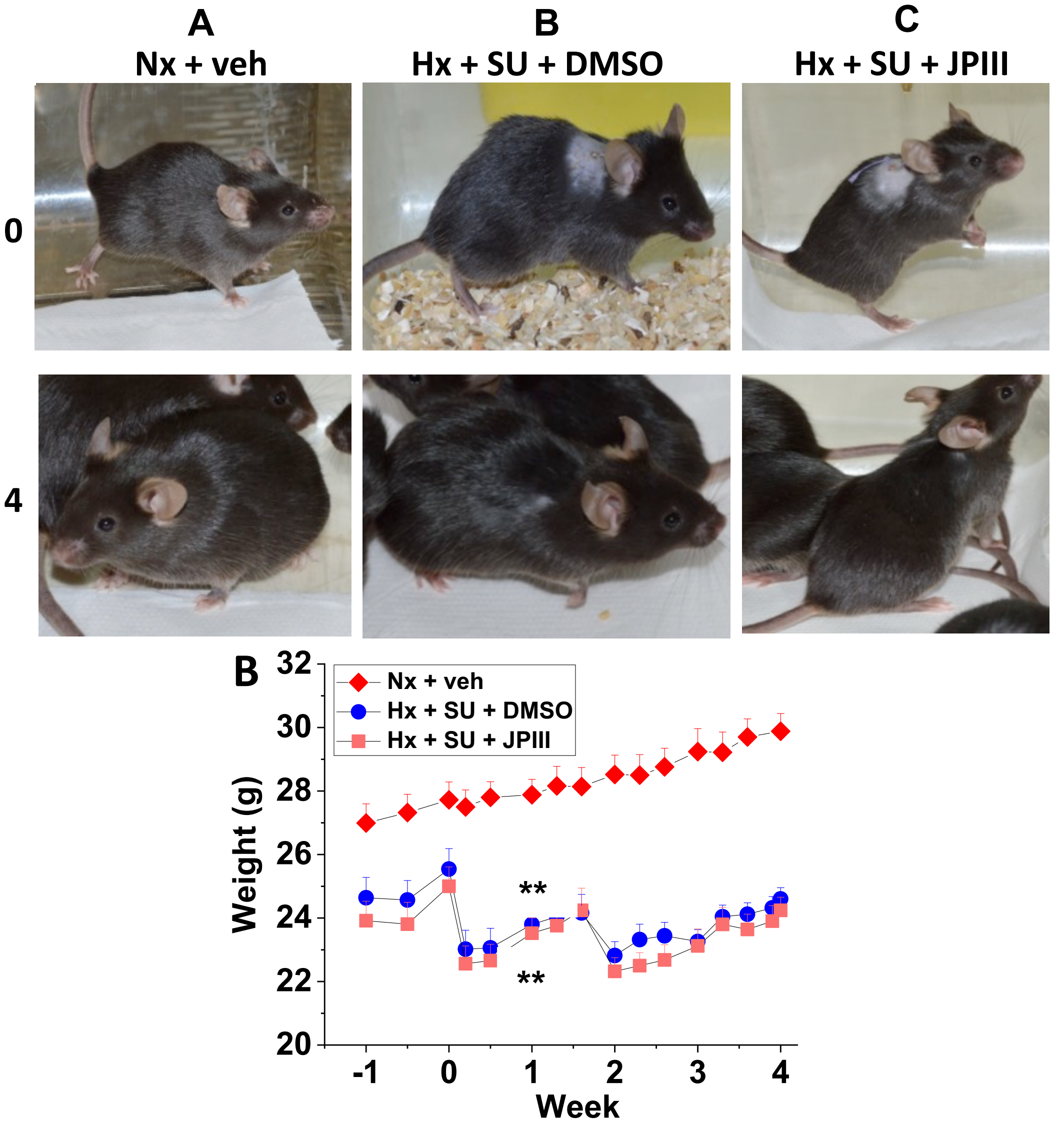

Figure 5.13. JPIII does not protect from hypoxia-induced weight loss in mice.

Mice were exposed to either *Nx + veh* (A), *Hx + SU5416 + DMSO* (B) or *Hx + SU5416 + JPIII* (C) and body weight monitored. No significant difference between body weight of JPIII-infused mice versus vehicle-infused mice was observed, indicating that JPIII does not protect against hypoxia-induced weight loss. Data were analysed using one-way ANOVA followed by Tukey's post-hoc test. ** = $p<0.01$ between *Hx + SU5416 + JPIII* group and *Nx + veh* group (below symbol), or between *Hx + SU5416 + DMSO* and *Nx + veh* groups (above symbol) n=5 per group.

Representative images of mice from each group are presented in Figure 5.13 (A), which shows that mice in the *Hx + SU5416 + DMSO* and *Hx + SU5416 + JPIII* groups weighed less than those in the *Nx + veh* group by week 4.

To examine the effect of selective Orai1 inhibition on morphological cardiac indices, the left lungs and whole hearts were harvested, kept in 4% PFA for two hours before being transferred to DPBS and stored at 4ºC. Tissues were then dissected according to the protocol outlined in 2.8.10 and illustrated in Figure 2.7.

In contrast to earlier experiments, which demonstrated a significant increase in lung weight in the *Hx + SU5416* group (Figure 5.2, A), no significant increase in lung weight was observed here in the *Hx + SU5416 + DMSO* group (Figure 5.14, A). The reason for this discrepancy is unclear. Lung weight was 26.81% greater in the *Hx + SU5416 + JPIII* compared to the *Nx + veh* group (Figure 5.14, A).

After removal of the atria, appendices and fat, the remaining cleaned heart (LV, RV and S) was weighed. In keeping with earlier experiments, cleaned heart weight was normalised to TBW (Figure 5.14, B) to identify *true* differences. When normalised to TBW, no difference in cleaned heart weight was observed between the *Hx + SU5416 + DMSO* group compared to the *Nx + veh* group. In earlier experiments, an increase in cleaned heart weight was observed (Figure 5.2, B), but this was non-significant. No difference in cleaned heart weight was observed in the *Hx + SU5416 + JPIII* group compared to the *Nx + veh* group.

In agreement with earlier experiments (Figure 5.2, C), Figure 5.14 (C) demonstrates that Fulton's index (RV/[LV+S]) was 40.82% greater in the *Hx + SU5416 + DMSO* group compared to the *Nx + veh* group ($p<0.05$). Fulton's

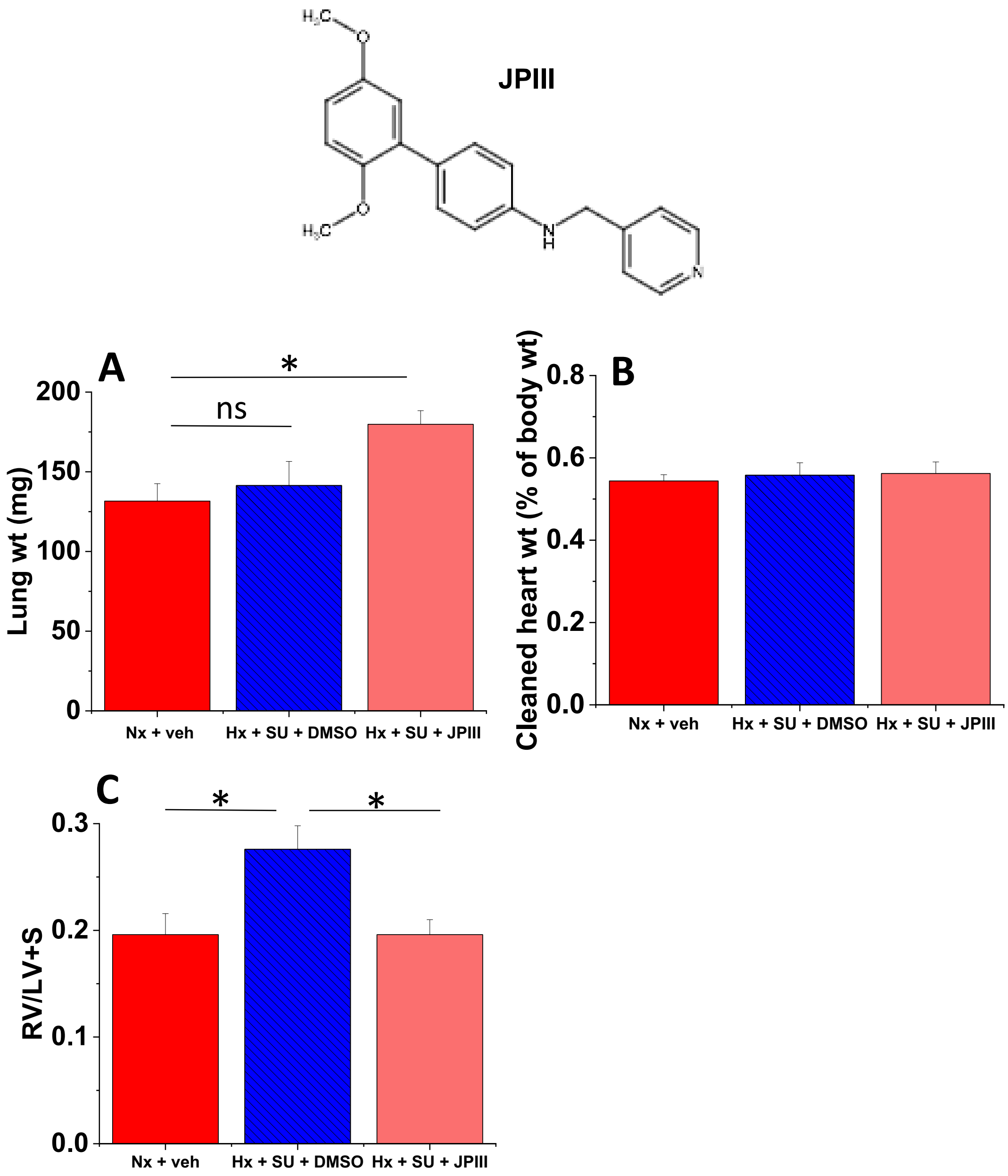

Figure 5.14. JPIII protects against RV hypertrophy in the SuHx mouse model of CH-induced PH.

Mice were exposed to either *Nx + veh*, *Hx + SU5416 + DMSO* or *Hx + SU5416 + JPIII* and morphological cardiac indices monitored. No significant difference in lung weight between the *Hx + SU5416 + DMSO* group and the *Nx + veh* group was observed, while a significant increase in lung weight between the *Hx + SU5416 + JPIII* and the *Nx + veh* group was observed (A). No increase in cleaned heart weight was observed between groups when normalised to body weight (B). A significant increase in Fulton's index was observed in the *Hx + SU5416 + DMSO* group compared to the *Nx + veh* group, which was significantly reduced by JPIII infusion (C). Data were analysed by one-way ANOVA followed by Tukey's multiple comparison test. * = $p<0.05$ (n=5 per group).

index was significantly reduced in the *Hx* + *SU5416* + *JPIII* group compared to the *Hx* + *SU5416* + *DMSO* group (*p*<0.05). Fulton's index in the *Hx* + *SU5416* + *JPIII* group was no different to the *Nx* + *veh* group. These data suggest that JPIII protects from the hypoxia-induced increase in Fulton's index (*p*<0.05). In keeping with earlier experiments, small arterioles were located and Z-stacks (63x magnification) performed on three lateral parasagittal sections per animal (small arterioles distal to bronchioles), with three animals in the *Hx* + *SU5416* + *DMSO* group (one was culled using a method listed under Schedule 1 of the UK Scientific Procedures Act after exceeding 15% weight loss) and four animals in the *Hx* + *SU5416* + *JPIII* group. Out-of-focus slices were removed and the number of slices per section was consistent between samples.

Figure 5.15 demonstrates two-dimensional images of small arterioles from SM-mTmG-Cre mice in the *Hx* + *SU5416* + *DMSO* group (A) and the *Hx* + *SU5416* + *JPIII group* (B) to observe whether selective inhibition of Orai1 using JPIII protects from distal muscularisation. Figure 5.15 (B) demonstrates a reduction in the intensity of GFP+ lineage tracing within small arterioles of SM-mTmG-Cre mice in the *Hx* + *SU5416* + *JPIII* group when visually compared to the *Hx* + *SU5416* + *DMSO* group. To quantify these observations, direct cell counting was performed on Z-stacks of equal thickness (10 µm, interval 0.26 µm, 40 slices per section) using ImageJ.

Figure 5.16 (A) demonstrates that in the *Hx* + *SU5416* + *JPIII* group, 38% ± 5% of cells were GFP+ compared to 60% ± 5% in the *Hx* + *SU5416* + *DMSO* group. Figure 5.16 (B) also demonstrates that in the *Hx* + *SU5416* + *JPIII* group, 71 ± 7% of cells were tomato+ compared to 40% ± 5% in the *Hx* + *SU5416* + *DMSO* group. Overall, the percentage of GFP+ SMCs in the *Hx* + *SU5416* + *JPIII* group was significantly reduced compared to the percentage of GFP+ SMCs in the *Hx* + *SU5416* + *DMSO* group, while the percentage of tomato+ cells was significantly greater. These data suggest that JPIII protects from VSMC phenotypic switching and the associated increase in distal muscularisation associated with CH-induced PH.

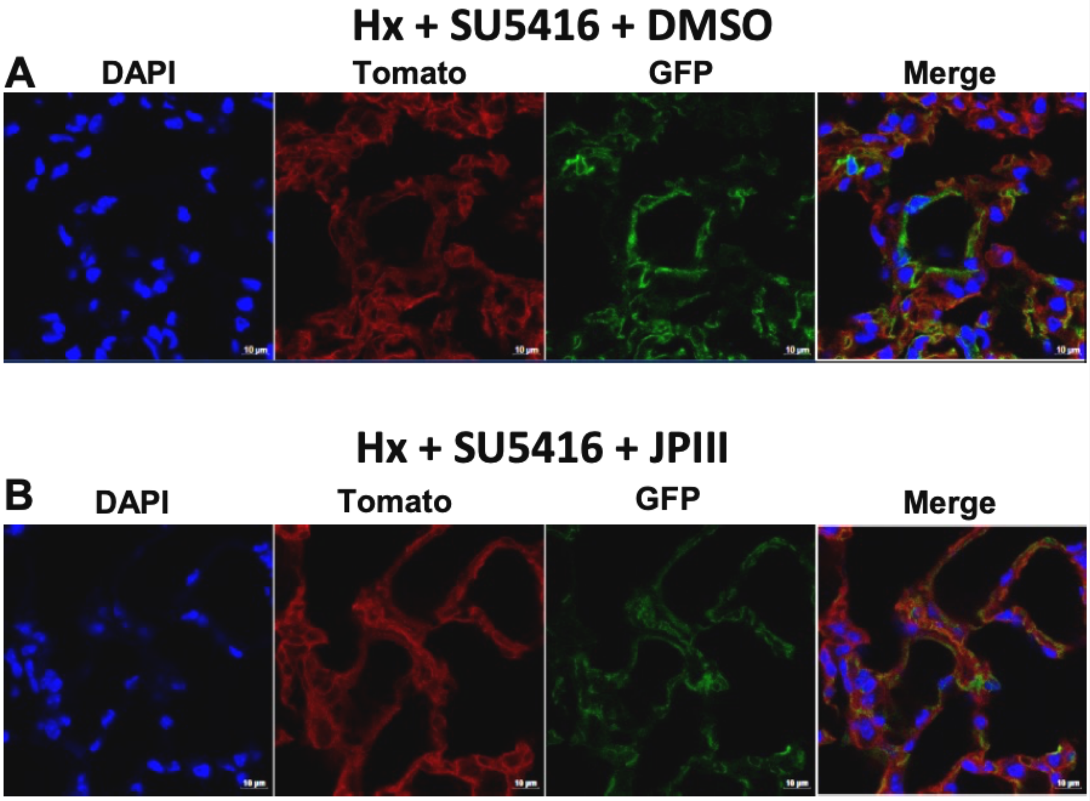

Figure 5.15. Representative fluorescent images of small vessels from SM-mTmG-Cre peripheral lung sections from mice treated with JPIII or DMSO.

Using a LSM700 confocal microscope, Z-stacks (63x magnification) were performed on three lateral parasagittal sections per animal with either three or four animals per group and slices examined to identify small arterioles. One representative image of small vessels from animals maintained in each of *Hx + SU5416 + DMSO* (n=3/N=9) (A) and *Hx + SU5416 + JPIII* (n=4/N=12) (B) is demonstrated. Channels were separated to visualise cell nuclei (DAPI), SMCs (GFP+) and all other cell types (tomato+) separately, and a merged image presented. Scale bar = 10 um. SMCs, smooth muscle cells; GFP, green fluorescent protein.

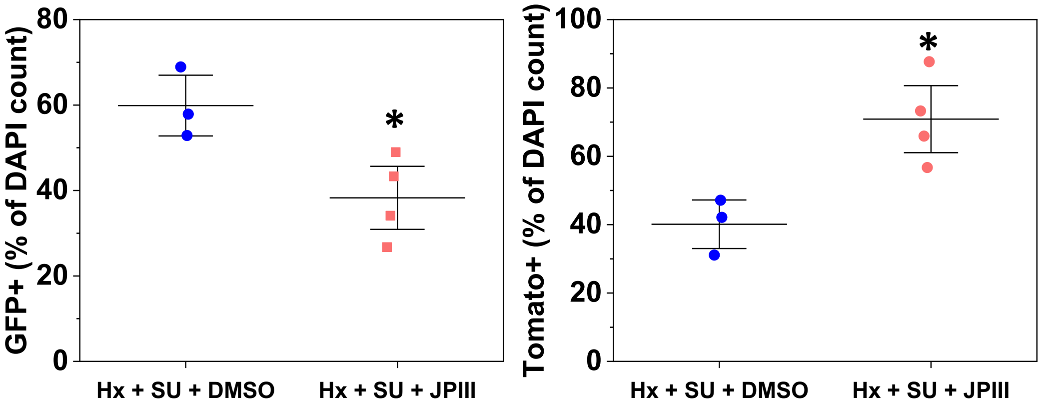

Figure 5.16. The percentage of GFP+ cells was significantly reduced in the *Hx* + *SU5416* + *JPIII* group compared to the *Hx* + *SU5416* + *DMSO* group.

ImageJ software was used to quantify the percentage of total cells that were for GFP+ (A) and tomato+ (B) and expressed as a percentage of the total DAPI count in each of *Hx* + *SU5416* + *DMSO* (n=3/N=9) and *Hx* + *SU5416* + *JPIII* (n=4/N=12). Data were analysed using a two sample t-test. * = p<0.05.

5.3 Summary of aims and key findings

The initial aims of this study were to: 1) reproduce the CH and SuHx mouse models of CH-induced PH for the first time at the University of Leeds; 2) observe morphological cardiac indices and cardiac haemodynamics, and quantify distal muscularisation in animals exposed to hypoxia for four weeks; and 3) study the effects of selective Orai1 inhibition using the novel inhibitor, JPIII, on the cardiac indices and distal muscularisation associated with SuHx CH-induced PH. Below, the limitations of the data presented in this chapter are discussed. Further interpretation of the data in the context of existing literature is provided in Chapter 6.

The main limitations of the *in-vivo* studies were the small sample sizes used throughout. The importance of the power calculation is recognised, but due to breeding limitations of the Sm-mTmG-Cre mouse line, it was not possible to reach suitable numbers within the time available. In future studies, further animals should be tested under the same experimental conditions to further validate the observations presented in this chapter. Since the observations of this study were novel (the combination of the four-week hypoxic exposure, the inclusion of JPIII as an Orai1 inhibitor *in vivo* in the context of CH-induced PH, and quantification of distal muscularisation under these conditions), the data presented in this thesis could be used as pilot data on which to base power calculations in the future.

The findings from this study demonstrate that all animals exposed to hypoxia presented with weight loss within the first week, irrespective of genotype. Weight loss within the first week was observed in the *Hx* + *veh* and *Hx* + *SU5416* groups when compared with the *Nx* + *veh* group even when accounting for differences in starting weight, which is in agreement with existing literature (Leal et al., 1995; Schols and Westerterp, 2002; Murray and Montgomery, 2014).

To circumvent the limitations of *in-vitro* approaches that were discussed earlier, Ca^{2+} channel subunit expression was assessed in lung tissues from mice exposed to both atmospheric O_2 conditions and hypoxia (10% O_2) to assess hypoxia-induced changes in gene expression. In this instance, the partial pressure of O_2 to which cells were exposed under atmospheric conditions reflected that of normal physiology and thus provided a true reflection of Ca^{2+} channel subunit expression, providing confidence that the *in-vivo* qPCR data from this study was physiologically relevant.

Quantitative PCR data was quite variable, possibly because RNA from whole lungs was used as opposed to RNA from small arterioles only. Because gene expression is variable across the vascular bed, studies to identify gene expression in small arterioles to assess the Ca^{2+} channel subunits that contribute specifically to distal muscularisation would be beneficial. This is discussed further in Section 6.2.

Figure 5.3 (B) demonstrates a significant increase in Fulton's index in the *Hx + SU5416* group, supporting that this model reproduces the cardiac indices associated with CH-induced PH to a greater extent than CH alone. Also supporting the *Hx + SU5416* model as a superior alternative to CH alone for reproducing the cardiac indices associated with CH-induced PH was the observation that LV EF and LV FS were reduced in the *Hx + SU5416* group to a greater extent than the *Hx + veh* group. Since LV failure can occur secondary to RV failure, these data support that the *Hx + SU5416* model produces more severe cardiac indices than CH alone, which is in agreement with existing literature (Taraseviciene-Stewart et al., 2001; Ciuclan et al., 2011).

The number of animals that underwent successful haemodynamic analysis was limited in the *Hx + SU5416* group, due to the observation that three of the four animals in this group did not remain anaesthetised using a standard anaesthetic protocol, suggesting impaired pulmonary uptake of inhalational isoflurane. To circumvent this, these animals were supplemented with injectable lidocaine to allow PV loops to be performed. However, upon RV cardiac catheterisation, exsanguination occurred and PV recordings were unsuccessful. More data is required to assess haemodynamics in mice exposed to *Hx + SU5416*. However, the observation that pulmonary uptake of inhalational isoflurane was impaired in these animals, and RV catheterisation caused these animals to bleed out is a good indicator that the haemodynamic phenotype was more severe in these animals, which suggests an overall worse CH-induced PH phenotype in the *Hx + SU5416* group.

Figure 5.7 (B) demonstrates a significant increase in ESP in the *Hx + veh* group when compared with the *Nx + veh* group. Since ESP is closely associated with end PAP (Vonk-Noordegraaf and Westerhof, 2013), this is a good indicator of the CH-induced PH phenotype, which is clinically characterised by elevated PAP. Figure 5.7 (A) also demonstrates a significant increase in ESV in the *Hx + veh* group when compared with the *Nx + veh* group. Since ESV is calculated by end-diastolic volume (EDV) minus stroke volume (SV), an increase in ESV indicates that SV is reduced. In CH-induced PH, SV can decrease when an increase in PAP causes an increase in RV afterload, meaning the heart has to contract more forcefully to eject blood. Since heart failure is associated with CH-induced PH, inotropy cannot be increased effectively, causing a reduction in SV and an increase in ESV.

Figure 5.7 (C) also indicates a non-significant increase in E_a, which is used as a measure of PVR. E_a is the product of PVR and heart rate. Since heart rate was unchanged (Figure 5.7, E), but E_a was increased, PVR must also be increased, which is characteristic of CH-induced PH (Vonk-Noordegraaf and Westerhof, 2013).

In terms of distal muscularisation, when using both GFP lineage tracing and α-SMA staining as markers of smooth muscle cells, no significant difference was observed in the smooth muscle population between the *Nx + veh* and *Hx + SU5416* groups, despite significant differences being demonstrated when quantifying GFP lineage tracing alone (Figures 5.10, B and 5.12, A). Thus, in corroboration with previously published literature (Ng et al., 1998; Sousa et al., 2001; Rensen et al., 2007; Choi et al., 2018), these observations demonstrate that α-SMA is not a reliable marker of smooth muscle cells for quantification of vascular remodelling. In fact, its inclusion in this study impeded the detection of statistically significant increases in the smooth muscle cell population in the *Hx + SU5416* group. Thus, smooth muscle lineage tracing technology is a superior approach to assess the smooth muscle remodelling processes associated with CH-induced PH, which supports claims made by Shankman et al. (2015).

Due to time limitations, focus was placed on investigating the influence of selective Orai1 inhibition with JPIII on morphological cardiac indices, specifically Fulton’s index; and distal muscularisation. However, future work to investigate the benefits of Orai1 inhibition on RV haemodynamics would be beneficial.

When assessing the effect of JPIII on distal muscularisation, due to the small number of SM-mTmG-Cre animals available, no *Nx* + *veh* group was used. Thus, studies were carried out on mice exposed to either *Hx* + *SU5416* + *DMSO* or *Hx* + *SU5416* + *JPIII.* Quantification of these data revealed a significant reduction in the percentage of GFP+ cells in the *Hx* + *SU5416* + *JPIII* group when compared with the *Hx* + *SU5416* + *DMSO* group, providing convincing evidence that selective Orai1 inhibition reduces the distal muscularisation and arteriolar remodelling associated with CH-induced PH. These findings dramatically advance existing knowledge, since neither distal muscularisation or the effect of JPIII on distal muscularisation have been investigated or quantified in *in-vivo* models of CH-induced PH. These data are the result of preliminary investigations and further studies will be required to elucidate the potential of Orai1 as an anti-proliferative target in CH-induced PH.

In conclusion, these data demonstrate that the SuHx mouse model of CH-induced PH produces a more severe phenotype than CH alone, which is in agreement with existing literature (Taraseviciene-Stewart et al., 2001; Ciuclan et al., 2011). The findings also support lineage tracing technology as a more useful approach than traditional staining approaches to study the VSMC population in proliferative vascular diseases. For the first time, this thesis demonstrates that selective Orai1 inhibition with JPIII protects from distal muscularisation and RV hypertrophy in the SuHx model of CH-induced PH.

Chapter 6

Discussion

The original aim of this thesis was to investigate whether T-type Ca^{2+} channels and Orai1 are viable anti-proliferative targets in hypoxia-induced pulmonary VSMC proliferation and CH-induced PH. To achieve this, the main objectives of this study were to:

1. Validate commercially available HPASMCs as an *in-vitro* model to study hypoxia-induced pulmonary VSMC proliferation
2. Investigate the ability of widely used T-type Ca^{2+} channel inhibitors to reduce hypoxia-induced VSMC proliferation
3. Investigate the ability of the novel, selective Orai1 inhibitor, JPIII, to reduce hypoxia-induced VSMC proliferation
4. Reproduce CH-induced PH *in vivo*
5. Investigate the effect of selective Orai1 inhibition on parameters of CH-induced PH *in vivo*

6.1 Objective 1: Validating HPASMCs as an *in-vitro* model to study hypoxia-induced pulmonary VSMC proliferation

The key observations from this investigation were that commercially available HPASMCs cultured in hypoxia proliferate faster, adopt a rhomboid morphology and demonstrate downregulation of contractile markers. This is in corroboration with existing literature, which has also demonstrated a hypoxia-induced increase in pulmonary VSMC proliferation (Cooper and Beasley, 1999; Voelkel and Tuder, 2000; Humbert et al., 2004; House et al., 2008; Stenmark et al., 2009), and more generally, a rhomboid morphology (Steucke et al., 2015;

Zhang et al., 2016) and downregulation of contractile markers (Rensen et al., 2007; Choi et al., 2018) in VSMCs. Although there were limitations to the data presented (Section 3.3), the observations went some way to validating the identity of commercially available HPASMCs and provided sufficient insight that HPASMCs cultured in 1% O_2 were a suitable *in-vitro* model to study the mechanisms of hypoxia-induced pulmonary VSMC proliferation.

One limitation worthy of further consideration in future research in general is the use of a standard cell culture environment of ~20% O_2 (partial pressure of 140 mmHg)—a level at which cells in the human body would not be exposed (Prabhakar and Semenza, 2012). Ast and Mootha (2019) explained that a partial pressure of 140 mmHg is greater than that of the lung alveoli (110 mmHg), which experience the highest partial pressure of O_2 of any site in the human body. Thus, even in the pulmonary system, standard cell culture conditions of ~20% O_2 are supraphysiological (Place et al., 2017; Stuart et al., 2018). This is a substantial limitation in mammalian cell culture generally, since cells cultured in normoxia are used as a representation of normal cellular physiology, when in reality, the characteristics of cultured cells represent those observed under a PO_2 that is physiologically irrelevant.

The consideration of *hyperoxia* is even more pertinent when directly studying the effect of variable O_2 conditions on the characteristics of cells. For example, the high O_2 tension of standard cell culture conditions may suppress the expression of genes that would normally be expressed in normoxic tissues *in situ.* With relevance to this research, the expression of the transcription factor, HIF1α, is reduced as O_2 tension is increased (Semenza, 2012). HIF1α has been linked to regulation of Ca^{2+} channel subunit expression, specifically Orai2 (Wang et al., 2017), $Ca_v3.2$ (González-Rodríguez et al., 2015) and $Ca_v1.2$ (Li et al., 2015). Thus, assessing Ca^{2+} channel subunit expression in a standard cell culture environment of ~20% O_2 may not reflect the expression of these Ca^{2+} channel subunits *in situ*.

Given the above, although *in-vitro* observations cannot be extrapolated to reflect normal physiology, they can be interpreted in the context of the literature, where standard cell culture conditions are widely used to represent normoxia *in vitro* (Cimmino et al., 2019).

In summary, future efforts should address this limitation when using *in-vitro* approaches more generally. Where appropriate, *in-vivo* models should be used to support *in-vitro* data, which was achieved in Chapter 5 of this research.

6.2 Objective 2: Investigating the ability of widely used T-type Ca^{2+} channel inhibitors to reduce hypoxia-induced pulmonary VSMC proliferation

The validated *in-vitro* model of hypoxia-induced pulmonary VSMC proliferation was used to observe the anti-proliferative effects of widely used T-type Ca^{2+} channel inhibitors. This objective also aimed to confirm lack of off-target modulation of these inhibitors on other Ca^{2+} entry pathways associated with hypoxia-induced VSMC proliferation, including Orai1-mediated SOCE and TRPC1/4-mediated Ca^{2+} entry.

The key findings from this investigation confirmed that T-type Ca^{2+} channel blockers, particularly mibefradil and NNC55-0396, are poorly selective. For the first time, it was shown that these inhibitors exert off-target effects on Orai1-mediated SOCE, which adds to the extensive list of alternative targets that are modulated by these inhibitors (Nilius et al., 1997; Ernst and Kelly, 1998; Liu et al., 1999; Chouabe et al., 2000; Perchenet and Clement-Chomienne, 2000;

Wandel et al., 2000; Bui et al., 2008). This observation is particularly important in studies that have employed these inhibitors to elucidate the anti-proliferative potential of T-type Ca^{2+} channels, not just in the context of PH, but also in other proliferative diseases such as cancer (Lijnen et al., 1999; Lu et al., 2008; Dziegielewska et al., 2014; Huang et al., 2015).

Although mibefradil and NNC55-0396 were poorly selective for the T-type Ca^{2+} channel, TTA-A2 did not demonstrate off-target effects on Orai1-mediated SOCE or TRPC1/4-mediated Ca^{2+} entry. TTA-A2 also reduced pulmonary VSMC proliferation in this study, which is in support of previous studies that demonstrated that treatment of CH rats with TTA-A2, and $Ca_v3.1$ deletion, inhibited RV hypertrophy, vascular remodelling and CH-induced PH (Chevalier et al., 2014). Thus, it is likely that T-type Ca^{2+} channels contribute, at least in part, to pulmonary VSMC proliferation. Despite this, this thesis demonstrates that T-type Ca^{2+} channel mRNA was not upregulated in response to hypoxia either *in vitro* or *in vivo,* forcing us to re-evaluate the contribution of these channels to pulmonary vascular remodelling in CH-induced PH. This was surprising given that Wan et al. (2013) reported a significant increase in T-type Ca^{2+} channel mRNA in pulmonary arteries of mice with CH-induced PH. It was speculated that these discrepancies may be due to differences in the percentage O_2 used to define hypoxia. However, the gas composition (1% O_2), species (mouse), period of hypoxic exposure (four weeks), and qPCR data analysis method ($2^{-\Delta\Delta Ct}$) were identical. It is possible that the analysis of RNA from whole lungs in this thesis, as opposed to RNA specifically from isolated pulmonary VSMCs may account for the contradiction. Since gene expression is variable across the vascular bed, an assessment of Ca^{2+} channel gene expression specifically in pulmonary VSMCs from vessels that are most susceptible to distal muscularisation, such as small arterioles, would be beneficial.

Taken together, absence of any hypoxia-induced upregulation in T-type Ca^{2+} channel mRNA, limited availability of highly selective inhibitors and complete lack of T-type Ca^{2+} channel blockers in the clinic limits the potential of T-type Ca^{2+} channels as anti-proliferative targets in hypoxia-induced VSMC proliferation and CH-induced PH.

Conversely, both *in-vitro* and *in-vivo* qPCR data showed upregulation of *ORAI1* and *TRPC1*—a finding that pivoted the study to investigate the potential of selective Orai1 inhibition as an anti-proliferative approach for hypoxia-induced pulmonary VSMC proliferation.

6.3 Objective 3: Investigating the ability of the novel Orai1 inhibitor, JPIII, to reduce hypoxia-induced pulmonary VSMC proliferation

The key findings from this investigation revealed that the Orai1 inhibitor, JPIII, which had previously demonstrated superior selectivity against 44 other targets (Figure 4.18) exhibited no off-target effects on T-type Ca^{2+} current. JPIII potently inhibited Orai1-mediated SOCE in WT HEK293 cells, which is in agreement with unpublished findings from Dr Marc Bailey’s laboratory. For the first time, this research investigated the anti-proliferative effect of selective Orai1 inhibition on pulmonary VSMC proliferation and demonstrated that JPIII significantly reduced HPASMC proliferation in a validated *in-vitro* model.

Upregulation of *ORAI1 in vitro* and *in vivo* combined with a significant reduction in HPASMC proliferation by JPIII reasserted promise for Orai1 as an anti-proliferative target in CH-induced PH, which is in agreement with evidence presented in a recent review by Rode et al. (2018). The observation that JPIII reduces proliferation of hypoxic HPASMCs *in vitro* is novel and can be used as pilot data for future investigations with larger samples sizes.

6.4 Objective 4: Reproducing CH-induced PH *in vivo*

The findings from Chapter 4 progressed the study to reproduce the CH and SuHx mouse models of CH-induced PH for the first time at the University of Leeds, which was achieved upon observing the morphological cardiac indices, cardiac haemodynamics and distal muscularisation associated with CH-induced PH that have previously been outlined in the literature (Taraseviciene-Stewart et al., 2001; Stenmark et al., 2009; Ciuclan et al., 2011; Vitali et al., 2014).

The main findings from this investigation were that the SuHx mouse model produced a more severe phenotype than that produced by CH alone, which is in agreement with previous publications (Taraseviciene-Stewart et al., 2001; Ciuclan et al., 2011). Specifically, the SuHx mouse model presented with significant weight loss, a significant increase in Fulton's index (indicating RV hypertrophy) and a reduction in LV EF and FS (indicating heart failure), all of which were more marked than that observed in mice exposed to CH alone.

The observation that *STIM1* was upregulated in the *Hx* + *SU5416* group but not the *Hx* + *veh* group is interesting, since the interaction of Orai1 with STIM1 is required for Orai1-dependent SOCE, raising speculation that the worsened CH-induced PH phenotype observed in the SuHx group may be due to the enhanced interaction between STIM1 and Orai1, increasing SOCE, pulmonary VSMC proliferation and distal muscularisation. In support of this speculation, Hou et al. (2013) showed that knockdown of *STIM1* inhibited hypoxia-induced proliferation by inhibition of SOCE in isolated rat pulmonary VSMCs. STIM1 and

Orai1 upregulation have also been observed in previous studies (Chen et al., 2017; Wang et al., 2017; He et al., 2018).

To provide novelty to this research and advance earlier studies that used traditional approaches such as haematoxylin and eosin staining and immunohistochemistry to assess pulmonary vascular remodelling and distal muscularisation in the SuHx model (Stewart et al., 2001; Casserly et al., 2011; Ciuclan et al., 2011), lineage tracing technology was used to quantify distal muscularisation. It appears that α-SMA staining is limited to the detection of differentiated (contractile) VSMCs that express this marker at the protein level at the particular period in time when staining is carried out. Upon phenotypic switching to the proliferative phenotype, α-SMA is downregulated and thus is no longer an effective marker of VSMCs. Thus, this traditional staining approach misses a substantial proportion of the phenotypic switching and vascular remodelling that occurs in CH-induced PH (Shankman et al., 2015). This should be considered when interpreting previously published literature using α-SMA staining as a measure of vascular remodelling, as it is possible that the true extent of remodelling may have been underestimated. Thus, α-SMA is not a reliable marker of SMCs for quantification of vascular remodelling (Ng et al., 1998; Sousa et al., 2007). Lineage tracing technology circumvents this issue and is therefore a more reliable approach to measure distal muscularisation and remodelling in CH-induced PH and more generally, in other proliferative vascular diseases.

6.5 Objective 5: Investigating the effect of selective Orai1 inhibition on the development of CH-induced PH *in vivo*

After concluding a more severe phenotype in the SuHx mouse model, this model was used to investigate the effect of selective Orai1 inhibition on parameters of CH-induced PH *in vivo.* Due to time and money limitations, specific focus was placed on measuring the effect of JPIII on the cardiac indices and distal muscularisation associated with CH-induced PH.

For the first time, lineage tracing revealed that selective Orai1 inhibition with JPIII significantly reduced the distal muscularisation associated with CH-induced PH. JPIII also protected from RV hypertrophy, supporting Orai1 as a viable target with great promise in CH-induced PH.

To advance this knowledge in future work, studies using the SMC-ERT2+Orai1-FL mouse line crossed with the floxed mTmG reporter mouse line would be valuable since this would enable the use of lineage tracing technology to study the effects of Orai1 knockdown on distal muscularisation. This mouse line was in the process of being developed at the University of Leeds towards the end of this PhD project, thus insight on this approach is possible in the near future. To avoid the undesirable effects of global knockdown, efforts should also be made to achieve pulmonary-specific Orai1 knockdown to elucidate the role of Orai1 in the distal muscularisation observed in CH-induced PH.

Providing selective Orai1 inhibition continues to show benefit for CH-induced PH in future studies, long-term focus should be on synthesising novel Orai1 inhibitors that can be selectively administered to the pulmonary circulation *in vivo.* Since Orai1 is widely expressed in mammals, selective pulmonary administration would avoid off-target effects that may be associated with constitutive Orai1 inhibition. Improved pharmacokinetics would also beneficial, such as an extended half-life to avoid the need for continuous infusion. The superior selectivity of JPIII makes this compound a useful starting point for synthesis of novel compounds.

6.6 Conclusion

In conclusion, selective inhibition of Orai1 significantly reduces pulmonary VSMC proliferation *in vitro*, and RV hypertrophy and distal muscularisation *in vivo*, and is a viable anti-proliferative target worthy of further investigation in CH-induced PH for a translational drug development programme.

References

Abramowitz, J. and Birnbaumer, L. 2009. Physiology and pathophysiology of canonical transient receptor potential channels. *Faseb j.* **23**(2), pp.297-328.

Aherrarou, R. 2018. PHACTR1 and Smooth Muscle Cell Behavior. https://www.rc.virginia.edu/project/smooth-muscle-cells/.

Alexander, M.R. and Owens, G.K. 2012. Epigenetic control of smooth muscle cell differentiation and phenotypic switching in vascular development and disease. *Annu Rev Physiol.* **74**, pp.13-40.

Antoniu, S.A. 2012. Targeting PDGF pathway in pulmonary arterial hypertension. *Expert Opin Ther Targets.* **16**(11), pp.1055-1063.

Archer, S.L., Souil, E., Dinh-Xuan, A.T., Schremmer, B., Mercier, J.C., El Yaagoubi, A., Nguyen-Huu, L., Reeve, H.L. and Hampl, V. 1998. Molecular identification of the role of voltage-gated K+ channels, Kv1.5 and Kv2.1, in hypoxic pulmonary vasoconstriction and control of resting membrane potential in rat pulmonary artery myocytes. *J Clin Invest.* **101**(11), pp.2319-2330.

Archer, S.L., Weir, E.K. and Wilkins, M.R. 2010. Basic science of pulmonary arterial hypertension for clinicians: new concepts and experimental therapies. *Circulation.* **121**(18), pp.2045-2066.

Ast, T. and Mootha, V.K. 2019. Oxygen and mammalian cell culture: are we repeating the experiment of Dr. Ox? *Nature Metabolism.* **1**(9), pp.858-860.

Baba, Y., Hayashi, K., Fujii, Y., Mizushima, A., Watarai, H., Wakamori, M., Numaga, T., Mori, Y., Iino, M., Hikida, M. and Kurosaki, T. 2006. Coupling of STIM1 to store-operated Ca2+ entry through its constitutive and inducible movement in the endoplasmic reticulum. *Proc Natl Acad Sci U S A.* **103**(45), pp.16704-16709.

Babij, P., Kawamoto, S., White, S., Adelstein, R.S. and Periasamy, M. 1992. Differential expression of SM1 and SM2 myosin isoforms in cultured vascular smooth muscle. *American Journal of Physiology-Cell Physiology.* **262**(3), pp.C607-C613.

Badesch, D.B., Champion, H.C., Sanchez, M.A., Hoeper, M.M., Loyd, J.E., Manes, A., McGoon, M., Naeije, R., Olschewski, H., Oudiz, R.J. and Torbicki, A. 2009. Diagnosis and assessment of pulmonary arterial hypertension. *J Am Coll Cardiol.* **54**(1 Suppl), pp.S55-66.

Balasubramaniam, V., Le Cras, T.D., Ivy, D.D., Grover, T.R., Kinsella, J.P. and Abman, S.H. 2003. Role of platelet-derived growth factor in vascular remodeling during pulmonary hypertension in the ovine fetus. *Am J Physiol Lung Cell Mol Physiol.* **284**(5), pp.L826-833.

Baliga, R.S., MacAllister, R.J. and Hobbs, A.J. 2011. New perspectives for the treatment of pulmonary hypertension. *Br J Pharmacol.* **163**(1), pp.125-140.

Barrow JC, KAS, B., RV, C., MC, M., TS, R., Y, S., Z-Q, Y. and Merck & Co., I., assignee. 2007. Pyridyl amide T-type calcium channel antagonists.

Barst, R.J. 2005. PDGF signaling in pulmonary arterial hypertension. *The Journal of clinical investigation.* **115**(10), pp.2691-2694.

Beech, D.J. 2013. Characteristics of transient receptor potential canonical calcium-permeable channels and their relevance to vascular physiology and disease. *Circ J.* **77**(3), pp.570-579.

Beech, D.J., Xu, S.Z., McHugh, D. and Flemming, R. 2003. TRPC1 store-operated cationic channel subunit. *Cell Calcium.* **33**(5), pp.433-440.

Bilder, G., Wentz, T., Leadley, R., Amin, D., Byan, L., O'Conner, B., Needle, S., Galczenski, H., Bostwick, J., Kasiewski, C., Myers, M., Spada, A., Merkel, L., Ly, C., Persons, P., Page, K., Perrone, M. and Dunwiddie, C. 1999. Restenosis Following Angioplasty in the Swine Coronary Artery Is Inhibited By an Orally Active PDGF-Receptor Tyrosine Kinase Inhibitor, RPR101511A. *Circulation.* **99**(25), pp.3292-3299.

Bisaillon, J.M., Motiani, R.K., Gonzalez-Cobos, J.C., Potier, M., Halligan, K.E., Alzawahra, W.F., Barroso, M., Singer, H.A., Jourd'heuil, D. and Trebak, M. 2010. Essential role for STIM1/Orai1-mediated calcium influx in PDGF-induced smooth muscle migration. *Am J Physiol Cell Physiol.* **298**(5), pp.C993-1005.

Bodi, I., Mikala, G., Koch, S.E., Akhter, S.A. and Schwartz, A. 2005. The L-type calcium channel in the heart: the beat goes on. *J Clin Invest.* **115**(12), pp.3306-3317.

Bourinet, E., Mangoni, M.E. and Nargeot, J. 2004. Dissecting the functional role of different isoforms of the L-type Ca2+ channel. *The Journal of clinical investigation.* **113**(10), pp.1382-1384.

Bowes, J., Brown, A.J., Hamon, J., Jarolimek, W., Sridhar, A., Waldron, G. and Whitebread, S. 2012. Reducing safety-related drug attrition: the use of in vitro pharmacological profiling. *Nat Rev Drug Discov.* **11**(12), pp.909-922.

Brogden, R.N. and Markham, A. 1997. Drugs. https://doi.org/10.2165/00003495-199754050-00010.

Brown, L. M., Chen, H., Halpern, S., Taichman, D., McGoon, M. D., Farber, H. W., Frost, A. E., Liou, T. G., Turner, M., Feldkircher, K., Miller, D. P. and Elliott, C. G. 2011. Delay in recognition of pulmonary arterial hypertension: factors identified from the REVEAL Registry. *Chest,* 140**,** 19-26.

Bruno, S. and Darzynkiewicz, Z. 1992. Cell cycle dependent expression and stability of the nuclear protein detected by ki-67 antibody in HL-60 cells. *Cell Proliferation.* **25***,* pp.31-40.

Bui, P.H., Quesada, A., Handforth, A. and Hankinson, O. 2008. The Mibefradil Derivative NNC55-0396, a Specific T-Type Calcium Channel Antagonist, Exhibits Less CYP3A4 Inhibition than Mibefradil. *Drug Metabolism and Disposition.* **36**(7), pp.1291-1299.

Burg, E.D., Remillard, C.V. and Yuan, J.X. 2008. Potassium channels in the regulation of pulmonary artery smooth muscle cell proliferation and apoptosis: pharmacotherapeutic implications. *Br J Pharmacol.* **153 Suppl 1**, pp.S99-s111.

Cahalan, M.D. 2009. STIMulating store-operated Ca(2+) entry. *Nature cell biology.* **11**(6), pp.669-677.

Capes-Davis, A., Theodosopoulos, G., Atkin, I., Drexler, H.G., Kohara, A., MacLeod, R.A., Masters, J.R., Nakamura, Y., Reid, Y.A., Reddel, R.R. and Freshney, R.I. 2010. Check your cultures! A list of cross-contaminated or misidentified cell lines. *Int J Cancer.* **127**(1), pp.1-8.

Carbone, E. and Lux, H.D. 1984. A low voltage-activated, fully inactivating Ca channel in vertebrate sensory neurones. *Nature.* **310**(5977), pp.501-502.

Carson, C., Raman, P., Tullai, J., Xu, L., Henault, M., Thomas, E., Yeola, S., Lao, J., McPate, M., Verkuyl, J.M., Marsh, G., Sarber, J., Amaral, A., Bailey, S., Lubicka, D., Pham, H., Miranda, N., Ding, J., Tang, H.-M., Ju, H., Tranter, P., Ji, N., Krastel, P., Jain, R.K., Schumacher, A.M., Loureiro, J.J., George, E., Berellini, G., Ross, N.T., Bushell, S.M., Erdemli, G. and Solomon, J.M. 2015. Englerin A Agonizes the TRPC4/C5 Cation Channels to Inhibit Tumor Cell Line Proliferation. *PLOS ONE.* **10**(6), pe0127498.

Casserly, B., Mazer, J.M., Vang, A., Harrington, E.O., Klinger, J.R., Rounds, S. and Choudhary, G. 2011. C-type natriuretic peptide does not attenuate the development of pulmonary hypertension caused by hypoxia and VEGF receptor blockade. *Life Sci.* **89**(13-14), pp.460-466.

Chakraborty, R., Sikarwar, A. S., Hinton, M., Dakshinamurti S. and Chelikani, P. 2017. Characterization of GPCR signaling in hypoxia. *Methods Cell Biol,* 142**,** 101-110.

Chemin, J., Monteil, A., Briquaire, C., Richard, S., Perez-Reyes, E., Nargeot, J. and Lory, P. 2000. Overexpression of T-type calcium channels in HEK-293 cells increases intracellular calcium without affecting cellular proliferation. *FEBS Lett.* **478**(1-2), pp.166-172.

Chen, T.X., Xu, X.Y., Zhao, Z., Zhao, F.Y., Gao, Y.M., Yan, X.H. and Wan, Y. 2017. Hydrogen peroxide is a critical regulator of the hypoxia-induced alterations of store-operated Ca(2+) entry into rat pulmonary arterial smooth muscle cells. *Am J Physiol Lung Cell Mol Physiol.* **312**(4), pp.L477-l487.

Cheng, K.T., Liu, X., Ong, H.L., Swaim, W. and Ambudkar, I.S. 2011. Local Ca(2)+ entry via Orai1 regulates plasma membrane recruitment of TRPC1 and controls cytosolic Ca(2)+ signals required for specific cell functions. *PLoS Biol.* **9**(3), pe1001025.

Cheng, G. S., Zhang, Y. S., Zhang, T. T., He, L. and Wang, X. Y. 2017. Bone marrow-derived mesenchymal stem cells modified with IGFBP-3 inhibit the proliferation of pulmonary artery smooth muscle cells. *Int J Mol Med,* 39**,** 223-230.

Chevalier, M., Gilbert, G., Roux, E., Lory, P., Marthan, R., Savineau, J.P. and Quignard, J.F. 2014. T-type calcium channels are involved in hypoxic pulmonary hypertension. *Cardiovasc Res.* **103**(4), pp.597-606.

Choi, S., Park, M., Kim, J., Park, W., Kim, S., Lee, D.-K., Hwang, J.Y., Choe, J., Won, M.-H., Ryoo, S., Ha, K.-S., Kwon, Y.-G. and Kim, Y.-M. 2018. TNF-α elicits phenotypic and functional alterations of vascular smooth muscle cells by miR-155-5p–dependent down-regulation of cGMP-dependent kinase 1. *Journal of Biological Chemistry.* **293**(38), pp.14812-14822.

Chouabe, C., Drici, M.D., Romey, G. and Barhanin, J. 2000. Effects of calcium channel blockers on cloned cardiac K+ channels IKr and IKs. *Therapie.* **55**(1), pp.195-202.

Christen, T., Bochaton-Piallat, M.L., Neuville, P., Rensen, S., Redard, M., van Eys, G. and Gabbiani, G. 1999. Cultured porcine coronary artery smooth muscle cells. A new model with advanced differentiation. *Circ Res.* **85**(1), pp.99-107.

Christen, T., Verin, V., Bochaton-Piallat, M.-L., Popowski, Y., Ramaekers, F., Debruyne, P., Camenzind, E., Eys, G. and Gabbiani, G. 2001. Mechanisms of neointima formation and remodeling in the porcine coronary artery. *Circulation.* **103**, pp.882-888.

Christman, B.W., McPherson, C.D., Newman, J.H., King, G.A., Bernard, G.R., Groves, B.M. and Loyd, J.E. 1992. An imbalance between the excretion of thromboxane and prostacyclin metabolites in pulmonary hypertension. *N Engl J Med.* **327**(2), pp.70-75.

Cimmino, F., Avitabile, M., Lasorsa, V.A., Montella, A., Pezone, L., Cantalupo, S., Visconte, F., Corrias, M.V., Iolascon, A. and Capasso, M. 2019. HIF-1 transcription activity: HIF1A driven response in normoxia and in hypoxia. *BMC Medical Genetics.* **20**(1), p37.

Ciuclan, L., Bonneau, O., Hussey, M., Duggan, N., Holmes, A.M., Good, R., Stringer, R., Jones, P., Morrell, N.W., Jarai, G., Walker, C., Westwick, J. and Thomas, M. 2011. A novel murine model of severe pulmonary arterial hypertension. *Am J Respir Crit Care Med.* **184**(10), pp.1171-1182.

Clapham, D.E. 2003. TRP channels as cellular sensors. *Nature.* **426**(6966), pp.517-524.

Clunn, G.F., Sever, P.S. and Hughes, A.D. 2010. Calcium channel regulation in vascular smooth muscle cells: synergistic effects of statins and calcium channel blockers. *International journal of cardiology.* **139**(1), pp.2-6.

Cooper, A.L. and Beasley, D. 1999. Hypoxia stimulates proliferation and interleukin-1α production in human vascular smooth muscle cells. *American Journal of Physiology - Heart and Circulatory Physiology.* **277**(4), pp.H1326-H1337.

Cooper, R.A. and Huxtable, R.J. 1999. The relationship between reactivity of metabolites of pyrrolizidine alkaloids and extrahepatic toxicity. *Proceedings of the Western Pharmacology Society.* **42**.

Cribbs, L.L. 2006. T-type Ca2+ channels in vascular smooth muscle: multiple functions. *Cell Calcium.* **40**(2), pp.221-230.

Demuro, A., Penna, A., Safrina, O., Yeromin, A.V., Amcheslavsky, A., Cahalan, M.D. and Parker, I. 2011. Subunit stoichiometry of human Orai1 and Orai3 channels in closed and open states. *Proc Natl Acad Sci U S A.* **108**(43), pp.17832-17837.

Deyo, J.A., Reed, R.L., Buhler, D.R. and Kerkvliet, N.I. 1994. Role of metabolism in monocrotaline-induced immunotoxicity in C57BL/6 mice. *Toxicology.* **94**(1-3), pp.209-222.

Di Sabatino, A., Rovedatti, L., Kaur, R., Spencer, J.P., Brown, J.T., Morisset, V.D., Biancheri, P., Leakey, N.A., Wilde, J.I., Scott, L., Corazza, G.R., Lee, K., Sengupta, N., Knowles, C.H., Gunthorpe, M.J., McLean, P.G., MacDonald, T.T. and Kruidenier, L. 2009. Targeting gut T cell Ca2+ release-activated Ca2+ channels inhibits T cell cytokine production and T-box transcription factor T-bet in inflammatory bowel disease. *J Immunol.* **183**(5), pp.3454-3462.

Dolphin, A.C. 2006. A short history of voltage-gated calcium channels. *British Journal of Pharmacology.* **147**(S1), pp.S56-S62.

Dolphin, A.C. 2016. Voltage-gated calcium channels and their auxiliary subunits: physiology and pathophysiology and pharmacology. *J Physiol.* **594**(19), pp.5369-5390.

Duckles, H., Boycott, H.E., Al-Owais, M.M., Elies, J., Johnson, E., Dallas, M.L., Porter, K.E., Giuntini, F., Boyle, J.P., Scragg, J.L. and Peers, C. 2015. Heme oxygenase-1 regulates cell proliferation via carbon monoxide-mediated inhibition of T-type Ca2+ channels. *Pflugers Arch.* **467**(2), pp.415-427.

Dumitrascu, R., Koebrich, S., Dony, E., Weissmann, N., Savai, R., Pullamsetti, S.S., Ghofrani, H.A., Samidurai, A., Traupe, H., Seeger, W., Grimminger, F. and Schermuly, R.T. 2008. Characterization of a murine model of monocrotaline pyrrole-induced acute lung injury. *BMC pulmonary medicine.* **8**, pp.25-25.

Dunham-Snary, K.J., Wu, D., Sykes, E.A., Thakrar, A., Parlow, L.R.G., Mewburn, J.D., Parlow, J.L. and Archer, S.L. 2017. Hypoxic Pulmonary Vasoconstriction: From Molecular Mechanisms to Medicine. *Chest.* **151**(1), pp.181-192.

DURECT. 2019. ALZET Osmotic Pumps: Mechanism of Operation. *Available from: https://www.alzet.com/products/alzet_pumps/how-does-it-work/.*

Dziegielewska, B., Brautigan, D.L., Larner, J.M. and Dziegielewski, J. 2014. T-Type Ca²⁺ Channel Inhibition Induces p53-Dependent Cell Growth Arrest and Apoptosis through Activation of p38-MAPK in Colon Cancer Cells. *Molecular Cancer Research.* **12**(3), pp.348-358.

Ernst, M.E. and Kelly, M.W. 1998. Mibefradil, a pharmacologically distinct calcium antagonist. *Pharmacotherapy.* **18**(3), pp.463-485.

Evans, C.E., Bendahl, P.-O., Belting, M., Branco, C. and Johnson, R.S. 2016. Diverse roles of cell-specific hypoxia-inducible factor 1 in cancer-associated hypercoagulation. *Blood.* **127**(10), pp.1355-1360.

Feske, S., Gwack, Y., Prakriya, M., Srikanth, S., Puppel, S.H., Tanasa, B., Hogan, P.G., Lewis, R.S., Daly, M. and Rao, A. 2006. A mutation in Orai1 causes immune deficiency by abrogating CRAC channel function. *Nature.* **441**(7090), pp.179-185.

Feske, S. and Prakriya, M. 2013. Conformational dynamics of STIM1 activation. *Nature Structural &Amp; Molecular Biology.* **20**, p918.

Firth, A.L., Remillard, C.V., Platoshyn, O., Fantozzi, I., Ko, E.A. and Yuan, J.X. 2011. Functional ion channels in human pulmonary artery smooth muscle cells: Voltage-dependent cation channels. *Pulm Circ.* **1**(1), pp.48-71.

Fox, A.P., Nowycky, M.C. and Tsien, R.W. 1987. Kinetic and pharmacological properties distinguishing three types of calcium currents in chick sensory neurones. *J Physiol.* **394**, pp.149-172.

Frost, A. E., Badesch, D. B., Barst, R. J., Benza, R. L., Elliott, C. G., Farber, H. W., Krichman, A., Liou, T. G., Raskob, G. E., Wason, P., Feldkircher, K., Turner, M. & McGoon, M. D. 2011. The changing picture of patients with pulmonary arterial hypertension in the United States: how REVEAL differs from historic and non-US Contemporary Registries. *Chest,* 139**,** 128-37.

Fukushima, M., Tomita, T., Janoshazi, A. and Putney, J.W. 2012. Alternative translation initiation gives rise to two isoforms of Orai1 with distinct plasma membrane mobilities. *Journal of Cell Science.* **125**(18), pp.4354-4361.

Galie, N., Corris, P.A., Frost, A., Girgis, R.E., Granton, J., Jing, Z.C., Klepetko, W., McGoon, M.D., McLaughlin, V.V., Preston, I.R., Rubin, L.J., Sandoval, J., Seeger, W. and Keogh, A. 2013. Updated treatment algorithm of pulmonary arterial hypertension. *J Am Coll Cardiol.* **62**(25 Suppl), pp.D60-72.

Galie, N., Manes, A. and Branzi, A. 2003. Prostanoids for pulmonary arterial hypertension. *Am J Respir Med.* **2**(2), pp.123-137.

Ghofrani, H.A., Morrell, N.W., Hoeper, M.M., Olschewski, H., Peacock, A.J., Barst, R.J., Shapiro, S., Golpon, H., Toshner, M., Grimminger, F. and Pascoe, S. 2010. Imatinib in pulmonary arterial hypertension patients with inadequate response to established therapy. *Am J Respir Crit Care Med.* **182**(9), pp.1171-1177.

Ghofrani, H.A., Seeger, W. and Grimminger, F. 2005. Imatinib for the Treatment of Pulmonary Arterial Hypertension. *New England Journal of Medicine.* **353**(13), pp.1412-1413.

Giaid, A., Yanagisawa, M., Langleben, D., Michel, R.P., Levy, R., Shennib, H., Kimura, S., Masaki, T., Duguid, W.P. and Stewart, D.J. 1993. Expression of endothelin-1 in the lungs of patients with pulmonary hypertension. *N Engl J Med.* **328**(24), pp.1732-1739.

Gollasch, M., Haase, H., Ried, C., Lindschau, C., Morano, I., Luft, F.C. and Haller, H. 1998. L-type calcium channel expression depends on the differentiated state of vascular smooth muscle cells. *The FASEB Journal.* **12**(7), pp.593-601.

Golovina, V.A., Platoshyn, O., Bailey, C.L., Wang, J., Limsuwan, A., Sweeney, M., Rubin, L.J. and Yuan, J.X. 2001. Upregulated TRP and enhanced capacitative Ca(2+) entry in human pulmonary artery myocytes during proliferation. *Am J Physiol Heart Circ Physiol.* **280**(2), pp.H746-755.

Gomez-Arroyo, J., Saleem, S.J., Mizuno, S., Syed, A.A., Bogaard, H.J., Abbate, A., Taraseviciene-Stewart, L., Sung, Y., Kraskauskas, D., Farkas, D., Conrad, D.H., Nicolls, M.R. and Voelkel, N.F. 2012. A brief overview of mouse models of pulmonary arterial hypertension: problems and prospects. *Am J Physiol Lung Cell Mol Physiol.* **302**(10), pp.L977-991.

González-Rodríguez, P., Falcón, D., Castro, M.J., Ureña, J., López-Barneo, J. and Castellano, A. 2015. Hypoxic induction of T-type Ca(2+) channels in rat cardiac myocytes: role of HIF-1α and RhoA/ROCK signalling. *The Journal of physiology.* **593**(21), pp.4729-4745.

Grosberg, A., Nesmith, A.P., Goss, J.A., Brigham, M.D., McCain. M.L., Parker, K.K. 2012. Muscle on a chip: *In vitro* contractility assays for smooth and striated muscle. *Journal of Pharmacological and Toxicological Methods, 2012.* doi:10.1016/j.vascn.2012.04.001

Hagiwara, N., Irisawa, H. and Kameyama, M. 1988. Contribution of two types of calcium currents to the pacemaker potentials of rabbit sino-atrial node cells. *J Physiol.* **395**, pp.233-253.

Hao, M., Li, M. and Li, W. 2017. Galectin-3 inhibition ameliorates hypoxia-induced pulmonary artery hypertension. *Mol Med Rep,* 15**,** 160-168.

Hartshorne, D.J., Ito, M. and Erdodi, F. 1998. Myosin light chain phosphatase: subunit composition, interactions and regulation. *J Muscle Res Cell Motil.* **19**(4), pp.325-341.

He, X., Song, S., Ayon, R.J., Balisterieri, A., Black, S.M., Makino, A., Wier, W.G., Zang, W.J. and Yuan, J.X. 2018. Hypoxia selectively upregulates cation channels and increases cytosolic [Ca(2+)] in pulmonary, but not coronary, arterial smooth muscle cells. *Am J Physiol Cell Physiol.* **314**(4), pp.C504-c517.

Heldin, C.H. and Westermark, B. 1999. Mechanism of action and in vivo role of platelet-derived growth factor. *Physiol Rev.* **79**(4), pp.1283-1316.

Hoeper, M.M., Barst, R.J., Bourge, R.C., Feldman, J., Frost, A.E., Galie, N., Gomez-Sanchez, M.A., Grimminger, F., Grunig, E., Hassoun, P.M., Morrell, N.W., Peacock, A.J., Satoh, T., Simonneau, G., Tapson, V.F., Torres, F., Lawrence, D., Quinn, D.A. and Ghofrani, H.A. 2013. Imatinib mesylate as add-on therapy for pulmonary arterial hypertension: results of the randomized IMPRES study. *Circulation.* **127**(10), pp.1128-1138.

Hofmann, T., Schaefer, M., Schultz, G. and Gudermann, T. 2002. Subunit composition of mammalian transient receptor potential channels in living cells. *Proc Natl Acad Sci U S A.* **99**(11), pp.7461-7466.

Hogan, P.G. and Rao, A. 2015. Store-operated calcium entry: Mechanisms and modulation. *Biochemical and biophysical research communications.* **460**(1), pp.40-49.

Hoth, M. and Penner, R. 1992. Depletion of intracellular calcium stores activates a calcium current in mast cells. *Nature.* **355**(6358), pp.353-356.

Hou, X., Chen, J., Luo, Y., Liu, F., Xu, G. and Gao, Y. 2013. Silencing of STIM1 attenuates hypoxia-induced PASMCs proliferation via inhibition of the SOC/Ca2+/NFAT pathway. *Respir Res.* **14**, p2.

Hou, X., Pedi, L., Diver, M.M. and Long, S.B. 2012. Crystal structure of the calcium release-activated calcium channel Orai. *Science.* **338**(6112), pp.1308-1313.

House, S.J., Potier, M., Bisaillon, J., Singer, H.A. and Trebak, M. 2008. The non-excitable smooth muscle: calcium signaling and phenotypic switching during vascular disease. *Pflugers Arch.* **456**(5), pp.769-785.

Houtchens, J. Martin, D. and Klinger, J.R. 2011. Diagnosis and Management of Pulmonary Arterial Hypertension. *Pulmonary Medicine,* vol. 2011, Article ID 845864, 13 pages.

Huang, G.N., Zeng, W., Kim, J.Y., Yuan, J.P., Han, L., Muallem, S. and Worley, P.F. 2006. STIM1 carboxyl-terminus activates native SOC, I(crac) and TRPC1 channels. *Nat Cell Biol.* **8**(9), pp.1003-1010.

Huang, L., Keyser, B.M., Tagmose, T.M., Hansen, J.B., Taylor, J.T., Zhuang, H., Zhang, M., Ragsdale, D.S. and Li, M. 2004. NNC 55-0396 [(1S,2S)-2-(2-(N-[(3-benzimidazol-2-yl)propyl]-N-methylamino)ethyl)-6-fluoro-1,2,3,4-tetrahydro-1-isopropyl-2-naphtyl cyclopropanecarboxylate dihydrochloride]: a new selective inhibitor of T-type calcium channels. *Journal of Pharmacology and Experimental Therapeutics.* **309**(1), pp.193-199.

Huang, W., Lu, C., Wu, Y., Ouyang, S. and Chen, Y. 2015. T-type calcium channel antagonists, mibefradil and NNC-55-0396 inhibit cell proliferation and induce cell apoptosis in leukemia cell lines. *Journal of experimental & clinical cancer research : CR.* **34**(1), pp.54-54.

Hubbi, M.E. and Semenza, G.L. 2015. Regulation of cell proliferation by hypoxia-inducible factors. *Am J Physiol Cell Physiol.* **309**(12), pp.C775-782.

Humbert, M., Monti, G., Fartoukh, M., Magnan, A., Brenot, F., Rain, B., Capron, F., Galanaud, P., Duroux, P., Simonneau, G. and Emilie, D. 1998. Platelet-derived growth factor expression in primary pulmonary hypertension: comparison of HIV seropositive and HIV seronegative patients. *Eur Respir J.* **11**(3), pp.554-559.

Humbert, M., Morrell, N.W., Archer, S.L., Stenmark, K.R., MacLean, M.R., Lang, I.M., Christman, B.W., Weir, E.K., Eickelberg, O., Voelkel, N.F. and Rabinovitch, M. 2004. Cellular and molecular pathobiology of pulmonary arterial hypertension. *J Am Coll Cardiol.* **43**(12 Suppl S), pp.13s-24s.

Humbert, M., Sitbon, O., Chaouat, A., Bertocchi, M., Habib, G., Gressin, V., Yaici, A., Weitzenblum, E., Cordier, J. F., Chabot, F., Dromer, C., Pison, C., Reynaud-Gaubert, M., Haloun, A., Laurent, M., Hachulla, E. and Simonneau, G. 2006. Pulmonary arterial hypertension in France: results from a national registry. *Am J Respir Crit Care Med,* 173**,** 1023-30.

Humbert, M., Sitbon, O., Yaici, A., Montani, D., O'Callaghan, D.S., Jais, X., Parent, F., Savale, L., Natali, D., Gunther, S., Chaouat, A., Chabot, F., Cordier, J.F., Habib, G., Gressin, V., Jing, Z.C., Souza, R. and Simonneau, G. 2010. Survival in incident and prevalent cohorts of patients with pulmonary arterial hypertension. *Eur Respir J.* **36**(3), pp.549-555.

Hutchings, C. J., Colussi, P. and Clark, T. G. 2019. Ion channels as therapeutic antibody targets. *mAbs,* 11**,** 265-296.

Ikebe, M. and Hartshorne, D.J. 1985. Phosphorylation of smooth muscle myosin at two distinct sites by myosin light chain kinase. *J Biol Chem.* **260**(18), pp.10027-10031.

Jernigan, N.L., Resta, T.C. and Walker, B.R. 2004. Contribution of oxygen radicals to altered NO-dependent pulmonary vasodilation in acute and chronic hypoxia. *Am J Physiol Lung Cell Mol Physiol.* **286**(5), pp.L947-955.

Jones, D.A., Benjamin, C.W. and Linseman, D.A. 1995. Activation of thromboxane and prostacyclin receptors elicits opposing effects on vascular smooth muscle cell growth and mitogen-activated protein kinase signaling cascades. *Mol Pharmacol.* **48**(5), pp.890-896.

Joshi, S., Balan, P. and Gurney, A.M. 2006. Pulmonary vasoconstrictor action of KCNQ potassium channel blockers. *Respir Res.* **7**, p31.

Joshi, S., Sedivy, V., Hodyc, D., Herget, J. and Gurney, A.M. 2009. KCNQ modulators reveal a key role for KCNQ potassium channels in regulating the tone of rat pulmonary artery smooth muscle. *J Pharmacol Exp Ther.* **329**(1), pp.368-376.

Kandathil, A. and Chamarthy, M. 2018. Pulmonary vascular anatomy and anatomical variants. *Cardiovasc Diagn Ther.* **8**(3), pp.201-207.

Kessler, R., Chaouat, A., Weitzenblum, E., Oswald, M., Ehrhart, M., Apprill, M. and Krieger, J. 1996. Pulmonary hypertension in the obstructive sleep apnoea syndrome: prevalence, causes and therapeutic consequences. *Eur Respir J,* 9**,** 787-94.

Killilea, D.W., Hester, R., Balczon, R., Babal, P. and Gillespie, M.N. 2000. Free radical production in hypoxic pulmonary artery smooth muscle cells. *Am J Physiol Lung Cell Mol Physiol.* **279**(2), pp.L408-412.

Kim, H. J., Yoo, H. Y., Jang, J. H., Lin, H. Y., Seo, E. Y., Zhang, Y. H. & Kim, S. J. 2016. Wall stretch and thromboxane A(2) activate NO synthase (eNOS) in pulmonary arterial smooth muscle cells via H(2)O(2) and Akt-dependent phosphorylation. *Pflugers Arch,* 468**,** 705-16.

Kozaki, K., Kaminski, W.E., Tang, J., Hollenbach, S., Lindahl, P., Sullivan, C., Yu, J.-C., Abe, K., Martin, P.J., Ross, R., Betsholtz, C., Giese, N.A. and Raines, E.W. 2002. Blockade of Platelet-Derived Growth Factor or Its Receptors Transiently Delays but Does Not Prevent Fibrous Cap Formation in ApoE Null Mice. *The American Journal of Pathology.* **161**(4), pp.1395-1407.

Kraus, R.L., Li, Y., Gregan, Y., Gotter, A.L., Uebele, V.N., Fox, S.V., Doran, S.M., Barrow, J.C., Yang, Z.-Q., Reger, T.S., Koblan, K.S. and Renger, J.J. 2010. In Vitro Characterization of T-Type Calcium Channel Antagonist TTA-A2 and In Vivo Effects on Arousal in Mice. *Journal of Pharmacology and Experimental Therapeutics.* **335**(2), pp.409-417.

Kuhr, F.K., Smith, K.A., Song, M.Y., Levitan, I. and Yuan, J.X.J. 2012. New mechanisms of pulmonary arterial hypertension: role of Ca(2+) signaling. *American Journal of Physiology - Heart and Circulatory Physiology.* **302**(8), pp.H1546-H1562.

Kuo, I.Y. and Ehrlich, B.E. 2015. Signaling in muscle contraction. *Cold Spring Harbor perspectives in biology.* **7**(2), pp.a006023-a006023.

Kuo, I.Y.T., Wölfle, S.E. and Hill, C.E. 2011. T-type calcium channels and vascular function: the new kid on the block? *J Physiol.* **589**(Pt 4), pp.783-795.

Labrousse-Arias, D., Castillo-Gonzales, R., Rogers, N. M., Torres-Capelli, M., Barreira, B., Aragones, J., Cogolludo, A., Isenberg, J. S. and Calzada, M. J. 2016. HIF-2alpha-mediated induction of pulmonary thrombospondin-1 contributes to hypoxia-driven vascular remodelling and vasoconstriction. *Cardiovasc Res,* 109**,** 115-30.

Leal, T.L., Alippi, R.M., Vargas, M., Leon-Velarde, F. and Bozzini, C.E. 1995. Body weight loss during acute hypoxia: effects of increased convective oxygen transport or previous acclimation. *Acta Physiol Pharmacol Ther Latinoam.* **45**(1), pp.9-14.

Lemos, V.S., Poburko, D., Liao, C.-H., Cole, W.C. and Breemen, C.v. 2007. Na+ entry via TRPC6 causes Ca2+ entry via NCX reversal in ATP stimulated smooth muscle cells. *Biochemical and Biophysical Research Communications.* **352**(1), pp.130-134.

Lewis, R.S. 2011. Store-operated calcium channels: new perspectives on mechanism and function. *Cold Spring Harb Perspect Biol.* **3**(12).

Lewis, R.S. and Cahalan, M.D. 1989. Mitogen-induced oscillations of cytosolic Ca2+ and transmembrane Ca2+ current in human leukemic T cells. *Cell Regul.* **1**(1), pp.99-112.

Li, J., Cubbon, R.M., Wilson, L.A., Amer, M.S., McKeown, L., Hou, B., Majeed, Y., Tumova, S., Seymour, V.A.L., Taylor, H., Stacey, M., O'Regan, D., Foster, R., Porter, K.E., Kearney, M.T. and Beech, D.J. 2011a. Orai1 and CRAC channel dependence of VEGF-activated Ca2+ entry and endothelial tube formation. *Circulation research.* **108**(10), pp.1190-1198.

Li, J., McKeown, L., Ojelabi, O., Stacey, M., Foster, R., O'Regan, D., Porter, K.E. and Beech, D.J. 2011b. Nanomolar potency and selectivity of a Ca(2)(+) release-activated Ca(2)(+) channel inhibitor against store-operated Ca(2)(+) entry and migration of vascular smooth muscle cells. *Br J Pharmacol.* **164**(2), pp.382-393.

Li, M., Hansen, J.B., Huang, L., Keyser, B.M. and Taylor, J.T. 2005. Towards selective antagonists of T-type calcium channels: design, characterization and potential applications of NNC 55-0396. *Cardiovasc Drug Rev.* **23**(2), pp.173-196.

Li, R., Wang, Y., Yang, Z., He, Y., Zhao, T., Fan, M., Wang, X., Zhu, L. and Wang, X. 2015. Hypoxia-inducible factor-1alpha regulates the expression of L-type voltage-dependent Ca(2+) channels in PC12 cells under hypoxia. *Cell Stress Chaperones.* **20**(3), pp.507-516.

Liang, S.J., Zeng, D.Y., Mai, X.Y., Shang, J.Y., Wu, Q.Q., Yuan, J.N., Yu, B.X., Zhou, P., Zhang, F.R., Liu, Y.Y., Lv, X.F., Liu, J., Ou, J.S., Qian, J.S. and Zhou, J.G. 2016. Inhibition of Orai1 Store-Operated Calcium Channel Prevents Foam Cell Formation and Atherosclerosis. *Arterioscler Thromb Vasc Biol.* **36**(4), pp.618-628.

Liao, Y., Erxleben, C., Abramowitz, J., Flockerzi, V., Zhu, M.X., Armstrong, D.L. and Birnbaumer, L. 2008. Functional interactions among Orai1, TRPCs, and STIM1 suggest a STIM-regulated heteromeric Orai/TRPC model for SOCE/Icrac channels. *Proc Natl Acad Sci U S A.* **105**(8), pp.2895-2900.

Lijnen, P., Fagard, R. and Petrov, V. 1999. Mibefradil-induced inhibition of proliferation of human peripheral blood mononuclear cells. *J Cardiovasc Pharmacol.* **33**(4), pp.595-604.

Lin, M.J., Leung, G.P., Zhang, W.M., Yang, X.R., Yip, K.P., Tse, C.M. and Sham, J.S. 2004. Chronic hypoxia-induced upregulation of store-operated and receptor-operated Ca2+ channels in pulmonary arterial smooth muscle cells: a novel mechanism of hypoxic pulmonary hypertension. *Circ Res.* **95**(5), pp.496-505.

Lin, M.J., Yang, X.R., Cao, Y.N. and Sham, J.S. 2007. Hydrogen peroxide-induced Ca2+ mobilization in pulmonary arterial smooth muscle cells. *Am J Physiol Lung Cell Mol Physiol.* **292**(6), pp.L1598-1608.

Liou, J., Kim, M.L., Heo, W.D., Jones, J.T., Myers, J.W., Ferrell, J.E., Jr. and Meyer, T. 2005. STIM is a Ca2+ sensor essential for Ca2+-store-depletion-triggered Ca2+ influx. *Curr Biol.* **15**(13), pp.1235-1241.

Liu, J.H., Bijlenga, P., Occhiodoro, T., Fischer-Lougheed, J., Bader, C.R. and Bernheim, L. 1999. Mibefradil (Ro 40-5967) inhibits several Ca2+ and K+ currents in human fusion-competent myoblasts. *British journal of pharmacology.* **126**(1), pp.245-250.

Liu, J.Q., Sham, J.S., Shimoda, L.A., Kuppusamy, P. and Sylvester, J.T. 2003. Hypoxic constriction and reactive oxygen species in porcine distal pulmonary arteries. *Am J Physiol Lung Cell Mol Physiol.* **285**(2), pp.L322-333.

Liu, X., Wang, W., Singh, B.B., Lockwich, T., Jadlowiec, J., O' Connell, B., Wellner, R., Zhu, M.X. and Ambudkar, I.S. 2000. Trp1, a Candidate Protein for the Store-operated Ca2+Influx Mechanism in Salivary Gland Cells. *Journal of Biological Chemistry.* **275**(5), pp.3403-3411.

Liu, Y., Tian, H. Y., Yan, X. L., Fan, F. L., Wang, W. P., Han, J. L., Zhang, J. B., Ma, Q., Meng, Y. and Wei, F. 2013. Serotonin inhibits apoptosis of pulmonary artery smooth muscle cell by pERK1/2 and PDK through 5-HT1B receptors and 5-HT transporters. *Cardiovasc Pathol,* 22**,** 451-7.

Lorsch, J.R., Collins, F.S. and Lippincott-Schwartz, J. 2014. Cell Biology. Fixing problems with cell lines. *Science (New York, N.Y.).* **346**(6216), pp.1452-1453.

Lu, F., Chen, H., Zhou, C., Liu, S., Guo, M., Chen, P., Zhuang, H., Xie, D. and Wu, S. 2008. T-type Ca2+ channel expression in human esophageal carcinomas: a functional role in proliferation. *Cell Calcium.* **43**(1), pp.49-58.

Lu, W., Wang, J., Peng, G., Shimoda, L.A. and Sylvester, J.T. 2009. Knockdown of stromal interaction molecule 1 attenuates store-operated Ca2+ entry and Ca2+ responses to acute hypoxia in pulmonary arterial smooth muscle. *American Journal of Physiology-Lung Cellular and Molecular Physiology.* **297**(1), pp.L17-L25.

Luik, R.M., Wu, M.M., Buchanan, J. and Lewis, R.S. 2006. The elementary unit of store-operated Ca2+ entry: local activation of CRAC channels by STIM1 at ER-plasma membrane junctions. *J Cell Biol.* **174**(6), pp.815-825.

Lumb, A.B. and Slinger, P. 2015. Hypoxic Pulmonary Vasoconstriction: Physiology and Anesthetic Implications. *Anesthesiology: The Journal of the American Society of Anesthesiologists.* **122**(4), pp.932-946.

Malczyk, M., Veith, C., Fuchs, B., Hofmann, K., Storch, U., Schermuly, R.T., Witzenrath, M., Ahlbrecht, K., Fecher-Trost, C., Flockerzi, V., Ghofrani, H.A., Grimminger, F., Seeger, W., Gudermann, T., Dietrich, A. and Weissmann, N. 2013. Classical transient receptor potential channel 1 in hypoxia-induced pulmonary hypertension. *Am J Respir Crit Care Med.* **188**(12), pp.1451-1459.

Marshall, C., Mamary, A.J., Verhoeven, A.J. and Marshall, B.E. 1996. Pulmonary artery NADPH-oxidase is activated in hypoxic pulmonary vasoconstriction. *Am J Respir Cell Mol Biol.* **15**(5), pp.633-644.

Martin, R.L., Lee, J.H., Cribbs, L.L., Perez-Reyes, E. and Hanck, D.A. 2000. Mibefradil block of cloned T-type calcium channels. *J Pharmacol Exp Ther.* **295**(1), pp.302-308.

McKeown, L., Moss, N.K., Turner, P., Li, J., Heath, N., Burke, D., O'Regan, D., Gilthorpe, M.S., Porter, K.E. and Beech, D.J. 2012. Platelet-derived growth factor maintains stored calcium through a nonclustering Orai1 mechanism but evokes clustering if the endoplasmic reticulum is stressed by store depletion. *Circ Res.* **111**(1), pp.66-76.

McNulty, M.M. and Hanck, D.A. 2004. State-dependent mibefradil block of Na+ channels. *Mol Pharmacol.* **66**(6), pp.1652-1661.

Mercer, J.C., Dehaven, W.I., Smyth, J.T., Wedel, B., Boyles, R.R., Bird, G.S. and Putney, J.W., Jr. 2006. Large store-operated calcium selective currents due to co-expression of Orai1 or Orai2 with the intracellular calcium sensor, Stim1. *J Biol Chem.* **281**(34), pp.24979-24990.

Miano, J.M., Cserjesi, P., Ligon, K.L., Periasamy, M. and Olson, E.N. 1994. Smooth muscle myosin heavy chain exclusively marks the smooth muscle lineage during mouse embryogenesis. *Circ Res.* **75**(5), pp.803-812.

Minamino, T., Mitsialis, S.A. and Kourembanas, S. 2001. Hypoxia Extends the Life Span of Vascular Smooth Muscle Cells through Telomerase Activation. *Mol Cell Biol.* **21**(10), pp.3336-3342.

Minard, A., Bauer, C.C., Wright, D.J., Rubaiy, H.N., Muraki, K., Beech, D.J. and Bon, R.S. 2018. Remarkable Progress with Small-Molecule Modulation of TRPC1/4/5 Channels: Implications for Understanding the Channels in Health and Disease. *Cells.* **7**(6), p52.

Miranda, C.L., Henderson, M.C., Schmitz, J.A. and Buhler, D.R. 1983. Protective role of dietary butylated hydroxyanisole against chemical-induced acute liver damage in mice. *Toxicology and Applied Pharmacology.* **69**(1), pp.73-80.

Miyauchi, T., Yorikane, R., Sakai, S., Sakurai, T., Okada, M., Nishikibe, M., Yano, M., Yamaguchi, I., Sugishita, Y. and Goto, K. 1993. Contribution of endogenous endothelin-1 to the progression of cardiopulmonary alterations in rats with monocrotaline-induced pulmonary hypertension. *Circ Res.* **73**(5), pp.887-897.

Mo, P. and Yang, S. 2018. The store-operated calcium channels in cancer metastasis: from cell migration, invasion to metastatic colonization. *Frontiers in bioscience (Landmark edition).* **23**, pp.1241-1256.

Montani, D., Savale, L., Natali, D., Jais, X., Herve, P., Garcia, G., Humbert, M., Simonneau, G. and Sitbon, O. 2010. Long-term response to calcium-channel blockers in non-idiopathic pulmonary arterial hypertension. *Eur Heart J.* **31**(15), pp.1898-1907.

Morrell, N.W. 2006. Pulmonary hypertension due to BMPR2 mutation: a new paradigm for tissue remodeling? *Proc Am Thorac Soc.* **3**(8), pp.680-686.

Morrell, N.W., Adnot, S., Archer, S.L., Dupuis, J., Jones, P.L., MacLean, M.R., McMurtry, I.F., Stenmark, K.R., Thistlethwaite, P.A., Weissmann, N., Yuan, J.X. and Weir, E.K. 2009. Cellular and molecular basis of pulmonary arterial hypertension. *J Am Coll Cardiol.* **54**(1 Suppl), pp.S20-31.

Muik, M., Frischauf, I., Derler, I., Fahrner, M., Bergsmann, J., Eder, P., Schindl, R., Hesch, C., Polzinger, B., Fritsch, R., Kahr, H., Madl, J., Gruber, H., Groschner, K. and Romanin, C. 2008. Dynamic coupling of the putative coiled-coil domain of ORAI1 with STIM1 mediates ORAI1 channel activation. *J Biol Chem.* **283**(12), pp.8014-8022.

Murray, A.J. and Montgomery, H.E. 2014. How wasting is saving: weight loss at altitude might result from an evolutionary adaptation. *Bioessays.* **36**(8), pp.721-729.

Nagaoka, T., Muramatsu, M., Sato, K., McMurtry, I., Oka, M. and Fukuchi, Y. 2001. Mild hypoxia causes severe pulmonary hypertension in fawn-hooded but not in Tester Moriyama rats. *Respiration Physiology.* **127**(1), pp.53-60.

Ng, L.C., McCormack, M.D., Airey, J.A., Singer, C.A., Keller, P.S., Shen, X.-M. and Hume, J.R. 2009. TRPC1 and STIM1 mediate capacitative Ca2+ entry in mouse pulmonary arterial smooth muscle cells. *The Journal of physiology.* **587**(Pt 11), pp.2429-2442.

Ng, L.C., Ramduny, D., Airey, J.A., Singer, C.A., Keller, P.S., Shen, X.-M., Tian, H., Valencik, M. and Hume, J.R. 2010. Orai1 interacts with STIM1 and mediates capacitative Ca2+ entry in mouse pulmonary arterial smooth muscle cells. *American journal of physiology. Cell physiology.* **299**(5), pp.C1079-C1090.

Ng, Y.Y., Huang, T.P., Yang, W.C., Chen, Z.P., Yang, A.H., Mu, W., Nikolic-Paterson, D.J., Atkins, R.C. and Lan, H.Y. 1998. Tubular epithelial-myofibroblast transdifferentiation in progressive tubulointerstitial fibrosis in 5/6 nephrectomized rats. *Kidney Int.* **54**(3), pp.864-876.

Nguyen, N., Biet, M., Simard, É., Béliveau, É., Francoeur, N., Guillemette, G., Dumaine, R., Grandbois, M. and Boulay, G. 2013. STIM1 participates in the contractile rhythmicity of HL-1 cells by moderating T-type Ca2+ channel activity. *Biochimica et Biophysica Acta (BBA) - Molecular Cell Research.* **1833**(6), pp.1294-1303.

Nilius, B., Prenen, J., Kamouchi, M., Viana, F., Voets, T. and Droogmans, G. 1997. Inhibition by mibefradil, a novel calcium channel antagonist, of Ca(2+)- and volume-activated Cl- channels in macrovascular endothelial cells. *British journal of pharmacology.* **121**(3), pp.547-555.

Okada, T., Shimizu, S., Wakamori, M., Maeda, A., Kurosaki, T., Takada, N., Imoto, K. and Mori, Y. 1998. Molecular Cloning and Functional Characterization of a Novel Receptor-activated TRP Ca2+ Channel from Mouse Brain. *Journal of Biological Chemistry.* **273**(17), pp.10279-10287.

Ong, H.L., Cheng, K.T., Liu, X., Bandyopadhyay, B.C., Paria, B.C., Soboloff, J., Pani, B., Gwack, Y., Srikanth, S., Singh, B.B., Gill, D.L. and Ambudkar, I.S. 2007. Dynamic assembly of TRPC1-STIM1-Orai1 ternary complex is involved in store-operated calcium influx. Evidence for similarities in store-operated and calcium release-activated calcium channel components. *J Biol Chem.* **282**(12), pp.9105-9116.

Owsianik, G., Talavera, K., Voets, T. and Nilius, B. 2006. Permeation and selectivity of TRP channels. *Annu Rev Physiol.* **68**, pp.685-717.

Paddenberg, R., Ishaq, B., Goldenberg, A., Faulhammer, P., Rose, F., Weissmann, N., Braun-Dullaeus, R.C. and Kummer, W. 2003. Essential role of complex II of the respiratory chain in hypoxia-induced ROS generation in the pulmonary vasculature. *Am J Physiol Lung Cell Mol Physiol.* **284**(5), pp.L710-719.

Pak, O., Aldashev, A., Welsh, D. and Peacock, A. 2007. The effects of hypoxia on the cells of the pulmonary vasculature. *European Respiratory Journal.* **30**(2), pp.364-372.

Paredes, R.M., Etzler, J.C., Watts, L.T., Zheng, W. and Lechleiter, J.D. 2008. Chemical calcium indicators. *Methods (San Diego, Calif.).* **46**(3), pp.143-151.

Park, C.Y., Hoover, P.J., Mullins, F.M., Bachhawat, P., Covington, E.D., Raunser, S., Walz, T., Garcia, K.C., Dolmetsch, R.E. and Lewis, R.S. 2009. STIM1 clusters and activates CRAC channels via direct binding of a cytosolic domain to Orai1. *Cell.* **136**(5), pp.876-890.

Parker, N.J., Begley, C.G., Smith, P.J. and Fox, R.M. 1996. Molecular Cloning of a Novel Human Gene (D11S4896E) at Chromosomal Region 11p15.5. *Genomics.* **37**(2), pp.253-256.

Patel, J.J., Srivastava, S. and Siow, R.C. 2016. Isolation, Culture, and Characterization of Vascular Smooth Muscle Cells. *Methods Mol Biol.* **1430**, pp.91-105.

Peacock, A. J., Murphy, N. F., McMurray, J. J., Cabalerro, L. and Stewart, S. 2007. An epidemiological study of pulmonary arterial hypertension. *Eur Respir J,* 30**,** 104-9.

Peinelt, C., Vig, M., Koomoa, D.L., Beck, A., Nadler, M.J., Koblan-Huberson, M., Lis, A., Fleig, A., Penner, R. and Kinet, J.P. 2006. Amplification of CRAC current by STIM1 and CRACM1 (Orai1). *Nat Cell Biol.* **8**(7), pp.771-773.

Peng, G., Ran, P., Lu, W., Zhong, N. and Wang, J. 2013. Acute hypoxia activates store-operated Ca(2+) entry and increases intracellular Ca(2+) concentration in rat distal pulmonary venous smooth muscle cells. *Journal of thoracic disease.* **5**(5), pp.605-612.

Penner, R., Matthews, G. and Neher, E. 1988. Regulation of calcium influx by second messengers in rat mast cells. *Nature.* **334**(6182), pp.499-504.

Perchenet, L. and Clement-Chomienne, O. 2000. Characterization of mibefradil block of the human heart delayed rectifier hKv1.5. *J Pharmacol Exp Ther.* **295**(2), pp.771-778.

Perez-Reyes, E. 2003. Molecular Physiology of Low-Voltage-Activated T-type Calcium Channels. *Physiological Reviews.* **83**(1), pp.117-161.

Perros, F., Montani, D., Dorfmüller, P., Durand-Gasselin, I., Tcherakian, C., Pavec, J.L., Mazmanian, M., Fadel, E., Mussot, S., Mercier, O., Hervé, P., Emilie, D., Eddahibi, S., Simonneau, G., Souza, R. and Humbert, M. 2008b. Platelet-derived Growth Factor Expression and Function in Idiopathic Pulmonary Arterial Hypertension. *American Journal of Respiratory and Critical Care Medicine.* **178**(1), pp.81-88.

Philipp, S., Hambrecht, J., Braslavski, L., Schroth, G., Freichel, M., Murakami, M., Cavalié, A. and Flockerzi, V. 1998. A novel capacitative calcium entry channel expressed in excitable cells. *The EMBO Journal.* **17**(15), pp.4274-4282.

Place, T.L., Domann, F.E. and Case, A.J. 2017. Limitations of oxygen delivery to cells in culture: An underappreciated problem in basic and translational research. *Free Radical Biology and Medicine.* **113**, pp.311-322.

Platoshyn, O., Golovina, V.A., Bailey, C.L., Limsuwan, A., Krick, S., Juhaszova, M., Seiden, J.E., Rubin, L.J. and Yuan, J.X. 2000. Sustained membrane depolarization and pulmonary artery smooth muscle cell proliferation. *Am J Physiol Cell Physiol.* **279**(5), pp.C1540-1549.

Platoshyn, O., Yu, Y., Golovina, V.A., McDaniel, S.S., Krick, S., Li, L., Wang, J.Y., Rubin, L.J. and Yuan, J.X. 2001. Chronic hypoxia decreases K(V) channel expression and function in pulmonary artery myocytes. *Am J Physiol Lung Cell Mol Physiol.* **280**(4), pp.L801-812.

Pourmahram, G.E., Snetkov, V.A., Shaifta, Y., Drndarski, S., Knock, G.A., Aaronson, P.I. and Ward, J.P. 2008. Constriction of pulmonary artery by peroxide: role of Ca2+ release and PKC. *Free Radic Biol Med.* **45**(10), pp.1468-1476.

Pozeg, Z.I., Michelakis, E.D., McMurtry, M.S., Thebaud, B., Wu, X.C., Dyck, J.R., Hashimoto, K., Wang, S., Moudgil, R., Harry, G., Sultanian, R., Koshal, A. and Archer, S.L. 2003. In vivo gene transfer of the O2-sensitive potassium channel Kv1.5 reduces pulmonary hypertension and restores hypoxic pulmonary vasoconstriction in chronically hypoxic rats. *Circulation.* **107**(15), pp.2037-2044.

Prabhakar, N.R. and Semenza, G.L. 2012. ADAPTIVE AND MALADAPTIVE CARDIORESPIRATORY RESPONSES TO CONTINUOUS AND INTERMITTENT HYPOXIA MEDIATED BY HYPOXIA-INDUCIBLE FACTORS 1 AND 2. *Physiol Rev.* **92**(3), pp.967-1003.

Prakriya, M., Feske, S., Gwack, Y., Srikanth, S., Rao, A. and Hogan, P.G. 2006. Orai1 is an essential pore subunit of the CRAC channel. *Nature.* **443**(7108), pp.230-233.

Prins, K. W. and Thenappan, T. 2016. World Health Organization Group I Pulmonary Hypertension: Epidemiology and Pathophysiology. *Cardiology clinics,* 34**,** 363-374.

Pugliese, S.C., Poth, J.M., Fini, M.A., Olschewski, A., El Kasmi, K.C. and Stenmark, K.R. 2015. The role of inflammation in hypoxic pulmonary hypertension: from cellular mechanisms to clinical phenotypes. *American journal of physiology. Lung cellular and molecular physiology.* **308**(3), pp.L229-L252.

Raines, E.W. 2004. PDGF and cardiovascular disease. *Cytokine Growth Factor Rev.* **15**(4), pp.237-254.

Remillard, C.V., Tigno, D.D., Platoshyn, O., Burg, E.D., Brevnova, E.E., Conger, D., Nicholson, A., Rana, B.K., Channick, R.N., Rubin, L.J., O'Connor, D.T. and Yuan, J.X.-J. 2007. <div xmlns="http://www.w3.org/1999/xhtml">Function of Kv1.5 channels and genetic variations of KCNA5 in patients with idiopathic pulmonary arterial hypertension</div>. *American Journal of Physiology - Cell Physiology.* **292**(5), pp.C1837-C1853.

Rensen, S.S., Doevendans, P.A. and van Eys, G.J. 2007. Regulation and characteristics of vascular smooth muscle cell phenotypic diversity. *Neth Heart J.* **15**(3), pp.100-108.

Rich, S., Dantzsker, D. R., Ayres, S. M., Bergofsky, E. H., Brundage, B. H., Detre, K. M., Fishman, A. P., Goldring, R. M., Groves, B. M., and Koerner, S. K. 1987. Primary pulmonary hypertension. A national prospective study. *Ann Intern Med,* 107**,** 216-23.

Rich, S., Kaufmann, E. and Levy, P.S. 1992. The effect of high doses of calcium-channel blockers on survival in primary pulmonary hypertension. *N Engl J Med.* **327**(2), pp.76-81.

Richard, S., Neveu, D., Carnac, G., Bodin, P., Travo, P. and Nargeot, J. 1992. Differential expression of voltage-gated Ca2+-currents in cultivated aortic myocytes. *Biochimica et Biophysica Acta (BBA) - Protein Structure and Molecular Enzymology.* **1160**(1), pp.95-104.

Rode, B., Bailey, M.A., Marthan, R., Beech, D.J. and Guibert, C. 2018. ORAI Channels as Potential Therapeutic Targets in Pulmonary Hypertension. *Physiology.* **33**(4), pp.261-268.

Rodman, D.M., Reese, K., Harral, J., Fouty, B., Wu, S., West, J., Hoedt-Miller, M., Tada, Y., Li, K.X., Cool, C., Fagan, K. and Cribbs, L. 2005. Low-voltage-activated (T-type) calcium channels control proliferation of human pulmonary artery myocytes. *Circ Res.* **96**(8), pp.864-872.

Roos, J., DiGregorio, P.J., Yeromin, A.V., Ohlsen, K., Lioudyno, M., Zhang, S., Safrina, O., Kozak, J.A., Wagner, S.L., Cahalan, M.D., Velicelebi, G. and Stauderman, K.A. 2005. STIM1, an essential and conserved component of store-operated Ca2+ channel function. *J Cell Biol.* **169**(3), pp.435-445.

Rosenberg, H.C. and Rabinovitch, M. 1988. Endothelial injury and vascular reactivity in monocrotaline pulmonary hypertension. *Am J Physiol.* **255**(6 Pt 2), pp.H1484-1491.

Roux, F., D'ambrosio, C. and Mohsenin, V. 2000. Sleep-related breathing disorders and cardiovascular disease. *Am J Med,* 108**,** 396-402.

Rubaiy, H.N., Ludlow, M.J., Henrot, M., Gaunt, H.J., Miteva, K., Cheung, S.Y., Tanahashi, Y., Hamzah, N., Musialowski, K.E., Blythe, N.M., Appleby, H.L., Bailey, M.A., McKeown, L., Taylor, R., Foster, R., Waldmann, H., Nussbaumer, P., Christmann, M., Bon, R.S., Muraki, K. and Beech, D.J. 2017. Picomolar, selective, and subtype-specific small-molecule inhibition of TRPC1/4/5 channels. *The Journal of biological chemistry.* **292**(20), pp.8158-8173.

Rubaiy, H. N., Seitz, T., Hahn, S., Choidas, A., Habenberger, P., Klebl, B., Dinkel, K., Nussbaumer P., Waldmann, H., Christmann, M. and Beech, D. J. 2018. Identification of an (-)-englerin A analogue, which antagonizes (-)-englerin A at TRPC1/4/5 channels. *British journal of pharmacology,* 175**,** 830-839.

Rudolph, A.M. 1979. Fetal and neonatal pulmonary circulation. *Annu Rev Physiol.* **41**, pp.383-395.

Rzucidlo, E.M., Martin, K.A. and Powell, R.J. 2007. Regulation of vascular smooth muscle cell differentiation. *Journal of Vascular Surgery.* **45**(6), pp.A25-A32.

Salvaterra, C.G. and Goldman, W.F. 1993. Acute hypoxia increases cytosolic calcium in cultured pulmonary arterial myocytes. *Am J Physiol.* **264**(3 Pt 1), pp.L323-328.

Sato, K., Webb, S., Tucker, A., Rabinovitch, M., O'Brien, R.F., McMurtry, I.F. and Stelzner, T.J. 1992. Factors influencing the idiopathic development of pulmonary hypertension in the fawn hooded rat. *Am Rev Respir Dis.* **145**(4 Pt 1), pp.793-797.

Schaefer, M., Plant, T.D., Obukhov, A.G., Hofmann, T., Gudermann, T. and Schultz, G. 2000. Receptor-mediated regulation of the nonselective cation channels TRPC4 and TRPC5. *J Biol Chem.* **275**(23), pp.17517-17526.

Schermuly, R.T., Dony, E., Ghofrani, H.A., Pullamsetti, S., Savai, R., Roth, M., Sydykov, A., Lai, Y.J., Weissmann, N., Seeger, W. and Grimminger, F. 2005. Reversal of experimental pulmonary hypertension by PDGF inhibition. *J Clin Invest.* **115**(10), pp.2811-2821.

Schermuly, R.T., Ghofrani, H.A., Wilkins, M.R. and Grimminger, F. 2011. Mechanisms of disease: pulmonary arterial hypertension. *Nat Rev Cardiol.* **8**(8), pp.443-455.

Schols, A.M.W.J. and Westerterp, K.R. 2002. Hypoxia, nitrogen balance and body weight. *European Respiratory Journal.* **20**(2), pp.252-253.

Sellak, H., Zhou, C., Liu, B., Chen, H., Lincoln, T.M. and Wu, S. 2014. Transcriptional regulation of alpha1H T-type calcium channel under hypoxia. *Am J Physiol Cell Physiol.* **307**(7), pp.C648-656.

Semenza, Gregg L. 2012. Hypoxia-Inducible Factors in Physiology and Medicine. *Cell.* **148**(3), pp.399-408.

Shankman, L.S., Gomez, D., Cherepanova, O.A., Salmon, M., Alencar, G.F., Haskins, R.M., Swiatlowska, P., Newman, A.A.C., Greene, E.S., Straub, A.C., Isakson, B., Randolph, G.J. and Owens, G.K. 2015. KLF4-dependent phenotypic modulation of smooth muscle cells has a key role in atherosclerotic plaque pathogenesis. *Nature medicine.* **21**(6), pp.628-637.

Shcheglovitov, A., Vitko, I., Bidaud, I., Baumgart, J.P., Navarro-Gonzalez, M.F., Grayson, T.H., Lory, P., Hill, C.E. and Perez-Reyes, E. 2008. Alternative splicing within the I-II loop controls surface expression of T-type Ca(v)3.1 calcium channels. *FEBS letters.* **582**(27), pp.3765-3770.

Shimoda, L.A. and Laurie, S.S. 2013. Vascular remodeling in pulmonary hypertension. *Journal of Molecular Medicine.* **91**(3), pp.297-309.

Sihvola, R., Koskinen, P., Myllärniemi, M., Loubtchenkov, M., Häyry, P., Buchdunger, E. and Lemström, K. 1999. Prevention of Cardiac Allograft Arteriosclerosis by Protein Tyrosine Kinase Inhibitor Selective for Platelet-Derived Growth Factor Receptor. *Circulation.* **99**(17), pp.2295-2301.

Smirnov, S.V., Robertson, T.P., Ward, J.P. and Aaronson, P.I. 1994. Chronic hypoxia is associated with reduced delayed rectifier K+ current in rat pulmonary artery muscle cells. *Am J Physiol.* **266**(1 Pt 2), pp.H365-370.

Smith, K.A., Voiriot, G., Tang, H., Fraidenburg, D.R., Song, S., Yamamura, H., Yamamura, A., Guo, Q., Wan, J., Pohl, N.M., Tauseef, M., Bodmer, R., Ocorr, K., Thistlethwaite, P.A., Haddad, G.G., Powell, F.L., Makino, A., Mehta, D. and Yuan, J.X. 2015. Notch Activation of Ca(2+) Signaling in the Development of Hypoxic Pulmonary Vasoconstriction and Pulmonary Hypertension. *Am J Respir Cell Mol Biol.* **53**(3), pp.355-367.

Solik, P., Lesny, P., Luknar, M., Varga, I. and Goncalvesova, E. 2013. The long-term response to treatment with calcium channel blockers in a patient with idiopathic pulmonary arterial hypertension. *Bratisl Lek Listy.* **114**(5), pp.283-286.

Somlyo, A.P. and Somlyo, A.V. 1994. Smooth muscle: excitation-contraction coupling, contractile regulation, and the cross-bridge cycle. *Alcohol Clin Exp Res.* **18**(1), pp.138-143.

Somlyo, A.P. and Somlyo, A.V. 2003. Ca2+ sensitivity of smooth muscle and nonmuscle myosin II: modulated by G proteins, kinases, and myosin phosphatase. *Physiol Rev.* **83**(4), pp.1325-1358.

Sousa, A.M., Liu, T., Guevara, O., Stevens, J., Fanburg, B.L., Gaestel, M., Toksoz, D. and Kayyali, U.S. 2007. Smooth muscle alpha-actin expression and myofibroblast differentiation by TGFbeta are dependent upon MK2. *Journal of cellular biochemistry.* **100**(6), pp.1581-1592.

Speich, R., Treder, U., Domenighetti, G., Huber, L.C. and Ulrich, S. 2014. Weaning from intravenous prostanoids and normalization of hemodynamics by long-term imatinib therapy in severe idiopathic pulmonary arterial hypertension. *International Journal of Clinical Pharmacy.* **36**(2), pp.256-260.

Speich, R., Ulrich, S., Domenighetti, G., Huber, L.C., Fischler, M., Treder, U. and Breitenstein, A. 2015. Efficacy and Safety of Long-Term Imatinib Therapy for Pulmonary Arterial Hypertension. *Respiration.* **89**(6), pp.515-524.

Spinelli, A.M., Gonzalez-Cobos, J.C., Zhang, X., Motiani, R.K., Rowan, S., Zhang, W., Garrett, J., Vincent, P.A., Matrougui, K., Singer, H.A. and Trebak, M. 2012. Airway smooth muscle STIM1 and Orai1 are upregulated in asthmatic mice and mediate PDGF-activated SOCE, CRAC currents, proliferation, and migration. *Pflugers Arch.* **464**(5), pp.481-492.

Spinelli, A.M. and Trebak, M. 2016. Orai channel-mediated Ca2+ signals in vascular and airway smooth muscle. *Am J Physiol Cell Physiol.* **310**(6), pp.C402-413.

Stathopulos, P.B., Zheng, L., Li, G.Y., Plevin, M.J. and Ikura, M. 2008. Structural and mechanistic insights into STIM1-mediated initiation of store-operated calcium entry. *Cell.* **135**(1), pp.110-122.

Stenmark, K.R., Meyrick, B., Galie, N., Mooi, W.J. and McMurtry, I.F. 2009. Animal models of pulmonary arterial hypertension: the hope for etiological discovery and pharmacological cure. *Am J Physiol Lung Cell Mol Physiol.* **297**(6), pp.L1013-1032.

Steucke, K.E., Tracy, P.V., Hald, E.S., Hall, J.L. and Alford, P.W. 2015. Vascular smooth muscle cell functional contractility depends on extracellular mechanical properties. *Journal of biomechanics.* **48**(12), pp.3044-3051.

Strassheim, D., Karoor, V., Stenmark, K., Verin, A. and Gerasimovskaya, E. 2018. A current view of G protein-coupled receptor - mediated signaling in pulmonary hypertension: finding opportunities for therapeutic intervention. *Vessel Plus.* **2**.

Striessnig, J. 1999. Pharmacology, structure and function of cardiac L-type Ca(2+) channels. *Cell Physiol Biochem.* **9**(4-5), pp.242-269.

Striessnig, J., Pinggera, A., Kaur, G., Bock, G. and Tuluc, P. 2014. L-type Ca(2+) channels in heart and brain. *Wiley interdisciplinary reviews. Membrane transport and signaling.* **3**(2), pp.15-38.

Stuart, J.A., Fonseca, J., Moradi, F., Cunningham, C., Seliman, B., Worsfold, C.R., Dolan, S., Abando, J. and Maddalena, L.A. 2018. How Supraphysiological Oxygen Levels in Standard Cell Culture Affect Oxygen-Consuming Reactions. *Oxidative Medicine and Cellular Longevity.* **2018**, p13.

Suganuma, N., Ito, S., Aso, H., Kondo, M., Sato, M., Sokabe, M. and Hasegawa, Y. 2012. STIM1 regulates platelet-derived growth factor-induced migration and Ca2+ influx in human airway smooth muscle cells. *PLoS One.* **7**(9), pe45056.

Suresh, K. and Shimoda, L.A. 2016. Lung Circulation. *Compr Physiol.* **6**(2), pp.897-943.

Sweeney, M., Yu, Y., Platoshyn, O., Zhang, S., McDaniel, S.S. and Yuan, J.X. 2002. Inhibition of endogenous TRP1 decreases capacitative Ca2+ entry and attenuates pulmonary artery smooth muscle cell proliferation. *Am J Physiol Lung Cell Mol Physiol.* **283**(1), pp.L144-155.

Sztuka, K. and Jasinska-Stroschein, M. 2017. Animal models of pulmonary arterial hypertension: A systematic review and meta-analysis of data from 6126 animals. *Pharmacol Res.* **125**(Pt B), pp.201-214.

Tannenberg, P., Chang, Y.-T., Muhl, L., Laviña, B., Gladh, H., Genové, G., Betsholtz, C., Folestad, E. and Tran-Lundmark, K. 2018. Extracellular retention of PDGF-B directs vascular remodeling in mouse hypoxia-induced pulmonary hypertension. *American Journal of Physiology-Lung Cellular and Molecular Physiology.* **314**(4), pp.L593-L605.

Tarasevicienе-Stewart, L., Kasahara, Y., Alger, L., Hirth, P., Mc Mahon, G., Waltenberger, J., Voelkel, N.F. and Tuder, R.M. 2001. Inhibition of the VEGF receptor 2 combined with chronic hypoxia causes cell death-dependent pulmonary endothelial cell proliferation and severe pulmonary hypertension. *Faseb j.* **15**(2), pp.427-438.

Thenappan, T., Shah, S.J., Rich, S. and Gomberg-Maitland, M. 2007. A USA-based registry for pulmonary arterial hypertension: 1982-2006. *Eur Respir J.* **30**(6), pp.1103-1110.

Thompson, J.L. and Shuttleworth, T.J. 2012. A plasma membrane-targeted cytosolic domain of STIM1 selectively activates ARC channels, an arachidonate-regulated store-independent Orai channel. *Channels (Austin, Tex.).* **6**(5), pp.370-378.

Townsend, D. 2016. Measuring Pressure Volume Loops in the Mouse. *Journal of visualized experiments : JoVE.* (111), p10.3791/53810.

Townsley, M.I. 2012. Structure and composition of pulmonary arteries, capillaries, and veins. *Comprehensive Physiology.* **2**(1), pp.675-709.

Toyota, M.. Ho, C., Ohe-Toyota M., Baylin, S.B., Issa, J-P. J. Inactivation of CACNA1G, a T-type Calcium Channel Gene, by Abberant Methylation of Its 5' CpG Island in Human Tumours. *Cancer Research.* **59**(18).

Trebak, M., St. J. Bird, G., McKay, R.R., Birnbaumer, L. and Putney, J.W. 2003. Signaling Mechanism for Receptor-activated Canonical Transient Receptor Potential 3 (TRPC3) Channels. *Journal of Biological Chemistry.* **278**(18), pp.16244-16252.

Tucker, W.D. and Mahajan, K. 2019. Anatomy, Blood Vessels. *StatPearls.* Treasure Island (FL): StatPearls Publishing LLC.

Uebele, V.N., Gotter, A.L., Nuss, C.E., Kraus, R.L., Doran, S.M., Garson, S.L., Reiss, D.R., Li, Y., Barrow, J.C., Reger, T.S., Yang, Z.Q., Ballard, J.E., Tang, C., Metzger, J.M., Wang, S.P., Koblan, K.S. and Renger, J.J. 2009. Antagonism of T-type calcium channels inhibits high-fat diet-induced weight gain in mice. *J Clin Invest.* **119**(6), pp.1659-1667.

Vaeth, M., Yang, J., Yamashita, M., Zee, I., Eckstein, M., Knosp, C., Kaufmann, U., Karoly Jani, P., Lacruz, R.S., Flockerzi, V., Kacskovics, I., Prakriya, M. and Feske, S. 2017. ORAI2 modulates store-operated calcium entry and T cell-mediated immunity. *Nat Commun.* **8**, p14714.

Vannier, B., Zhu, X., Brown, D. and Birnbaumer, L. 1998. The Membrane Topology of Human Transient Receptor Potential 3 as Inferred from Glycosylation-scanning Mutagenesis and Epitope Immunocytochemistry. *Journal of Biological Chemistry.* **273**(15), pp.8675-8679.

Vazquez, G., Lievremont, J.-P., St. J. Bird, G. and Putney, J.W. 2001. Human Trp3 forms both inositol trisphosphate receptor-dependent and receptor-independent store-operated cation channels in DT40 avian B lymphocytes. *Proceedings of the National Academy of Sciences.* **98**(20), pp.11777-11782.

Veronese, M.L., Gillen, L.P., Dorval, E.P., Hauck, W.W., Waldman, S.A. and Greenberg, H.E. 2003. Effect of mibefradil on CYP3A4 in vivo. *J Clin Pharmacol.* **43**(10), pp.1091-1100.

Vig, M., Beck, A., Billingsley, J.M., Lis, A., Parvez, S., Peinelt, C., Koomoa, D.L., Soboloff, J., Gill, D.L., Fleig, A., Kinet, J.P. and Penner, R. 2006. CRACM1 multimers form the ion-selective pore of the CRAC channel. *Curr Biol.* **16**(20), pp.2073-2079.

Vitali, S.H., Hansmann, G., Rose, C., Fernandez-Gonzalez, A., Scheid, A., Mitsialis, S.A. and Kourembanas, S. 2014. The Sugen 5416/hypoxia mouse model of pulmonary hypertension revisited: long-term follow-up. *Pulm Circ.* **4**(4), pp.619-629.

Voelkel, N.F., Gomez-Arroyo, J., Abbate, A., Bogaard, H.J. and Nicolls, M.R. 2012. Pathobiology of pulmonary arterial hypertension and right ventricular failure. *The European respiratory journal.* **40**(6), pp.1555-1565.

Voelkel, N.F. and Tuder, R.M. 2000. Hypoxia-induced pulmonary vascular remodeling: a model for what human disease? *The Journal of Clinical Investigation.* **106**(6), pp.733-738.

Vonk-Noordegraaf, A. and Westerhof, N. 2013. Describing right ventricular function. *European Respiratory Journal.* **41**(6), pp.1419-1423.

Vorkapic, E., Dugic, E., Vikingsson, S., Roy, J., Mäyränpää, M.I., Eriksson, P. and Wågsäter, D. 2016. Imatinib treatment attenuates growth and inflammation of angiotensin II induced abdominal aortic aneurysm. *Atherosclerosis.* **249**, pp.101-109.

Waldron, R.T., Chen, Y., Pham, H., Go, A., Su, H.-Y., Hu, C., Wen, L., Husain, S.Z., Sugar, C.A., Roos, J., Ramos, S., Lugea, A., Dunn, M., Stauderman, K. and Pandol, S.J. 2019. The Orai Ca2+ channel inhibitor CM4620 targets both parenchymal and immune cells to reduce inflammation in experimental acute pancreatitis. *The Journal of Physiology.* **597**(12), pp.3085-3105.

Wan, J., Yamamura, A., Zimnicka, A.M., Voiriot, G., Smith, K.A., Tang, H., Ayon, R.J., Choudhury, M.S., Ko, E.A., Wang, J., Wang, C., Makino, A. and Yuan, J.X. 2013. Chronic hypoxia selectively enhances L- and T-type voltage-dependent Ca2+ channel activity in pulmonary artery by upregulating Cav1.2 and Cav3.2. *Am J Physiol Lung Cell Mol Physiol.* **305**(2), pp.L154-164.

Wandel, C., Kim, R.B., Guengerich, F.P. and Wood, A.J. 2000. Mibefradil is a P-glycoprotein substrate and a potent inhibitor of both P-glycoprotein and CYP3A in vitro. *Drug Metab Dispos.* **28**(8), pp.895-898.

Wang, J., Shimoda, L.A., Weigand, L., Wang, W., Sun, D. and Sylvester, J.T. 2005. Acute hypoxia increases intracellular [Ca2+] in pulmonary arterial smooth muscle by enhancing capacitative Ca2+ entry. *Am J Physiol Lung Cell Mol Physiol.* **288**(6), pp.L1059-1069.

Wang, J., Xu, C., Zheng, Q., Yang, K., Lai, N., Wang, T., Tang, H. and Lu, W. 2017b. Orai1, 2, 3 and STIM1 promote store-operated calcium entry in pulmonary arterial smooth muscle cells. *Cell Death Discovery.* **3**, p17074.

Wang, R., Wang, Z. and Wu, L. 1997. Carbon monoxide-induced vasorelaxation and the underlying mechanisms. *Br J Pharmacol.* **121**(5), pp.927-934.

Wei, C., LI, H. Z., Wang, Y. H., Peng, X., Shao, H. J., Li, H. X., Bai, S. Z., Lu, X. X., Wu, L. Y., Wang, R. and Xu, C. Q. 2016. Exogenous spermine inhibits the proliferation of human pulmonary artery smooth muscle cells caused by chemically-induced hypoxia via the suppression of the ERK1/2- and PI3K/AKT-associated pathways. *Int J Mol Med,* 37**,** 39-46.

Wes, P.D., Chevesich, J., Jeromin, A., Rosenberg, C., Stetten, G. and Montell, C. 1995. TRPC1, a human homolog of a Drosophila store-operated channel. *Proc Natl Acad Sci U S A.* **92**(21), pp.9652-9656.

Williams, R.T., Manji, S.S., Parker, N.J., Hancock, M.S., Van Stekelenburg, L., Eid, J.P., Senior, P.V., Kazenwadel, J.S., Shandala, T., Saint, R., Smith, P.J. and Dziadek, M.A. 2001. Identification and characterization of the STIM (stromal interaction molecule) gene family: coding for a novel class of transmembrane proteins. *Biochem J.* **357**(Pt 3), pp.673-685.

Wilson, D.P. 2011. Mechanisms of Vascular Disease: A Reference Book for Vascular Specialists [Internet].

Wilson, D.W., Segall, H.J., Pan, L.C., Lame, M.W., Estep, J.E. and Morin, D. 1992. Mechanisms and pathology of monocrotaline pulmonary toxicity. *Crit Rev Toxicol.* **22**(5-6), pp.307-325.

Wu, S., Zhang, M., Vest, P.A., Bhattacharjee, A., Liu, L. and Li, M. 2000. A mibefradil metabolite is a potent intracellular blocker of L-type Ca2+ currents in pancreatic β-cells. *The Journal of pharmacology and experimental therapeutics.* **292**, pp.939-943.

Xia, Y., Yang, X.-R., Fu, Z., Paudel, O., Abramowitz, J., Birnbaumer, L. and Sham, J.S.K. 2014. Classical transient receptor potential 1 and 6 contribute to hypoxic pulmonary hypertension through differential regulation of pulmonary vascular functions. *Hypertension (Dallas, Tex. : 1979).* **63**(1), pp.173-180.

Xiao, Y., Peng, H., Hong, C., Chen, Z., Deng, X., Wang, A., Yang, F., Yang, L., Chen, C. and Qin, X. 2017. PDGF Promotes the Warburg Effect in Pulmonary Arterial Smooth Muscle Cells via Activation of the PI3K/AKT/mTOR/HIF-1α Signaling Pathway. *Cellular Physiology and Biochemistry.* **42**(4), pp.1603-1613.

Xu, P., Lu, J., Li, Z., Yu, X., Chen, L. and Xu, T. 2006a. Aggregation of STIM1 underneath the plasma membrane induces clustering of Orai1. *Biochem Biophys Res Commun.* **350**(4), pp.969-976.

Xu, S.Z., Muraki, K., Zeng, F., Li, J., Sukumar, P., Shah, S., Dedman, A.M., Flemming, P.K., McHugh, D., Naylor, J., Cheong, A., Bateson, A.N., Munsch, C.M., Porter, K.E. and Beech, D.J. 2006b. A sphingosine-1-phosphate-activated calcium channel controlling vascular smooth muscle cell motility. *Circ Res.* **98**(11), pp.1381-1389.

Yeromin, A.V., Zhang, S.L., Jiang, W., Yu, Y., Safrina, O. and Cahalan, M.D. 2006. Molecular identification of the CRAC channel by altered ion selectivity in a mutant of Orai. *Nature.* **443**(7108), pp.226-229.

Yuan, J.X., Aldinger, A.M., Juhaszova, M., Wang, J., Conte, J.V., Jr., Gaine, S.P., Orens, J.B. and Rubin, L.J. 1998a. Dysfunctional voltage-gated K+ channels in pulmonary artery smooth muscle cells of patients with primary pulmonary hypertension. *Circulation.* **98**(14), pp.1400-1406.

Yuan, X.-J., Wang, J., Juhaszova, M., Gaine, S.P. and Rubin, L.J. 1998b. Attenuated K+ channel gene transcription in primary pulmonary hypertension. *The Lancet.* **351**(9104), pp.726-727.

Zhang, Y.-n., Xie, B.-d., Sun, L., Chen, W., Jiang, S.-L., Liu, W., Bian, F., Tian, H. and Li, R.-K. 2016. Phenotypic switching of vascular smooth muscle cells in the ‘normal region’ of aorta from atherosclerosis patients is regulated by miR-145. *Journal of Cellular and Molecular Medicine.* **20**(6), pp.1049-1061.

Zhao, Y., Vanhoutte, P. and Leung, S. 2015. Vascular nitric oxide: Beyond eNOS. *Journal of pharmacological sciences.* **129**.

Zhu, X., Chu, P.B., Peyton, M. and Birnbaumer, L. 1995. Molecular cloning of a widely expressed human homologue for the Drosophila trp gene. *FEBS Lett.* **373**(3), pp.193-198.

Zitt, C., Zobel, A., Obukhov, A.G., Harteneck, C., Kalkbrenner, F., Lückhoff, A. and Schultz, G. 1996. Cloning and Functional Expression of a Human Ca2+-Permeable Cation Channel Activated by Calcium Store Depletion. *Neuron.* **16**(6), pp.1189-1196.